



الجامعة الإسلامية بالمدينة المنورة
ISLAMIC UNIVERSITY OF MADINAH

**The Islamic University Journal
of Applied Sciences (IUJAS)**
Refereed periodical scientific journal



Volume: VII Issue: I Year: 2025

بِسْمِ اللَّهِ الرَّحْمَنِ الرَّحِيمِ

Paper version

Filed at the King Fahd National Library No. 8742/1439 on 17/09/1439
AHInternational serial number of periodicals (ISSN) 1658-7936

Online version

Filed at the King Fahd National Library No. 8742/1439 on 17/09/1439
AHInternational Serial Number of Periodicals (e-ISSN) 1658-7944

The Journal's Website

<https://journals.iu.edu.sa/jesc> (New Website)

<https://jesc.iu.edu.sa> (Old Website)

(The views expressed in the published papers reflect the views of the researchers only, and do not necessarily reflect the opinion of the journal)

Publication Rules of the Journal (*)

❖ General rules:



- Report original scientific research (the main results and conclusions must not have been published or submitted elsewhere).
- Fit with the topics of the journal.
- Report novel results, innovative work and show a new scientific contribution.
- Not to bear similarity of more than 25% of a previously published work of the same author(s).
- Follow the rules, regulation and authentic research methodologies.
- Fulfill the required items and the format of the journal provided in appendix below related to the guide for author.
- Opinions expressed in published articles commit the authors themselves only and not necessarily the opinion of the journal.

❖ For all articles:




- The exclusive right to publish and distribute an article, and to grant rights to others, including commercial purposes.
- For open access articles, IU will apply the relevant third-party user license where IU publishes the article on its online platforms.
- The right to provide the article in all forms and media so the article can be used on the latest technology even after publication.
- The authority to enforce the rights in the article, on behalf of an author, against third parties, for example in the case of plagiarism or copyright infringement.




(*) These general rules are explained in details along with other rules for Author's guide in the journal's website:
<https://journals.iu.edu.sa/jesc>

Editorial Board

	<p>Editor-in-Chief: Mohamed Benganem</p> <p>Professor, Faculty of Science, Islamic University of Madinah, Saudi Arabia.</p> <p>Orcid: https://orcid.org/ 0000-0002-2527-8741</p>
	<p>Managing Editor: Ahmad B. Alkhodre</p> <p>Professor, Computer science, Islamic University of Madinah. Saudi Arabia</p> <p>Orcid: https://orcid.org/0000-0001-6168-3552</p>

Editorial Board Members

	<p>Aly Ramadan Seadawy</p> <p>Professor, Mathematics, Taibah University, Madinah, Saudi Arabia</p> <p>Orcid: https://orcid.org/0000-0002-7412-4773</p>
	<p>Reda Abdelmonsef A. Ibrahim</p> <p>Professor, Biology, Kafrelsheikh University, Egypt</p> <p>Orcid: https://orcid.org/0000-0001-6472-5666</p>
	<p>Mussa. A. Said</p> <p>Professor, Chemistry, Islamic University of Madinah, Saudi Arabia.</p> <p>Orcid: https://orcid.org/0000-0003-3073-5449</p>

	<p>Fazal Noor</p> <p>Professor, Computer science and engineering, Islamic University of Madinah. Saudi Arabia</p> <p>Orcid: https://orcid.org/0000-0002-0096-3435</p>
	<p>Basem Rashid Alamri</p> <p>Associate Professor, Electrical Engineering, Taif University, Saudi Arabia</p> <p>https://orcid.org/0000-0002-8667-0042</p>
	<p>Saad Talal Alharbi</p> <p>Professor in Computer Science, ♦ Human Computer Interaction, Faculty of Computers, Taibah University, Saudi Arabia</p> <p>https://orcid.org/0000-0003-0913-8631</p>
	<p>Yazed Alsaawy</p> <p>Associate Professor, Computer and information systems, Islamic University of Madinah. Saudi Arabia</p> <p>Orcid: https://orcid.org/0000-0001-5031-3388</p>
	<p>Abdul Qadir Bhatti</p> <p>Professor, Civil Engineering, Faculty of Engineering, Islamic University of Madinah. Saudi Arabia</p> <p>ORCID Link https://orcid.org/0000-0001-5433-7803</p>

	<p>Shamsuddin Ahmed</p> <p>Professor, Industrial Engineering, The Faculty of Computer and Information Systems Islamic University of Madinah, Saudi Arabia.</p> <p>https://orcid.org/ orcid.org/</p>
---	--

Editorial Secretary

	<p>Ahmad Ziad Al-Zuhaily</p> <p>Assistant Editor, Computer science, Engineer, Islamic University of Madinah. Saudi Arabia</p>
	<p>Abdulrahman Saeed Odeh</p> <p>Assistant Editor, Computer science, Engineer, Islamic University of Madinah. Saudi Arabia</p>



**Islamic University Journal of Applied Sciences
(IUJAS)**



***The Islamic University Journal of Applied Sciences
(IUJAS)***

Issued By

Islamic University of Madinah, Madinah, Saudi Arabia

July 2025

Table of Contents

Article	Page
Effect of Inner Body Shapes on Natural Convection in Square Enclosures	1
Thermodynamic and Mechanistic Insights into Paracetamol Removal from Aqueous Solutions by Graphitic Carbon Nitride Nanosheets	27
Analysis of Magnetic Properties and Critical Current Density of Tl-2234 High-Temperature Superconductor Using AC Magnetic Susceptibility Measurements	44
Ab Initio Study of Structural, Thermal Stability and Electronic Properties of LiRuPO ₄ Compound: A Storage Energy Application	55
Effect of Thermal Configurations in Multi-pipe Heat Exchangers on MHD Natural Convection within a Square Enclosure with Curved Corners	62
Enhanced Catalytic Conversion of Benzaldehyde to Benzoic Acid using Silica Coated Hydrated Iron Oxide (HFO)	74
FTIR Characterization of Date Syrup	97
Influence of Internal Obstacle Size and Position on Magnetohydrodynamic Convection in Square Cavities	110

Chua Chaotic System Parameters Estimation using PSO Algorithm to increase its Dynamics	138
Synergy of (L1, H2, H ∞) norms for Nonlinear Optimal PEMFC Dynamic MIMO Model Reduction using a Novel ANN-BBO Approach	149
Photovoltaic Cells Fed a Dual Open-End Winding Induction Motor Driven by Fuzzy Field-Oriented Control	168
Associated Use of Design of Experiments in Numerical Energy Simulation for Energy Use Optimization in Residential Buildings	181
Power Optimization in MIMO-NOMA VLC Systems Using Fractional and Dynamic Frequency Reuse	209
Application of Machine Learning to Developing an Internet Community Model	227
Diversity of Information Diffusion in Online Social Networks: A Comparative Study	244
Recent Advances in Stability and Seepage Analysis of Earth Dams: A Review Leveraging Numerical Methods and Computational Intelligence	258
Vitamin C as adjuvant therapy in diabetes management	266



Effect of Inner Body Shapes on Natural Convection in Square Enclosures

Wedad Hassan Asiri ¹, Ammar Abdulkadhim ², Halemah Ibrahim Elsaeedy ¹, Nejla Mahjoub Said ^{1,*}

¹ Department of Physics, College of Science, King Khalid University, Abha 61413, Saudi Arabia,
445816980@kku.edu.sa; halsayed@kku.edu.sa; nalmahjoub@kku.edu.sa

² Mechanical Engineering Department, University of Al-Qadisiyah, Al-Qadisiyah 58001, Iraq,
ammar.abdulkadhim@qu.edu.iq

*Corresponding author: (N. Mahjoub), *Email Address*: nalmahjoub@kku.edu.sa

Abstract

This review focuses on the effects of inner body shapes on magnetohydrodynamic (MHD) natural convection heat transfer within square enclosures, summarizing advancements from 2015 to 2024 and identifying future research directions. The influence of different geometric shapes such as circular, square, triangular, and elliptical on heat transfer performance and flow behavior is critically examined. The review also addresses the roles of Rayleigh and Hartmann numbers in modulating convection characteristics in the presence of a magnetic field. Key trends and findings are highlighted, along with observed research gaps, to guide future studies aiming to enhance thermal management in MHD driven systems.

Keywords: Natural convection, Magnetic field, Square enclosures, Inner bodies, Hartmann number.

<https://doi.org/10.63070/jesc.2025.001>

Received 16 March 2025; Revised 25 April 2025; Accepted 03 May 2025.

Available online 15 May 2025.

Published by Islamic University of Madinah on behalf of *Islamic University Journal of Applied Sciences*. This is a free open access article.

1. Introduction

Natural convection is a critical heat transfer process driven by fluid motion from internal forces rather than external sources. This motion arises from buoyancy effects, where temperature-induced density gradients in the fluid initiate flow. Natural convection plays a vital role in numerous applications in engineering, including electrical component cooling, building insulation, solar energy systems, heat exchangers, material drying, and thermal storage. Unlike forced convection, it operates without input of external energy, which makes it inherently energy efficient. Understanding the mechanics of natural convection and evaluating thermal performance are therefore crucial for optimizing these systems. Due to the intricate interactions between the fluid and boundary layers on horizontal and vertical surfaces, this phenomenon presents a complex internal flow problem. A wealth of studies have explored natural convection's heat transfer processes across diverse fields, each aiming to enhance specific performance outcomes [1].

Nanofluids, comprising nanoparticles suspended in base fluids such as water or oil, exhibit enhanced thermal properties that surpass those of conventional fluids. These specialized fluids play a crucial role in advancing heat transfer across various high-demand industrial applications, including solar energy systems, nuclear reactors, and high-performance electronic devices. Their effectiveness in electronic cooling, particularly for critical components like microprocessors, enables sustained high-efficiency performance. The stable dispersion of nanoparticles within the fluid prevents common issues like sedimentation and conduit blockages, which are often associated with larger particles. Future research into nanofluids is anticipated to further enhance thermal efficiency, leading to the development of more compact and efficient heating and cooling systems across industries [2].

Kasaeian et al. [3] have highlighted an important focus in the field of heat transfer, particularly in exploring methods to enhance the performance of energy devices. Among the recent techniques investigated for this purpose are using nanofluids and porous media within heat exchangers. Nanofluids are defined as suspensions of solid nanoparticles in base fluids, such as water. This paper provides a thorough analysis of various studies examining the combined application of nanofluids and porous media within thermal systems, considering diverse geometrical structures and flow regimes.

Das et al. [4] examine internal natural convection heat transfer enclosures characterized by triangular, trapezoidal, parallelogrammatic, and curved walls, incorporating both fluids and porous media. The study also explores enclosures filled with nanofluids. Key parameters such as aspect ratio and the base angle of triangular and rhombic/parallelogrammatic enclosures significantly impact flow distribution. Furthermore, flow patterns are influenced by the number of undulations in the walls and the amplitude-

to-wavelength ratio. The review highlights various strategies aimed at enhancing convection heat transfer performance, providing valuable insights into potential improvement techniques in this area.

Biswal and Basak [5] present a comprehensive review focusing on the investigation of entropy production in natural convection across a range of applications and geometries. The review elucidates the mathematical formulation of fundamental equations, calculation procedures, and methodologies for conducting thorough evaluations. A central challenge addressed is the trade-off between minimizing entropy generation and maximizing heat transfer rates for optimal configurations that enhance energy efficiency. The process of natural convection is crucial for converting renewable energy into usable forms, making the analysis of entropy production an essential consideration in the design of effective energy systems. Furthermore, the article offers insights and discussions aimed at guiding future research on improving energy efficiency within renewable energy systems.

Sadeghi et al. [6] provide a comprehensive review of recent literature on the natural convection of nanofluids across various container geometries, including triangular, trapezoidal, square, circular, and non-traditional forms. The study explores the relationship between thermophysical properties and the geometric configuration of the cases, employing numerical methods and microscopic models to support their findings.

Giwa et al. [7] investigate the control of Heat transmission via spontaneous convection and the flow characteristics of nanofluids in square cavities utilizing magnetic field sources. The study examines the influence of various parameters, For the magnetohydrodynamic (MHD) behaviors of natural convection, these include heat distribution techniques, thermal and concentration boundary conditions, governing parameters, magnetic field types, numerical schemes, thermophysical correlations, nanofluid types, slip conditions, Brownian motion, and thermophoresis.

Hemmat et al. [8] review of natural convective heat transfer in nanofluid-filled cavities influenced by Magnetic Fields (M.F). The paper provides an introduction to nanofluids and their applications, along with an evaluation of numerical studies on magnetic nanofluids. It classifies the literature based on common geometries and effective parameters relevant to nanofluids under free convection and magnetic field effects. The findings indicate that when the magnetic field strength increases, the rate of heat transmission falls.

As the field of natural convection continues to evolve, numerous researchers have contributed to the understanding of heat transfer mechanisms in various geometries and configurations. These studies have significantly advanced our knowledge, exploring factors such as the impact of nanofluids, geometric shapes, and magnetic fields on natural convection performance. The following section will

highlight key findings and methodologies from previous studies, offering a comprehensive overview of the advancements in this area.

2. The most selected parameters in the previous publications

A substantial body of literature discusses natural convection in square enclosures, looking at a number of variables such as the Rayleigh number (Ra), which quantifies the ratio of buoyancy forces to viscous forces. Studies, including those conducted by Chen et al. [9], have demonstrated that increasing the Rayleigh number correlates with an enhanced pace at which heat is transferred by natural convection. Flow patterns and the amount of heat transferred are significantly influenced by the Rayleigh and Hartmann numbers, which serve as critical variables in determining flow behavior; an increase in the Rayleigh number results in more complex flow structures and consequently enhances the heat transfer rate. Studies by Chen et al. [9] show that because a magnetic field inhibits fluid motion, raising the Hartmann number (Ha) lowers heat transfer rates within square cavities. [9, 10]. Numerical modeling and experimental analysis are essential for understanding these dynamics. Techniques For example, the Finite Volume Method (FVM) and the Finite Element Method (FEM) offer valuable predictive insights into temperature variations within the cavity under changing parameters. However, experimental validation is necessary to ensure the reliability of numerical results against actual data, thus enhancing the credibility of the findings [9, 10].

2.1. Conventional Square enclosure in the absence of the magnetic field

Joshi and Pattamatta [11] conducted an experimental investigation on buoyancy induced Using Al_2O_3 /Water and MWCNT/Water nanofluids in a square cavity for convective heat transfer. Their findings revealed that the MWCNT/Water nanofluid exhibited higher Nusselt numbers compared to the Al_2O_3 /nanofluid of water at certain volume fractions. The volume ratios used to create the MWCNT/Water nanofluid were 0.1%, 0.3%, and 0.5%.and the study analyzed its performance across a Rayleigh number range from 7×10^5 to 1×10^7 .

Hidayathulla et al. [12] conducted Examining unstable heat and momentum transfer numerically in a Newtonian fluid that fills a square hole. Their analysis the governing equations are solved using the Harlow-Welch Marker and Cell (MAC) finite difference method. In their study, they varied the thermal Grashof number (Gr) while maintaining a Prandtl number (Pr) of 0.7 (for air) and a Reynolds number (Re) of 10, indicating laminar flow conditions.

Khatamifar et al. [13] investigated the heat transfer from transient conjugate natural convection in a differentially heated cavity numerically, considering the effects of finite partition thickness and thermal conductivity. The study explored a range of Rayleigh numbers (Ra) from 10^3 to 10^8 , with dimensionless partition thicknesses between 0.05 and 0.2 and the partition's thermal conductivity ratio to the liquid between 0.1 and 1000. The results illustrate the transient development of natural convection flow within the partitioned cavity for various values of Ra (10^3 , 10^4 , 10^5 , 10^6 , 10^7 and 10^8), k_r (0.1, 1, 10, 100, 500 and 1000) and T_p (0.05, 0.1 and 0.2), all maintaining a constant $X_p = 0.5$, $H/L = 1$, and Prandtl number (Pr) of 0.71.

Kumar et al. [14] investigated the beginning of the free thermal flow of a silver nanofluid in a closed square chamber with isothermal vertical walls at different temperatures and adiabatic horizontal walls filled with a saturated porous media. Using the Boussinesq approximation and the Darcy model, they used a two-temperature nonequilibrium model to construct the governing boundary layer equations. Setting $\Gamma = 1$, $\gamma = 1$, $H = 10$, $Ra = 100$, and $R_d = 0.3$ as default settings for the emerging flow parameters was done by the study.

2.2. Conventional Square Enclosure without Inner Body in the Presence of a Magnetic Field

Many researchers have examined the impact of magnetic fields on natural convection heat transfer within square enclosures. For instance, Mansour and Bakier [15] a computational investigation of the flow of nanofluids and the heat transfer related to natural convection in the presence of an angled magnetic field and varied thermal boundary conditions. They looked into a lot of different things, like the heat source's length ($0.2 < B < 0.8$), its location ($0.3 < D < 0.7$), the solid volume fraction ($0 < \phi < 0.2$), the inclination angle ($0 < \Phi < 90^\circ$), the Rayleigh number ($10^3 < Ra < 10^5$), the Prandtl number ($Pr = 6.2$), and the Hartmann number ($0 < Ha < 100$). The results indicated that the inclination angle significantly affects heat distribution; as the angle increases, convection is enhanced, and the presence of nanoparticles improves conduction, thereby increasing the heat transfer rate. The study concluded that the temperature distribution within the cavity is influenced solely by the volume fraction of nanoparticles, a finding supported by numerous prior studies.

Furthermore, the article presents a numerical investigation of natural convection under the influence of magnetic fields in a square container containing an ethylene glycol-copper nanofluid, employing COMSOL Multiphysics for simulation. The authors concluded that the impact of the Hartmann number on the y-directional velocity component are more pronounced than those of the Rayleigh number. With a Prandtl number set at $Pr = 151$, they inspected the impacts of the relevant parameters, specifically the Rayleigh and Hartmann numbers, on the flow dynamics and heat transfer performance

within the enclosure. The study also highlighted that enhanced ethylene glycol nanofluids exhibited superior thermal conductivity compared to other nanoparticles, as noted by Ben Hamida and Charrada [16].

Sreedevi and Reddy [17] looked over heat transport by natural convection in a square cavity with a Tiwari-Das nanofluid model, considering magnetic field and thermal radiation. The system's nonlinear partial differential equations were solved using the finite difference method. Their study investigated the impact of a number of critical parameters on the flow and heat transfer properties of the TiO_2 -EG nanofluid, such as the volume fraction ($0.01 \leq \phi \leq 0.09$), the magnetic field parameter ($1.0 \leq M \leq 3.0$), the Rayleigh number ($100 \leq Ra \leq 1000$), the radiation parameter ($0.1 \leq R \leq 0.9$), the Reynolds number ($0.1 \leq Re \leq 0.5$), the Rayleigh number ($1.0 \leq Pr \leq 7.2$), and the Prandtl number ($5.2 \leq Pr \leq 7.2$). Graphs show how these factors affect the behavior of nanofluids and how they affect the performance of heat transfer and flow.

Haritha et al. [18] analyzed free convection heat transfer in a porous medium-filled square cavity saturated with nanofluids containing various nanoparticles, under the influence of an applied magnetic field and viscous dissipation. Using Darcy's model, they applied the finite element method based on the weighted Galerkin residual scheme to solve the governing equations. Parameters included Rayleigh number ($Ra = 50, 200, 800$), magnetic field parameter ($M = 0.5, 1, 1.5$), and nanofluid volume fraction ($\phi = 0.02, 0.2, 0.6$). The study found that heat transfer and flux density were highest with Cu nanoparticles and lowest with Al_2O_3 , with Figure 1 illustrating changes in heat transfer for varying Eckert numbers and volume fractions of nanoscale copper ($\phi = 0.02, 0.2, 0.6$).

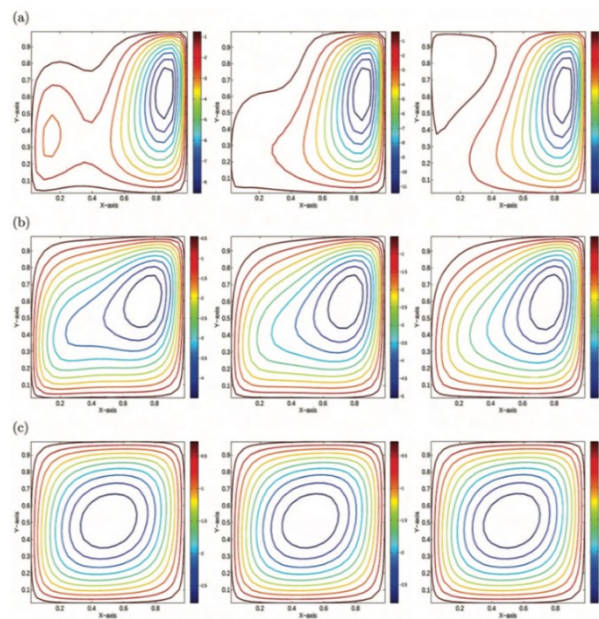


Figure 1. streamlines with $Ec = 0.01, 0.02, \text{ and } 0.03$ and $\phi = 0.02, 0.2, \text{ and } 0.6$, respectively [18].

Mehryan et al. [19] showed how a periodic magnetic field affected the Fe_3O_4 nanofluid's natural convection and entropy production in a square cavity. To solve the governing partial differential equations, they used the Galerkin finite element method, concentrating on dimensionless parameters like the nanoparticle volume fraction ($\phi = 0-0.08$), period number ($\lambda = 0.1 - 1.0$), Rayleigh number ($Ra = 10^3-10^6$), and Hartmann number ($Ha = 0-50$), which indicates the amplitude of the magnetic field. The results showed that total entropy production (St) under the periodic magnetic field was higher than that under a uniform magnetic field, regardless of Ha and λ values.

Mansour et al. [20] treated entropy generation, MHD convective flow, and heat transfer in a square porous cavity. Using finite difference methodology, they assessed parameters such as the magnetic field ($0 \leq Ha \leq 100$), heat source ($-4.0 \leq Q \leq 4.0$), volume fraction of nanoparticles ($0.03 \leq \phi \leq 0.1$), and permeability ($10^{-6} \leq Da \leq 10^{-2}$). Their findings showed that adding copper nanoparticles achieved the highest heat transfer rates among the materials tested.

Al Kalbani et al. [21] studied the effects of a directed magnetic field on the heat transfer and fluid flow properties of natural convection in an inclined square container filled with different nanofluids containing different forms of nanoparticles. The governing non-dimensional partial differential equations were solved using the weighted Galerkin residual finite element technique. Their study considered different values for the following: inclination angle ($0^\circ \leq \delta \leq 90^\circ$), Hartmann number ($0 \leq Ha \leq 60$), magnetic field orientation ($0^\circ \leq \gamma \leq 90^\circ$), Rayleigh number ($10^3 \leq Ra \leq 10^6$), and nanoparticle volume percent ($0 \leq \phi \leq 0.05$).

Mahapatra and Parveen [22] analyzed spontaneous convection flow in a copper-water nanofluid-filled container with a sinusoidal top wall that was differentially heated and subjected to a continuous vertical magnetic field. A constant Prandtl number of $Pr = 6.2$ was maintained throughout their investigation as they investigated a number of parameters, such as Rayleigh number ($10^2 \leq Ra \leq 10^6$), sinusoidal wall amplitude ($0 \leq a \leq 0.4$), nanoparticle volume fraction ($0.0 \leq \phi \leq 0.2$), and Hartmann number ($0 \leq Ha \leq 50$), using the Bi-CGStab method for numerical simulations. Increasing the Rayleigh number from 10^2 to 10^4 improved flow strength, heat transfer rate, and entropy formation, according to their findings, both with and without magnetic fields.

Uddin et al. [23] assessed natural convection heat transfer using a heterogeneous dynamical model in a square jar filled with a copper oxide nanofluid, exposed to a uniform magnetic field, and having a wavy top wall. They discussed the effects of several control parameters on the flow and thermal fields, such as Hartmann number, magnetic field inclination angle, gravitational inclination angle, solid

volume fraction, nanoparticle diameter, and dimensionless time, by applying the Galerkin finite element method to the governing equations. Their study's main goal was to assess the improvement in heat transmission under various parameter combinations for real-world uses.

Rajarithnam and Chamkha [24] investigated the effects of partial convection in a water-based nanofluid within a square cavity subjected to a magnetic field. They addressed the governing unstable non-dimensional partial differential equations using the SIMPLE algorithm in conjunction with the finite volume method. Their results, presented in Figure 2, encompass various relevant parameters, including the Hartmann number ($0 \leq Ha \leq 100$), Rayleigh number ($10^2 \leq Ra \leq 10^6$), solid volume fraction ($0.0 \leq \phi \leq 0.04$), and three distinct opening configurations. The study reveals that the vertical velocity component at the cavity's center achieves its maximum when both buoyancy forces and velocity boundary conditions are absent, influencing the flow behavior across all positions.

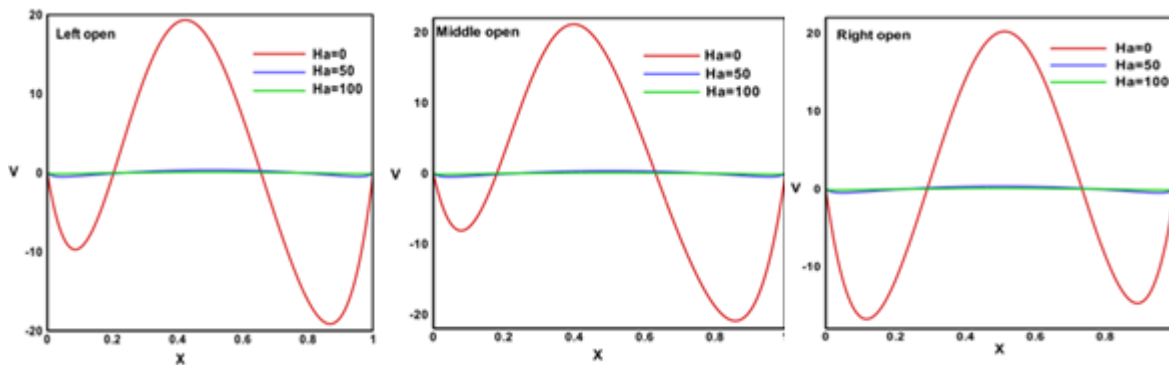


Figure 2. Vertical velocity profiles for various Hartmann numbers and opening positions at $Y=0.5$, with $Ra = 10^4$ and $\phi = 0.02$. [24]

Devi et al. [25] explored the influence of magnetic wire on the viscous Casson flow in a container with opposing temperature gradients and cadaveric upper and lower walls, utilizing the MAC technique for numerical analysis. The work concentrated on controlling the following fluid flow parameters: Casson fluid parameter $\beta = 0 - \infty$, Hartmann number ($0 - 8$), Rayleigh number ($10^3 - 10^5$), and a constant Prandtl number $Pr = 6.8$. According to their research, buoyant force causes the temperature gradient to rise.

Nishad et al. [26] analyzed heat transfer and flow in a copper-water nanofluid-filled undulating container while subjected to a magnetic field using a parallel grid-free method. Using the element-free Galerkin method (EFGM), the equations governing the transport phenomena were numerically solved. Their findings were obtained for a number of parameters, such as the magnetic field inclination angle ($0^\circ \leq g \leq 80^\circ$), nanoparticle volume fraction ($0 \leq w \leq 0.5$), Rayleigh number ($10^3 \leq Ra \leq 10^5$), and

Hartmann number ($0 \leq Ha \leq 60$). The study found that a greater Hartmann number Lorentz force suppresses fluid motion and lowers the cavity's heat transfer rate, which in turn reduces stream functions.

2.3. Previous studies with inner Bodies

2.3.1 Square inner Body

Munshi et al. [27] performed a numerical analysis of a square's natural convection container characterized by an irregularly unheated bottom wall and a hot mass in the shape of a square. They explored the influence of various Prandtl numbers (0.71, 1.0, and 1.5) on Heat transmission and fluid flow within the enclosure. Their parametric analysis revealed that as the Prandtl number increases, free convection is suppressed, leading to a predominance of heat transmission via conduction. The results indicated that the heat transfer processes, temperature distribution, and flow characteristics inside the cavity are significantly influenced by the Rayleigh number as well as the magnetic field's strength.

Boulahia et al. [28] performed a numerical investigation into the natural thermal transfer of a nanofluid (Cu-water) within a square enclosure containing a cold rectangular obstacle. They employed the finite difference method to solve the transport equations using the Alternating Direction Implicit (ADI) approach. Their study identified several dimensionless groups, including the height of the obstacle ($0.125 \leq H \leq 0.5$), the Rayleigh number ($10^3 \leq Ra \leq 10^6$), and the volume fraction of nanoparticles ($0 \leq \phi \leq 0.2$), while maintaining the obstacle's width at $0.25L$ and the Prandtl number for pure water at $Pr = 6.2$. The findings demonstrated that heat transfer was enhanced by increasing both the Rayleigh number and the volume fraction of nanoparticles.

2.3.2 Elliptical inner body

Munshi et al. [29] examined how fluid flow and heat transfer were affected by magnetohydrodynamic (MHD) natural convection in a square cavity that held an electrically conducting fluid with an elliptical adiabatic mass. Using numerical techniques, the study produced predictions over a wide range of Hartmann numbers (Ha) and Rayleigh numbers (Ra) while keeping the Prandtl number constant at 0.733. The governing equations pertaining to the parameters of heat production were solved using the finite element method. The findings indicated that an increase in the Rayleigh number enhances the buoyant force, necessitating a stronger magnetic field to reduce natural convection effects, particularly at lower Rayleigh numbers.

Adegun et al. [30] conducted a numerical investigation of normal convective heat transfer and fluid flow within a concentric square ring featuring an internal inclined elliptical cylinder subjected to isothermal heating and cooling, as illustrated in Figure 3. The researchers employed the Galerkin finite

element method to solve the governing elliptic conservation equations. The parameters evaluated included Rayleigh numbers ranging from 10^3 to 10^3 and elliptical orientation angles varying from 0° to 90° . Additionally, an aspect ratio was considered, with values ranging from 1 to 3. This study provides insights into the effects of geometric configuration and thermal conditions on convective heat transfer characteristics.

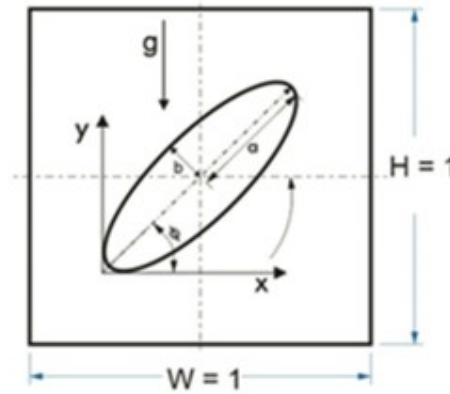


Figure 3. Physical coordinate geometry. [30]

Cho, Ha et al. [31] investigated two-dimensional natural convection numerically in a square container with a vertical arrangement of two elliptical cylinders. They used the Immersed Boundary Method (IBM), which combines the FVM and Immersed Boundary Method, to precisely depict the cylinders' virtual wall limits. There was a range of 0.25 to 4.00 for the elliptical cylinders' aspect ratio (AR) and 10^4 to 10^6 for their Rayleigh number (Ra). The study's main objective was to examine how the elliptical cylinders' varying aspect ratios affected the flow and heat fields.

Zhang et al. [32] focused on the numerical study of steady natural convection in a cold outer square enclosure containing a hot inner elliptical cylinder. They utilized the multiscale element-free Galerkin (VMEFG) method to conduct their numerical investigations. The study maintained a constant Prandtl number ($Pr = 0.71$) and an eccentricity of $\epsilon = 0.9$ while examining different values of the dimensionless major axis ($a = 0.2, 0.3, 0.4$), the inclined angle of the outer square enclosure ($\gamma = 0^\circ, 15^\circ, 30^\circ, 45^\circ$), and the Rayleigh number ($Ra = 10^3, 10^4, 5 \times 10^4, 10^5, 10^6$). Their study's findings are shown in Figure 4, which highlights the intricate relationship between the system's thermal dynamics and geometric design.

Park et al. [33] considered two-dimensional natural convection numerically in a square enclosure with a vertical array of heated circular and elliptical cylinders, with Rayleigh numbers between $10^4 \leq Ra \leq 10^6$. Their study kept the Prandtl number constant at 0.7. The cylinder walls' borders were precisely

captured by them using an immersed boundary approach. Their primary objective was to determine the impacts of the elliptical cylinder's inclination angle in this design statistically (Figure 5).

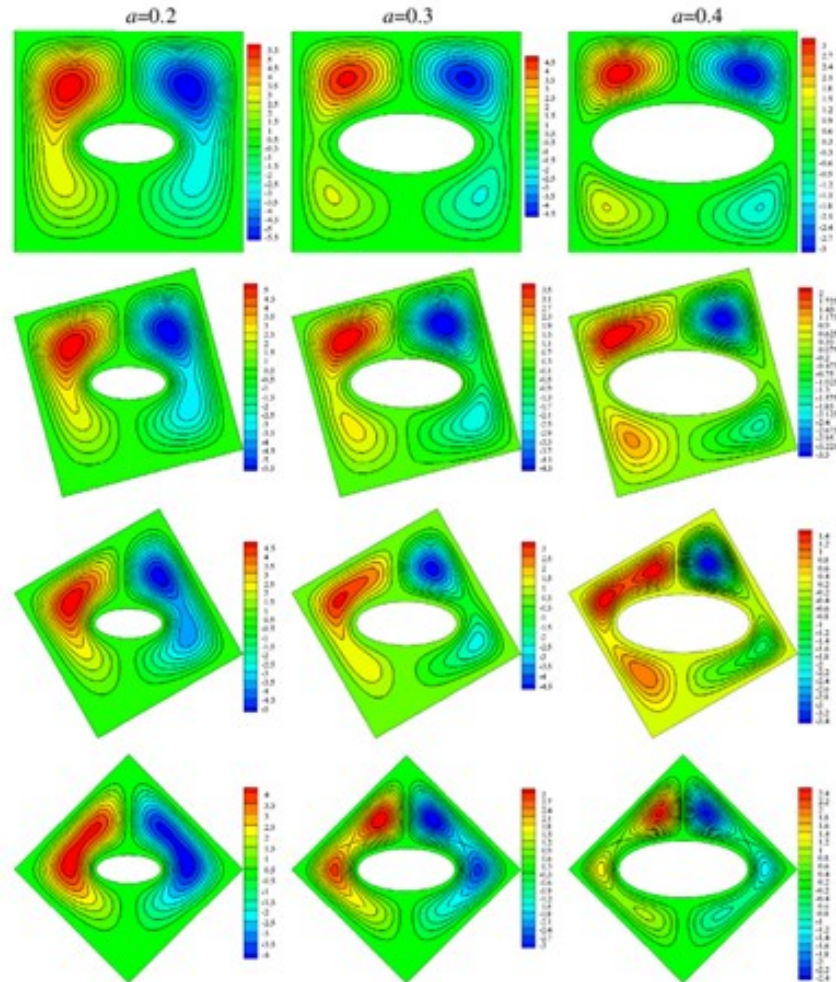


Figure 4. Streamlines for various a and γ values when $Ra = 5 \times 10^4$ [32]

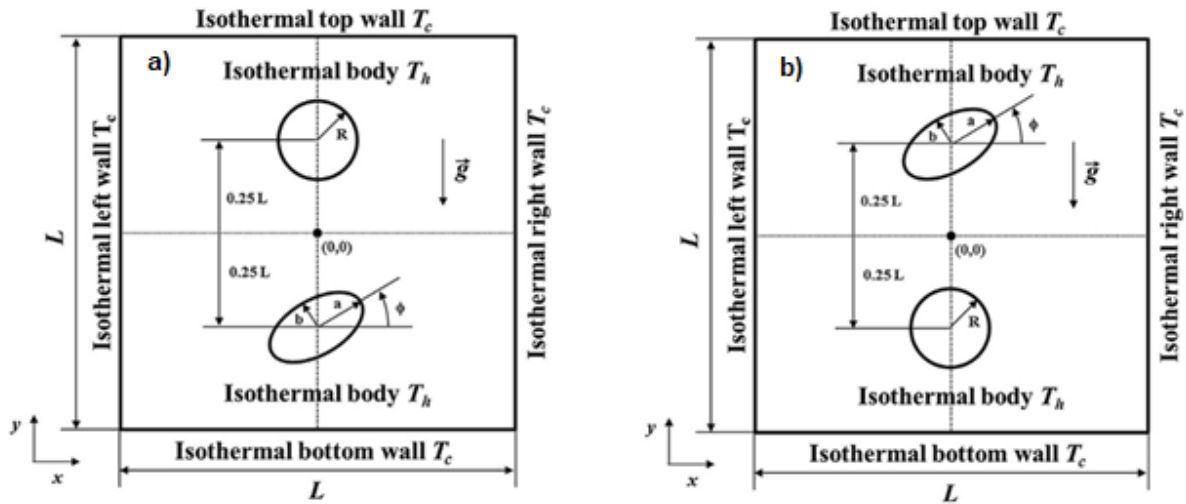


Figure 5. Physical model boundary conditions, coordinate system, and computational domain: (a) lower elliptical cylinder; (b) upper elliptical cylinder.[33]

Ibrahim et al. [34] studied natural convection inside cavities to introduce nanoparticles into the core fluid to improve heat transmission in various package forms. For their numerical computations, they used the COMSOL software, which is based on the Galerkin finite element method. The following parameters were used: the radius of the inner circle ($R = 0.15$), the radii of the inner elliptical cylinder ($R_x = 0.2$ and $R_y = 0.15$), the inclination angles ($-45^\circ, -30^\circ, 0^\circ, 30^\circ, 45^\circ$), the solid volume percent ($\phi = 0.05$), and the Rayleigh number Ra (varying from 10^3 to 10^6).

2.3.3 Inner circular body and cylinder

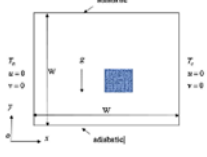
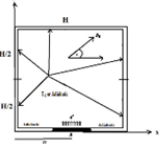
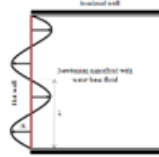
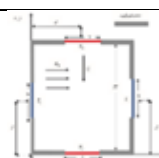
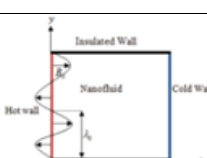
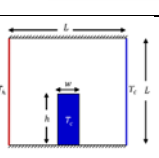
The magneto-hydrodynamic (MHD) heat transfer problem in a square open cavity containing a heated circular cylinder at the center has been investigated by Hossain et al. [35]. This study's objective is to explain how MHD affects flow and thermal fields when a heated circular cylinder is present, as visualized through graphical representations. They employed a numerical technique based on the weighted Galerkin residual method for finite element formulation. Heat transfer and fluid movement within the cavity depend on the Rayleigh number (Ra), Hartmann number (Ha), and heat flux (q). In this inquiry, the Prandtl number is fixed at $Pr = 0.72$ and the heat flow $q = 100$. The ranges for Ra and Ha are 10^3 to 10^4 and 0 to 400, respectively.

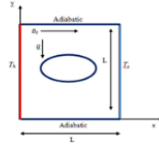
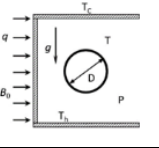
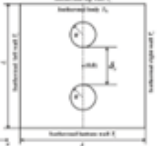

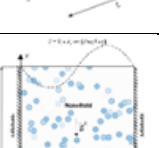
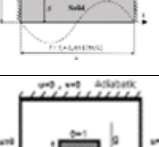
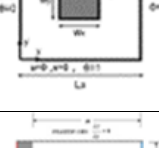
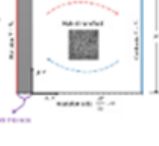

Shruti et al. [36] evaluated the combined effects of variations in Darcy and Rayleigh numbers on natural convection around two vertically arranged heated porous cylinders of different diameters in a square container. They employed the D_2Q_9 model to perform numerical simulations using a Boltzmann network. The following variations in flow and heat transmission were analyzed in relation to the Darcy

2.4. Triangular inside a square with MHD

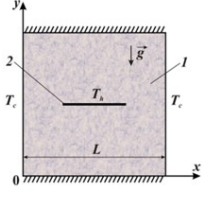
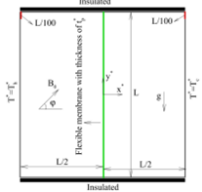
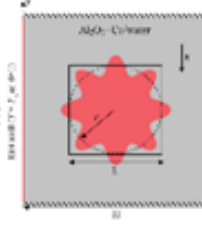
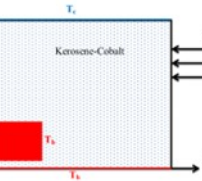
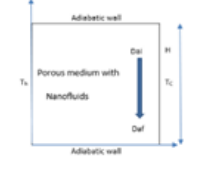
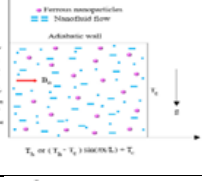
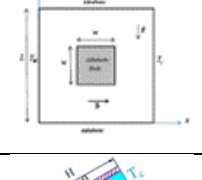
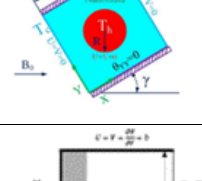
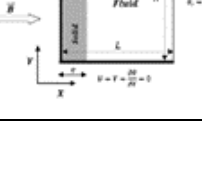
Vijaybabu and Dhinakaran [39] explored, using the Boltzmann method, the natural convection heat transfer between a cold square cavity and a hot, permeable triangular cylinder affected by a magnetic field.. The study studied the effects of key parameters, specifically Rayleigh numbers ranging from 10^4 to 10^6 and Darcy numbers from 10^{-6} to 10^{-2} . For Hartmann numbers $Ha= 0, 25$, and 50 , the results are shown using streamlines, velocity profiles, isotherms, and local, surface, and mean Nusselt numbers. The results indicate that the high viscous resistance within the porous triangular cylinder at $Da = 10^{-6}$ effectively blocks fluid flow through it, regardless of Rayleigh or Hartmann values.

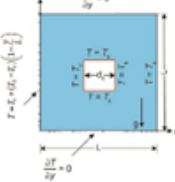
Table 1. A summary of the Effect of Different Internal and external bodies in Square Containers on Natural Convection

Reference	Major topic	Enclosure shape	Results
[14]	Natural convection in silver nanofluid		<ul style="list-style-type: none"> - Increasing H and y strengthens solid isotherms - Average Nusselt number increases.
[15]	MHD Natural convection		<ul style="list-style-type: none"> - Average Nusselt number increases with solid volume fraction.
[19]	MHD entropy generation in a ferrofluid		<ul style="list-style-type: none"> - Periodic magnetic field leads to higher total entropy than uniform field - Effect is consistent across Ha and λ values
[20]	MHD convection		<ul style="list-style-type: none"> - Fluid speed decreases significantly with increasing Hartmann number
[26]	MHD convection with nanofluid		<ul style="list-style-type: none"> - Heat transfer rate increases with magnetic field inclination angle (up to critical angle)
[28]	Natural convection with cold obstacle		<ul style="list-style-type: none"> - Heat transfer improves with increasing Rayleigh number, nanoparticle volume fraction, and cold mass height

[29]	MHD convection with elliptic shape		- Buoyant force increases with Rayleigh number
[35]	MHD free convection		- Heat flow decreases with increasing Hartmann number
[40]	Double inner cylinders		- Flow transitions from stable to unstable at $Ra = 10^6$.
[41]	Nanofluid convection in porous media		- Stable natural convection behavior in inclined porous media
[42]	Conjugate natural convection		- Phase deviation significantly alters flow and temperature distribution
[43]	Hot obstacle convection		Nusselt number decreases on cold walls - Shape coefficient increases as surface ratio decreases
[44]	Hybrid nanofluid flow		- Local Nusselt number sharply drops from bottom to top of cavity
[45]	Heated cylinder convection		- Average Nusselt number increases with thermal conductivity ratio at specific Grashof numbers
[46]	Nanofluid with thermal source		- Nanoparticles <6% enhance heat transfer at high Ra and inclination angles <30°

[47]	Wavy surfaces		<ul style="list-style-type: none"> - Nu_m and Be increase while S_t decreases with increasing ϕ and aa_w.
[48]	Round barriers & curved corners		<ul style="list-style-type: none"> - Central temperature increases by 400% as barrier radius grows from 0.1 to 0.3
[49]	MHD convection under slope		<ul style="list-style-type: none"> - Stream function and vorticity decrease with Ha - Increase with Ra
[50]	Alumina nanofluid convection		<ul style="list-style-type: none"> - Heat transfer improves with higher solid volume fraction and Rayleigh number
[51]	Finned nanofluid cavity		<ul style="list-style-type: none"> - Heat transfer enhanced by increasing Rayleigh number, fin number, location, and length
[52]	Sinusoidal heating		<ul style="list-style-type: none"> - Flow strength decreases when $N > 1$
[53]	3D convection		<ul style="list-style-type: none"> - Vertical plates transfer heat more efficiently than horizontal plates across Ac and Ha
[54]	Entropy and inclination effects		<ul style="list-style-type: none"> - Nusselt number and entropy more sensitive to tilt angle (θ) than Hartmann number

[55]	Heated plate in porous cavity		- Higher radiation parameter, plate length, and Darcy number enhance heat transfer
[56]	MHD convection with flexible membrane		- Hartmann number changes affect heat transfer and membrane shape
[57]	Hybrid nanofluid & wavy cylinder		- Convective flow increases with Ra and conductivity - Decreases with Hartmann number and undulation effects
[58]	Ferrofluid in porous cavity		- Nusselt number increases with Darcy and Rayleigh numbers - Decreases with Hartmann number
[59]	Nanofluid in porous cavity		- Low permeability reduces flow and heat transfer - High permeability improves nanofluid mobility
[60]	Uneven wall heating		- Flow rate declines with higher nanoparticle concentration and Hartmann number
[61]	MHD with adiabatic flow		- Magnetic field significantly alters flow at high Prandtl and Hartmann numbers
[62]	Inclined cavity with circular baffle		- Heat transfer rate increases on right wall and decreases on left with increased inclination angle
[63]	Uneven heat source with solid wall		- Fluid flow strength rises with Ra_f regardless of k_f

[64]	Heated cylinder		<ul style="list-style-type: none"> - Right-wall local Nusselt number increases with Ra - Stronger eddies observed
------	-----------------	---	---

2.5. Inner body studies without MHD

Cho et al. [40] conducted a numerical investigation into two-dimensional natural convection within a square container, examining various configurations of two internal cylinders at Rayleigh numbers ranging from $10^3 \leq Ra \leq 10^6$. Their simulations, based on the immersed boundary method, provided precise solutions. Results indicated that, at lower Rayleigh numbers, the solutions remained stable regardless of variations in δ . However, when the Rayleigh number increased to $Ra = 10^6$, the solutions became unstable for configurations with $\delta_h = 0.1 L$, and $\delta_d = 0.2L$. Additionally, the average Nusselt number $\langle \overline{Nu_c} \rangle$ increased by approximately 29.2%, 12.8%, and 30.8% for the cases of δ_v , δ_h , and δ_d , respectively. Similarly, the average values of $\langle \overline{Nu_{En}} \rangle$ rose by around 27.7%, 12.4%, and 31.0% in these configurations.

Alsabery et al. [41] used a finite difference approach to study natural convection heat transport in an inclined square cavity with a porous layer and a nanofluid. The study concentrated on the effects of the following important parameters: cavity inclination angle ($0^\circ \leq \phi \leq 90^\circ$), phase deviation ($0 \leq \gamma \leq \pi$), amplitude ratio ($0 \leq \varepsilon \leq 1$), porous layer thickness ($0.1 \leq S \leq 0.9$), the Darcy number ($10^{-5} \leq Da \leq 10^{-3}$), and nanoparticle volume fraction ($0 \leq \phi \leq 0.2$). Rayleigh number ($Ra_{bf} = 10^4, 10^5$) and Prandtl number ($Pr_{bf} = 6.2$). Average Nusselt number values were computed for various ϕ and S values, revealing significant flow structure enhancement at lower inclination angles. The flow was observed as a cell in the nanofluid layer that rotates clockwise.

In another study, Alsabery [42] investigated conjugate natural convection in a square cavity including sinusoidal temperature fluctuations along the horizontal walls, focusing on a nanofluid devoid of an interior body. The study employed the finite difference method to investigate the effects of various parameters, including Rayleigh number ($10^5 \leq Ra \leq 10^8$), nanoparticle volume fractions ($0 \leq \phi \leq 0.2$), phase deviations ($0 \leq \gamma \leq \pi$), amplitude ratio ($0 \leq \varepsilon \leq 1$), wall-to-nanofluid thermal conductivity ratio ($0.44 \leq k_r \leq 23.8$), and wall thickness-to-height ratio ($0 \leq S \leq 0.7$).

Alturaihi et al. [44] explored natural convection within a heated cylinder located in a square cavity filled with a porous medium. Key parameters, including the Prandtl number ($Pr = 0.7$) and Darcy number ($Da = 0.01$), were selected for analysis. Five levels of porosity ($\varepsilon = 0.4, 0.5, 0.55, 0.6$ and 0.65)

were considered, in addition to different values of the thermal conductivity ratio (kr) and Grashof number (Gr). Their findings revealed that increased porosity significantly enhances convective heat transfer within the cavity by strengthening fluid flow patterns. In a related study, Ghalambaz et al. [45] numerically investigated Spontaneous natural convection in a square cavity containing a hybrid nanofluid of Ag, MgO, and water. They treated Rayleigh numbers between 10^3 and 10^5 and a nanoparticle volume percent between 0 and 0.02 with a fixed Prandtl number of $Pr = 6.2$ by solving the governing equations using the finite element method. According to their findings, hybrid nanofluids do not always improve the cavity's natural convection heat transmission.

El Mehdi et al. [46] studied the lattice Boltzmann flow behavior of a Cu/water nanofluid in a square cavity. Their simulations covered various Rayleigh numbers (from 10^5 to 0.5×10^7), cavity inclination angles (0° to 90°), and nanoparticle volume percentages (0 – 8%). The study assessed the effects of these parameters on fluid rheology and isothermal distributions within the cavity. Findings revealed that adding 8% nanoparticles effectively prevented flow separation.

Cho et al. [47] presented the natural convection of nanofluids in a porous cavity with wavy top and bottom surfaces and a vertical wall that is partially heated. They conducted numerical simulations to examine the effects of several parameters, including the irreversibility distribution (χ) divided by the Bejan number (Be), the length of the heated wall surface (L_H^*), the surface wavy amplitude (a_w), the Rayleigh number (Ra), the Darcy number (Da), the porosity (ϵ), and the nanoparticle volume fraction (ϕ). The average Nusselt number (Nu_m), energy flow vector distribution, and total entropy generation (S_t) were among the main topics of their investigation. Using the Tri-Diagonal Matrix Algorithm (TDMA), they were able to solve the governing systems.

2.6. Conventional Enclosure without inner body

Tezer-Sezgin et al. [49] surveyed natural convection in a square container containing hydrated aluminum oxide (Al_2O_3) when an external oblique magnetic field was present. This study employed two numerical techniques, specifically DRBEM, or Dual Reciprocity Boundary Element Method, and FEM, or Finite Element Method, utilizing different meshing types. The research focused on the effects of key flow parameters, including Rayleigh (Ra) and Hartmann (Ha) numbers, inclination angle (γ), and solid volume fraction (ϕ) are among them. Rayleigh and Hartmann numbers were as high as 10^7 and 300, respectively, for numerical simulations with inclination angles of $\gamma = 0, \pi/4, \pi/3$, and $\pi/2$ with a solid volume fraction range of $0 \leq \phi \leq 0.20$. Notably, as illustrated in Figure 8, the DRBEM achieved mesh independence with 200 fixed boundary elements, while the FEM used 1152 quadratic triangular elements to ensure similar independence.

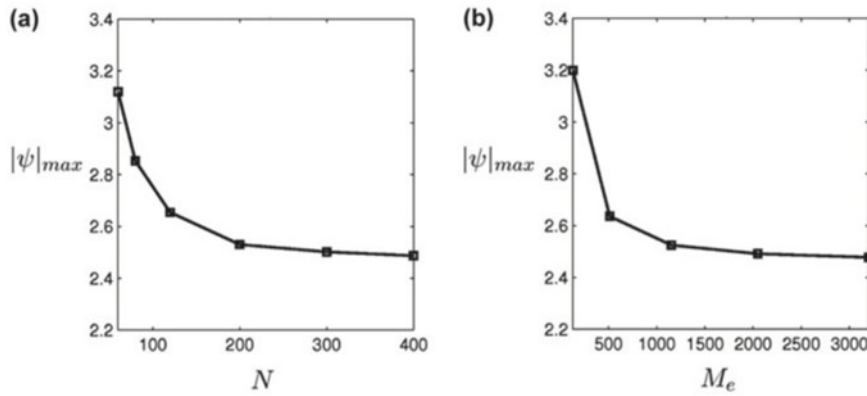


Figure 8. For $Ha = 60$, $Ra = 10^5$, and $\phi = 0.03$ when $\gamma = 0$, the grid dependency is (a) DRBEM, (b) FEM.. [49]

Bouamoud and Houat [50] treated natural convection flow in two dimensions in a square hole with vertical walls that varied somewhat. Using a coupled population technique and the thermal grid Boltzmann method, they performed numerical simulations on a homogeneous nanofluid with alumina nanoparticles and pure water ($Pr = 6.2$) at solid volume fractions of $\phi = 0.02, 0.04, 0.06$, and 0.08 in the laminar domain. According to their findings, the solid volume percentage of the nanoparticles has a major impact on the improvement of the heat transfer rate inside the cavity.

Chandra et al. [52] examined how different levels of polarization affected natural convection using the SIMPLER and Brinkman-extended-Darcy models, as well as the Alternating Direction Implicit (ADI) approach in certain situations. Eight non-dimensional parameters the Prandtl number (Pr), the Darcy number (Da), the Rayleigh number (Ra), the permeability ratio (K^*), the direction angle (ϕ), the thermal conductivity ratio (K^*), the periodicity parameter (N), and the porosity (ϵ) governed the velocity field and heat transfer rate, which they studied in relation to temperature.

Purusothaman et al. [53] investigated the finite volume method numerically for fluid flow and heat transfer in a cubic cavity caused by three-dimensional natural convection. Among the many parameters they calculated were the Hartmann number ($0 \leq H \leq 300$), the Prandtl number ($0.025 \leq Pr \leq 25$), and the plate's various aspect ratios ($AC = 0.5$ and 1.0). while keeping the Rayleigh number fixed at 10^7 . They concluded that both the heat transfer rate and the flow characteristics within the cavity are significantly influenced by the strength of the magnetic field for Prandtl numbers greater than or equal to 0.71 .

In another study, Mamourian et al. [54] investigated natural convection heat transfer and entropy generation in Al_2O_3 aqueous nanofluids within a square cavity subjected to an inclination angle and a constant axial magnetic field. They employed the governing equations are numerically solved using the finite volume approach. and utilized response surface methodology (RSM) for effective parameter

analysis. The impacts of inclination angles (0° , 30° , and 90°), Hartmann numbers (0, 10, 30, and 50), and Rayleigh numbers (10^3 , 10^5 , and 10^6) were investigated. At $\theta = 0.05$, they also investigated the effects of the inclination angle, Hartmann number, and Rayleigh number

Sivaraj and Sheremet [55] conducted A numerical simulation of thermal radiation and natural convection in a square porous cavity with a thin, isothermal heated plate sitting either vertically or horizontally in the middle. They solved the governing equations using an evenly layered grid structure and the finite volume approach. Their results showed that the radiation parameter, plate length, and Darcy number all considerably improve overall heat transmission in the cavity. A Rayleigh number of $Ra = 10^7$ was used to examine the effects of the radiation parameters ($0 \leq R_d \leq 2$), plate length ($0.25 \leq D \leq 0.75$), and Darcy number ($10^{-5} \leq Da \leq 10^{-2}$)

Mehryan et al. [56] numerically investigated unstable natural convection in a square cavity separated by an elastic membrane that is impermeable. They modeled the fluid-membrane interaction using the arbitrary Lagrangian-Eulerian (ALE) technique in conjunction with the finite element method. Their study included a parametric analysis of key factors, including the Rayleigh number ($10^5 - 10^8$), Hartmann number (0 - 200), and magnetic field direction ($0 - 180^\circ$). Their results indicated that the rotation of the fluid flow was enhanced with increasing magnetic field strength and directional adjustments.

2.7. inner body studies with MHD

Javed et al. [58] presented numerical results for free convection within a square container with a ferrofluid-saturated porous media inside, subjected to a constant magnetic field applied along the x-axis. They carried out numerical simulations using the finite element approach across a variety of flow parameters, such as the Rayleigh number, Hartmann number, Darcy number, and Prandtl number. Using constant values of $Pr = 6.2$, $Ra = 10^6$, $Ha = 30$, and nanoparticle volume fraction $\phi = 0.15$, their study specifically assessed the effects of the Darcy number on heat transmission and flow architectures at different blockage locations. They observed that as the Darcy parameter increases, the strength of clockwise rotation intensifies, as indicated by the maximum current function magnitude (ψ). Specifically, ψ values reached 0.09, 1.06, and 1.89 for $Da = 10^{-5}$, 10^{-4} , and 10^{-3} respectively, in the case of left boundary condition (LBC), while in the right boundary condition (RBC), they were 0.007, 0.08 and 1.9 for $Da = 10^{-5}$, 10^{-4} and 10^{-3} , respectively.

Sivaraj and Sheremet [65] considered natural convection within an inclined porous cavity containing a centrally placed, heat-conducting solid body, under the influence of a magnetic field oriented from various directions. They used a finite volume method on a uniformly meshed grid to solve the coupled

partial differential equations governing fluid flow and heat transfer. The study focused on the effects of Hartmann number ($0 \leq Ha \leq 50$), cavity inclination angle ($-45^\circ \leq \xi \leq 90^\circ$), and magnetic field inclination angle ($0^\circ \leq \gamma \leq 180^\circ$) on flow properties, isotherms, and the average Nusselt number. Results showed that the average Nusselt number peaks at a cavity inclination of $\xi = 30^\circ$ without a magnetic field, while in the presence of a magnetic field ($Ha = 50$), it reaches its maximum at $\xi = 45^\circ$.

2.8. Previous studies without inner body and Without MHD

Cherifa et al. [59] treated the Galerkin finite element method was used to solve the dimensionless equations and the Buongiorno model was used to study laminar natural convection in a porous square cavity filled with nanofluids. They analyzed various parameters with a cavity height of $H = 2m$, a Prandtl number of 5.82, Rayleigh number of 10^5 , Darcy number of 10^{-2} , Lewis number of 1, and Brownian motion, thermophoresis, and buoyant force ratios all set to 0.1 ($N_r = N_b = N_t = 0.1$). Further investigations were performed across ranges of Rayleigh ($10^4 \leq Ra \leq 10^6$), Darcy ($10^{-5} \leq Da \leq 10^{-2}$), and an initial Darcy number that decreased to a final Darcy number of 10^{-5} .

Acharya et al. [60] explored the hydrothermal behavior of radiative aqueous nanofluid Fe_3O_4 within a square chamber. They employed the Galerkin finite element technique after transforming the main dimensional equations into dimensionless form using similarity variables. Their simulations checked the impacts of the following fixed values: $Ra=10^4$, $Ha = 5$, $N = 0.5$, $\phi = 0.02$, $Pr = 6.2$, thermal radiation ($0.5 \leq N \leq 1.5$), Rayleigh number ($10^3 \leq Ra \leq 10^5$), and Hartmann number ($5 \leq Ha \leq 25$).

Scott et al. [66] studied the impact of various volume concentrations of AL_2O_3 -MWCNT (10:90) water-based hybrid nanofluids on heat transfer performance within a square cavity. Their findings indicated that hybrid nanofluids considerably outperformed single-nanoparticle nanofluids, with a maximum enhancement of 43.78% in heat transfer efficiency (h_{av}) at a concentration of 0.10 vol% at $50^\circ C$ compared to deionized (DI) water. As Rayleigh numbers increased, the average Nusselt number (Nu_{av}) increased as well. for AL_2O_3 -MWCNT hybrid samples across different concentrations and base fluids, highlighting hybrid nanofluids' potential as effective heat transfer fluids.

3. Conclusion

This review presents a comprehensive overview of recent studies on natural convection heat transfer (NCHT) within square enclosures, both with and without the presence of internal bodies, and examines the influence of magnetic fields on fluid flow and thermal performance. Covering research conducted between 2015 and 2024, the review highlights key advancements as well as gaps in current knowledge, emphasizing areas where further investigation could significantly advance the field.

The analysis identifies several promising directions for future research:

- While circular internal bodies have been extensively examined, elliptical geometries remain underexplored. Further studies in this area may uncover distinctive thermal behaviors arising from their unique flow patterns.
- Most existing literature focuses on single-body configurations, or occasionally, systems with two or four bodies. Extending this research to include multi-body arrangements could improve understanding of complex thermal interactions and contribute to optimized enclosure designs for enhanced heat transfer.
- Future investigations should consider how varying magnetic field strengths and orientations interact with different internal body shapes, as this may provide new strategies for enhancing or controlling heat transfer.
- Unconventional geometries, such as pentagonal and hexagonal bodies, have the potential to significantly influence fluid dynamics and heat distribution. Exploring these shapes may reveal novel approaches for maximizing heat transfer within enclosures.

In summary, although substantial progress has been made in understanding NCHT in square enclosures, the outlined research directions are critical for further advancing theoretical models and practical applications. Continued exploration in these areas will enable more precise control over heat transfer processes, particularly in systems influenced by internal geometries and magnetic fields, and will contribute meaningfully to both engineering and environmental technologies.

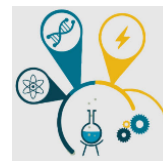
References

- [1] Tasnim, S., A. Mitra, H. Saha, M.Q. Islam, and S. Saha, MHD conjugate natural convection and entropy generation of a nanofluid filled square enclosure with multiple heat-generating elements in the presence of Joule heating. *Results in Engineering*, 17 (2023) :100993.
- [2] Wang, X.-Q. and A.S. Mujumdar, A review on nanofluids-part I: theoretical and numerical investigations. *Brazilian journal of chemical engineering*, 25 (2008) 613-630.
- [3] Kasaeian, A., R. Daneshzarian, O. Mahian, L. Kolsi, A.J. Chamkha, S. Wongwises, and I. Pop, Nanofluid flow and heat transfer in porous media: a review of the latest developments. *International Journal of Heat and Mass Transfer*, 107 (2017) 778-791.
- [4] Das, D., M. Roy, and T. Basak, Studies on natural convection within enclosures of various (non-square) shapes—A review. *International Journal of Heat and Mass Transfer*, 106 (2017) 356-406.
- [5] Biswal, P. and T. Basak, Entropy generation vs energy efficiency for natural convection based energy flow in enclosures and various applications: a review. *Renewable and Sustainable Energy Reviews*, 80 (2017) 1412-1457.
- [6] Sadeghi, M.S., N. Anadalibkhah, R. Ghasemiasl, T. Armaghani, A.S. Dogonchi, A.J. Chamkha, H. Ali, and A. Asadi, On the natural convection of nanofluids in diverse shapes of enclosures: an exhaustive review. *Journal of Thermal Analysis and Calorimetry*, (2020) 1-22.
- [7] Giwa, S., M. Sharifpur, M. Ahmadi, and J. Meyer, A review of magnetic field influence on natural convection heat transfer performance of nanofluids in square cavities. *Journal of Thermal Analysis and Calorimetry*, 145 (2021) 2581-2623.
- [8] Hemmat Esfe, M., M. Afrand, and S. Esfandeh, Investigation of the effects of various parameters on the natural convection of nanofluids in various cavities exposed to magnetic fields: a comprehensive review. *Journal of Thermal Analysis and Calorimetry*, 140 (2020) 2055-2075.
- [9] Chen, S., W. Gong, and Y. Yan, Conjugate natural convection heat transfer in an open-ended square cavity partially filled with porous media. *International Journal of Heat and Mass Transfer*, 201 :124 .8p. 368-380.

- [10] Belhaj, S. and B. Ben-Beya, Numerical simulation of unsteady MHD natural convection of CNT-water nanofluid in square cavity heated sinusoidally from below. *Particulate Science and Technology*, 37(7) (2019) 851-870.
- [11] Joshi, P.S. and A. Pattamatta, Enhancement of natural convection heat transfer in a square cavity using MWCNT/Water nanofluid: an experimental study. *Heat and Mass Transfer*, 54 (2018) 2295-2303.
- [12] Hidayathulla Khan, B.M., K. Venkatadri, O. Anwar Bég, V. Ramachandra Prasad, and B. Mallikarjuna, Natural convection in a square cavity with uniformly heated and/or insulated walls using Marker-and-Cell Method. *International Journal of Applied and Computational Mathematics*, 4 (2018) 1-18.
- [13] Khatamifar, M., W. Lin, and L. Dong, Transient conjugate natural convection heat transfer in a differentially-heated square cavity with a partition of finite thickness and thermal conductivity. *Case Studies in Thermal Engineering*, 25 (2021) 100952.
- [14] Kumar, R., A. Bhattacharyya, and G. Seth, Heat transfer analysis on unsteady natural convection flow of silver nanofluid in a porous square cavity using local thermal non-equilibrium model. *Indian Journal of Physics*, (2021). 1-14.
- [15] Mansour, M. and M. Bakier, Influence of thermal boundary conditions on MHD natural convection in square enclosure using Cu–water nanofluid. *Energy Reports*, 1 (2015) 134-144.
- [16] Ben Hamida, M. and K. Charrada, Natural convection heat transfer in an enclosure filled with an ethylene glycol–copper nanofluid under magnetic fields. *Numerical Heat Transfer, Part A: Applications*, 67(8) (2015) 902-920.
- [17] Sreedevi, P. and P.S. Reddy, Effect of magnetic field and thermal radiation on natural convection in a square cavity filled with TiO₂ nanoparticles using Tiwari-Das nanofluid model. *Alexandria Engineering Journal*, 61(2) (2022)-1529-1541.
- [18] Haritha, C., B.C. Shekar, and N. Kishan, MHD natural convection heat transfer in a porous square cavity filled by nanofluids with viscous dissipation. *J. Nanofluids*, 7(5) (2018) 928-938.
- [19] Mehryan, S., M. Izadi, A.J. Chamkha, and M.A. Sheremet, Natural convection and entropy generation of a ferrofluid in a square enclosure under the effect of a horizontal periodic magnetic field. *Journal of Molecular Liquids*, 263 (2018) 510-525.
- [20] Mansour, M., S. Siddiqua, R.S.R. Gorla, and A. Rashad, Effects of heat source and sink on entropy generation and MHD natural convection of Al₂O₃-Cu/water hybrid nanofluid filled with square porous cavity. *Thermal Science and Engineering Progress*, 6 (2018) 57-71.
- [21] Al Kalbani, K.S., M.M. Rahman, S. Alam, N. Al-Salti, and I.A. Eltayeb, Buoyancy induced heat transfer flow inside a tilted square enclosure filled with nanofluids in the presence of oriented magnetic field. *Heat Transfer Engineering*, 39(6) (2018) 511-525.
- [22] Mahapatra, T. and R. Parveen, Entropy generation in MHD natural convection within curved enclosure filled with Cu-water nanofluid. *Journal of Nanofluids*, 8(5) (2019)1051-1065.
- [23] Uddin, M., S. Rasel, M. Rahman, and K. Vajravelu, Natural convective heat transfer in a nanofluid-filled square vessel having a wavy upper surface in the presence of a magnetic field. *Thermal Science and Engineering Progress*, 19 (2020) 100660.
- [24] Rajarathinam, M. and A. Chamkha, Effect of partial open on natural convection heat transfer of CNT–water nanofluid in a square cavity with magnetic field. *The European Physical Journal Plus*, 136(1) (2021) 52.
- [25] Devi, T.S., C.V. Lakshmi, K. Venkatadri, and M.S. Reddy, Influence of external magnetic wire on natural convection of non-Newtonian fluid in a square cavity. *Partial Differential Equations in Applied Mathematics*, 4 (2021) 100041.
- [26] Nishad, S., S. Jain, and R. Bhargava, Numerical simulation of natural convection within wavy square enclosure filled with nanofluid under magnetic field using EFGM with parallel algorithm. *International Journal of Numerical Methods for Heat & Fluid Flow*, 31(12) (2021) 3505-3526.
- [27] Munshi, M.J.H., A. Bhuiyan, and M. Alim, A numerical study of natural convection in a square enclosure with non-uniformly heated bottom wall and square shape heated block. *Am. J. Eng. Res.(AJER)*,4(5) (2015) 124-137.
- [28] Boulahia, Z., A. Wakif, and R. Sehaqui, Natural convection heat transfer of the nanofluids in a square enclosure with an inside cold obstacle. *International journal of innovation and scientific research*, 21(2) (2016) 367-375.
- [29] Munshi, M.J.H., M. Alim, A. Bhuiyan, and G. Mostafa, Effect of a Magneto-hydrodynamic Natural Convection in a Square Cavity with Elliptic Shape Adiabatic Block. *American Journal of Engineering Research*, 4 (2015) 10-22.
- [30] Adegun, I., S. Ibitoye, and A. Bala, Effect of selected geometric parameters on natural convection in concentric square annulus. *Australian Journal of Mechanical Engineering*, 20(4) (2022) 1142-1153.
- [31] Cho, H.W., M.Y. Ha, and Y.G. Park, Natural convection in a square enclosure with two hot inner cylinders, Part II: The effect of two elliptical cylinders with various aspect ratios in a vertical array. *International Journal of Heat and Mass Transfer*, 135 (2019) 962-973.
- [32] Zhang, P., X. Zhang, J. Deng, and L. Song, A numerical study of natural convection in an inclined square enclosure with an elliptic cylinder using variational multiscale element free Galerkin method. *International Journal of Heat and Mass Transfer*, 99 (2016) 721-737.
- [33] Park, S.H., Y.M. Seo, M.Y. Ha, and Y.G. Park, Natural convection in a square enclosure with different positions and inclination angles of an elliptical cylinder Part I: A vertical array of one elliptical cylinder and one circular cylinder. *International Journal of Heat and Mass Transfer*, 126 (2018) 173-183.

- [34] Ibrahim, M.N.J., K.A. Hammoodi, A.D. Abdulsahib, and M.A. Flayyih, Study of natural convection inside inclined nanofluid cavity with hot inner bodies (circular and ellipse cylinders). *International Journal of Heat and Technology*, 40(3) (2022) 699-705.
- [35] Hossain, S.A., M. Alim, and S. Saha, A finite element analysis on MHD free convection flow in open square cavity containing heated circular cylinder. *American Journal of Computational Mathematics*, 5(01) (2015) 41-54.
- [36] Shruti, B., M.M. Alam, A. Parkash, and S. Dhinakaran, Darcy number influence on natural convection around porous cylinders in an enclosure using Darcy-Brinkman-Forchheimer model: LBM study. *Case Studies in Thermal Engineering*, 45 (2023) 102907.
- [37] Ahmed, S.E. and A.M. Aly, Natural convection in a nanofluid-filled cavity with solid particles in an inner cross shape using ISPH method. *International Journal of Heat and Mass Transfer*, 141 (2019) 390-406.
- [38] Ali, M.M., R. Akhter, and M. Alim, Hydromagnetic natural convection in a wavy-walled enclosure equipped with hybrid nanofluid and heat generating cylinder. *Alexandria Engineering Journal*, 60(6) (2021) 5245-5264.
- [39] Vijaybabu, T. and S. Dhinakaran, MHD Natural convection around a permeable triangular cylinder inside a square enclosure filled with Al₂O₃- H₂O nanofluid: An LBM study. *International Journal of Mechanical Sciences*, 153 (2019) 500-516.
- [40] Cho, H.W., Y.M. Seo, G.S. Mun, M.Y. Ha, and Y.G. Park, The effect of instability flow for two-dimensional natural convection in a square enclosure with different arrays of two inner cylinders. *International Journal of Heat and Mass Transfer*, 114 (2017) 307-317.
- [41] Alsabery, A., A. Chamkha, H. Saleh, and I. Hashim, Natural convection flow of a nanofluid in an inclined square enclosure partially filled with a porous medium. *Scientific reports*, 7(1) (2017) 2357.
- [42] Alsabery, A., A. Chamkha, H. Saleh, and I. Hashim, Heatline visualization of conjugate natural convection in a square cavity filled with nanofluid with sinusoidal temperature variations on both horizontal walls. *International Journal of Heat and Mass Transfer*, 100 (2016) 835-850.
- [43] Rahmati, A. and A. Tahery, Numerical study of nanofluid natural convection in a square cavity with a hot obstacle using lattice Boltzmann method. *Alexandria engineering journal*, 57(3) (2018) 1271-1286.
- [44] Alturaihi, M.H., L. Jassim, A.R. ALguboori, L.J. Habeeb, and H.K. Jalghaf, Porosity influence on natural convection heat transfer from a heated cylinder in a square porous enclosure. *Journal of Mechanical Engineering Research and Developments*, 43(6) (2020) 236-254.
- [45] Ghalambaz, M., A. Doostani, E. Izadpanahi, and A.J. Chamkha, Conjugate natural convection flow of Ag-MgO/water hybrid nanofluid in a square cavity. *Journal of Thermal Analysis and Calorimetry*, 139(3) (2020) 2321-2336.
- [46] El Mehdi, B., Lattice Boltzmann Computations of Natural Convection Heat Transfer of Nanofluid in a Square Cavity Heated by Protruding Heat Source. *Journal of Thermal Science and Engineering Applications*, 20 (2020) 001000-1.
- [47] Cho, C.-C., Effects of porous medium and wavy surface on heat transfer and entropy generation of Cu-water nanofluid natural convection in square cavity containing partially-heated surface. *International Communications in Heat and Mass Transfer*, 119 (2020) 104925.
- [48] Hamid, M., M. Usman, W.A. Khan, R.U. Haq, and Z. Tian, Characterizing natural convection and thermal behavior in a square cavity with curvilinear corners and central circular obstacles. *Applied Thermal Engineering*, 248 (2024) 123133.
- [49] Tezer-Sezgin, M., C. Bozkaya, and Ö. Türk, Natural convection flow of a nanofluid in an enclosure under an inclined uniform magnetic field. *European Journal of Computational Mechanics*, 25(1-2) (2016) 2-23.
- [50] Bouamoud, B. and S. Houat, Mesoscopic study of natural convection in a square cavity filled with alumina-based nanofluid. *Energy Procedia*. 139 (2017) 758-765.
- [51] Arjun, K. and K. Rakesh, MHD natural convection heat transfer in a nanofluid filled finned square cavity. *Journal of Mechanical Engineering Research & Developments*, 40 (2017) 481-489.
- [52] Chandra, H., P. Bera, and A.K. Sharma, Natural convection in a square cavity filled with an anisotropic porous medium due to sinusoidal heat flux on horizontal walls. *Numerical Heat Transfer, Part A: Applications*, 77(3) (2020) 317-341.
- [53] Purusothaman, A., H. Oztop, N. Nithyadevi, and N.H. Abu-Hamdeh, 3D natural convection in a cubical cavity with a thermally active heater under the presence of an external magnetic field. *Computers & Fluids*, 128 (2016) 30-40.
- [54] Mamourian, M., K.M. Shirvan, and I. Pop, Sensitivity analysis for MHD effects and inclination angles on natural convection heat transfer and entropy generation of Al₂O₃-water nanofluid in square cavity by Response Surface Methodology. *International Communications in Heat and Mass Transfer*, 79 (2016) 46-57.
- [55] Sivaraj, C. and M.A. Sheremet, Natural convection coupled with thermal radiation in a square porous cavity having a heated plate inside. *Transport in Porous Media*, 114(2016) 843-857.
- [56] Mehryan, S., M. Ghalambaz, M.A. Ismael, and A.J. Chamkha, Analysis of fluid-solid interaction in MHD natural convection in a square cavity equally partitioned by a vertical flexible membrane. *Journal of Magnetism and Magnetic Materials*, 424 (2017) 161-173.
- [57] Tayebi, T. and A.J. Chamkha, Effects of various configurations of an inserted corrugated conductive cylinder on MHD natural convection in a hybrid nanofluid-filled square domain. *Journal of Thermal Analysis and Calorimetry*, 143(2) (2021) 1399-1411.
- [58] Javed, T., Z. Mehmood, and Z. Abbas, Natural convection in square cavity filled with ferrofluid saturated porous medium in the presence of uniform magnetic field. *Physica B: condensed matter*, 506 (2017) 122-132.

- [59] Cherifa, B., B. Mohamed, M. Abderrahim, and K. Fatima-Zohra, Unsteady natural convection in a porous square cavity saturated by nanofluid using buongiorno model: variable permeability effect on homogeneous porous medium. *CFD Letters*, 14(7) (2022) 42-61.
- [60] Acharya, N., Finite element analysis on the hydrothermal pattern of radiative natural convective nanofluid flow inside a square enclosure having nonuniform heated walls. *Heat Transfer*, 51(1) (2022) 323-354.
- [61] Hussein, A.K., H. Ashorynejad, S. Sivasankaran, L. Kolsi, M. Shikholeslami, and I. Adegun, Modeling of MHD natural convection in a square enclosure having an adiabatic square shaped body using Lattice Boltzmann Method. *Alexandria Engineering Journal*, 55(1) (2016) 203-214.
- [62] Li, Z., A.K. Hussein, O. Younis, M. Afrand, and S. Feng, Natural convection and entropy generation of a nanofluid around a circular baffle inside an inclined square cavity under thermal radiation and magnetic field effects. *International Communications in Heat and Mass Transfer*, 116 (2020) 104650.
- [63] Bouchair, R., A. Bourouis, and A. Omara, Conjugate MHD natural convection in a square cavity with a non-uniform heat source thick solid partition. *International Journal for Computational Methods in Engineering Science and Mechanics*, (5)23 (2022) 396-411.
- [64] Sivarami Reddy, C., V. Ramachandra Prasad, and K. Jayalakshmi, Numerical simulation of natural convection heat transfer from a heated square cylinder in a square cavity filled with micropolar fluid. *Heat Transfer*, (6)50(2021:) 5267-5285.
- [65] Sivaraj, C. and M.A. Sheremet, MHD natural convection in an inclined square porous cavity with a heat conducting solid block. *Journal of Magnetism and Magnetic materials*, 426 (2017) 351-360.
- [66] Scott, T.O., D.R. Ewim, and A.C. Eloka-Eboka, Experimental investigation of natural convection Al₂O₃-MWCNT/water hybrid nanofluids inside a square cavity. *Experimental Heat Transfer*, 37(3) (2024) 294-312.



Thermodynamic and Mechanistic Insights into Paracetamol Removal from Aqueous Solutions by Graphitic Carbon Nitride Nanosheets

Ayyob M. Bakry ¹, Abdulmajeed M. Jabbari ², Zeinhom H. Mohamed ¹, Mohammed B. Hawsawi ³,
Nasser Amri ¹ and R E Azooz ^{1,*}

¹ Department of Physical Sciences, Chemistry Division, College of Science, Jazan University, P.O. Box. 114, Jazan 45142, Kingdom of Saudi Arabia.

² Department of Pharmaceutical Chemistry, College of Pharmacy, University of Hail, 81442, Hail, Saudi Arabia

³ Department of Chemistry, Faculty of Science, Umm Al-Qura University, Makkah 21955, Saudi Arabia

*Corresponding author: (R E Azooz), Email Address: rramadan@jazanu.edu.sa

Abstract

This study explored the potential of raw graphitic carbon nitride (g-C₃N₄) as a low-cost adsorbent for removing paracetamol from water. The material's structure and properties were analyzed using various techniques, including X-ray diffraction (XRD), Fourier-transform infrared spectroscopy (FTIR), Ultraviolet visible (UV-Vis) spectroscopy, and Transmission electron microscopy (TEM). Factors affecting paracetamol adsorption, such as pH, contact time, adsorbent dosage, and initial paracetamol concentration, were investigated. The results showed that a maximum adsorption capacity of 1.1 mg/g was achieved at 25 °C within 60 minutes. Both Langmuir and pseudo-second-order models accurately described the adsorption behavior. Density functional theory (DFT) confirms the stability of the complex formed between Paracetamol and Graphitic carbon nitride (g-C₃N₄), and Molecular dynamics (MD) and FTIR confirm the stability of H-bond formation a high adsorption energy of -38.640×10^{-3} kcal/mol. These findings suggest that modified graphitic carbon nitride can be a promising, eco-friendly, and affordable adsorbent for removing pharmaceutical contaminants from water.

Keywords: Paracetamol, Adsorption, g-C₃N₄, Density functional theory, Molecular dynamics, Adsorption energy and Removal.

<https://doi.org/10.63070/jesc.2025.002>

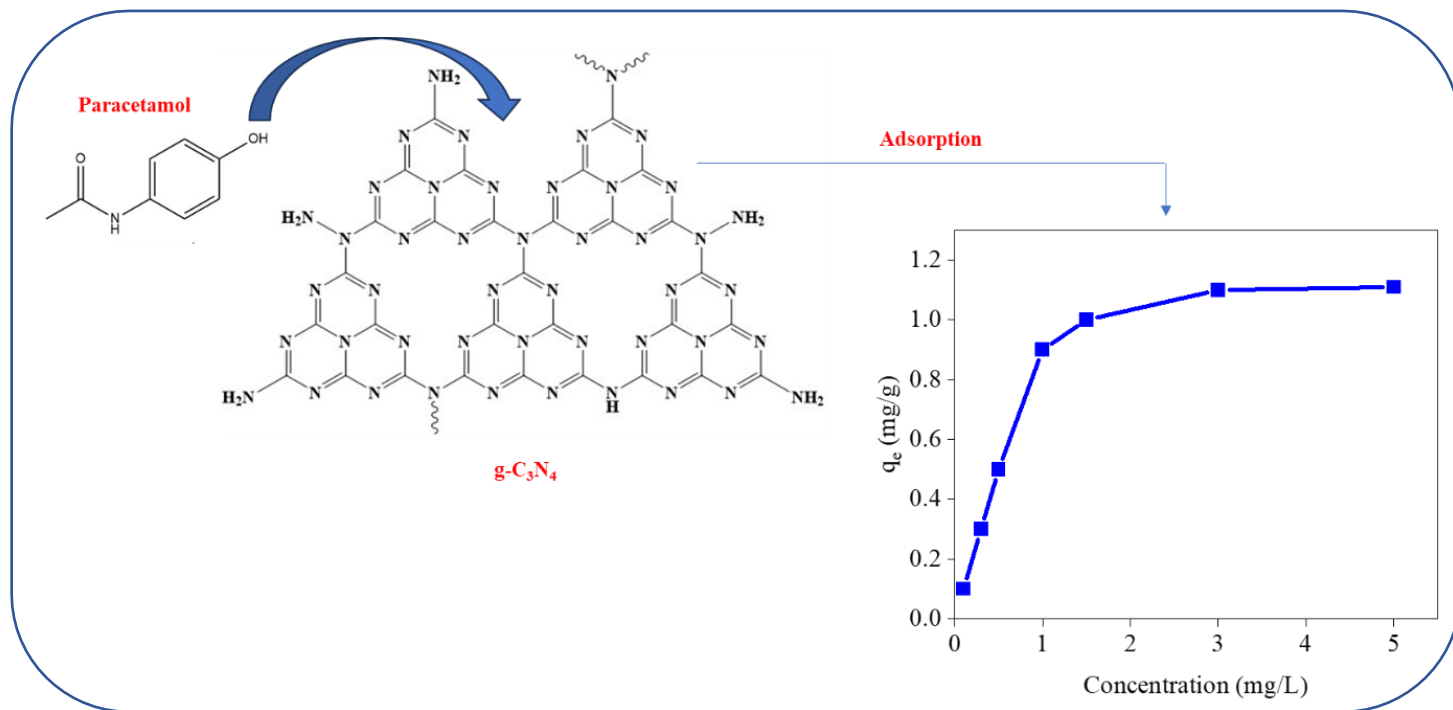
Received 09 February 2025; Revised 25 April 2025; Accepted 08 May 2025.

Available online 16 May 2025.

Published by Islamic University of Madinah on behalf of *Islamic University Journal of Applied Sciences*. This is a free open access article.

Graphical Abstract

TOF



1. Introduction

Pharmaceutical water contamination is a global concern due to the widespread use of pharmaceuticals and their potential to pollute water sources. These contaminants can enter water bodies through various pathways, including wastewater discharges, improper disposal, and agricultural runoff. The presence of pharmaceuticals in water can have adverse effects on aquatic ecosystems, human health, and the environment.[1, 2] Pharmaceuticals can disrupt the hormonal balance of aquatic organisms, leading to reproductive issues and developmental abnormalities. In humans, exposure to contaminated water can have long-term health consequences, such as antibiotic resistance and endocrine disruption. Addressing pharmaceutical water contamination requires a multi-faceted approach, including improved wastewater treatment, proper medication disposal practices, and the development of sustainable pharmaceutical manufacturing processes.[2, 3] Among these contaminants, paracetamol is particularly concerning due to its frequent detection in water and wastewater. While concentrations may seem low, higher levels have been found in waste effluents, highlighting the need for effective removal methods to mitigate these environmental impacts.[4, 5]

Numerous techniques, such as photodegradation, membrane filtration, and ozonation, have been utilized for wastewater treatment.[5, 6] However, adsorption has emerged as a preferred method due to its simplicity, effectiveness, and environmental friendliness. This process involves the capture of pollutants onto the surface of an adsorbent material. One of the key advantages of adsorption is its versatility. Adsorbents can be modified to selectively target specific contaminants, like paracetamol, even in the presence of other molecules. This makes it particularly suitable for industrial wastewater treatment. Furthermore, adsorbed paracetamol can often be regenerated using appropriate eluents, allowing for the reuse of the adsorbent and reducing waste generation.[7, 8] A variety of materials have been explored for paracetamol adsorption, including activated carbon,[9] nitrogen-doped porous carbons,[10] and various frameworks.[11] The choice of adsorbent depends on factors like the specific properties of paracetamol and the desired water quality.

g-C₃N₄ is a promising alternative to activated carbon for adsorption applications. Unlike activated carbon, which is expensive and difficult to regenerate, g-C₃N₄ offers a more cost-effective and sustainable solution. This two-dimensional polymer boasts a honeycomb structure similar to graphene, composed of carbon and nitrogen atoms arranged in a triazine ring unit. This unique structure provides exceptional thermal and chemical stability, as well as a high surface area. The layered structure and abundant surface area of g-C₃N₄ create numerous binding sites for various molecules, making it an effective adsorbent. Moreover, the high nitrogen content of g-C₃N₄ enables strong interactions with pollutants, particularly those containing polar functional groups.[12-14] This combination of factors positions g-C₃N₄ as a promising adsorbent for a wide range of contaminants, including dyes, heavy metals, and organic pollutants from wastewater and air.

This study aimed to investigate the effectiveness of g-C₃N₄ as an adsorbent for removing paracetamol from aqueous solutions. Various experimental parameters were evaluated to optimize the adsorption process, including pH (2-12), concentration (0.1-5 ppm), temperature (25-50 °C), and contact time (5-480

min). Kinetic, isothermal, and thermodynamic analyses were conducted to gain a comprehensive understanding of the adsorption mechanism and equilibrium. Additionally, spectroscopic, DFT calculations and MD simulation were employed to explore the interaction between paracetamol and g-C₃N₄ during adsorption.

2. Experimental Section

2.1. Chemicals: All chemicals employed in this investigation were commercially accessible and exhibited high purity. Melamine (99.8%), sodium hydroxide (99%), hydrochloric acid (37%), methanol (99.5%), isopropanol (99.5%), ethanol (99.5%), and paracetamol (99.9%) were utilized. Deionized water (DIW) was the solvent for preparing the Paracetamol stock solution.

2.2. Synthesis of SNP-g-C₃N₄: Bulk g-C₃N₄ was synthesized by heating 10 grams of melamine in a ceramic crucible at 520°C for 4 hours in a digital furnace, using a heating rate of 5°C per minute. To produce g-C₃N₄ nanosheets, 100 milligrams of bulk g-C₃N₄ were dispersed in 1000 milliliters of a 3:1 isopropanol-to-water mixture. The suspension was then sonicated for 24 hours at room temperature. After centrifugation and washing with deionized water (3 times) and ethanol (1 time), the nanosheets were dried in an oven at 100°C for 6 hours.

2.3. Preparations of paracetamol solutions: 0.2 grams of paracetamol were precisely weighed and dissolved in 200 milliliters of DDW. The solution was then sonicated for 30 minutes to ensure complete dissolution and homogeneity. This stock solution was subsequently used to prepare solutions of varying concentrations (0.1, 0.3, 0.5, 1, 1.5, 3, and 5 ppm) in 100-milliliter volumetric flasks using DIW. A UV-visible spectrophotometer was employed to determine the concentration profile of paracetamol at its maximum absorbance wavelength (λ_{max}) of 249 nanometers.

2.4. Adsorption Optimization and Analysis: To determine optimal adsorption conditions, a series of experiments were conducted using a one-factor-at-a-time approach. Variables explored included pH (2-12), g-C₃N₄ dose (10 mg /10 mL), contact time (5-180 minutes), and temperature (25-50 °C). Drug solutions were prepared in separate glass flasks and incubated with the desired adsorbent dose. After reaching equilibrium, the solutions were centrifuged and filtered before analysis. The adsorption capacity (q_e), and adsorption efficiency (% R_e) were calculated using **Equations (1, and 2)**. To identify the rate-limiting step, kinetic studies were conducted. The adsorption rate of paracetamol was determined by quantifying the adsorbed amount at varying time intervals (q_t). **Equation (3)** was used for this calculation.

$$q_e = \frac{(C_0 - C_e)}{C_0} \times \frac{V}{W} \quad (1)$$

$$\%R_e = \frac{(C_0 - C_e)}{C_0} \times 100 \quad (2)$$

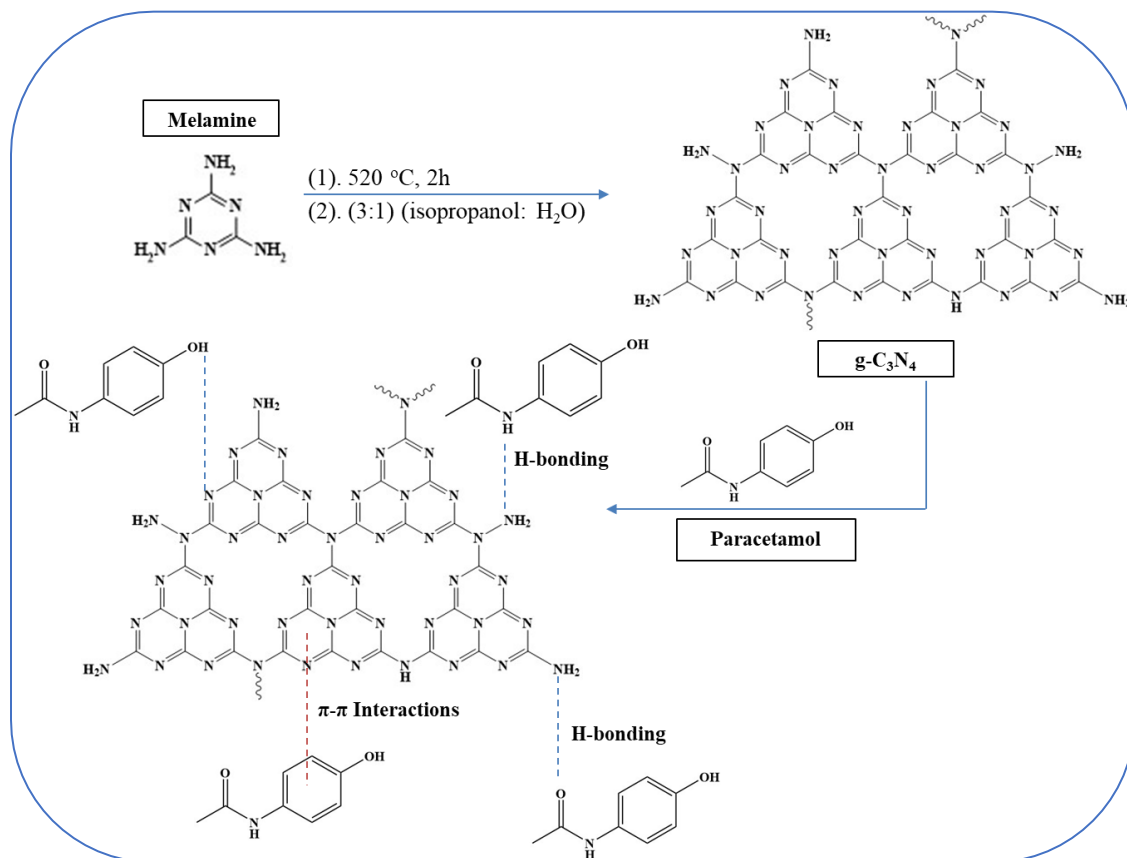
$$q_t = \frac{(C_0 - C_t)}{C_0} \times \frac{V}{W} \quad (3)$$

Where C_0 is the Initial drug concentration (mg/L), C_e is the Equilibrium drug concentration (mg/L), V is Solution volume (L), q_t is the adsorbed amount (mg/g), C_t is the concentration at time t (mg/L), and W is Adsorbent weight (g).

2.5. Instrumentation: To elucidate the structural and morphological properties of the synthesized g-C₃N₄ nanosheets, a suite of characterization techniques was employed. Crystal Structure: XRD using a Shimadzu XRD-LabX-600 diffractometer with Cu K α radiation ($\lambda = 1.54056 \text{ \AA}$) was utilized to assess the crystalline structure. The operating conditions were set at 40 mA/30 kV, with a scanning range of $2\theta = 5-80^\circ$ and a scan speed of 2° per minute. Morphology: TEM using a JEOL JEM-2100F HRTEM operated at 120 kV provided further insights into the nanosheets' morphology. A 1 μL aliquot of the suspension in methanol was placed on a Cu grid and dried under vacuum at 80°C overnight before TEM analysis. Functional Groups: FTIR using a Shimadzu Prestige 21 instrument was employed to identify and characterize functional groups present on the nanoparticles in the range of $450-4000 \text{ cm}^{-1}$. Optical Properties: UV-Vis absorbance spectra were recorded using an Agilent HP-8453 optics system equipped with a Hydrogen-Deuterium lamp for ultraviolet light and a Tungsten lamp for visible light.

2.6. Computational Study: DFT calculations, performed using the DMol3 module of the Materials Studio software (V2022) with the generalized gradient approximation (GGA) function at Perdew–Burke–Ernzerh (PBE) level for optimization, and MD simulation (Adsorption locator) module was employed to investigate the adsorption of drugs onto graphitic carbon nitride (g-C₃N₄). [15, 16] This research aimed to understand the underlying interaction mechanisms and optimize g-C₃N₄ for environmental applications.

3. Results and Discussions



Scheme 1. Procedure to prepare g-C₃N₄ from melamine by thermal decomposition at 520 °C and the possible pathways for paracetamol adsorption.

3.1. Material Design and Characterizations: g-C₃N₄ can be synthesized from melamine through a thermal decomposition process at 520°C as summarized in **Scheme 1**. This reaction involves the condensation and polymerization of melamine molecules, forming a highly conjugated polymer structure. The resulting g-C₃N₄ material exhibits a layered structure similar to graphite, with its unique electronic properties and large surface area making it an excellent candidate for various applications, including adsorption.[12, 17] The ability of g-C₃N₄ to absorb paracetamol is due to its polar surface and the presence of nitrogen-containing functional groups, which can interact with the polar functional groups of paracetamol. This interaction, mainly through hydrogen bonding and dipole-dipole forces, enables the effective adsorption of acetaminophen molecules onto the surface of g-C₃N₄. In addition, π - π interactions between the electron-rich π systems of aromatic rings can contribute to the adsorption process. These interactions can occur in either a parallel or perpendicular arrangement. Hydrogen bonding is a strong dipole-dipole interaction between a hydrogen atom bonded to a highly electronegative atom (e.g., oxygen, nitrogen) and another electronegative atom.[8, 18]

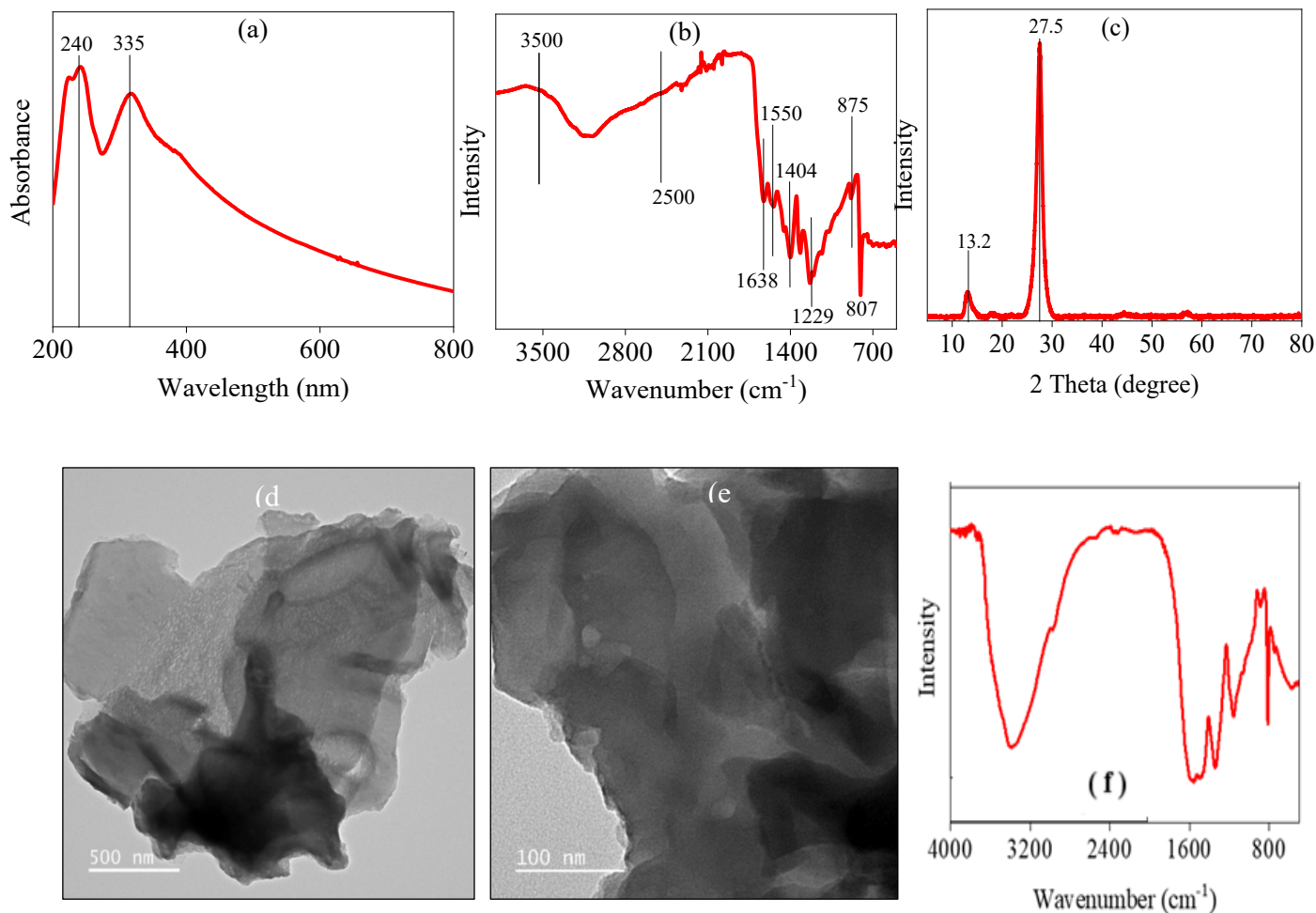


Figure 1. Characterization of $g\text{-C}_3\text{N}_4$: (a) UV-Vis spectrum, (b) FTIR spectrum of $g\text{-C}_3\text{N}_4$, (c) XRD patterns, (d, e) TEM images and (f) FTIR spectrum of $g\text{-C}_3\text{N}_4$ after adsorption of paracetamol.

3.2. Adsorbent Characterization: The synthesized $g\text{-C}_3\text{N}_4$ was characterized using various analytical techniques, including UV-VIS, FTIR, XRD, and TEM. UV-Vis spectroscopy was employed to determine its electronic properties. As shown in **Figure 1a**, the UV-Vis spectrum of $g\text{-C}_3\text{N}_4$ exhibits absorption peaks characteristic of a semiconductor, with wavelengths ranging from 200 to 450 nm. These peaks are attributed to the transfer of electrons from the nitrogen 2p orbitals in the valence band to the carbon 2p orbitals in the conduction band. Additionally, a sharp peak at 240 nm is associated with (n to π^*) transitions, while another peak at 335 nm is due to (n to π^*) transitions arising from electron transfer from nitrogen nonbonding orbitals to aromatic anti-bonding orbitals.[13, 19] FTIR spectroscopy was used to characterize the surface functional groups of $g\text{-C}_3\text{N}_4$. As depicted in **Figure 1b**, the FTIR spectrum of $g\text{-C}_3\text{N}_4$ showed two prominent peaks at 813 and 886 cm^{-1} indicative of triazine ring vibrations. C-N stretching vibrations were confirmed by peaks around 1630-1640 cm^{-1} and 1500-1550 cm^{-1} . C-H stretching vibrations, if present, may be observed around 3200-3400 cm^{-1} . Similarly, N-H stretching vibrations can be detected around 3300-3500 cm^{-1} if amino or imino groups are present. XRD analysis

was conducted to investigate the crystallinity of g-C₃N₄. [20, 21] As shown in **Figure 1c**, the XRD pattern revealed sharp peaks, indicating a crystalline structure. A prominent peak at $2\theta = 28.0^\circ$ corresponds to the stacking of (022) planes, while a weaker peak at $2\theta = 13.3^\circ$ is attributed to the (100) planes of heptazine repeating units in g-C₃N₄. The morphology of g-C₃N₄ was examined using TEM. As depicted in **Figures 1d** and **1e**, the TEM images revealed a sheet-like structure for the g-C₃N₄ nanosheets. These thin, flat sheets often stack on top of each other, forming a layered structure reminiscent of graphite. [12, 18]. After paracetamol adsorption (**Figure 1f**), the FTIR spectrum reveals notable changes, confirming interactions between paracetamol and g-C₃N₄. A new band near 1660 cm^{-1} appears, corresponding to the C=O stretch of the amide group in paracetamol. The broad band between $3000\text{--}3500\text{ cm}^{-1}$, associated with O–H and N–H stretching, shows increased intensity and a slight shift, suggesting hydrogen bonding between paracetamol's phenolic group and nitrogen sites on g-C₃N₄. Additional bands emerge at 1590 cm^{-1} and 1500 cm^{-1} , likely due to aromatic ring vibrations from paracetamol, while the band at 1230 cm^{-1} may arise from C–O stretching in the phenolic group. These modifications—new peaks, shifted intensities, and altered band positions—collectively demonstrate successful paracetamol adsorption. The interactions likely involve hydrogen bonding (e.g., O–H \cdots N or N–H–N) and π – π stacking between paracetamol's aromatic ring and g-C₃N₄'s conjugated structure.

3.3. Adsorption Results

3.3.1. The Effect of Initial pH: The point of zero charge (PZC) of g-C₃N₄ at 4.3 (**Figure 2a**) indicates that its surface is positively charged at pH values below 4.3 and negatively charged above it. Paracetamol, being a weak acid with a pK_a around 9.5, primarily exists in its neutral form at pH values below its pK_a. As the pH increases towards the PZC, the positive surface charge of g-C₃N₄ decreases, reducing electrostatic repulsion and promoting adsorption. This is evident in **Figure 2b**, where the adsorption efficiency (R_e) increases significantly as the pH approaches the PZC. However, at pH values significantly above the PZC, the negatively charged g-C₃N₄ surface may repel the anionic form of paracetamol, which starts to form as the pH approaches the pK_a of paracetamol. This leads to a decrease in adsorption efficiency, as observed in **Figure 2b** at higher pH values. Therefore, the optimal pH for paracetamol adsorption onto g-C₃N₄ lies around the PZC, where the balance between electrostatic interactions and other adsorption mechanisms is favorable. This optimal pH range is approximately 4-6, as indicated by the peak in the adsorption efficiency curve in **Figure 2b**. [22, 23]

3.3.2. The Effect of Concentration and Adsorption Isotherms: To investigate the adsorption capacity of g-C₃N₄ for paracetamol, experiments were carried out at varying initial concentrations. As depicted in **Figure 2c**, the amount of paracetamol adsorbed increased with increasing initial concentration, reaching a maximum of 1.11 mg/g. This trend can be explained by the Langmuir adsorption isotherm, which is expressed by **Equation 4**. [24]

$$\frac{1}{q_e} = \frac{1}{bq_m} + \frac{1}{q_m} C_e \quad (4)$$

$$R_L = \frac{1}{1 + bC_0} \quad (5)$$

Where: C_e is the equilibrium concentration of the solute (mg/L), q_e is the amount of solute adsorbed per unit mass of adsorbent (mg/g), b is Langmuir constant related to the affinity between the adsorbent and adsorbate (L/mg), q_m is the maximum adsorption capacity (mg/g). The dimensionless equilibrium parameter (R_L) is a crucial characteristic of the Langmuir isotherm, given by **Equation 5**. [25]

Table 1. Parameters of the Langmuir-isotherms model for the Adsorption of paracetamol on g-C₃N₄.

R^2	b (L/mg)	$q_{\max, \text{fitted}}$	q_{exp}	R_L
0.9998	76.69	1.10	1.11	0.012

The experimental data exhibited excellent agreement with the Langmuir model, as shown in **Figure 2d** and **Table 1**. The high correlation coefficient ($R^2 = 0.9998$) and favorable R_L values ($0 < R_L < 0.1$) further support the Langmuir model's applicability. The calculated maximum adsorption capacity (q_{\max}) from the Langmuir model (1.10 mg/g) is in close agreement with the experimental data (1.1 mg/g), reinforcing the monolayer adsorption mechanism. The exceptional adsorption performance of g-C₃N₄ for paracetamol can be attributed to its high surface area and the presence of nitrogen-containing functional groups, such as amino groups. These functional groups facilitate strong hydrogen bonding and electrostatic interactions with paracetamol, leading to efficient adsorption.

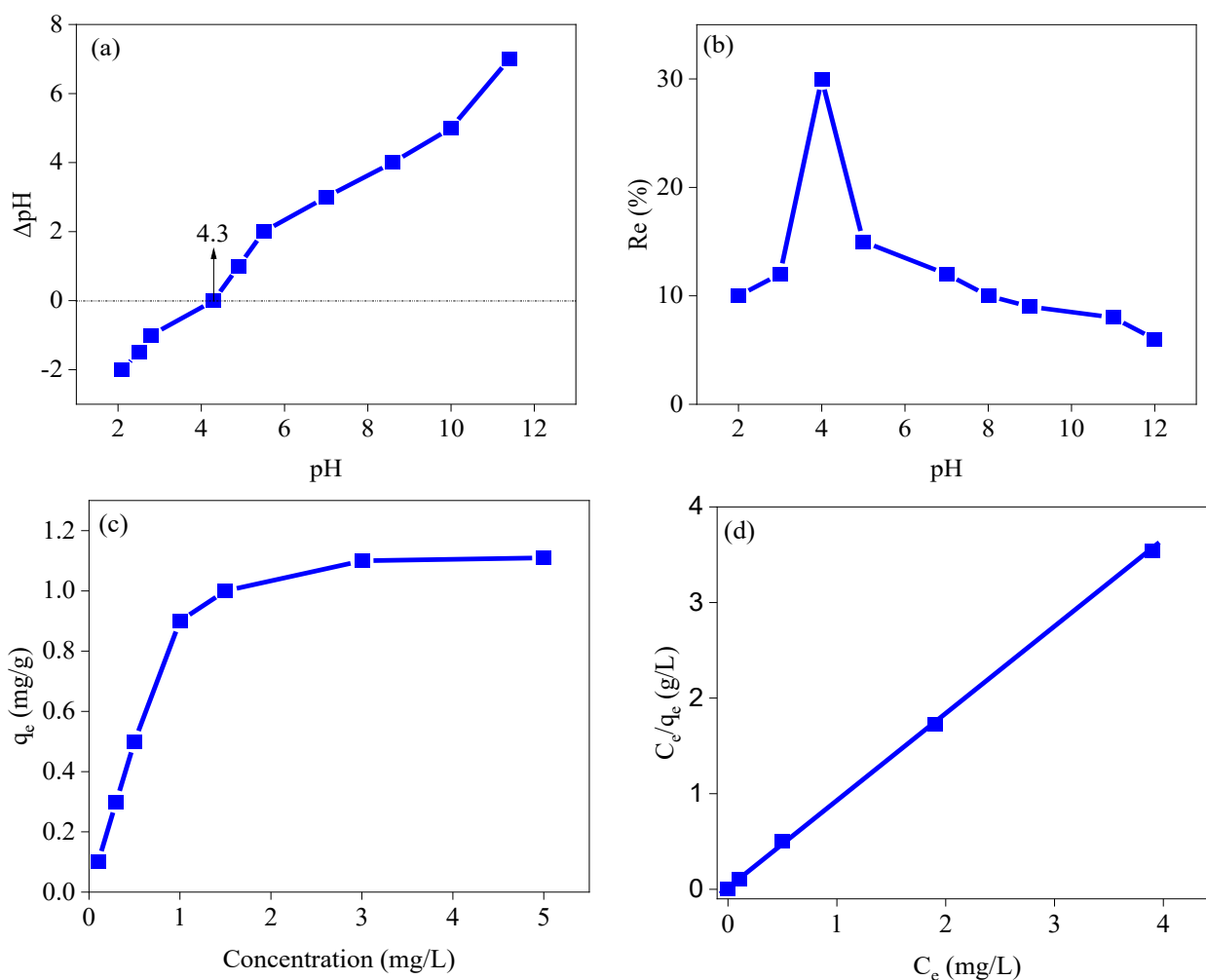


Figure 2. The effect of pH on the adsorption of paracetamol onto g-C₃N₄. (a) shows the point of zero charge (PZC) of g-C₃N₄, which is 4.3. (b) shows the adsorption efficiency of paracetamol onto g-C₃N₄ as a function of pH. (c) the effect of concentration on the adsorption of paracetamol onto g-C₃N₄ [Conditions: $C_0 = 0.1, 0.3, 0.5, 1, 1.5, 3, 5$ ppm, pH = 4, $T = 298$ K, $t = 420$ min, adsorbent dose = 0.01 g/10 mL]. (d) Langmuir isotherm model for the adsorption.

3.3.3. The Effect of Contact Time and Adsorption Kinetics: Adsorption is a time-dependent process, and the impact of contact time can significantly influence the overall efficiency. This study investigated the effect of contact time within 30 to 180 minutes. As illustrated in **Figure 3a**, the adsorption rate was initially slow, but accelerated notably after 15 minutes, reaching equilibrium at approximately 60 minutes. Beyond this point, no further adsorption was observed, and even desorption might have occurred. This behavior can be attributed to the gradual saturation of active sites on the adsorbent surface. As the surface becomes increasingly occupied, the availability of free sites decreases, leading to a decline in the adsorption rate.[9, 26] Kinetic modeling was employed to gain insights into the underlying mechanisms of the adsorption process. The pseudo-second-order kinetic model was used as in **Equation 6**. Where: k_2

($\text{g.mole}^{-1}.\text{min}^{-1}$) is the second-order rate constant of adsorption, q_e and q_t are the adsorbed amount (mg/g) at equilibrium and at time t (min), respectively.[24]

$$\frac{t}{q_t} = \frac{1}{k_2 q_e^2} + \frac{t}{q_e} \quad (6)$$

The results in **Figure 3b** and **Table 2** best fit the experimental data, as evidenced by the high correlation coefficient ($R^2 = 0.9866$) and the close agreement between the calculated and experimental equilibrium adsorption capacities ($q_{e, \text{fitted}}$ and $q_{e, \text{exp}}$). This suggests that the rate-limiting step in the adsorption process involves the interaction between the adsorbate molecules and the active sites on the adsorbent surface.

Table 2. Kinetic Parameters for Adsorption of Paracetamol on g-C₃N₄.

R^2	$q_{\text{max, fitted}}$	q_{exp}	k_2
0.9866	0.568	0.500	0.10173

3.3.4. The Effect of Temperature and Adsorption Thermodynamics: The impact of temperature on the adsorption capacity of paracetamol onto g-C₃N₄ was investigated. Experiments were conducted at pH 4, with a contact time of 420 minutes, a g-C₃N₄ dosage of 10 mg/L, and paracetamol concentrations ranging from 0.1 to 5 mg/L. Three temperatures were tested: 25, 35, and 50 °C. As the temperature increased, the maximum adsorption capacity rose from 1.1 to 3.2 mg/g as **Figure 3c** shows, likely due to increased molecular mobility and kinetic energy at higher temperatures.[26] Thermodynamic parameters (ΔH , ΔS , and ΔG) were determined using **Equations 7 and 8**. Where ΔG° represents the change in free energy, ΔH° represents the change in enthalpy, ΔS° represents the change in entropy, R is the gas constant, T is the temperature, and K_c is the equilibrium constant.[27, 28]

$$\Delta G^\circ = -RT \ln K_c \quad (7)$$

$$\ln K_c = \left(\frac{\Delta S^\circ}{R}\right) - \left(\frac{\Delta H^\circ}{R}\right) \frac{1}{T} \quad (8)$$

The data and the calculated thermodynamic parameters are presented in **Figure 3d** and **Table 3**, respectively. The negative ΔG values indicate that the adsorption process is spontaneous and favorable at all temperatures, with the process becoming more favorable at higher temperatures. This suggests a potential expansion of adsorbent pores at higher temperatures, facilitating increased diffusion of paracetamol molecules. The positive ΔH value confirms the endothermic nature of the process, consistent with the increased adsorption capacity at higher temperatures. Additionally, the positive ΔS value suggests an increase in disorder at the solid-solution interface during adsorption.[23, 26] These findings indicate a strong affinity between paracetamol and the g-C₃N₄ adsorbent, with the adsorption mechanism primarily physical in nature.

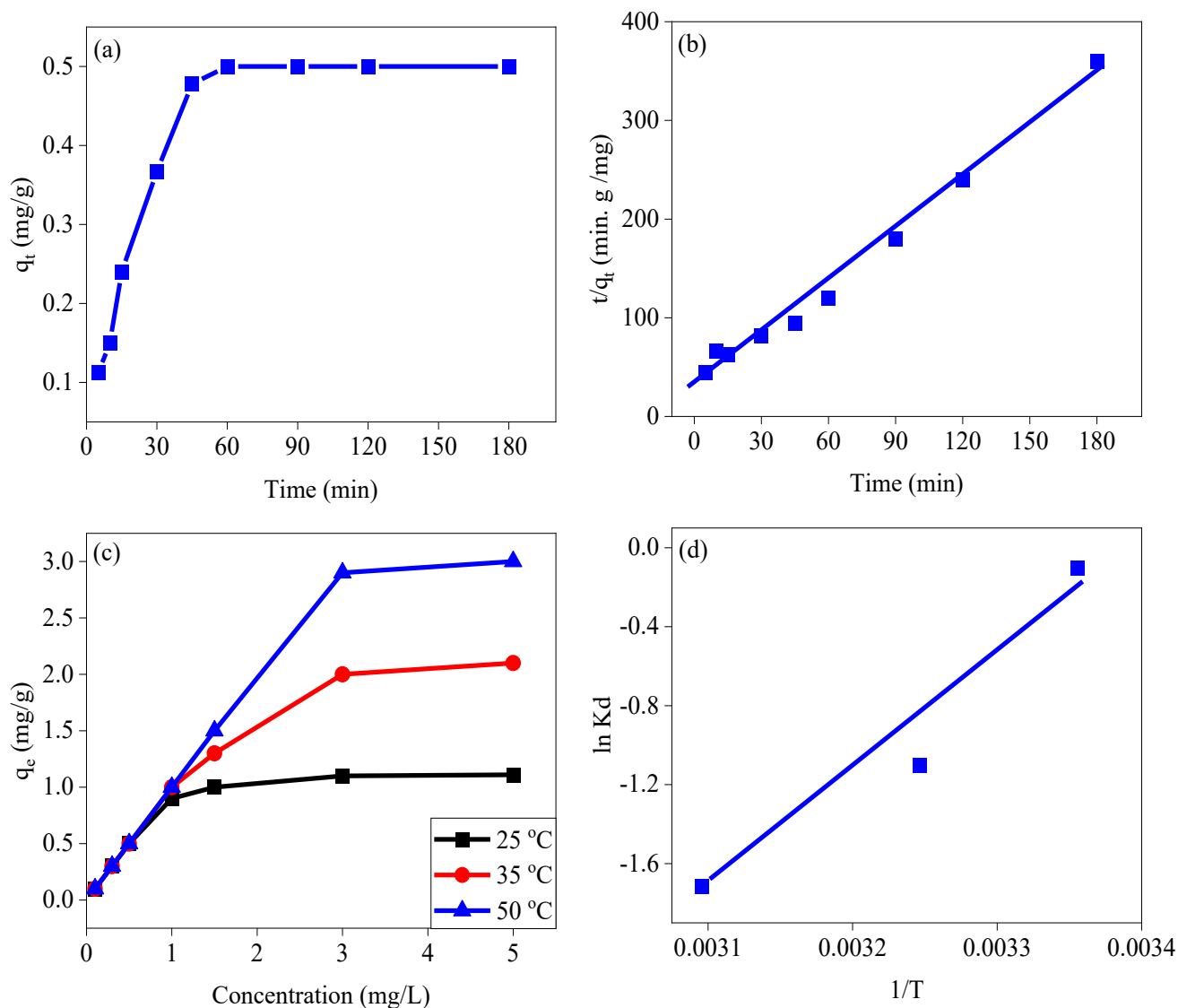


Figure 3: (a) Impact of contact time on paracetamol removal by g-C₃N₄ (pH 4, adsorbent dose = 0.001 g/10 mL, T = 298 K). (b) Pseudo-second-order kinetic model for paracetamol adsorption onto g-C₃N₄. (c) Influence of temperature on paracetamol removal by g-C₃N₄ (pH 4, adsorbent dose = 0.001 g/10 mL, T = 298, 308, 323 K, t = 420 min). (d) Thermodynamic assessment via Van't Hoff plot reveals the endothermic nature of paracetamol adsorption on g-C₃N₄ (ΔH° > 0).

Table 3: Thermodynamic parameters for the adsorption of paracetamol on g-C₃N₄.

ΔG (kJ mol ⁻¹)			ΔH (kJ mol ⁻¹)	ΔS (kJ mol ⁻¹ T ⁻¹)	R ²
298 K	308 K	323 K	48.356	0.1509	0.9987
-21.059	-23.456	-27.525			

3.5. Theoretical calculation Results: DFT was employed to investigate the adsorption of drugs onto g-C₃N₄, [29-32] aiming to elucidate the underlying interaction mechanisms and optimize this material for environmental remediation applications. The favorable interaction between g-C₃N₄ and paracetamol is likely attributed to the unique surface chemistry and structural features of g-C₃N₄, which enhance its affinity for organic molecules. [33] Structural interactions between paracetamol and g-C₃N₄ are likely mediated through π - π stacking and hydrogen bonding, with the triazine groups of g-C₃N₄ playing a crucial role in governing the adsorption efficiency. DFT provides valuable insights into the stability and electronic properties of the g-C₃N₄-drug complex. The calculations reveal that adsorption induces alterations in electron density and facilitates charge transfer, which is critical for understanding the adsorption process and optimizing g-C₃N₄ for efficient drug removal from water. [32, 34].

Table 4: DFT calculated parameters from Optimization processes for Paracetamol, g-C₃N₄, and Paracetamol-g-C₃N₄ complex.

Parameter		g-C ₃ N ₄	Paracetamol	g-C ₃ N ₄ -Paracetamol complex
(E _{LUMO})	E _{HOMO}	-5.706	-4.921	-5.031
(E _{HOMO})	E _{LUMO}	-3.436	-1.12	-3.481
(ΔE_g)	$\Delta E_{(HOMO-LUMO)}$	-2.27	-3.801	-1.55
(I)	Ionization energy (I)	5.706	4.921	5.031
(A)	Electron affinity (A)	3.436	1.12	3.481
(η)	Electronegativity (X)	4.571	3.021	4.256
(χ)	Global hardness (η)	1.135	1.901	0.775
(μ)	Chemical potential (μ)	-4.571	-3.021	-4.256
(σ)	Global softness (σ)	0.881	0.526	1.290
(ω)	Global electrophilicity (ω)	9.204	2.400	11.686
(ω^+)	Electroaccepting (ω^+) power	7.061	1.128	9.655
(ω^-)	Electrodonating (ω^-) power	11.632	4.148	13.911
(ω^\pm)	Net electrophilicity ($\Delta\omega^{+-}$)	18.692	5.276	23.566
(ϵ)	Nucleophilicity (ϵ)	0.109	0.417	0.086
(Q _{max})	Fraction of transferred electrons (ΔN)	-2.014	-0.795	-2.746
(ΔN)	Electronic charge accepting capability Q _{max}	4.027	1.589	5.492
E _f	Formation energy (eV)	-490.217	-101.818	-591.031

Table 4 summarizes the electronic parameters derived from the optimization of paracetamol, g-C₃N₄, and their complex. The data reveals that the interaction between g-C₃N₄ and paracetamol results in shifts in both the highest occupied molecular orbital (HOMO) and lowest unoccupied molecular orbital (LUMO) energies, signifying a modification of the electronic structure upon complexation. The observed decrease in the energy gap (ΔE_g) between HOMO and LUMO for the complex suggests the formation of a more stable compound with lower energy. The ionization energy of the complex lies between those of paracetamol and g-C₃N₄, indicating a balanced electronic interaction. Conversely, the electron affinity of the complex is closer to that of g-C₃N₄, suggesting that g-C₃N₄ primarily governs the electron-accepting behavior of the complex. The reduced global hardness of the complex implies increased reactivity and a higher likelihood of interaction. Its electronegativity falls within an intermediate range, signifying a balanced distribution of electron density. The complex's chemical potential aligns more closely with that of g-C₃N₄, indicating that g-C₃N₄ exerts a significant influence on the overall chemical behavior of the complex. Furthermore, the increased global softness of the complex suggests enhanced reactivity and flexibility. The elevated net electrophilicity of the complex points towards a higher overall reactivity. Conversely, the observed decrease in nucleophilicity implies a reduced tendency to donate electrons in the complex.

Table 5 . Lower adsorption configuration output results from the Adsorption Locator model.

Structures	Total energy <i>kcal mol⁻¹</i>	Adsorption energy <i>kcal mol⁻¹</i>	Rigid adsorption energy <i>kcal mol⁻¹</i>	Deformation energy <i>kcal mol⁻¹</i>	dE_{ad}/dN_i <i>kcal mol⁻¹</i>
Paracetamol + g-C ₃ N ₄	-85.696×10^3	-38.640×10^3	-36.000×10^3	-2.643	-38.640

The adsorption study reveals an electrostatic attraction between paracetamol and the g-C₃N₄ surface, evidenced by an increase in the bond lengths of NH and CN groups within g-C₃N₄ due to the interaction with paracetamol. The formation of hydrogen bonds (Paracetamol) N-H...N-H (g-C₃N₄) is likely, supported by the short distances observed between the nearest H and N atoms (1.678, 3.079, and 2.786 Å) after adsorption, as depicted in **Figure 4**, which confirms the FTIR results shown in **Figure 1f**. MD simulations indicate a strong interaction between paracetamol and g-C₃N₄, corroborated by the parameter analysis. The negative values for total energy, adsorption energy, and rigid adsorption energy in **Table 5** suggest a stable complex with strong intermolecular interactions. Furthermore, the low deformation energy confirms the stability of the complex by indicating minimal structural changes in the molecules during adsorption. These computational results are consistent with the experimental findings.

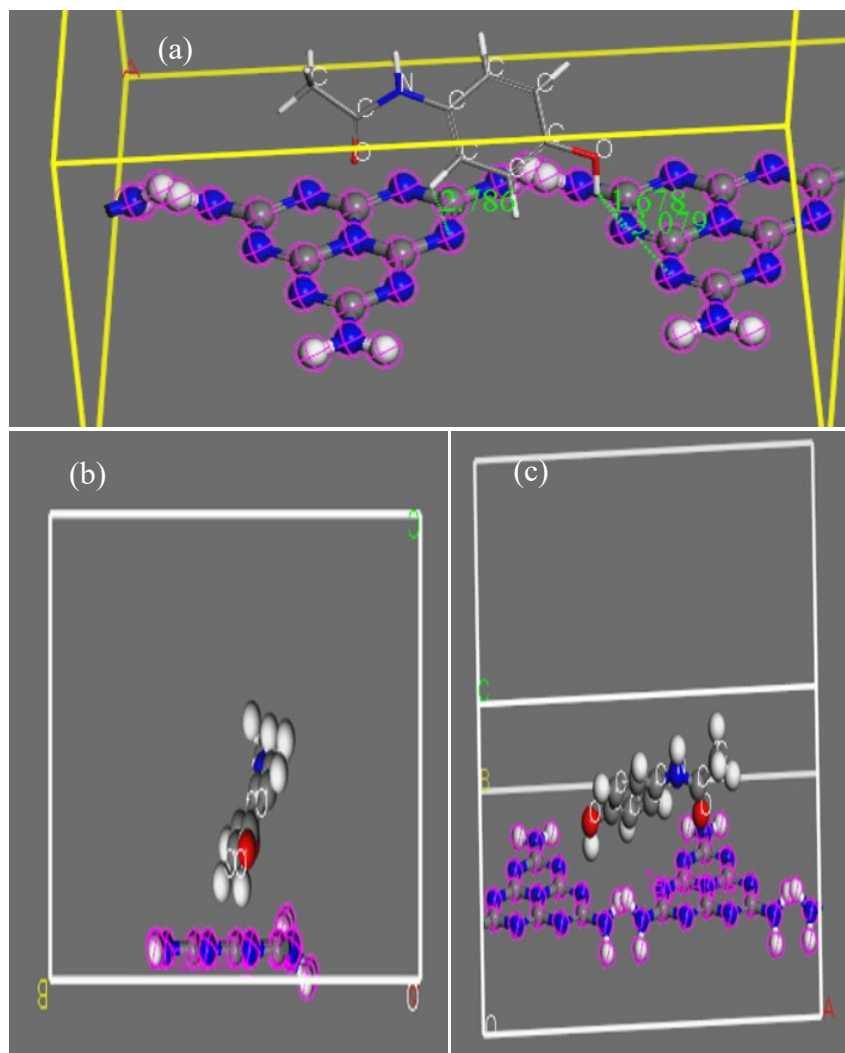


Figure 4. (a) The obtained energies for the most stable complex, (a) top view and (b) side view of the adsorption adsorbed paracetamol-g-C₃N₄ complex.

4. Conclusions and Outlooks

This study successfully demonstrated the feasibility of employing cost-effective raw graphitic carbon nitride for paracetamol removal from water. Comprehensive material characterization via XRD, XRF, FT-IR, and TEM elucidated the adsorbent's properties. Systematic investigation of key operational parameters, including pH, contact time, adsorbent dosage, and initial paracetamol concentration, revealed a maximum adsorption capacity of 1.1 mg/g achieved at 25°C within 60 minutes. The adsorption process was well-described by both Langmuir and pseudo-second-order kinetic models. Complementary DFT

calculations confirmed the stability of the paracetamol-g-C₃N₄ complex, while MD simulations indicated a high propensity for hydrogen bond formation, yielding a calculated adsorption energy of -38.640×10^{-3} kcal/mol. The strong synergy between these experimental and computational findings highlights the significant potential of raw graphitic carbon nitride as an environmentally benign and economical adsorbent for pharmaceutical contaminant removal from aqueous solutions. Future research should explore its efficacy in treating real wastewater samples and investigate the regeneration capabilities of the spent adsorbent to further establish its practical applicability.

References

- [1] Hejna, M., D. Kapuścińska, and A. Aksmann, *Pharmaceuticals in the Aquatic Environment: A Review on Eco-Toxicology and the Remediation Potential of Algae*. Int J Environ Res Public Health, 2022. **19**(13).
- [2] Eapen, J.V., et al., *A review of the effects of pharmaceutical pollutants on humans and aquatic ecosystem*. Exploration of Drug Science, 2024. **2**(5): p. 484-507.
- [3] Quesada, H.B., et al., *Surface water pollution by pharmaceuticals and an alternative of removal by low-cost adsorbents: A review*. Chemosphere, 2019. **222**: p. 766-780.
- [4] Pacheco-Álvarez, M., et al., *A critical review on paracetamol removal from different aqueous matrices by Fenton and Fenton-based processes, and their combined methods*. Chemosphere, 2022. **303**: p. 134883.
- [5] Al-howri, B.M., et al., *Paracetamol in diverse water sources: health hazards and treatment efficacy emphasizing adsorption techniques—a review*. International Journal of Environmental Science and Technology, 2024. **21**(15): p. 9743-9762.
- [6] Ivanova, D., G. Tzvetkov, and N. Kaneva *Degradation of Paracetamol in Distilled and Drinking Water via Ag/ZnO Photocatalysis under UV and Natural Sunlight*. Water, 2023. **15**, DOI: 10.3390/w15203549.
- [7] Islam, M., et al., *Adsorptive removal of paracetamol from aqueous media: A comprehensive review of adsorbent materials, adsorption mechanisms, recent advancements, and future perspectives*. Journal of Molecular Liquids, 2024.
- [8] Aminul Islam, M., et al., *Adsorptive removal of paracetamol from aqueous media: A review of adsorbent materials, adsorption mechanisms, advancements, and future perspectives*. Journal of Molecular Liquids, 2024. **396**: p. 123976.
- [9] Spaltro, A., et al., *Removal of paracetamol from aqueous solution by activated carbon and silica. Experimental and computational study*. Journal of Contaminant Hydrology, 2021. **236**: p. 103739.
- [10] Maneewong, Y., et al., *Paracetamol removal from water using N-doped activated carbon derived from coconut shell: Kinetics, equilibrium, cost analysis, heat contributions, and molecular-level insight*. Chemical Engineering Research and Design, 2022. **185**: p. 163-175.
- [11] Yilmaz, Ş., A. Zengin, and T. Şahan, *Effective utilization of Fe(III)-based metal organic framework-coated cellulose paper for highly efficient elimination from the liquid phase of paracetamol as a pharmaceutical pollutant*. Environmental Technology & Innovation, 2021. **24**: p. 101799.
- [12] Zhao, Z., Y. Sun, and F. Dong, *Graphitic carbon nitride based nanocomposites: a review*. Nanoscale, 2015. **7**(1): p. 15-37.
- [13] Zhao, G.-Q., et al., *A critical review on graphitic carbon nitride (g-C₃N₄)-based composites for environmental remediation*. Separation and Purification Technology, 2021. **279**: p. 119769.
- [14] Alaghmandfard, A. and K. Ghandi, *A Comprehensive Review of Graphitic Carbon Nitride (g-C₃N₄)–Metal Oxide-Based Nanocomposites: Potential for Photocatalysis and Sensing*. Nanomaterials, 2022. **12**(2): p. 294.
- [15] Bicheng, Z., et al., *Adsorption investigation of CO₂ on g-C₃N₄ surface by DFT calculation*. Journal of CO₂ Utilization, 2017. **21**: p. 327-335.

- [16]Iqbal, J., et al., *DFT study of therapeutic potential of graphitic carbon nitride (g-C₃N₄) as a new drug delivery system for carboplatin to treat cancer*. Journal of Molecular Liquids, 2021. **331**: p. 115607.
- [17]Zhu, J., et al., *Graphitic Carbon Nitride: Synthesis, Properties, and Applications in Catalysis*. ACS Applied Materials & Interfaces, 2014. **6**(19): p. 16449-16465.
- [18]Fronczak, M., *Adsorption performance of graphitic carbon nitride-based materials: Current state of the art*. Journal of Environmental Chemical Engineering, 2020. **8**(5): p. 104411.
- [19]Ghalkhani, M., M.H. Khaneghah, and E. Sohoul, *Chapter 13 - Graphitic carbon nitride: Synthesis and characterization*, in *Handbook of Carbon-Based Nanomaterials*, S. Thomas, et al., Editors. 2021, Elsevier. p. 573-590.
- [20]Sunasee, S., et al., *Sonophotocatalytic degradation of bisphenol A and its intermediates with graphitic carbon nitride*. Environmental Science and Pollution Research, 2019. **26**: p. 1-12.
- [21]Ahmaruzzaman, M. and S.R. Mishra, *Photocatalytic performance of g-C₃N₄ based nanocomposites for effective degradation/removal of dyes from water and wastewater*. Materials Research Bulletin, 2021. **143**: p. 111417.
- [22]Bernal, V., et al., *Effect of Solution pH on the Adsorption of Paracetamol on Chemically Modified Activated Carbons*. Molecules, 2017. **22**: p. 1032.
- [23]Terzyk, A.P., *The influence of activated carbon surface chemical composition on the adsorption of acetaminophen (paracetamol) in vitro: Part II. TG, FTIR, and XPS analysis of carbons and the temperature dependence of adsorption kinetics at the neutral pH*. Colloids and Surfaces A: Physicochemical and Engineering Aspects, 2001. **177**(1): p. 23-45.
- [24]Azizian, S. and S. Eris, *Chapter 6 - Adsorption isotherms and kinetics*, in *Interface Science and Technology*, M. Ghaedi, Editor. 2021, Elsevier. p. 445-509.
- [25]Vedenyapina, M., et al., *Adsorption of Heavy Metals on Activated Carbons (A Review)*. Solid Fuel Chemistry, 2021. **55**: p. 83-104.
- [26]Awad, F.S., et al., *Thiol- and Amine-Incorporated UiO-66-NH₂ as an Efficient Adsorbent for the Removal of Mercury(II) and Phosphate Ions from Aqueous Solutions*. Industrial & Engineering Chemistry Research, 2021. **60**(34): p. 12675-12688.
- [27]Allaoui, I., et al., *Adsorption equilibrium, kinetic, and thermodynamic studies on the removal of paracetamol from wastewater using natural and HDTMA-modified clay*. Desalination and Water Treatment, 2024. **318**: p. 100345.
- [28]Haro, N.K., et al., *Kinetic, equilibrium and thermodynamic studies of the adsorption of paracetamol in activated carbon in batch model and fixed-bed column*. Applied Water Science, 2021. **11**(2): p. 38.
- [29]Perveen, M., et al., *Therapeutic potential of graphitic carbon nitride as a drug delivery system for cisplatin (anticancer drug): A DFT approach*. Biophysical Chemistry, 2020. **267**: p. 106461.
- [30]Shamim, M., et al., *DFT study of therapeutic potential of graphitic carbon nitride (g-C₃N₄) as a new drug delivery system for carboplatin to treat cancer*. Journal of Molecular Liquids, 2021. **331**: p. 115607.
- [31]Perveen, M., et al., *DFT study of therapeutic potential of graphitic carbon nitride as a carrier for controlled release of melphalan: an anticancer drug*. Journal of Molecular Modeling, 2022. **28**(11): p. 359.
- [32]Negro, P., et al., *Combined DFT-D3 computational and experimental studies on g-C₃N₄: New insight into structure, optical, and vibrational properties*. Materials, 2023. **16**(10): p. 3644.
- [33]Jiménez-Salcedo, M., M. Monge, and M.T. Tena, *An organometallic approach for the preparation of Au–TiO₂ and Au-g-C₃N₄ nanohybrids: improving the depletion of paracetamol under visible light*. Photochemical & Photobiological Sciences, 2022. **21**(3): p. 337-347.
- [34]Luo, S., et al., *Effect of Pt doping on sensing performance of g-C₃N₄ for detecting hydrogen gas: a DFT study*. Vacuum, 2022. **200**: p. 111014.



Analysis of Magnetic Properties and Critical Current Density of Tl-2234 High-Temperature Superconductor Using AC Magnetic Susceptibility Measurements

Belqees Hassan

Department of Physics, College of Science, Qassim University, Buraydah 51452, Saudi Arabia

B.hassan@qu.edu.sa

Abstract

This study investigates the magnetic properties and critical current density of $\text{Tl}_2\text{Ba}_2\text{Ca}_3\text{Cu}_4\text{O}_{11+\delta}$ (Tl-2234) high-temperature superconductors through AC magnetic susceptibility measurements. Samples were synthesized using a one-step solid-state process with careful heat treatment protocols to minimize thallium evaporation. AC susceptibility measurements were conducted across temperatures ranging from 140 to 50K under various applied AC magnetic fields (0.5-8 mT). The analysis revealed a sharp transition primarily reflecting intragranular superconductivity, with the field dependence of the imaginary (χ'') component providing insights into flux dynamics within the grains. The imaginary component peaks shifted towards lower temperatures with increasing magnetic field strength, indicating enhanced magnetic field penetration and increased intra-grain pinning centers. Using Bean's critical-state model, with an estimated effective particle radius of $R \approx 44.5 \mu\text{m}$ based on sieve size, the critical current density (J_c) was calculated from the peak positions in $\chi''(T)$ curves. The temperature dependence of J_c followed an empirical scaling relation, yielding a zero-temperature critical current density $J_c(0)$ of $3.6 \times 10^5 \text{ A/cm}^2$ and a critical exponent of 1.26 ± 0.08 , quantifying key superconducting parameters of the prepared material.

Keywords: AC magnetic susceptibility; Current density; Flux pinning; Magnetic properties.

<https://doi.org/10.63070/jesc.2025.003>

Received 28 March 2025; Revised 28 April 2025; Accepted 13 May 2025.

Available online 21 May 2025.

Published by Islamic University of Madinah on behalf of *Islamic University Journal of Applied Sciences*. This is a free open access article.

1. Introduction

High-Temperature Superconductors (HTS) have emerged as materials of substantial scientific significance, owing to their transformative potential in energy-efficient technological applications, encompassing power transmission infrastructure, Magnetic Resonance Imaging (MRI) systems, and magnetic levitation technologies [1,2]. Within the broader classification of HTS materials, copper oxide-based (cuprate) superconductors demonstrate remarkable characteristics at operational temperatures substantially exceeding the liquid nitrogen boiling threshold (77 K), conferring distinct practical advantages over conventional superconducting systems [3]. Specifically, thallium-based cuprates (TBCCO) stand out for their relatively high critical temperature (T_c), which can be achieved under ambient pressure [4]. Within this family, the compound (Tl-2234) has gained attention due to its unique structural features and promising superconducting properties. Structurally, Tl-2234 belongs to the Tl-1223 family and is characterized by alternating layers of TlO and CuO₂, which play a crucial role in its magnetic and electronic properties [5-8]. These layered structures, combined with various types of crystal defects such as oxygen vacancies and grain boundaries, significantly influence the material's flux pinning mechanisms and, consequently, its critical current density (J_c). The analysis of alternating-current magnetic susceptibility has established itself as a sophisticated analytical technique for elucidating the intricate magnetic phenomena exhibited by high-temperature superconducting materials. This technique provides essential information about flux pinning mechanisms, critical current densities, and intergranular coupling in these materials. The AC susceptibility response is characterized by both real (χ') and imaginary (χ'') components, offering complementary insights into magnetic shielding and energy dissipation processes, respectively. The temperature and field dependence of these components reveals crucial details about flux penetration, pinning strength, and energy dissipation [9,10]. Despite the extensive research on Tl-2234, a comprehensive understanding of the correlations between its structural characteristics, AC magnetic susceptibility behavior, and critical current density remains incomplete. This knowledge gap is particularly significant given the material's potential for practical applications in high-field and high-temperature environments. This study aims to investigate the temperature and magnetic field dependence of AC susceptibility components (χ' and χ'') in Tl-2234, while analyzing the correlation between structural defects and magnetic properties through higher harmonic susceptibility measurements.

2. Experimental Methods

2.1 Sample Preparation

The synthesis of $\text{Tl}_2\text{Ba}_2\text{Ca}_3\text{Cu}_4\text{O}_{11+\delta}$ was initiated through the careful selection of high-purity precursor materials, including thallium oxide (Tl_2O_3), barium peroxide (BaO_2), calcium oxide (CaO), and copper oxide (CuO). The preparation followed a standard one-step solid-state process, where stoichiometric quantities of these precursors were thoroughly mixed using an agate mortar. To ensure homogeneity, the resulting powder was passed through an 89 μm sieve. The homogeneous powder mixture was subsequently compressed into a disc-shaped pellet with dimensions of diameter 1.5 cm and thickness 0.2 cm.

2.2 Heat Treatment

To minimize thallium evaporation during the heat treatment, the sample was carefully wrapped in silver foil. For safety considerations and to protect the furnace from potential hazardous effects, the wrapped sample was placed in a sealed quartz tube (diameter 1.5 cm \times length 15 cm), which was then enclosed within a protective stainless steel tube. The heat processing methodology consisted of positioning the hermetically sealed specimen in a horizontal orientation within a furnace chamber, followed by controlled heating at a $6^\circ\text{C}/\text{min}$ gradient until achieving 811°C . The specimen was held isothermally at this temperature for a duration of six hours, after which controlled cooling was implemented at $0.5^\circ\text{C}/\text{min}$ until reaching ambient temperature. Superconducting characteristics were further optimized through supplementary heat treatment in ambient atmosphere at 500°C .

2.3 Magnetic Measurements

Magnetic Characterization Magnetic measurements were conducted using a LakeShore Superconducting Magnet System integrated with a helium cryostat. AC magnetic susceptibility components (real and imaginary) were recorded across AC field amplitudes from 0.5 mT to 8 mT, spanning a temperature range of 50 -140 K. Sample preparation involved mechanical grinding and size classification through an 89 μm mesh to ensure homogeneous particle distribution. It is important to clarify that the 89 μm mesh was used for particle size classification to ensure homogeneity of the sample, and this mesh size represents the maximum size of particles that were allowed to pass through, effectively setting an upper limit on the particle size in the measured sample.

3. Results and Discussion

3.1 AC Magnetic Susceptibility Analysis

The complex AC magnetic susceptibility ($\chi = \chi' + i\chi''$) serves as a powerful analytical tool for investigating high-temperature superconductors, particularly in granular systems where both components (χ' and χ'') exhibit distinct temperature and field amplitude dependencies [11]. AC

susceptibility measurements have gained popularity due to their simplicity, cost-effectiveness, and high sensitivity, enabling sophisticated quantitative analysis [12]. When exposed to a periodic field, $H_a(t) = h \sin(2\pi vt)$, the sample exhibits a magnetic moment in opposition to the applied field, expressed as [13]:

$$\chi(h, v) = \chi' + i\chi'' \quad (1)$$

Where v is the frequency. The real component (χ') approximates zero-field-cooling susceptibility in DC measurements, quantifying the superconductor's shielding response, while the imaginary component (χ'') reflects energy dissipation. In polycrystalline high- T_c materials, temperature-dependent AC susceptibility reveals superconducting transitions. The real component (χ') shows a sharp drop associated primarily with the onset of intragranular superconductivity. While distinct intergranular coupling effects can sometimes be observed in bulk polycrystalline samples, in powder samples such as the current sample, where intergranular connections are inherently weaker or disrupted, any signature of a separate intergranular transition is often masked or convoluted with the

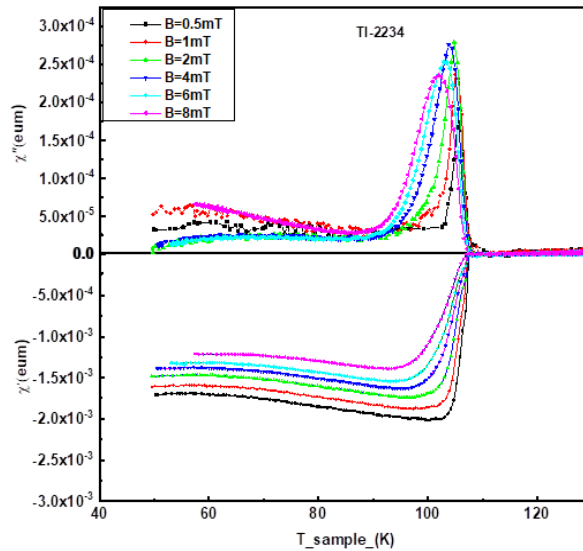


Figure 1. AC magnetic susceptibility vs. temperature for the powder sample TI-2234 under different AC field amplitudes.

dominant intragranular response [14]. The χ'' curve also shows predominantly one peak, typically associated with losses within the grains. Figure 1 presents the temperature dependence of both real and imaginary components of AC magnetic susceptibility for the TI-2234 sample under varying alternating magnetic fields. The sample demonstrates a well-defined superconducting transition, characterized by a sharp response with minimal broadening in the transition region. The real component exhibits modest field-dependent broadening across the transition. Notable features in the data include systematic shifts of the χ'' peaks toward lower temperatures with increasing alternating magnetic field amplitude. This behavior can be attributed to two primary mechanisms: first, the enhanced magnetic field strength within the grains leads to increased activation of intra-grain pinning centers, resulting from a reduction

in the effective superconducting volume fraction. Second, the progressive shift of the penetration temperature (T_p) to lower values with increasing field strength correlates with an expansion of the frozen volume fraction at inter-grain boundaries, consequently diminishing the overall superconducting phase fraction. These observations provide insights into both the intra-grain and inter-grain magnetic response of the Tl-2234 system. After presenting the AC susceptibility data, it is important to discuss the observed critical temperature (T_c) value of approximately 107 K, as shown in Figure 1. This value is somewhat lower than the commonly reported T_c range of 113-116 K for optimally doped and single-phase Tl-2234 compounds, as documented in the literature [15,16]. Several factors may explain this discrepancy. First, the oxygen stoichiometry in Tl-based cuprates is highly sensitive and can significantly impact superconducting properties, including T_c . Even minor deviations from the optimal oxygen content can lead to a reduction in T_c . Second, as noted in the introduction, Tl-based superconductors are susceptible to phase inhomogeneity and intergrowth of different Tl-Ba-Ca-Cu-O phases. The presence of minor secondary phases or intergrown members of the homologous series, even if not easily detectable by bulk techniques like AC susceptibility, can influence the overall superconducting behavior and potentially lower the observed T_c . Additionally, the method used to determine T_c can affect the measured value. In this study, T_c was identified based on the onset of the diamagnetic transition in the real part of the AC susceptibility (χ'). Other techniques, such as resistivity measurements or alternative criteria applied to susceptibility data, might yield slightly different T_c values. While the obtained T_c is slightly lower than expected, it still falls within a reasonable range for Tl-2234-based materials.

3.2 Critical Current Density

The imaginary component of AC magnetic susceptibility (χ'') provides valuable information about energy dissipation mechanisms in materials, including eddy current losses, magnetic hysteresis, and magnetic flux dynamics under alternating fields [17]. Quantitative analysis of $\chi''(T)$ curves, particularly the position and field dependence of their maxima, enables determination of the critical current density (J_c) in superconducting materials. For measurements conducted at low frequencies, the temperature and field evolution of AC susceptibility is conventionally interpreted through critical-state models [18]. These theoretical frameworks describe the distribution of penetrated supercurrents, which flow at a density equivalent to the material's critical current density (J_c). A fundamental assumption in these models is that J_c depends solely on the local internal field (H_i) [11]. Bean's critical-state model, which simplifies the analysis by assuming J_c is H_i -independent, offers a direct methodology for extracting J_c values from temperature-dependent χ'' measurements [19]. Within this framework, χ'' exhibits a maximum when the applied field achieves complete penetration of the superconducting

volume, specifically at the point where shielding currents match the sample's maximum current-carrying capacity [20]. As illustrated in Figure 2, the temperature dependence of critical current density can be systematically calculated from these χ'' maxima. When an external magnetic field fully penetrates the entire volume of a superconductor, a condition is reached where the shielding currents become equivalent to the maximum carrier capacity (determined by hole concentration) or the bulk critical current density.

At the characteristic temperature T_p , corresponding to the maximum in the imaginary component of magnetic susceptibility (χ''), the penetration field H_p achieves complete sample penetration, reaching the center of the specimen. This penetration process can be quantitatively described using Bean's critical state model, which establishes a mathematical relationship between the critical current density

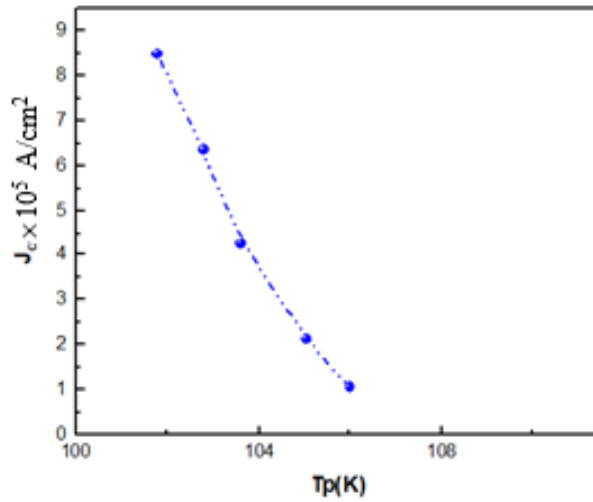


Figure 2. Temperature dependence of critical current density for the TI-2234.

J_c at the penetration temperature T_p and the penetration field H_p . This relationship has been well documented in previous studies [21-23], providing a fundamental framework for understanding the field penetration dynamics in superconducting materials.

$$J_c(T) = \frac{H_p}{R} \quad (2)$$

Equation (2) employs the parameter 'R', which is defined as the radius pertinent to the sample geometry. For cylindrical samples subjected to an axial magnetic field, 'R' directly corresponds to the cylinder radius, as detailed in reference [24]. However, for powder samples, R necessitates interpretation as an effective average particle radius, as established in reference [25]. In this study, the effective radius R for the powder sample was estimated based on the 89 μm sieve used for particle size classification and homogenization. This mesh size represents the maximum particle diameter allowed to pass. Therefore, an effective average particle radius of $R \approx 44.5 \mu\text{m}$ (half the maximum diameter)

was utilized in the J_c calculations using Equation (2). Subsequently, utilizing Equation (3), the critical current density was evaluated based on the peak position observed in the imaginary component (χ'') of the magnetic susceptibility. The critical current density J_c was calculated from the peak position of the imaginary part of AC magnetic susceptibility χ'' (Eq. 1). The temperature dependence of critical current density for the studied sample demonstrates strong agreement with the scaling relation expressed in equation (3) [14]:

$$J_c(T) = J_c(0) \left[1 - \frac{T}{T_c} \right]^\alpha \quad (3)$$

Here, $J_c(0)$ represents the critical current density at absolute zero temperature (0 Kelvin) and α is the critical exponent. The critical current density value was obtained from the peak position. The solid line in Figure (3) shows the correlation between the experimental critical current density measurements as a function of temperature and equation (3) and the fitting parameters $J_c(0)$ and α were found to be $J_c(0) = 3.6 \times 10^5 \text{ A/cm}^2$ and $\alpha = 1.26 \pm 0.08$. The study findings align well with prior research on thallium-based superconductors, highlighting the competitive superconducting characteristics of the Tl-2234 phase.

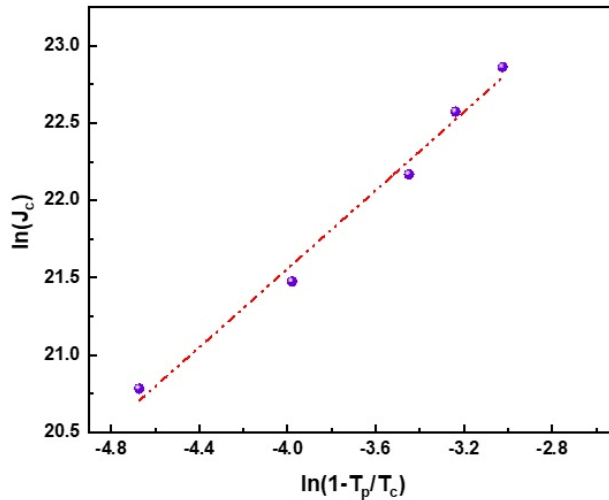


Figure 3. $\ln J_c(T)$ vs. $\ln (1-T/T_c)$ for the Tl-2234 sample. The slope of line determines the value of ' α ' specific to sample.

The observed critical current density $J_c(0) = 3.6 \times 10^5 \text{ A/cm}^2$ suggests the material is of good quality with strong pinning centers, which is typical for well-prepared thallium-based superconducting systems. The estimated critical current density at zero temperature, $J_c(0)$, for the Tl-2234 sample falls within the range of 10^5 to 10^6 A/cm^2 , consistent with the expected values for high-quality thallium-based superconductors. Reference [26] reports similar values for thallium cuprate superconductors, though measured at 77 K. In contrast, the $J_c(0)$ estimate in this study is extrapolated to 0 K,

demonstrating that the obtained values align with the known high critical current properties of these materials, even at absolute zero. The measured $J_c(0) = 3.6 \times 10^5 \text{ A/cm}^2$ is consistent with other thallium cuprate systems, such as Tl-2223 with $J_c(0) = 3.0 \times 10^6 \text{ A/cm}^2$ [27] and Tl-1223 with $J_c(0) \approx 2.8 \times 10^5 \text{ A/cm}^2$. Additionally, The critical exponent $\alpha = 1.26 \pm 0.08$ further demonstrates consistency with established flux creep models for high-temperature superconductors, supporting both the Anderson-Kim flux creep model predictions and the expectations of collective creep theory (where the typical α range is 1.0 - 1.5) [28-31].

4. Conclusion

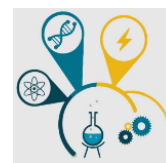
The AC magnetic susceptibility measurements revealed behavior dominated by the intragranular superconducting transition in the Tl-2234 system, as evidenced by the sharp drop in the real component (χ') and the characteristics of the imaginary component (χ''). The sharp transition observed in the susceptibility curves, accompanied by minimal broadening in the transition region, indicates good sample quality and homogeneity inferred from the magnetic response. The systematic shift of χ'' peaks toward lower temperatures with increasing alternating magnetic field strength provides evidence for enhanced magnetic field penetration effects and pinning within the grains. This behavior is attributed to an increase in intra-grain pinning centers, resulting from the synthesis and heat treatment process. Application of Bean's critical-state model to the AC susceptibility data, using an estimated effective particle radius of $R \approx 44.5 \text{ }\mu\text{m}$, enabled successful determination of the critical current density (J_c), assumed to primarily reflect the intragranular current carrying capacity in this powder sample. The temperature dependence of J_c followed the empirical scaling relation with remarkable precision, yielding a zero-temperature critical current density $J_c(0)$ of $3.6 \times 10^5 \text{ A/cm}^2$ and a critical exponent of 1.26 ± 0.08 . These findings contribute significantly to understanding the relationship between the magnetically inferred microstructural features and the magnetic properties in Tl-2234 superconductors. Future research directions could focus on optimizing synthesis conditions to further enhance the critical current density and investigating the effects of various dopants on the magnetic properties and pinning mechanisms within this system.

References

- [1] M. J. Qin and S. X. Dou, Superconductors high T_c , in *Encyclopedia of Condensed Matter Physics*, vol. 2, 2024, pp. 565–579. <https://doi.org/10.1016/B978-0-323-90800-9.00254-7>
- [2] A. Molodyk and D. C. Larbalestier, The prospects of high-temperature superconductors, *Science*, vol. 380, no. 6651, pp. 1220–1222, 2023, doi: 10.1126/science.abq4137.
- [3] H. Wu, Recent development in high temperature superconductor: Principle, materials, and applications, *Applied and Computational Engineering*, vol. 63, pp. 153–171, 2024, <https://doi.org/10.54254/2755-2721/63/20241015>
- [4] R. Shipra, J. C. Idrobo, and A. S. Sefat, "Structural and superconducting features of Tl-1223 prepared at ambient pressure," *Supercond. Sci. Technol.*, vol. 28, no. 11, p. 115006, 2015, doi: 10.1088/0953-2048/28/11/115006
- [5] Effects of Tl content and magnetic field on phase formation of $Tl_mBa_2Ca_{n-1}Cu_nO_{2n+2+\delta}$ ($m=1$ and 2, $n=4$) superconductors, *Physica C: Superconductivity and its Applications. Physica C: Superconductivity and its Applications*, vol. 586, p. 1353874, 2021, doi.org/10.1016/j.physc.2021.1353874.
- [6] B. Hassan, A. Alnakhlani, and M. Abdulhafiz, Investigating the effects of high magnetic fields on the phase stability of $Tl_2Ba_2Ca_2Cu_3O_{10-\delta}$ superconductor. *J. Phys. Sci.*, vol. 35, no. 2, pp. 33–45, 2024, doi: 10.21315/jps2024.35.2.3.
- [7] X. Chen and C. Gong, Dependence of the superconducting transition temperature on the type and number of CuO_2 layers in $Tl_2Ba_2Ca_{n-1}Cu_nO_{2n+4-\gamma}$. *Phys. Rev. B*, vol. 59, no. 6, pp. 4513–4523, 1999, doi: 10.1103/PhysRevB.59.4513.
- [8] A. A. Khurram and N. A. Khan, A search for a low anisotropic superconductor, *J. Electromagnetic Analysis & Applications*, vol. 2, pp. 63–74, 2010, doi: 10.4236/jemaa.2010.22010.
- [9] K. Buchkov, A. Galluzzi, E. Nazarova, and M. Polichetti, Complex AC magnetic susceptibility as a tool for exploring nonlinear magnetic phenomena and pinning properties in superconductors, *Materials*, vol. 16, no. 14, p. 4896, 2023, doi: 10.3390/ma16144896.
- [10] G. Kovács, I. Kirschner, I. Halász, R. Laiho, T. Porjesz, K. Tompa, and G. Zsolt, Structure and superconductivity of variously prepared Tl-Ca-Ba-Cu-O compounds, *Journal of the Less Common Metals*, vol. 150, pp. 229–240, 1989, doi: 10.1016/0022-5088(89)90275-0.

- [11] K.-H. Müller, AC susceptibility of high temperature superconductors in a critical state model, *Physica C: Superconductivity*, vol. 159, no. 6, pp. 717–726, 1989, doi: 10.1016/0921-4534(89)90143-3.
- [12] L. E. Wenger, W. Win, C. J. McEwan, J. T. Chen, E. M. Logothetis, and R. E. Soltis, The complex AC susceptibility - critical current relationship in oxide superconductors, in *High- T_c Superconductors*, H. W. Weber, Ed. Boston, MA: Springer, 1988, ch. 40. doi: 10.1007/978-1-4899-0846-9_40.
- [13] A. V. Silhanek, S. Raedts, M. Lange, and V. V. Moshchalkov, AC-susceptibility of superconducting films with a periodic pinning array, *Physica C: Superconductivity*, vol. 408–410, pp. 516–517, 2004, doi: 10.1016/j.physc.2004.03.073.
- [14] E. Nazarova, A. Zaleski, and K. Buchkov, Doping dependence of irreversibility line in $Y_{1-x}Ca_xBa_2Cu_3O_{7-\delta}$. *Physica C: Superconductivity*, vol. 470, no. 9–10, pp. 421–427, 2010, doi: 10.1016/j.physc.2010.03.002.
- [15] M. R. Presland, J. L. Tallon, P. W. Gilberd, and R. S. Liu, "Bulk single-superconducting-phase thallium “2234” superconductor - $Tl_{2-x}Ba_2Ca_{3+x}Cu_4O_{12-\delta}$, *Physica C: Superconductivity*, vol. 191, no. 3–4, pp. 307–315, 1992, doi: 10.1016/0921-4534(92)90923-Z.
- [16] T. Kaneko, K. Hamada, S. Adachi, H. Yamauchi, and S. Tanaka, Synthesis of Tl-based “2234” superconductors, *J. Appl. Phys.*, vol. 71, no. 5, pp. 2347–2350, 1992, doi: 10.1063/1.351087.
- [17] R. B. Goldfarb, M. Leental, and C. A. Thompson, "Alternating-Field Susceptometry and Magnetic Susceptibility of Superconductors, in *Magnetic Susceptibility of Superconductors and Other Spin Systems*, R. A. Hein, T. L. Francavilla, and D. H. Liebenberg, Eds. New York, NY: Plenum Press, 1991, pp. 49–80. doi: 10.1007/978-1-4899-2379-0_3.
- [18] C. P. Bean, "Magnetization of high-field superconductors, *Rev. Mod. Phys.*, vol. 36, no. 1, pp. 31–39, 1964, doi: 10.1103/RevModPhys.36.31.
- [19] F. Gömöry, Characterization of high-temperature superconductors by AC susceptibility measurements, *Supercond. Sci. Technol.*, vol. 10, no. 8, pp. 523–542, 1997, doi: 10.1088/0953-2048/10/8/001.
- [20] J. R. Clem, Granular and superconducting-glass properties of the high-temperature superconductors, *Physica C: Superconductivity*, vol. 153–155, pp. 50–55, 1988, doi: 10.1016/0921-4534(88)90491-1.

- [21] C. Lin, Bean's critical-state model as a consequence of the circuit model of non-linear resistance, *J. Appl. Phys.*, vol. 125, no. 3, p. 033901, 2019, doi: 10.1063/1.5084152.
- [22] C. Yang *et al.*, Improvement of critical current density J_c in powder-in-tube rapid heating, quenching and transformation Nb_3Al wires by doping with nano- SnO_2 , *Supercond. Sci. Technol.*, vol. 36, no. 6, p. 065001, 2023, doi: 10.1088/1361-6668/acc6f9.
- [23] J. Zhong, S. Zou, L. Lai, P. Chen, and S. Deng, Fast evaluation of the critical current of high-temperature superconducting coils based on the integral method, *J. Appl. Phys.*, vol. 132, no. 16, p. 163903, 2022, doi: 10.1063/5.0112003.
- [24] C. P. Bean, Magnetization of high-field superconductors, *Rev. Mod. Phys.*, vol. 36, no. 1, pp. 31–39, 1964, doi: 10.1103/RevModPhys.36.31.
- [25] M. W. Lee, M. F. Tai, S. C. Luo, and J. B. Shi, "Critical current densities in K_3C_{60}/Rb_3C_{60} powders determined from AC/DC susceptibility measurements, *Physica C: Superconductivity*, vol. 245, pp. 6–11, 1995, doi: 10.1016/0921-4534(95)00100-X.
- [26] M. Jergel, A. Conde Gallardo, C. Falcony Guajardo, and V. Strbik, TI-based superconductors for high-current, high-field applications," *Supercond. Sci. Technol.*, vol. 9, no. 6, pp. 427–446, 1996, doi: 10.1088/0953-2048/9/6/001.
- [27] R. Awad, S. G. Elsharkawy, I. H. Ibrahim, and B. H. Chazbeck, Superconducting properties of $(Tl_{1.6}Pb_{0.4})_{2223}$ substituted by praseodymium, *Asian Journal of Applied Sciences*, vol. 2, pp. 63–73, 2009, doi: 10.3923/ajaps.2009.63.73.
- [28] A. N. Lykov, Magnetic flux creep in HTSC and Anderson-Kim theory, *Low Temp. Phys.*, vol. 40, no. 9, pp. 773–795, 2014, doi: 10.1063/1.4896968.
- [29] M. P. Maley, J. O. Willis, H. Lessure, and M. E. McHenry, Dependence of flux-creep activation energy upon current density in grain-aligned $YBa_2Cu_3O_{7-x}$, *Phys. Rev. B*, vol. 42, no. 4, pp. 2639–2642, 1990, doi: 10.1103/PhysRevB.42.2639.
- [30] J. R. Thompson *et al.*, Enhanced current density J_c and extended irreversibility in single-crystal $Bi_2Sr_2Ca_1Cu_2O_8$ linear defects from heavy ion irradiation, *Appl. Phys. Lett.*, vol. 60, no. 19, pp. 2306–2308, 1992, doi: 10.1063/1.107012.
- [31] S. S. P. Parkin *et al.*, Model family of high-temperature superconductors: $Tl_mCa_{n-1}Ba_2Cu_nO_{2(n+1)+m}$ ($m=1, 2$; $n=1, 2, 3$). *Phys. Rev. B*, vol. 38, no. 10, pp. 6531–6535, 1988, doi: 10.1103/PhysRevB.38.6531.



Ab Initio Study of Structural, Thermal Stability and Electronic Properties of LiRuPO₄ Compound: A Storage Energy Application

Ahmed Memdough Younsi ^{1,*}, Mohamed Elbar ², Saïd Khoudiri ³

¹ University of Biskra, Laboratory of Physics of Photonics and Multifunctional Nanomaterials, BP 145, RP, 07000 Biskra, Algeria, Ahmed.younsi@univ-biskra.dz

² LAADI Laboratory, Faculty of Sciences and Technology, Ziane Achour University of Djelfa, P. O. B. 3117, Moudjbara Street, 17000 Djelfa, Algeria, m.elbar@univ-djelfa.dz

³ Electrical Engineering department, Faculty of Sciences and Technology, Ziane Achour University of Djelfa, P. O. B. 3117, Moudjbara Street, 17000 Djelfa, Algeria, s.khoudiri@univ-djelfa.dz

*Corresponding author: (A. M. Younsi), Email Address: Ahmed.younsi@univ-biskra.dz

Abstract

In this paper, we investigated the structural, electronic, and thermal stability of the LiRuPO₄ compound. We applied the ab-initio-density functional to conduct all our calculations. We used gradient generalized approximation with Hubbard correction implemented in the CASTEP (Cambridge Serial Total Energy Package) code. Results indicate that LRP crystallizes in the orthorhombic structure after phonons and thermal stability analysis. LRP is a semiconductor with an indirect gap after analysis of band structure curves within electronic properties and an energy gap of 2,18 eV. LiRuPO₄ will be an effective alternative to LiFePO₄ in storage energy applications such as electric batteries in vehicle fabrication technology.

Keywords: LiRuPO₄, density functional calculations, semiconductor, storage energy applications.

<https://doi.org/10.63070/jesc.2025.004>

Received 30 March 2025; Revised 29 April 2025; Accepted 15 May 2025.

Available online 22 May 2025.

Published by Islamic University of Madinah on behalf of *Islamic University Journal of Applied Sciences*. This is a free open access article.

1. Introduction

As the demand for electrical energy increases and the available sources are finite, efficient utilization of energy has become an important issue. In this regard, energy storage devices are required to ensure uninterrupted power supply and to regulate power generation. The lithium-ion battery is one of the smartest choices for energy storage devices due to its long charge/discharge cycling, low self-discharge, high energy density, and design flexibility. Improving the performance of lithium-ion batteries is a topic of interest, and numerous investigations have been performed to enhance the capacity and cycle stability of lithium-ion batteries. The cathodes of lithium-ion batteries are typically inorganic materials, and the most attractive cathode material is LiFePO_4 (LFP) due to its low cost and large operating voltage window. Although its operating voltage may be limited compared to NCM or LCO, these types of cathodes may fail explosively due to thermal runaway. LFP has better electronic conductivity than NCA and LCO. The poor electronic conductivity of pure LFP can be improved by cation and anion surface doping, and under optimum conditions, LFP shows about 10-11 orders of increased electronic conductivity. [1-3]

The driving force to study the LFP properties has been the significance of the ab-initio (DFT based) method available for studying the material properties down to the atomic scale level that links the material behavior at different length scales and the experimentation as well. Typically, available investigations were just based on experimental analysis. Various studies so far have been performed for LFP, like calculation of structural and electronic properties, effect of defects on the electrochemistry of LFP, lithium diffusion paths, electronic and ionic conductivities, etc.

In this work we studied a compound similar to LFP, which is LiRuPO_4 when we applied ab-initio study to calculation its structural, electronic and thermal stability properties of this compound. Lithium ruthenium phosphate, LiRuPO_4 , is a promising material for batteries in hybrid electric vehicles and for future nano-electronics, due to its stable ruthenium-redox potential and large lithium de-intercalation reaction occurring at a voltage around 3.5 V with respect to Li^+/Li . In an energy storage device, lithium is released (de-intercalated) from an electrode during the discharge process, where it reacts with an electrolyte phase and an electronic conductor to complete the intercalation reaction. [4, 5]

2. Computational Methods

The properties of LRP, including its structural, electronic, and thermal stability, were studied using ultra-soft pseudopotential plane waves in the CASTEP package [6]. The exchange-correlation potential was represented by the generalized gradient approximation of Perdew et al. with a Hubbard correction of 3 eV (GGA-PBE+U) [7, 8]. The plane wave cut-off energy was set at 480 eV, and a $6 \times$

6×6 special k-points mesh as per Monkhorst and Pack was used. Electrons and ions were relaxed when the variation of successive energies and forces exceeded 10^{-5} eV and 0.02 eV/Å, respectively. Energy convergence was considered achieved within an error of 10^{-5} .

3. Results And Discussion

3.1. Thermal Stability Properties

3.1.1. Phonons

Figure 1 shows stability thermal and energies are calculated as functions of the wave vector of phonons in the long-wavelength limit, and together these fold points become the complete phonon dispersion curves if extended over a whole reciprocal space of the appropriate size. In the frequency versus q-space plot (phonon curve), regions of linear dispersion correspond to frequencies of transverse phonons, while curvilinear dispersion corresponds to LA phonons. Branches with negative curvature also refer to (nonzero) low-frequency TA phonons. After the test of the stable crystal of LiRuPO_4 , The positive range of the density phonon of states and phonon dispersion indicate that the orthorhombic structure in Pnma space group is the stable structure of LRP.

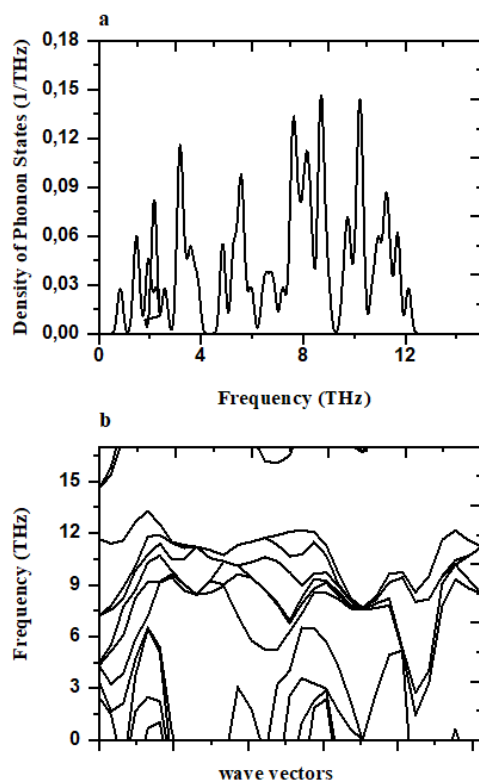


Figure 1. Phonons of LiRuPO_4 using GGA+U in Pnma orthorhombic structure.

3.1.2. Thermal Conductivity

In three-dimensional (3D) materials, the discussion of lattice thermal conductivity focuses on the transfer of phonon energy (see Figure 1). This energy transfer occurs through various mechanisms, including acoustic-optical interactions, regular and anharmonic processes, and Umklapp scattering, which are influenced by temperature and crystal structure. At low temperatures, research indicates that the thermal resistivity of these 3D crystals is proportional to the cube of the temperature, as explained by the Debye theory, which limits the density of states for phonons. Many studies prioritize thermal conductivity, a more practical parameter for applications that can be measured using experimental equipment. Generally, reducing thermal conductivity is essential for decreasing the thermal resistance of a given material. This knowledge is often applied in technologies for electronic devices, among other uses. However, lithium-ion systems have more stringent requirements for these materials, particularly regarding the interaction between battery and thermal systems, due to the significant heat generated while cycling high-specific energy storage.

From the phonons curves, the thermal conductivity (κ_L) of LiRuPO_4 is typically compared with that of other conducting nitride-phosphates that have pyrophosphate-related structures. It is generally understood that in LiMPO_4 materials, the thermal conductivity decreases as the conductivity of heat or Li^+ carriers diminishes. At elevated temperatures, the κ_L of LiRuPO_4 is comparable to the values found in many mixed characteristic materials; however, it is lower than that of Li^+ -high-conducting sulfates and oxides. To date, the temperature dependence of the κ_L of LiRuPO_4 has not been investigated. Therefore, it is essential to extend the previously studied characteristics of κ_L in LiRuPO_4 to higher temperatures, considering both thermally and structurally related properties.

3.2. Structural properties

Lithium Ruthenium phosphate (LiFePO_4) was the first olivine type cathode material for rechargeable lithium batteries. However, this compound belongs to the Pnma orthorhombic space group, This structure (Figure2) consists of 6-coordinated PO_4 tetrahedra sharing corners with RuO_6 octahedra in edge-shared chains of corner linked LiO_6 octahedra that run along the a coordinate. The endo-octahedra of the Ru chains complete the orthorhombic coordination of the Li atoms. There is a direct correlation between the Li^+ diffusion and the low dimensional octahedral interstices present in the Pnma orthorhombic space group of the olivine structure. First-principles calculations converge to the orthorhombic cell parameters ; $a = 10.38 \text{ \AA}$, $b = 5.99 \text{ \AA}$, and $c = 4.78 \text{ \AA}$, see (table1) and to the mitigated atomic coordinates to the Pnma crystal structure, with Li1 atoms in (4f) positions 0,0,z with $z = 0.20$ and 0.327 , Ru (4c) in $0.555, 0.25, 0.247$, P in (4e) $0.918, 0.25, 0.728$, and O in (4d) at

0.276, 0.25, 0.255 and 0.637, 0.25, 0.113. Bond valence sum analysis of LiRuPO_4 , using 25 val, 1.04 vil, and 3.84 μB per Ruthenium ion, providing bond lengths between semiconductor and ligands between 2 and 3 Å.

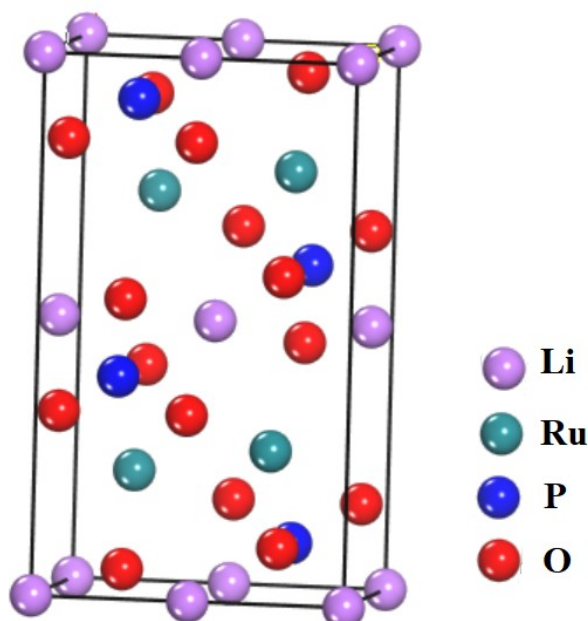


Figure 2. Primitive cell of LiRuPO_4 orthorhombic structure Pnma space group (No.62)

Table1. lattice parameter calculated of LiRuPO_4 in orthorhombic Pnma space group with using GGA+U (Hubbard correction $U = 3.0$ eV)

<i>Compound</i>	<i>Functional</i>	<i>Ground state energy (eV)</i>	<i>Lattice constants (Å)</i>	<i>Bulk modulus B_0(GPa)</i>
LiRuPO_4	GGA +U	-18889,71	a=10,38 b=5,99 c=4,78 $V=297,20\text{Å}^3$	236,62

3.3. Electronic properties

3.3.1 Band structures

The band structure of LiRuPO_4 has seen little theoretical focus, and that too via an effective one-electron single-electron-electron based theory. Here, using much more robust and rigorous computational quantum physics methods of GGA+U, we present in Figure3 the theoretical results of the band structure curves of LiRuPO_4 , The fermi level was fixed at 0 and we got indirect energy gap between two points in Brillouin zone, Z and X, the value of this gap is 2,18eV, so that LRP is semiconductor compound.

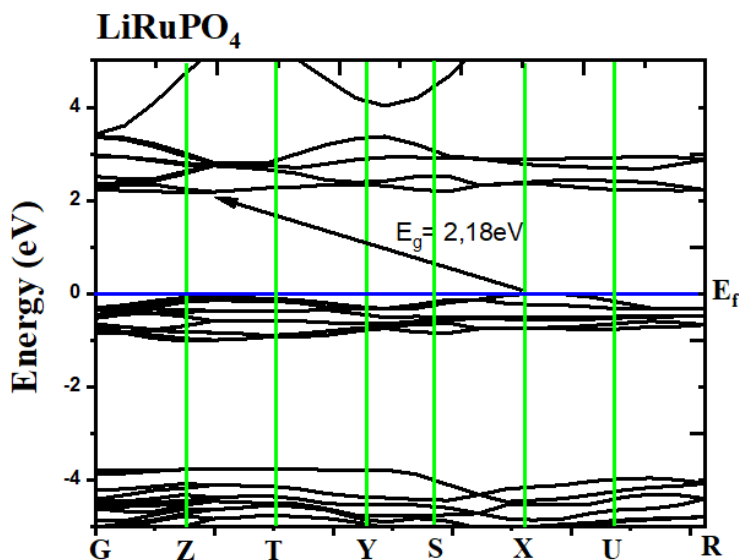


Figure 3. Band structure curve of LiRuPO₄ using GGA+U

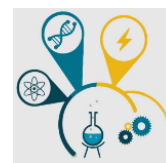
4. Conclusion

In this study, ab initio calculations based on Density Functional Theory (DFT) were used to examine the thermal stability, structural, and electronic properties of LiRuPO₄. The study employed the pseudo-potential plane waves method, using a primitive cell instead of the standard approach. This method determined that the concentration window for the atomic distance of the orthorhombic phase olivine-LiRuPO₄ (LRP) was about 0.05–0.1 Å of Li atoms per unit cell of LRP, a finding that is higher than the reported insertion composition of Li for phase transformation of LRP, and has significant implications for the understanding of LRP's behavior. Additionally, the material LRP exhibited semiconductive behavior.

Our ongoing efforts to extend the duration of the two-stage reduction process are nearing completion. The charge-discharge kinetics, primarily influenced by the intercalation reaction of lithium, are a key focus. In future research, we are exploring atomistic modeling of high capacities in both the cathode olivine LiRuPO₄ and the anode ternary orthosilicate Li_{4-δ}Ru_{1-x}Ti_xPO₄. This development aims to achieve rapid charging by combining efficient 3D lithium migration with excellent electronic and ionic conductivities. We are also proposing an analytical method for developing high-capacity silicon-based anodes with significantly less experimental screening work. The key parameters relevant to the reversible capacitive energy during the insertion process are under thorough study. After that, we have not forgotten the thermodynamics of the phosphate Li_{4-δ}Ru_{1-x}Ti_xPO₄ olivine in comparison to lithium lithiated phosphate phases and oxide spinel, providing comprehensive insight into the chemical behavior of the metastable phase.

5. References

- [1] Al-Samet, M. A. M. M. & Burgaz, E., Improving the lithium-ion diffusion and electrical conductivity of LiFePO_4 cathode material by doping magnesium and multi-walled carbon nanotubes. *Journal of Alloys and Compounds*. 947 (2023) 169680.
- [2] Erabhoina, H. & Thelakkat, M. Tuning of composition and morphology of LiFePO_4 cathode for applications in all solid-state lithium metal batteries. *Scientific reports*. 12 (2022) 5454.
- [3] Suarso, E., Setyawan, F. A., Subhan, A., Ramli, M. M., Ismail, N. S., Zainuri, M., ... & Darminto. Enhancement of LiFePO_4 (LFP) electrochemical performance through the insertion of coconut shell-derived rGO-like carbon as cathode of Li-ion battery. *Journal of Materials Science: Materials in Electronics*, 32 (2021) 28297-28306.
- [4] Zhao, Q. F., Zhang, S. Q., Hu, M. Y., Wang, C., & Jiang, G. H. Recent advances in LiFePO_4 cathode materials for lithium-ion batteries. first-principles research. *International Journal of Electrochemical Science*, 16 (2021) 211226.
- [5] Zhang, B., He, Y., Gao, H., Wang, X., Liu, J., Xu, H., ... & He, X.. Unraveling the doping mechanisms in lithium iron phosphate. *Energy Materials*, 2(2022).
- [6] CLARK, S.J.; SEGALL, M.D.; PICKARD, C.J.; HASNIP, P.J.; PROBERT, M.J.; REFSON, M.I.J.; PAYNE, M.C. First principles methods using CASTEP. *Z. Krist.*,v. 220 (2005) 567.
- [7] PERDEW, J.P.; BURKE, K.; ERNZERHOF, M. Generalized Gradient Approximation Made Simple. *Phys. Rev. Lett.*,v. 77 (1996) 3865.
- [8] Shih, B.C., Yates, J.R. Gauge-including projector augmented-wave NMR chemical shift calculations with DFT+ U. *Phys. Rev. B*. 96 (2017) 1-10.



Effect of Thermal Configurations in Multi-pipe Heat Exchangers on MHD Natural Convection within a Square Enclosure with Curved Corners

Wedad Hassan Asiri ¹, Ammar Abdulkadhim ², Halemah Ibrahim Elsaedy ¹, Nejla Mahjoub Said ^{1,*}

¹ Department of Physics, College of Science, King Khalid University, Abha 61413, Saudi Arabia,
445816980@kku.edu.sa; halsayede@kku.edu.sa; nalmahjoub@kku.edu.sa

² Mechanical Engineering Department, University of Al-Qadisiyah, Al-Qadisiyah 58001, Iraq,
ammar.abdulkadhim@qu.edu.iq

*Corresponding author: (N. Mahjoub), *Email Address*: nalmahjoub@kku.edu.sa

Abstract

This paper aims to study Magnetohydrodynamic (MHD) natural convection in a square enclosure with curved corners, particularly the thermal performance of multi-inner pipes used in heat exchangers. Numerical simulations are carried out to study the fluid flow behavior and thermal distribution in the presence of magnetic field by changing Hartmann number from [0-80] and varying Rayleigh number [1e4-1e6]. It can be seen that the layout of the inner pipes has a great influence on the enhancement of heat transfer rates and some recommendations for the improvement of the heat exchange design for engineering applications are provided. Finally, conclusions are made based on the numerical results of this study. The results showed that increasing Ra and reduced Ha reveals better heat transfer. Additionally, at high, case 1 give the best heat transfer bettering.

Keywords: Magnetohydrodynamics (MHD), Heat Transfer Enhancement, Nusselt Number (Nu), Nanofluid Thermodynamics, Numerical Simulations

<https://doi.org/10.63070/jesc.2025.005>

Received 02 April 2025; Revised 06 May 2025; Accepted 18 May 2025.

Available online 25 May 2025.

Published by Islamic University of Madinah on behalf of *Islamic University Journal of Applied Sciences*. This is a free open access article.

1. Introduction

There are thousands of published articles on natural convection within enclosures due to its applications in the heat exchangers industry. Generally, this field can be categorized into two major groups: (1) studies without an inner body and (2) studies with an inner body. The first category has been extensively examined by numerous researchers considering various thermal arrangements. Alasiri (2024) numerically investigated the effects of heater length and position on natural convection in a square enclosure filled with Cu-water nanofluid. A correlation for the Nusselt number was developed in terms of heater parameters, Rayleigh number, and nanoparticle loading.

Ghasemi and Aminossadati (2009) numerically analyzed the impact of inclination angle on heat transfer properties within a square enclosure filled with CuO -water nanofluid. For this purpose, the finite volume method was used in the numerical solution. Their results showed that the inclination angle plays a significant role in determining the heat transfer rate. The second category, which focuses on the role of the inner body, has also been widely studied.

For example, Kim et al. (2008) investigated the effects of the vertical position of an inner circular body located within a square enclosure under different Rayleigh numbers. The Immersed Boundary Method (IBM) was employed in the numerical simulations. Their findings indicated that the highest Nusselt number along the inner body occurs when it moves downward. Other studies have explored configurations with multiple inner bodies.

Garoosi et al. (2015) examined natural convection within a square enclosure containing multiple hot and cold inner bodies. The authors analyzed various types of nanofluids, including Cu, Al_2O_3 , and TiO_2 , along with different numbers and locations of inner bodies. Their results demonstrated that the placement of inner bodies significantly influences the heat transfer rate. Additionally, the role of the magnetic field was investigated to assess its impact on fluid flow and heat transfer characteristics.

Cho et al. (2019) conducted a numerical study on two-dimensional natural convection in a square container featuring a vertical array of two elliptical cylinders. They employed the Immersed Boundary Method (IBM) combined with the Finite Volume Method (FVM) to accurately capture the virtual wall boundaries of the cylinders. The aspect ratio (AR) of the elliptical cylinders varied from 0.25 to 4.00, while the Rayleigh number (Ra) ranged from 10^4 to 10^6 . The study analyzed changes in flow and thermal fields resulting from different aspect ratios of the elliptical cylinders.

Ibrahim et al. (2022) investigated natural convection inside cavities to enhance heat transfer in different package shapes by introducing nanoparticles into the core fluid. They used the COMSOL software, based on the Galerkin finite element approach, for their numerical calculations. The study considered

various parameters, including Rayleigh numbers (10^3 to 10^6), solid volume fraction ($\phi=0.05$), inclination angles (-45° , -30° , 0° , 30° , 45°), the radius of the inner circle ($R=0.15$), and the radii of the inner elliptical cylinder ($R_x=0.2$ and $R_y=0.15$).

Nammi et al. (2022) numerically investigated unsteady natural convection heat transfer in a porous square container containing four heated cylinders arranged in either a square or rectangular configuration. The results were presented using streamlines, isotherms, and time-averaged Nusselt numbers for the ranges $10^3 \leq Ra \leq 10^6$, $10^{-4} \leq Da \leq 10^{-2}$, and four different cylinder spacings ($0.3 \leq S \leq 0.6$).

Chatterjee and Kumar (2017) conducted a finite-volume numerical study on two-dimensional hydromagnetic natural convection in a cooled square container containing four uniformly shaped, heated inner circular cylinders. They assumed that all solid walls were electrically insulated. The simulations covered various control parameters, including Rayleigh numbers (10^3 to 10^6), Hartmann numbers (0 to 50), and dimensionless distances between cylinder centers (0.3 to 0.7). The study aimed to analyze how the placement of the cylinders along the diagonals of the enclosure influences magnetic heat transfer within the cavity.

The present work focuses on natural convection heat transfer within a square enclosure with curved corners, filled with different thermal arrangements of inner bodies, using the finite element method under a horizontal magnetic field. Numerical simulations were conducted to analyze the effects of various thermal arrangements and configurations of inner pipes on heat transfer performance. Using COMSOL Multiphysics, the fluid flow behavior and thermal distribution were studied under the influence of a magnetic field and varying Rayleigh numbers. The governing mathematical equations for fluid flow, heat transfer, and magnetic field interactions were solved to ensure accurate and reliable results. The findings demonstrated that the layout and configuration of the inner pipes significantly influence heat transfer rates, providing valuable insights into optimizing heat exchanger design for engineering applications. Based on the numerical results, recommendations were provided for improving thermal performance. Future studies could explore more complex geometries and turbulent flow conditions to further enhance the understanding of heat transfer mechanisms in magnetohydrodynamic (MHD) systems.

2. Material and method

The computation domain considering four different cases of inner hot and cold bodies presented in Figure 1. The governing equations had been inserted below;

$$\frac{\partial U}{\partial X} + \frac{\partial V}{\partial Y} = 0$$

$$U \frac{\partial U}{\partial X} + V \frac{\partial U}{\partial Y} - \frac{\partial P}{\partial X} + \frac{\mu_{nf}}{\rho_{nf} \alpha_f} \left(\frac{\partial^2 U}{\partial X^2} + \frac{\partial^2 U}{\partial Y^2} \right)$$

$$U \frac{\partial V}{\partial X} + V \frac{\partial V}{\partial Y} = - \frac{\partial P}{\partial Y} + \frac{\mu_{nf}}{\rho_{nf} \alpha_f} \left(\frac{\partial^2 V}{\partial X^2} + \frac{\partial^2 V}{\partial Y^2} \right) - Ha^2 \cdot PrV + Ra \cdot \frac{Pr(\rho\beta)_{nf}}{\rho_{nf} \beta_f} \theta$$

$$U \frac{\partial \theta}{\partial X} + V \frac{\partial \theta}{\partial Y} = \frac{\alpha_{nf}}{\alpha_f} \left(\frac{\partial^2 \theta}{\partial X^2} + \frac{\partial^2 \theta}{\partial Y^2} \right)$$

The following nondimensional parameters had been considered;

$$X = \frac{x}{L}, Y = \frac{y}{L}, A = \frac{a}{L}, B = \frac{b}{L}, U = \frac{uL}{\alpha_f}, V = \frac{vL}{\alpha_f}, P = \frac{\bar{P}L^2}{\rho_{nf} \alpha_f^2}, \theta = \frac{T - T_c}{T_h - T_c}$$

Three dimensionless numbers had been involved in the present study;

$$Ra = \frac{g \beta_f L^2 (T_h - T_c)}{v_f \alpha_f}, Ha = B_0 L \sqrt{\frac{\sigma_{nf}}{\rho_{nf} v_f}}, Pr = \frac{v_f}{\alpha_f}, Nu_m = \frac{1}{S} \int_0^S Nu(S) ds$$

where S is the surface area of the inner body

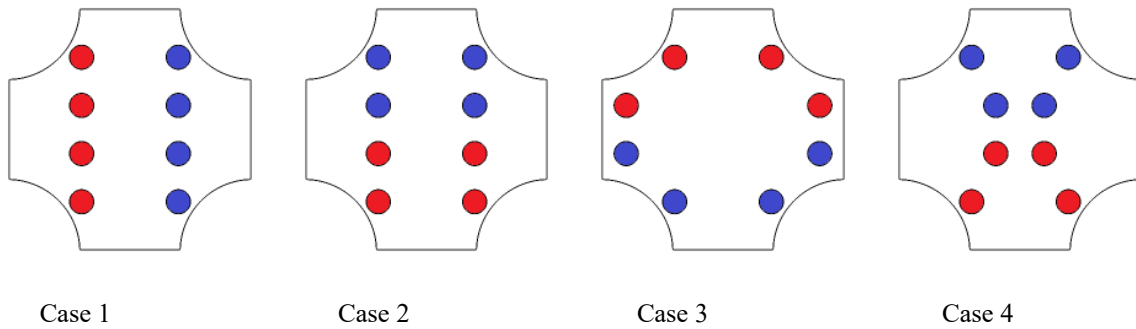


Figure 1. schematic representation of the problem

The properties of the nanofluid can be defined based on the properties of the pure liquid and solid nanoparticles (Oztop and Nada 2008)

$$\rho_{nf} = (1 - \phi) \rho_f + \phi \rho_s, (\rho\beta)_{nf} = (1 - \phi) (\rho\beta)_f + \phi (\rho\beta)_s$$

$$(\rho C_p)_{nf} = (1 - \phi) (\rho C_p)_f + \phi (\rho C_p)_s, \alpha_{nf} = \frac{k_{nf}}{(\rho C_p)_{nf}}, \sigma_{nf} = (1 - \phi) \sigma_f + \phi \sigma_s$$

$$k_{nf} = \frac{(k_p + 2k_f) - 2\phi(k_f - k_p)}{(k_f + 2k_p) + \phi(k_f + k_p)} k_f; \mu_{nf} = \mu_f (1 - \phi)^{-2.5}$$

Table 1. the thermophysical properties of the base fluid and CuO (Ghasemi and Aminossadati 2010)

	Pure water	CuO
ρ (kgm^{-3})	997.1	6320
C_p ($\text{Jkg}^{-1}\text{K}^{-1}$)	4179	531.8
K ($\text{Wm}^{-1}\text{k}^{-1}$)	0.613	76.5
$\beta \times 10^{+5}$ (k^{-1})	21	1.8

2.1 Mesh generation

COMSOL software was used to draw the model, generate the grid as presented in Figure 2, and then solve the governing equations using the finite element method.

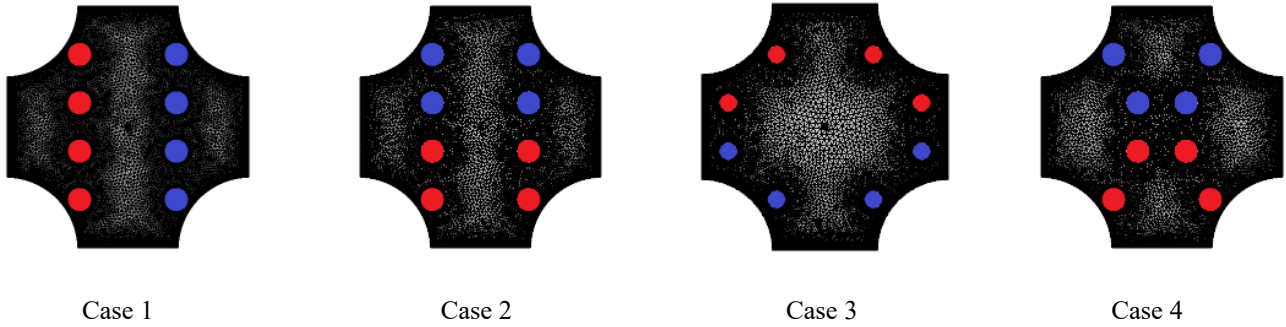


Figure 2. mesh generation for the four cases

2.2 Validation

The validation had been done with Davis (1983) in terms of Nusselt number as depicted in Figure 3 under various Rayleigh numbers.

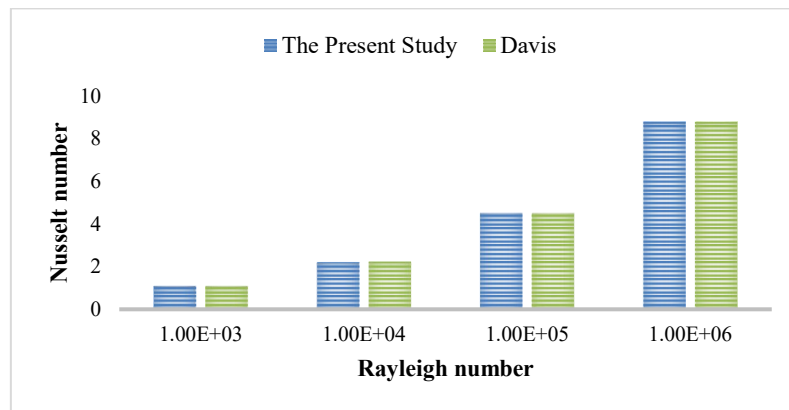


Figure 3. validation of the present work with Davis (1983)

3. Results and discussions

Figure 4.a. illustrates the streamlines and isothermal contours for different Hartmann numbers (Ha) at a constant Rayleigh number $Ra=10^4$ for case 1. The streamlines represent the flow behavior and circulation patterns within the domain, highlighting the magnetic field's influence on natural convection. At $Ha=0$, the flow exhibits strong vortex patterns with prominent buoyancy effects. As Ha increases ($Ha=40$ and $Ha=80$), the flow patterns become more organized due to the Lorentz force induced by the magnetic field, reducing circulation and minimizing flow disturbances. The isothermal contours illustrate the temperature distribution within the domain. At $Ha=0$, the contours are irregular and widely spaced, indicating convection-dominated heat transfer. As Ha increases, the isothermal contours become more uniform and closely spaced, reflecting the reduced impact of convection as the magnetic field enhances conduction. The combined effect of the magnetic field and higher Hartmann numbers reduces flow disturbances and promotes heat transfer through conduction, resulting in a more stable thermal distribution across the domain.

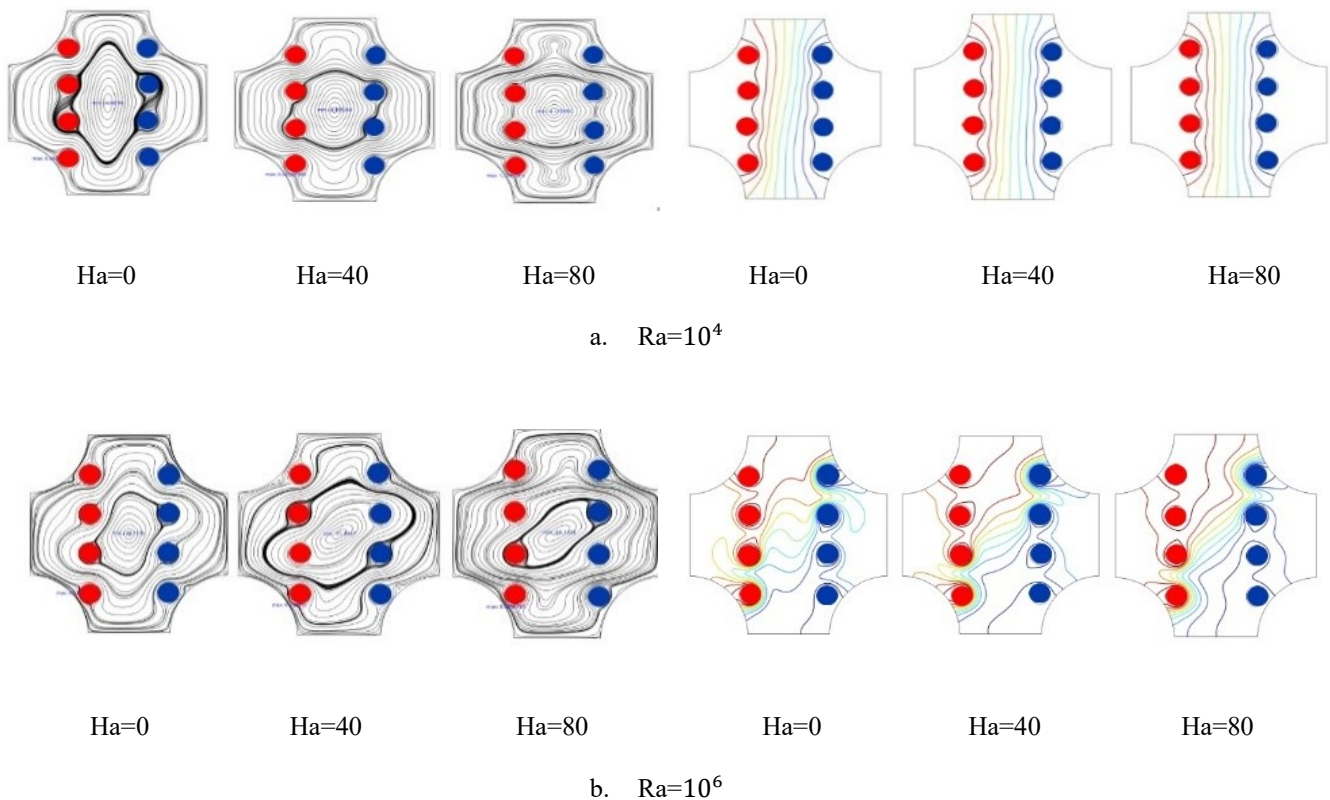


Figure 4. Streamlines and isotherms for various Hartmann numbers: case 1

Figure 4.b illustrates the streamlines and isothermal contours for different Hartmann numbers ($Ha=0$, 40, 80) at a constant Rayleigh number ($Ra=10^6$) for case 1. The streamlines depict variations in flow

behavior and circulation patterns within the domain, highlighting the influence of the magnetic field at different Hartmann numbers.

At $Ha=0$, the flow exhibits strong vortex structures due to the dominant buoyancy effect. As Ha increases, the flow patterns become more structured, demonstrating the magnetic field's role in suppressing natural convection and reducing flow disturbances. The isothermal contours represent the temperature distribution within the domain. At $Ha=0$, the contours appear distorted and irregular, indicating convection-dominated heat transfer. As Ha increases, the isothermal contours become more uniform, reflecting a transition toward conduction-dominated heat transfer under the influence of the magnetic field. The combined effect of the magnetic field and higher Hartmann numbers enhances thermal conduction while suppressing convection, leading to a more stable and uniform temperature distribution within the domain.

Figure 5.a illustrates the streamlines and isotherms for various Hartmann numbers ($Ha=0, 40, 80$) at a constant Rayleigh number ($Ra=10^4$) for case 2.

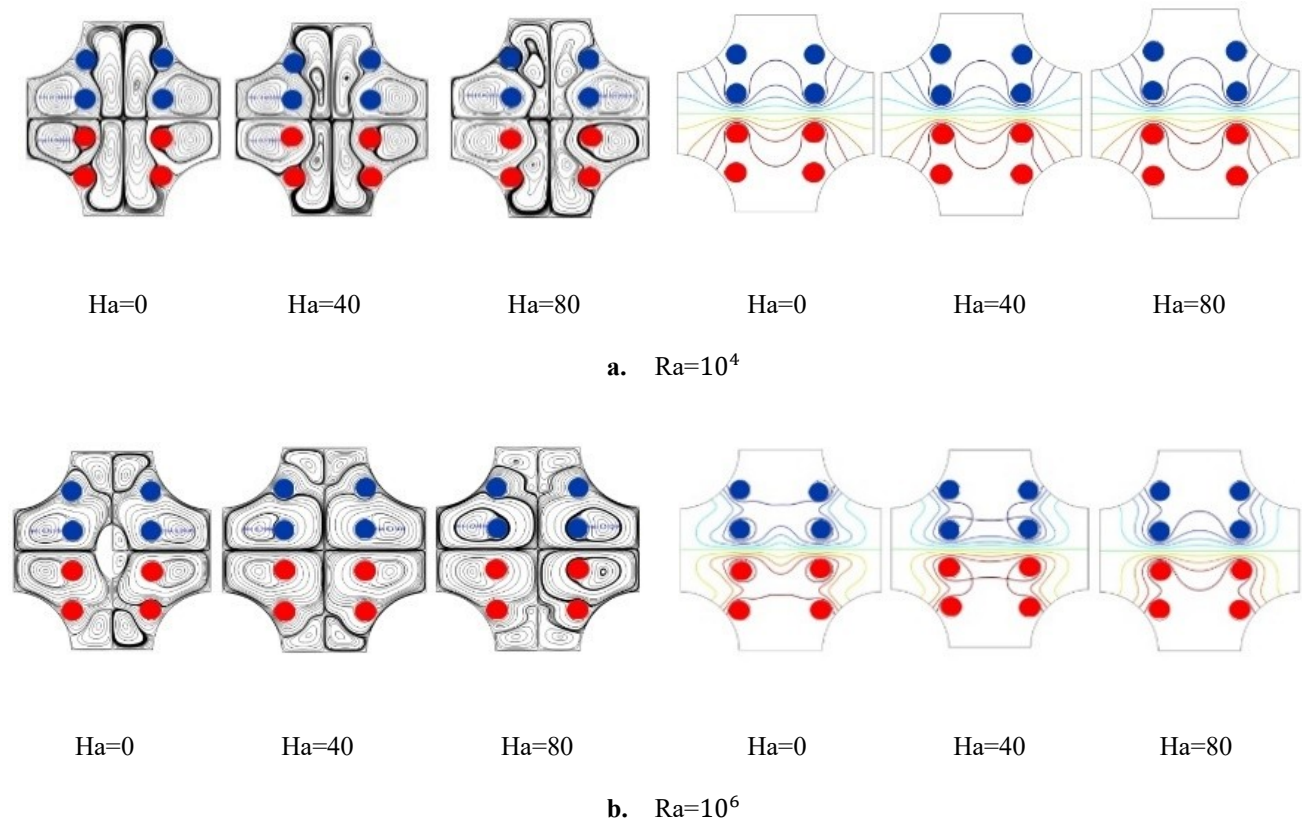


Figure 5. Streamlines and isotherms for various Hartmann numbers: case 2

The streamlines depict fluid flow behavior within the domain and the influence of the magnetic field on circulation patterns. At $Ha=0$, the flow exhibits strong vortical structures driven by natural convection. As Ha increases, the streamlines become more organized, reflecting the dampening effect of the magnetic field, which reduces flow disturbances and suppresses convective motion. The isotherms represent the temperature distribution within the domain. At $Ha=0$, they appear distorted and irregular, indicating convection-dominated heat transfer. As Ha increases, the isotherms become smoother and more uniform, signifying a transition to conduction-dominated heat transfer. This figure highlights the increasing influence of the magnetic field in suppressing convection and enhancing thermal conduction, leading to a more stable and uniform temperature distribution.

Figure 5.b. illustrates the streamlines and isotherms for various Hartmann numbers ($Ha=0,40,80$) at a constant Rayleigh number ($Ra=10^6$) for case 2. The streamlines depict the dynamic behavior of the flow and circulation patterns within the domain. At $Ha=0$, the flow exhibits strong vortices driven by natural convection in the absence of a magnetic field. As Ha increases to 40 and 80, the vortex intensity gradually decreases, with the flow becoming more stable and less dynamic due to the suppressive effect of the magnetic field on convection, with reduces flow velocity. The progressive change in flow patterns demonstrates how the magnetic field stabilizes the flow and mitigates disturbances caused by natural convection. The isotherms represent the temperature distribution within the domain. At $Ha=0$, the isotherms are highly distorted, indicating convection-dominated heat transfer. As Ha increases to 40 and 80, the isotherms become more uniform and parallel, signifying a transition to conduction-dominated heat transfer and a diminished influence of convection. This figure highlights the combined effects of the magnetic field and constant Rayleigh number, where the magnetic field enhances system stability, suppresses convective effects, and promotes heat transfer through conduction.

Figure 6.b. illustrates the streamlines and isotherms for various Hartmann numbers ($Ha=0, 40, 80$) at a constant Rayleigh number ($Ra=10^6$) for case 3. The streamlines depict the flow patterns within the domain. showing strong vortices at $Ha=0$, which indicate the dominance of natural convection in the absence of a magnetic field. As Ha increases to 40 and 80, the intensity of the vortices gradually diminishes, reflecting the suppressive effect of the magnetic field on convective motion and its role in stabilizing the flow. The magnetic field reduces the kinetic energy of convection and enhances the steadiness of the flow. The isotherms represent the heat distribution within the domain. At $Ha=0$, the isotherms are highly distorted due to intense heat transfer driven by strong convection. As Ha increases, the isotherms become more uniform and parallel, indicating the dominance of conduction over convection. This figure highlights the influence of the magnetic field in mitigating convection

and promoting conduction-based heat transfer, resulting in a more stable and efficient heat distribution system.

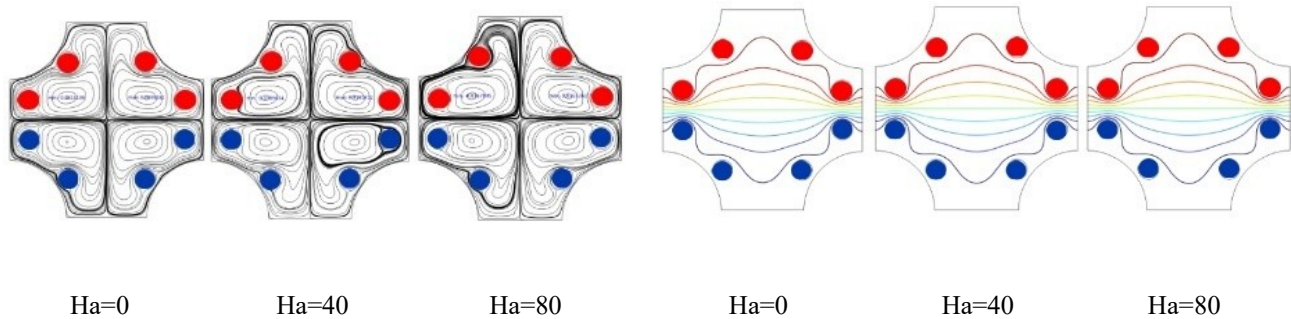


Figure 6. Streamlines and isotherms for various Hartmann numbers: case 3 at $Ra = 10^6$

Figure 7.a. illustrates the streamlines and isotherms for various Hartmann numbers Ha at a constant Rayleigh number $Ra = 10^4$ for case 4. In the top row, the streamlines depict the fluid flow patterns within the domain. At $Ha = 0$, the flow motion is prominent with strong vortices, reflecting the effects of unconstrained natural convection. As Ha increases to 40 and 80, the intensity of the vortices gradually decreases, indicating that the magnetic field restricts the flow motion and weakens the buoyancy effects. In the bottom row, the isotherms show the temperature distribution within the domain. At $Ha = 0$, the isotherms are highly distorted due to heat transfer dominated by convection. As Ha increases, the isotherms become more regular and align closer to the conductive pattern, highlighting the effect of the magnetic field in reducing convection intensity and enhancing conductive heat transfer. The figure emphasizes the interaction between buoyancy forces and the magnetic field, where the magnetic field suppresses thermal flow and modifies the heat distribution pattern

Figure 7.b. illustrates the streamlines and isotherms for various Hartmann numbers Ha at a constant Rayleigh number $Ra=10^6$ for case 4. The streamlines in the top section represent the flow behavior and circulation patterns within the domain, highlighting the influence of the magnetic field as Ha increases. At $Ha = 0$, the flow exhibits strong circulation patterns and well-defined vortices, reflecting the intense natural convection effects driven by buoyancy forces. As Ha increases to 40 and 80, the streamlines show a gradual reduction in circulation intensity, indicating that the magnetic field suppresses motion and diminishes the effects of convection. The isotherms in the bottom section depict the temperature distribution across the domain. At $Ha = 0$, the isotherms are highly distorted, indicating heat transfer dominated by convection. As Ha increases to 40 and 80, the isotherms become more regular and parallel, reflecting a transition to conduction-dominated heat transfer due to the influence

of the magnetic field. The figure demonstrates how the magnetic field reduces the intensity of convection and enhances conduction, contributing to a more stable and uniform heat distribution within the domain.

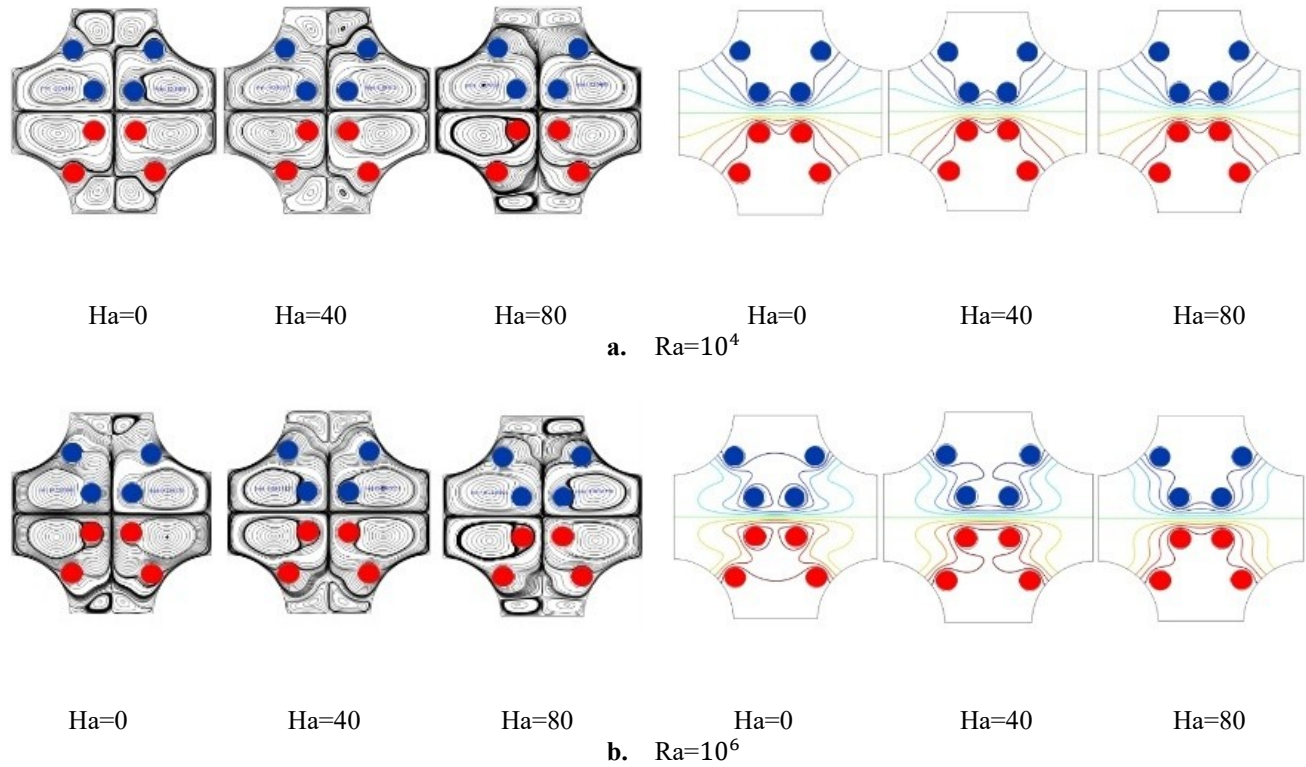


Figure 7. Streamlines and isotherms for various Hartmann numbers: case 4

Figure 8a illustrates the variation of the average Nusselt number (Nu) at a fixed Rayleigh number ($Ra = 10^4$) as the Hartmann number (Ha) increases. The graph shows that Nu remains constant, indicating that the magnetic field has an insignificant effect on heat transfer in this case. All the studied cases exhibit stable and similar behavior, suggesting that natural convection is relatively weak at this Rayleigh number. Consequently, the Lorentz force induced by the magnetic field is insufficient to significantly alter the thermal distribution. These findings suggest that at a low Ra, the magnetic field does not notably impact heat transfer through natural convection. Figure 8b illustrates the variation of the average Nusselt number (Nu) at a fixed Rayleigh number ($Ra = 10^6$) as the Hartmann number (Ha) increases. The graph shows a significant decrease in Nu, indicating that the magnetic field has a clear suppressive effect on heat transfer via natural convection at higher Ha values. The decline in Nu is more pronounced in the first case compared to the others, suggesting that the geometric configuration or nanofluid distribution influences the system's response to the magnetic field. The gradual decrease in heat transfer efficiency further indicates that the Lorentz force opposes the natural thermal flow,

limiting convective heat transfer. These findings suggest that the impact of the magnetic field becomes more pronounced as the Rayleigh number increases.

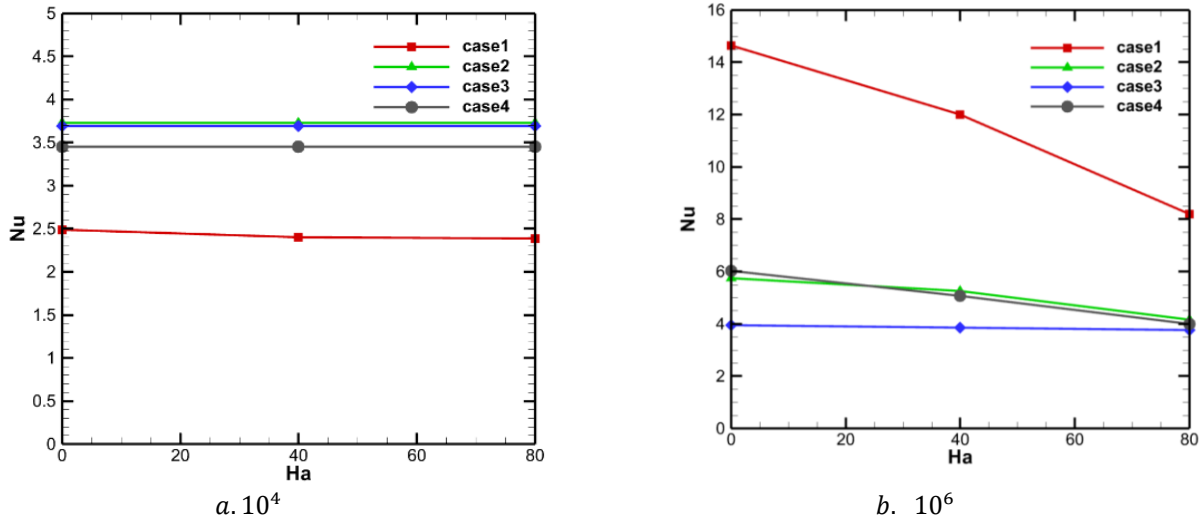


Figure 8. Nusselt number with Hartmann number considering four different cases

4. Conclusion

This study investigated Magnetohydrodynamic (MHD) natural convection in a square enclosure with curved corners, focusing on the thermal performance of multi-inner pipes used in heat exchangers. The key findings are summarized as follows:

1. At low Rayleigh number (Ra), case 1 recorded the lowest average Nusselt number (Nu).
2. In contrast, case 1 also exhibited the highest Nu under different conditions.
3. The impact of the Hartmann number (Ha) is significant for case 1, while it is negligible for case 3

Reference

- [1] Alasiri, A. (2024) The Role of Heater Size and Location in Modulating Natural Convection Behavior in Cu-Water Nanofluid-Loaded Square Enclosures. *Sustainability*, 16(22): p. 9648.
- [2] Chatterjee, D. and S. Kumar Gupta (2017) Magnetohydrodynamic natural convection in a square enclosure with four circular cylinders positioned at different rectangular locations. *Heat Transfer Engineering*, 38(17): 1449-1465.
- [3] Cho, H.W., M.Y. Ha, and Y.G. Park (2019) Natural convection in a square enclosure with two hot inner cylinders, Part II: The effect of two elliptical cylinders with various aspect ratios in a vertical array. *International Journal of Heat and Mass Transfer*, 135: 962-973.
- [4] Davis Vahl, G. (1983) Natural convection of air in a square cavity: a bench mark numerical solution. *International Journal for numerical methods in fluids*, 3(3): 249-264.

- [5] Garoosi, F., et al. (2015) Numerical simulation of natural convection of the nanofluid in heat exchangers using a Buongiorno model. *Applied Mathematics and Computation*, 254: 183-203.
- [6] Ghasemi, B. and S. Aminossadati (2009) Natural convection heat transfer in an inclined enclosure filled with a water-CuO nanofluid. *Numerical Heat Transfer, Part A: Applications*, 55(8): 807-823.
- [7] Ghasemi, B. and S. Aminossadati (2010) Brownian motion of nanoparticles in a triangular enclosure with natural convection. *International Journal of Thermal Sciences*, 49(6): 931-940.
- [8] Ibrahim, M.N.J., et al. (2022) Study of natural convection inside inclined nanofluid cavity with hot inner bodies (circular and ellipse cylinders). *International Journal of Heat and Technology*, 40(3): 699-705.
- [9] Kim, B.S., et al. (2008) A numerical study of natural convection in a square enclosure with a circular cylinder at different vertical locations. *International Journal of Heat and Mass Transfer*, 51(7): 1888-1906.
- [10] Nammi, G., et al. (2022) Natural convection heat transfer within a square porous enclosure with four heated cylinders. *Case Studies in Thermal Engineering*, 30: 101733.
- [11] Oztop, H.F. and E. Abu-Nada (2008) Numerical study of natural convection in partially heated rectangular enclosures filled with nanofluids. *International Journal of Heat and Fluid Flow*, 29(5): 1326-1336.



Enhanced Catalytic Conversion of Benzaldehyde to Benzoic Acid using Silica Coated Hydrated Iron Oxide (HFO)

Usama A. Soliman, Emad M. El-Telbani, Hind Ahmed Siddiq, Medhat Mohamed El-Moselhy, Sameh R. Elgogary, Mohamed S. Thabet, Rehab Azooz* and Zeinhom H. Mohamed

Department of Physical Sciences, Chemistry Division, College of Science, Jazan University, P.O. Box. 114, Jazan 45142, Saudi Arabia.

*Corresponding author: (R E Azooz), Email Address: rramadan@jazanu.edu.sa

Abstract

Hydrated oxide of iron-modified silicates (Si-Fe(n)) with varying iron contents were produced using a simple one-step loading process. The products were characterized using a variety of techniques, including FT-IR, scanning electron microscopy (SEM), transmission electron microscopy (TEM), energy dispersive X-ray spectroscopy (EDX), N₂-adsorption-desorption assays, and X-ray diffraction (XRD). The incorporation of Fe species does not cause any significant changes of crystal structure or phase composition of Silica gel particulates as reflected by the almost stable broadness of the main diffraction peak which could indicate the retained structure of silica gel even after the modification process. According to the results, which are based on variations in peak locations and intensities of the XRD diagram. According to EDX, most of the iron is evenly distributed within the silica matrix, with only a small amount visible on the surface. According to TEM, the average particle size was 12.5 nm. More Fe-loaded results in a larger surface area and OH groups bonded to Fe sites, according to IR. These structural changes indicate potential modifications to the material's properties that can be evaluated as benzaldehyde oxidation catalysts. The response's mechanism was explained.

Keyword: HFO modified silicates; Catalysis, Benzaldehyde oxidation, DFT

<https://doi.org/10.63070/jesc.2025.006>

Received 20 January 2025; Revised 25 April 2025; Accepted 18 May 2025.

Available online 25 May 2025.

Published by Islamic University of Madinah on behalf of *Islamic University Journal of Applied Sciences*. This is a free open access article.

1. Introduction

Carbonyl compounds are extensively used as intermediates in commercial as well as scientific settings, making oxidation an important step in organic synthesis. Several methods for converting aldehydes to carboxylic acids have been developed ^{1,2}. The most often used oxidants include acidic permanganates and chromates, fuming nitric acid, aqueous sodium hydroxide-silver oxide, ozone, and cyanide-silver oxide ². Various oxidants have disadvantages, such as high cost, low selectivity, environmental effect, and challenging working conditions³

Benzaldehyde is known to spontaneously undergo autoxidation to form benzoic acid when exposed to air at ambient temperature (20 °C)⁴. The presence of catalysts like transition-metal ions or free radical initiators such as benzoyl peroxide accelerates this oxidation ⁵. Photochemical excitation also aids this transformation, and it is widely accepted that this reaction follows a radical chain process.

Catalysis is critical in modern manufacturing, as it reduces energy input, suppresses undesirable side reactions, and increases product output ⁶. Catalysts lower the reaction energy barrier, accelerating chemical transformations without affecting the reactants or products ⁷. Catalysts are commonly employed in industrial synthesis because they are inexpensive, stable, and easy to separate. Chemists and engineers have worked for decades to improve efficiency in a variety of procedures.

Hybrid Fe-silicate is a promising new type of porous material with unique compositions and structure frameworks⁸. which have various applications, including water remediation⁹, Electrochemical Energy Storage¹⁰, adsorption of As cations ^{8,11} and catalysis¹², and more.

The oxidation of aldehydes to acids, namely benzaldehyde to benzoic acid, is a significant transition process. Benzoic acid is a pertinent chemical and a precursor for manufacturing numerous other compounds, and is one of the most prevalent organic acids, is widely utilized in medicine, food processing, and the chemical industry. More than 90% of the generic benzoic acid converts directly to phenol and caprolactam¹³, which have widespread applications, including as rubber polymerization activators and in the manufacturing of alkyd resins.

The oxidation of benzaldehyde to benzoic acid can be catalyzed by various compounds. Sodium tungstate dihydrate effectively catalyzes this reaction effectively, with acidic additives and surfactants improving the yield ¹⁴. Ni/Al-hydrotalcite-like-compounds in acetic acid, demonstrating stable activity and zero-order reaction kinetics ¹³. Sulfonic acid resin catalyzes the oxidation using hydrogen peroxide, with

electron-withdrawing substituents enhancing reactivity¹⁵. Rhodium and palladium compounds, also catalyze this reaction in benzene solution under an oxygen atmosphere¹⁶. These diverse catalytic systems offer various approaches to efficiently oxidize benzaldehyde to benzoic acid under different reaction conditions.

This paper presents an environmentally friendly and cost-effective method for converting benzaldehyde to benzoic acid utilizing a heterogeneous hybrid iron-modified silicate catalyst. Here, we concentrate on the reaction kinetics and other characteristics that lead to the investigation of a probable reaction mechanism. These fundamental discoveries may provide significant suggestions for further catalyst design and future research on the oxidation of other aromatic aldehydes.

2. Materials and Methods

2.1. Synthesis of hybrid iron-modified silicate

To create iron-modified hybrid silicate, we used high-purity silica gel from Sigma Aldrich's (pore size 60 Å; mesh size 60-120), anhydrous NaOH pellets (reagent grade, $\geq 98\%$) and $\text{Fe}_2(\text{SO}_4)_3$ (anhydrous, powder, P 99.99% trace metals base). Silica gel (50 g) was first treated with NaOH (1M) and kept under vigorous mechanical agitation for 10 minutes and washed with ion-free water several times until neutralized. The neutralized material after washing was divided into four equal portions and treated with certain amounts of $\text{Fe}_2(\text{SO}_4)_3$ solution ($7\% \text{ wt}/\text{v}$). Each sample was symbolized with a specific name to distinguish between different Fe-loadings.

2.2. Catalyst characterization

X-ray diffraction (XRD) was measured at room temperature using a Rigaku/Smart Lab diffractometer with non-monochromotographic Cu K α radiation ($\lambda=1.5 \text{ nm}$) operating at 40 kV and 100 mA. The measurement was taken at scanning speed of $8^\circ (2\theta) / \text{min}$ with a scanning range of $(5 - 65)^\circ$.

Scanning electron microscope (SEM) (JEOL/JSM-6610) and energy-dispersive X-ray (EDX) (OXFORD INSTRUMENTS INCA X-Act/51-ADD0013) were used to examine the surface morphology and particle size of iron-loaded samples to create a comprehensive map of the resulting hybrid iron-modified silicates. In addition, a JEOL-2100 TEM was used to evaluate the produced samples.

The specific surface area of the samples and the micropore volume were determined by collecting N_2 adsorption-desorption utilizing (AUTOSORB 1C) at 196°C . Samples were evacuated, heated to 200°C

°C, and then evacuated until a pressure of 1.3 Pa was achieved and maintained overnight before adsorption. Multipoint BET (Brunauer, Emmett, and Teller), t-plot, and DR (Dubinin-Radushkevich) were used to determine the surface area, total pore volume, and micropore volume, respectively.

The specific surface area and pore diameter of the synthesized samples were measured on an automatic Micromeritics ASAP2020 instrument (made in the USA) by nitrogen adsorption. Before testing, the instrument had to be set to a temperature 100 °C and a pressure of 101.325 kPa for 5h in advance. The adsorbate was high-purity nitrogen. The surface areas were determined by the BET method from the nitrogen adsorption data. The pore diameter and the pore size distribution were determined by the BJH method. The morphologies and dimensions of the synthesized products were examined using a JEOL JSM-6700F field emission scanning electron microscope (FE-SEM)

Atomic absorption spectroscopy (AAS) (GBC A 4382) was used to measure the amount of iron loaded in supernatants. Before AAS analysis, 0.1 g of all samples were treated with 10 ml (2 M) HCl to leach out the precipitated iron hydroxide, which allowed for the estimation of the iron content of silica.

Infrared adsorption measurements were carried out using a Fourier Transform Infrared (FT-IR) spectrophotometer (Bruker Optics-Alpha) of Si and iron-loaded Si samples. The FT-IR spectra were collected in the $400\sim 4000\text{ cm}^{-1}$ wavenumber region with a resolution of 4 cm^{-1} using a single bounce ATR with diamond crystal.

2.3. Oxidation of benzaldehyde to benzoic acid

A 250 mL three-necked flask, with a fixed condenser and thermometer, was fixed in a DF-101S magnetic force stirrer. 25 mL of benzaldehyde was added in absence or presence of the desired amount of catalyst sample (pretreated at 100 °C). Water cooling was used to reflux and stir it in the required temperature for a predetermined amount of time (8hr). The reaction mixture regarding (time, catalyst dose and required temperature), was refluxed and monitored using TLC. After the reaction was completed, the mixture was cooled, filtered, dried, and crystallized from hot water, to yield benzoic acid as a white crystal, 96% yield ($R_f = 0.39$, pet.ether : ethyl acetate, 10:1), m. p. 121-122 °C. The obtained product (benzoic acid) is confirmed by measuring its melting point and its infrared spectra.

3. Results and discussions

3.1. Sample Characterizations

3.1.1. Powder X-ray diffraction analysis

Fig.1 shows X-ray diffraction patterns of silica gel as well as the hybrid iron-modified silicate samples with varying Fe contents. All the samples have an amorphous form, with the absence of any diffraction lines indicating the presence of Fe-O species⁸. Zeng^{17,18}. The differences in peak positions and intensities show that Fe doping didn't change either the crystalline structure or phase composition of Si samples. This finding could reflect that iron well dispersed inside silicate matrix and still retaining the same crystallographic nature even after the modification process. Furthermore, the absence of diffraction lines that could be assigned to the presence of HFO phase might indicate that the incorporated HFO species occupy interstitial positions inside the silicate matrix and/or on the surface of the silicates with a very small particle size below the detection limit of the instrument.

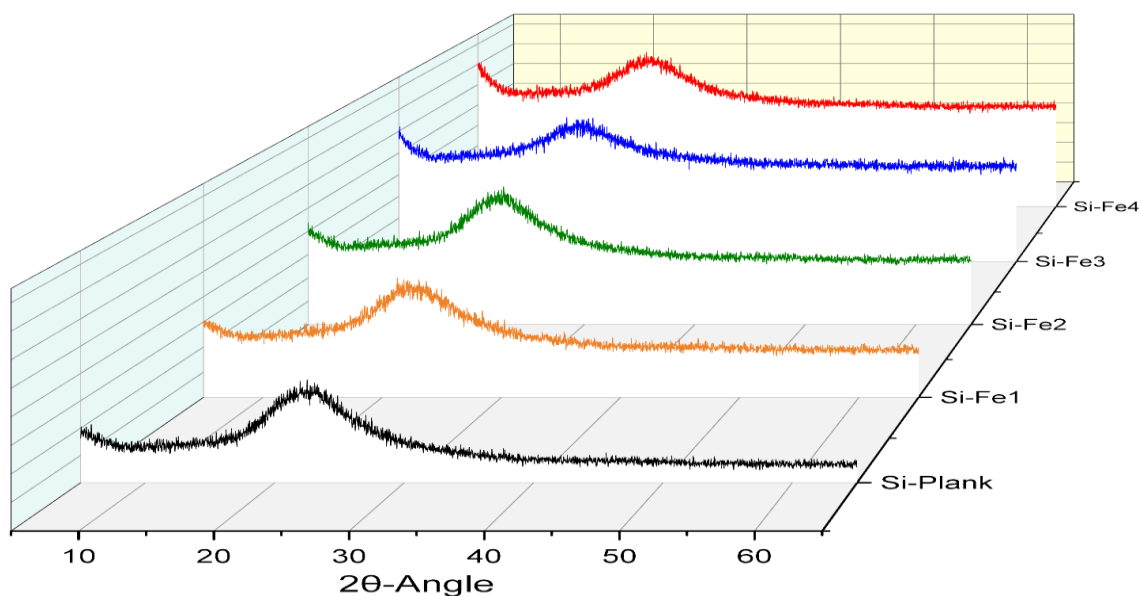


Fig 1: XRD patterns of samples

3.1.2. SEM and EDX spectroscopy

The two components in **Fig. 2** are an SEM spectrum on the right and an EDX (Energy Dispersive Spectroscopy) layered image on the left. The EDX Layered Image shows a microscopic view of a sample with different elements highlighted in different colors (Oxygen (O): Green, Silicon (Si): Blue, and Iron

(Fe): Red). The green color indicates a high content of oxygen throughout the sample, indicating that it is a major component of the matrix; the blue color indicates a significant presence of silicon, which likely forms the core structure of the sample side by side with oxygen; and the red color indicates a well distributed iron species on the surface, which is mainly localized along the examined specific areas. A homogeneous matrix is suggested by the distribution of different silica gel and HFO species reflecting the success of the process of modification and keeping the main structure of silicate matrix intact even after the incorporation of HFO.

On the other hand, the EDX Spectrum Interpretation also reveals that the iron peak (0.7 keV) is a minor component, the oxygen peak (0.5 keV) supports the high weight percentage of the sample, and the prominent peak (1.8 keV) confirms silicon is the major component. A quantitative assessment of the composition of the components is also given by the weight percentages (Wt%) and standard deviations (σ). Low standard deviations and a high percentage of silicon and oxygen suggest consistent and trustworthy data. The somewhat higher standard deviation and low percentage of iron point to distributional variability.

According to the statistics, only a small portion of the loaded iron is visible on the surface; the majority is hidden. The EDX data supports this observation, which indicates a reduced iron proportion. The only reason is that the iron burden is evenly distributed throughout the silica matrix.

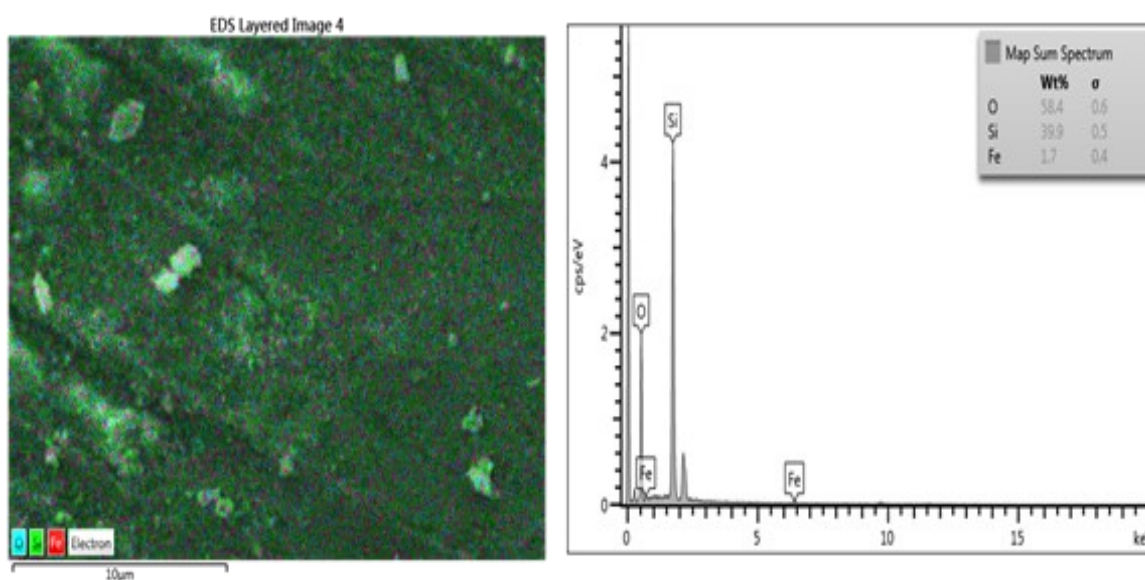


Fig. 2: SEM image and EDX mapping of Si-Fe4

Figure 3 shows a transmission electron microscopy (TEM) image of a sample (Si-Fe4). The sample appears to be composed of a network of interconnected particles or clusters. The multi distributed dark spots that circled and marked with "Fe" in red indicate that the iron is uniformly distributed inside the silicate matrix and exist with lower density on the surface which might support the result obtained from XRD. throughout the material but is instead concentrated in specific regions.

Localized iron plays a specific role in the functionality of the material. For example, iron can act as a catalytic site or as an activator to modify the electronic properties of the material¹⁹. The distribution of iron can also affect the magnetic properties of the material²⁰, which may be relevant for certain applications. The image reveals a complex network of interconnected particles, indicating a high degree of porosity and surface area. This structure is typical of materials designed for applications such as catalysis, energy storage, or adsorption. The particles appear to be relatively uniform in size, with diameters in the tens of nanometers range ($\leq 12.5 \text{ nm}$). The morphology of the particles is irregular, which can influence the properties of the materials, such as its catalytic activity or its adsorption capacity. loaded iron is mostly found inside the silicate matrix with average sizes in the nano range⁸, which is outside the range of XRD detection.

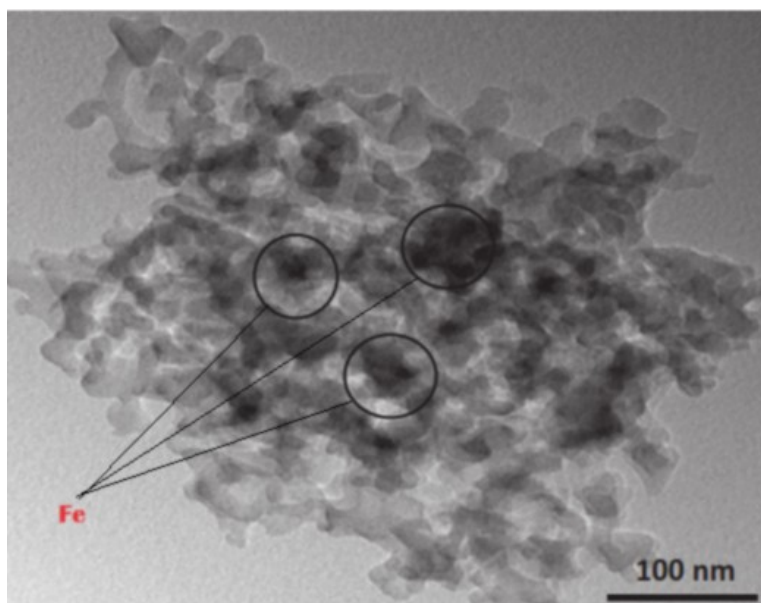


Fig. 3: Tunneling electron microscope (TEM) image of Si-Fe4

3.1.3 Surface area measurements

The adsorption isotherms of the various materials are shown in Figure 4. Si-Plank exhibits moderate adsorption capacity, with the adsorbed volume at $P/P_0 = 1.00$ reaching around $200 \text{ cm}^3 \text{ g}^{-1}$. In contrast, Si-Fe1 exhibits a higher adsorption capacity, with the adsorbed volume at $P/P_0 = 1.00$ reaching about $300 \text{ cm}^3 \text{ g}^{-1}$. Si-Fe2 with a marginally greater adsorption capacity than Si-Fe1, reaching about $320 \text{ cm}^3 \text{ g}^{-1}$ at $P/P_0 = 1.00$, with an adsorbed volume of around $380 \text{ cm}^3 \text{ g}^{-1}$ at $P/P_0 = 1.00$, Si-Fe3 shows the highest adsorption capacity of any sample. Si-Fe4 has a lower adsorption capacity than Si-Fe3 but a greater than Si-Plank, with an adsorbed volume of about $250 \text{ cm}^3 \text{ g}^{-1}$ at $P/P_0 = 1.00$.

Type II isotherms with characteristic upward deviation hysteresis loops are shown by Si-plank, Si-Fe1 and Si-Fe2, which may support the porous nature of the surface both before and after iron modification. The central portion of the flatter zone lies between $P/P_0 = 0.1\text{--}0.4$ and $0.1\text{--}0.6$, respectively, indicating the formation of a monolayer. Furthermore, the monolayer formation was initiated at the first knee through micropores filled with nitrogen gas at very low pressures. Conversely, capillary condensation happened at higher pressure levels, while multilayer development occurred at middle-pressure levels.

Type IV isotherm, with shorter upward deviation hysteresis loops, as seen in the Si-Fe3 and Si-Fe4 samples indicate mesoporous materials with capillary condensation occurring at higher relative pressures. The hysteresis loops observed in the isothermal curves suggest the presence of mesoporous materials and the occurrence of capillary condensation and evaporation.

Additionally, as shown in **Table 1**, the sharp rise in the knee at low pressure indicates a high surface area. The BET surface area indicates that the silica gel has a surface area of $90.3 \text{ m}^2 \text{ g}^{-1}$, and upon loading, the surface area of the hybrid iron-modified silicate decreases to 82.2 and $110.8 \text{ m}^2 \text{ g}^{-1}$ for Si-Fe1, and Si-Fe2. Furthermore, as **Table 1** shows, increasing the iron loading to three or four times (Si-Fe3 and Si-Fe4) results in extremely large surface areas (426.9 and $781.7 \text{ m}^2 \text{ g}^{-1}$, respectively). The resultant large surface areas may be due to the relatively dispersion of iron to occupy interstitial matrix spaces in the silica matrix. Pore volume Calculations show that the samples treated with silica gel and iron have distinct pore sizes based on how much hybrid iron-modified silicate is loaded. In addition, according to the findings, Si-Fe4 has highest surface area and total pore volume, making it highly suitable for adsorption applications. Additionally, micropore volume evaluations show that microporosity decrease with increasing iron content.

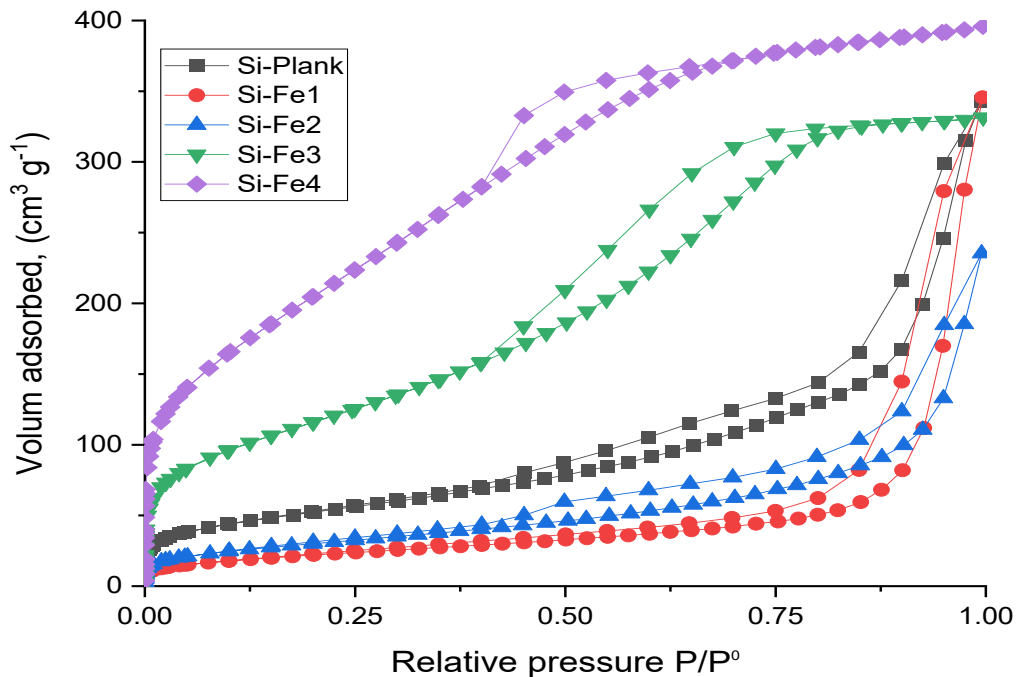


Fig. 4. Nitrogen adsorption-desorption isotherms of samples.

Table 1: Changes in surface areas and pore characteristics of silica concerning iron loading.

Sample	Multipoint BET method.	Volume adsorbed at $p/p^0 = 0.99$.	Micropore volume calculated by DR method	DP
	S_{BET} ($\text{m}^2 \text{g}^{-1}$)	V_{total} , ($\text{cm}^3 \text{g}^{-1}$)	V_{micro} , ($\text{cm}^3 \text{g}^{-1}$)	(A)
Si-Plank	190.3	0.53	0.077	55.8
Si-Fe1	82.2	0.54	0.03	130.9
Si-Fe2	110.8	0.37	0.008	65.1
Si-Fe3	426.9	0.53	0.029	24.2
Si-Fe4	781.7	0.62	0.022	15.6

3.1.4 Fourier transform infrared spectroscopy (FT-IR)

The most prominent band in the FT-IR spectrum of the parent silica gel appears at around 1100 cm^{-1} , which corresponding to the asymmetric stretching vibration of Si-O-Si bonds ^{21, 22}. The bands around $3400\text{-}3700 \text{ cm}^{-1}$ are attributed to the stretching vibrations of the surface silanol groups (Si-OH), and their intensities increase with increasing the amount of Fe loaded, which may be a result of increasing surface

area and OH groups attached to Fe sites. The bands around 800 cm^{-1} and 460 cm^{-1} are assigned to the symmetric stretching and bending vibrations of Si-O-Si bonds, respectively²¹⁻²⁴. The peak at 1621 cm^{-1} is due to the O-H bending mode of water molecules.

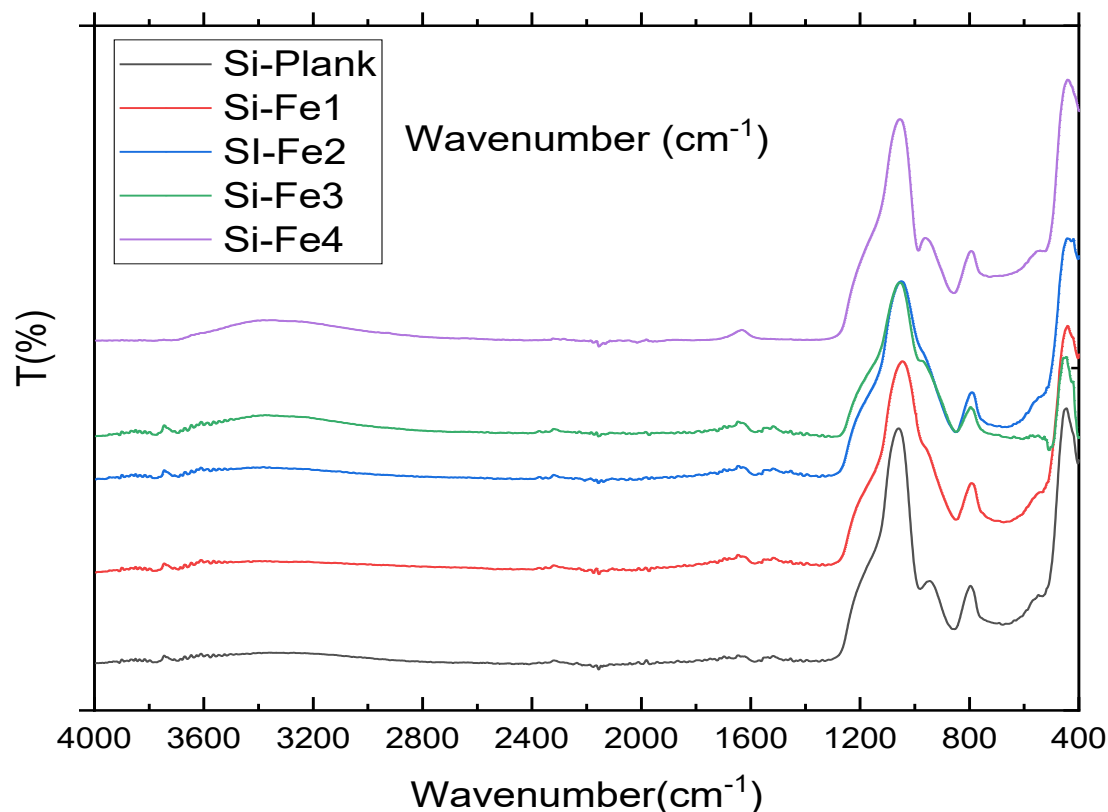


Fig. 5: FT-IR spectra of the prepared Samples

2.2. Oxidation of Benzaldehyde to Benzoic Acid

3.2.1 Effect of duration time

In the absence of a catalyst sample (Si-Fe4), benzaldehyde was not converted to benzoic acid under all reaction conditions. When 0.1 g Si-Fe4 was introduced into the reaction mixtures (as mentioned in section 3.2), the mixture cooled overnight before being filtered, washed, and dried to provide a white crystal product. The product was weighed, and the isolated yield was determined using the benzaldehyde

contained in the reaction flask. The melting point of the product was 121-122°C which is too close to the results of HL Ward²⁵ and FW Schwab²⁶. The IR (KBr) spectrum of white yield shows strong O-H stretching at 2500-3300 cm⁻¹, strong C=O stretching at 1680-1750 cm⁻¹, medium C-O stretching at 1300 cm⁻¹, and medium C-H bending of benzene ring at 900-1100 cm⁻¹. These results confirm the formation of benzoic acid due to the oxidation of benzaldehyde in the presence of a Si-Fe₄ catalyst. Other catalysts are used and the data obtained are shown in Fig. 6. The graph shows that iron-modified silicates (Si-Fe1 to Si-Fe4) are more efficient catalysts for the conversion of benzaldehyde to benzoic acid compared than unmodified silicate (Si-Plank). All iron-modified catalysts show an increase in conversion percentage over time, but the conversion rate varies significantly among them. Among the iron-modified catalysts, Si-Fe₄ shows the highest catalytic activity, achieving nearly 100% conversion within 8 hours. This indicates that the amount and distribution of iron play a crucial role in enhancing catalytic performance. The catalyst efficiency reaches ~96% for Si-Fe₄ and the order increases as follows:

$$Si - Plank < Si - Fe1 < Si - Fe2 < Si - Fe3 < Si - Fe4.$$

Other catalysts used in the oxidation of similar compounds are illustrated in **Table 2**.

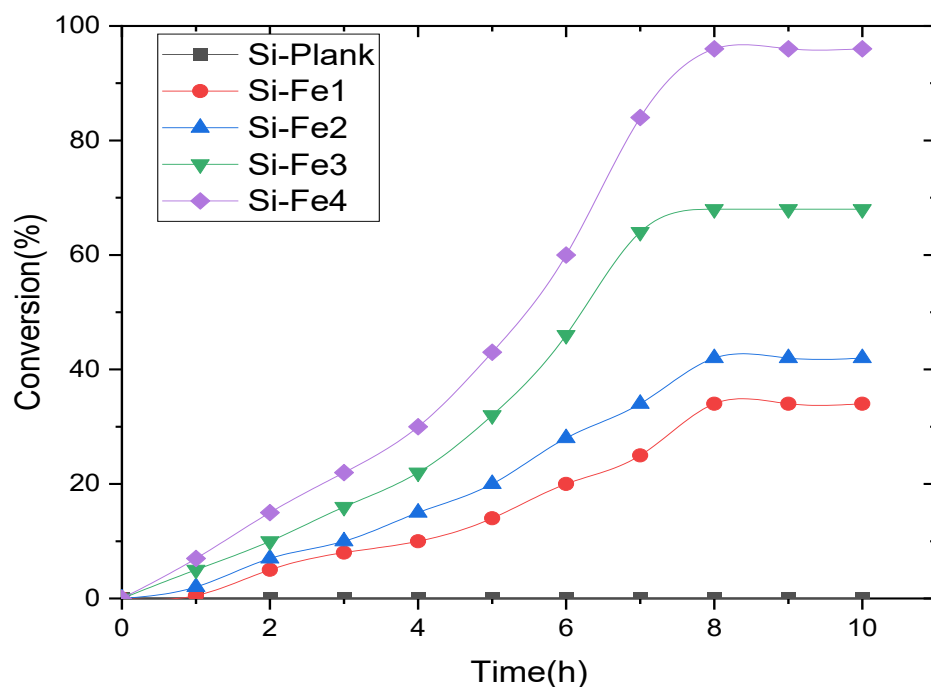


Fig. 6: time -conversion% curve for all used samples

Table 2: Some catalysts used in the oxidation of organic compounds

Catalyst/medium	Outcome measured	yield%	Ref.
$\text{Na}_2\text{WO}_4 \cdot 2\text{H}_2\text{O} - \text{H}_2\text{O}_2$	Benzaldehyde to benzoic acid.	70-90%	14
NiAl-hydrotalcite-like-compounds /Acid	Benzaldehyde to benzoic acid	---	13
transition metal complexes /benzene	Oxidation of benzaldehyde to benzoic acid and perbenzoic acid	Up to 83%	16
V_2O_5 , SnO_2 -promoted V_2O_5 , and MnO_2	Oxidation of benzaldehyde to benzoic acid	Up to 53%	27
Copper-based binary metal oxide catalysts/ O_2	Toluene to benzaldehyde, and with a longer reaction time, to benzoic acid..	Up to 25%	28
Co/ZSM-5	Styrene to benzaldehyde and benzoic acid	100%	29
Copper-iron-polyphthalocyanine / O_2	Oxidation of benzaldehyde to benzoic acid.	Up to 55%	30
Nickel(II) complex / O_2 /different solvents	Oxidation of aldehydes into carboxylic acids	Up to 91%	31
Methyltrioxorhenium / H_2O_2 / different solvents	Oxidation of benzaldehydes to phenols	75% for phenol 18% benzoic acid 22% ester	32
MoO_2 / H_2O_2	Oxidation of benzyl alcohol to benzaldehyde.	94%	33
A water-soluble palladium(II) bathophenanthroline complex /alcohols	Green, catalytic oxidation of a wider range of alcohols.	93%	34
Ir(III), Rh(III) and Pd(II) with H_2O_2	Oxidation of benzaldehyde to benzoic acid	82%.	35

3.2.2 Effect of catalysts dose

We use Si-Fe₄, the best catalysis sample, to change the dose and track the conversion at 80°C. The resulting data is shown in **Figure 7a**, where an increase in the additional dose improves the conversion rate. In **Figure 7.b**, a straight line ($r^2 = 0.998$) with a slope of 1.72 illustrates linear behavior. The Si-Fe₄ dose-related reaction order is therefore second-order.

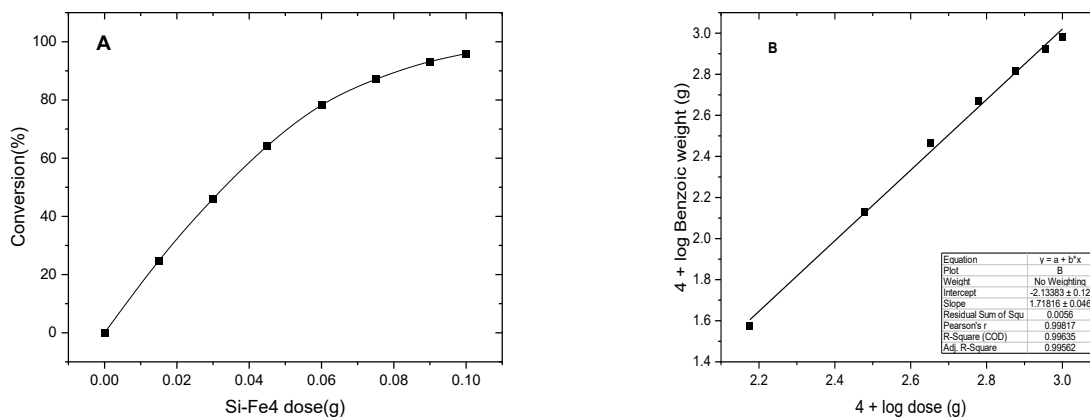


Fig. 7: (A) Effect of Si-Fe₄ dose on oxidation of benzaldehyde to benzoic acid at 80 °C (B) Double logarithmic plot of the benzoic yield versus Si-Fe₄ doses.

3.2.3. Effect of Temperature

At 8h and Si-Fe₄ dose (0.1 g), conversion ratio was studied by changing the reaction temperature, the obtained data is plotted in **Figure 8a** which shows a positive correlation between temperature and conversion ratio, indicating that as the temperature increases, the conversion percentage also increases. From **Figure 8b** the activation Energy ΔE was calculated from the slope of the Arrhenius equation straight line ($Slope = -\frac{\Delta E}{R}$) and is found to be 95.8 kJmol^{-1} and the entropy is calculated from the intercept of the line ($intercept = \frac{\Delta S}{R}$) and is found to be equal $-35.11 \text{ J K}^{-1} \text{ mol}^{-1}$. **Figure 8c** shows the relationship between free energy and temperature. The graph shows a negative linear relationship between ΔG and temperature, indicating that as the temperature increases, the value of ΔG decreases. The negative linear relationship indicates that the Gibbs free energy (ΔG) decreases with increasing temperature, indicating that the reaction becomes more spontaneous at higher temperatures.

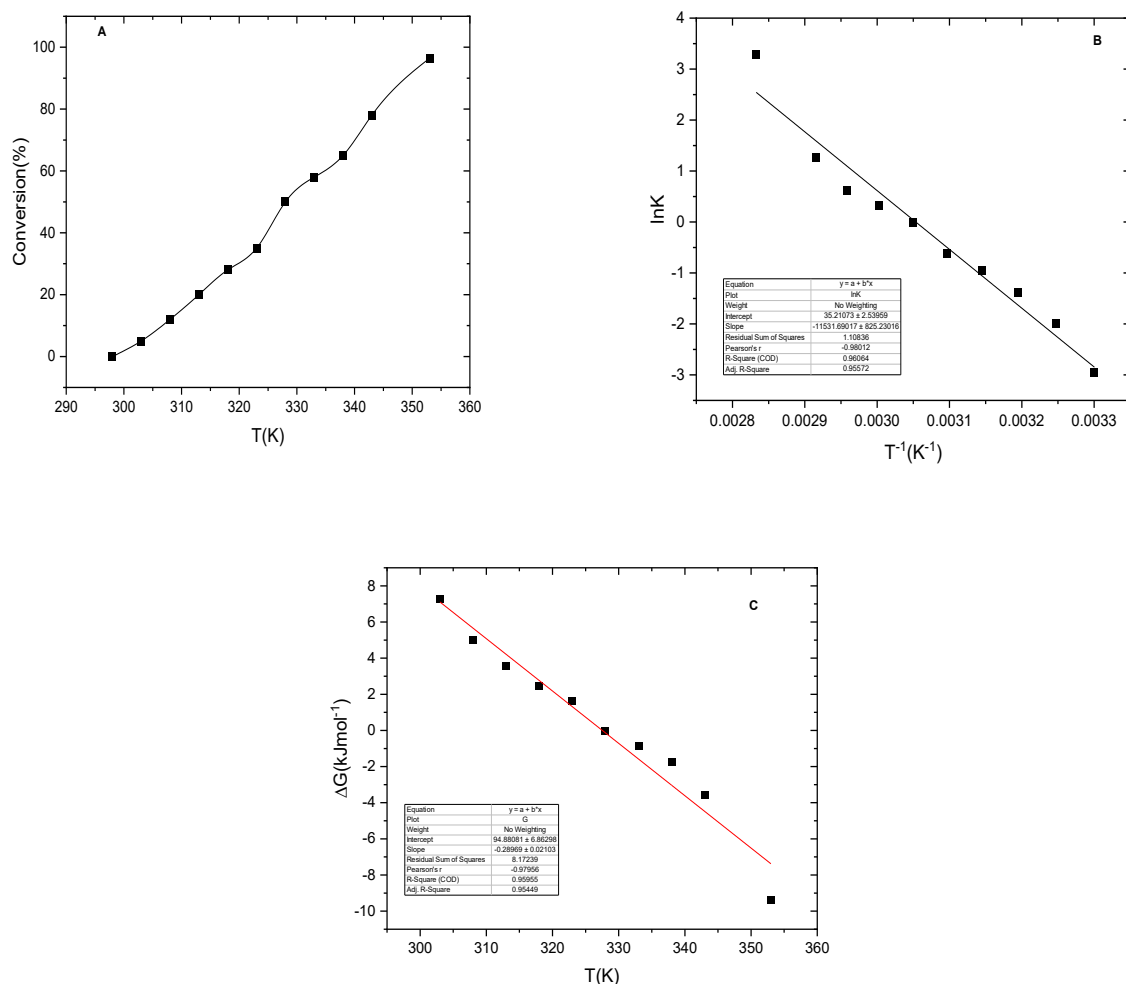


Fig. 8: (a) effect of temperature on oxidation of benzaldehyde, (b) Arrhenius plot relationship and (c) Free energy - temperature relationship

4. Computational study

The DMol3 calculation model, part of Materials Studio v2023, was used to optimize the geometry of this molecule. The electronic properties were functional GGA/PBE, zero charge, and controlled spin polarization. Each electron in the core treatment is regarded as part of the DNP Basis set. **Table 3** lists the calculations for E_{HOMO} and E_{LUMO} , which are visually shown in **Figure 9**. E_{HOMO} and E_{LUMO} are used to determine the energy gap, global hardness η , global softness S , ionization potential I , electron affinity A , absolute electronegativity χ , and global electrophilicity index ω .

Table 3: The calculated quantum chemical parameters

Compound	Fe(OH) ₃	benzaldehyde	Benzoic Acid
E_{HOMO}	-5.769	-5.544	-6.099
E_{LUMO}	-4.835	-2.572	-2.302
$\Delta E(HOMO-LUMO)$	-0.934	-2.972	-3.797
Ionization energy (I)	5.769	5.544	6.100
Electron affinity (A)	4.835	2.572	2.303
Electronegativity (X)	5.302	4.058	4.201
Global hardness (η)	0.467	1.486	1.898
Chemical potential (π)	-5.302	-4.058	-4.201
Global softness (σ)	2.142	0.673	0.527
Global electrophilicity (ω)	30.109	5.542	4.648
Electroaccepting (ω^+) power	27.516	3.698	2.785
Electrodonating (ω^-) power	32.819	7.7578	6.985
Net electrophilicity ($\Delta\omega^{+-}$)	60.335	11.455	9.770

Table 3 depicted that; The energy gap between E_{HOMO} and E_{LUMO} is smallest for Fe(OH)₃ (-0.934 eV), indicating it has the highest reactivity and lowest stability. In contrast, Benzoic acid has the largest energy gap (-3.797 eV), suggesting it is the most stable and least reactive. Fe(OH)₃ Shows the most electrophilicity, lowest stability, and maximum reactivity. It is extremely reactive because it is a powerful electron giver and acceptor. Moderate stability and reactivity are displayed by benzaldehyde; It is more electrophilic than benzoic acid but less than Fe(OH)₃. The most stable and least reactive substance is benzoic acid. Out of the three compounds, it is the hardest and least electrophilic.

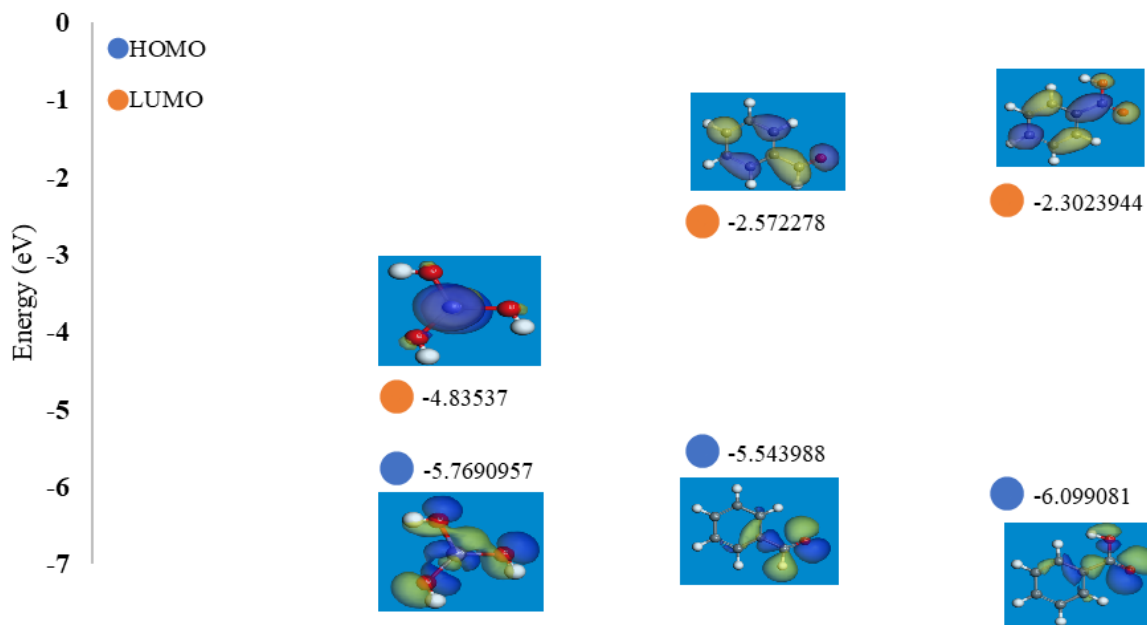


Fig9. 3D plots frontier orbital energies using the DFT method

The interaction between $\text{Fe}(\text{OH})_3$, benzaldehyde and benzoic acid was investigated using the adsorption-desorption module. The resulting three-dimensional structure is shown in **Figure 10**, where we can observe that the bond in the benzaldehyde/ $\text{Fe}(\text{OH})_3$ system is shorter, confirming the strong adsorption and possible coordination bond formation, while the longer bonds in $\text{Fe}(\text{OH})_3$ /benzoic acid indicate that benzoic acid can be removed from surfaces of the catalyst compounds more easily. The calculated binding energy is also stronger for benzoic acid/ $\text{Fe}(\text{OH})_3$ $-2483.202 \text{ kcal mol}^{-1}$ compared with benzaldehyde/ $\text{Fe}(\text{OH})_3$ $-2346.552 \text{ kcal mol}^{-1}$ as shown in Figure 10. The adsorption parameter is tabulated in **Table 4** where a negative value indicates that the adsorption process is exothermic, which means that energy is released when the compound adsorbs on $\text{Fe}(\text{OH})_3$. After the benzaldehyde molecules are adsorbed on the catalysis surface, accumulation occurs and coordination bonds may form between them. Then the adsorbed benzaldehyde ($E_{\text{adsorption}} = -5.516 \times 10^{-3} \text{ kcal mol}^{-1}$) is oxidized to form benzoic acid which is still strongly adsorbed on the catalyst surface ($E_{\text{adsorption}} = -16.209 \times 10^{-3} \text{ kcal mol}^{-1}$) and then it will be separated from the surface of the catalyst as will be discussed in the mechanism.

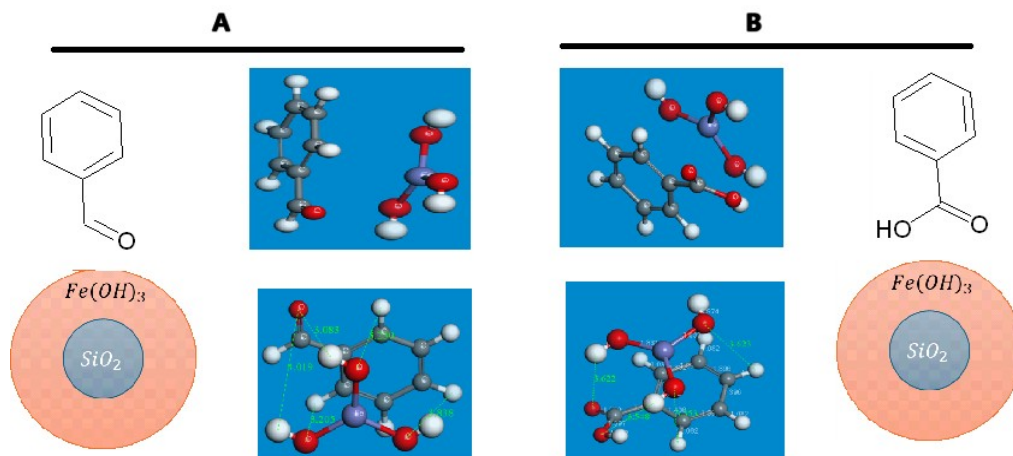


Figure 10: 3D plots frontier orbital after adsorption using DFT method (A) $\text{Fe}(\text{OH})_3$ /benzaldehyde (B) $\text{Fe}(\text{OH})_3$ /Benzoic acid

Table 4. Adsorption parameter by MD (Mont Carlo stimulation) Material studios

Structures	Total energy $\times 10^3$ kcal mol^{-1}	Adsorption energy $\times 10^3$ kcal mol^{-1}	Rigid adsorption energy $\times 10^3$ kcal mol^{-1}	Deformation energy kcal mol^{-1}	dE_{ad}/dN_i kcal mol^{-1}
$\text{Fe}(\text{OH})_3$	0000				
Benzoic acid	30.477				
Benzaldehyde	15.356				
$\text{Fe}(\text{OH})_3$ /Benzaldehyde	9.840	-5.516	-2.760	-2.756	-5.516
$\text{Fe}(\text{OH})_3$ /Benzoic acid	14.269	-16.209	-2.840	-13.369	-16.209

As shown in Figure 11, the total density of states (TDOS) and the projected density of states (PDOS) were calculated to further examine the structural properties of the silica gel substrate loaded with $\text{Fe}(\text{OH})_3$, benzaldehyde, benzoic acid, benzaldehyde/ $\text{Fe}(\text{OH})_3$ and benzoic/ $\text{Fe}(\text{OH})_3$. The density of states (DOS) provides information about the valence shells of different atoms at different energy intervals and how many states they occupy. The total density of states (TDOS) versus energy (eV) plot for optimized $\text{Fe}(\text{OH})_3$ is displayed in **Figure 11(a)**, where there is a continuous spread from the valence band to the

conduction band with sufficient peak height. With high TDOS, a continuous DOS pattern is observed, particularly at the Fermi level, with a maximal peak showing at approximately -1.99 eV with 17.56 DOS/eV. Changes in DOS, primarily in the vicinity of the Fermi level, would probably result in observable modifications to the resulting electrical characteristics, which would be advantageous for electrochemical applications³⁶. Different atomic contributions in $\text{Fe}(\text{OH})_3$ towards DOS are depicted in Figure 11(b); f contributes very little to TDOS, whereas Fe and O contribute significantly since Fe's electronic configuration is $[\text{Ar}]3d^6 4s^2$ and O's is $[\text{He}]2s^2 2p^4$. They provide three different orbital contributions to TDOS: d, p, and s. The p, d, and s orbitals of the PDOS distribution exhibit substantial hybridization, as evidenced by their strong overlap around the Fermi level at multiple eVs.

The numerous peaks in **Figure 11(C)** and **12(E)** for benzaldehyde and benzoic acid, respectively, and PDOS in **Figure 12(D)**, demonstrate the existence of electronic states capable of electrical conduction. The benzaldehyde orbitals' contributions range from -10 eV to -5 eV. The p and d orbitals contribute significantly, while the f orbital contributes less and the s orbital contributes very little. In contrast, PDOS in **Figure 11(F)** shows the contributions from the s, p, d, and f orbitals in benzoic acid. The p and d orbitals contribute significantly between -10 eV and -5 eV, while the f orbital contributes less. The s orbital contribute very little.

Benzaldehyde and benzoic adsorbed on $\text{Fe}(\text{OH})_3$ systems were studied to find the suitable mechanism of this catalytic reaction. Based on the analysis of DOS and PDOS in both systems respectively as shown in **Figure 12 (A,B)** and **(C,D)**, the bond between $\text{Fe}(\text{OH})_3$ and benzaldehyde can be inferred as follows; The p and d orbitals' substantial contributions, which range from -10 eV to -5 eV, demonstrate strong p-d hybridization. This suggests that interactions between the p orbitals of benzaldehyde and the d orbitals of $\text{Fe}(\text{OH})_3$ are involved in the bond between the two compounds. The strong electrical interactions are suggested by $\text{Fe}(\text{OH})_3/\text{benzaldehyde}$, which may be due to the formation of coordination bonds between the carbonyl group of benzaldehyde and the oxygen atoms of $\text{Fe}(\text{OH})_3$.

Benzaldehyde, benzoic acid, and $\text{Fe}(\text{OH})_3$ show strong electronic interactions and notable p-d hybridization when the DOS and PDOS graphs are carefully compared. The carbonyl group in benzaldehyde and the oxygen atoms in $\text{Fe}(\text{OH})_3$ are likely to form coordination bonds during the bonding process, which produces a stable electronic structure. The significant electronic states close to the Fermi level demonstrate the stability of the $\text{Fe}(\text{OH})_3/\text{benzaldehyde}$ system, indicating strong bonding interactions and electronic stability.

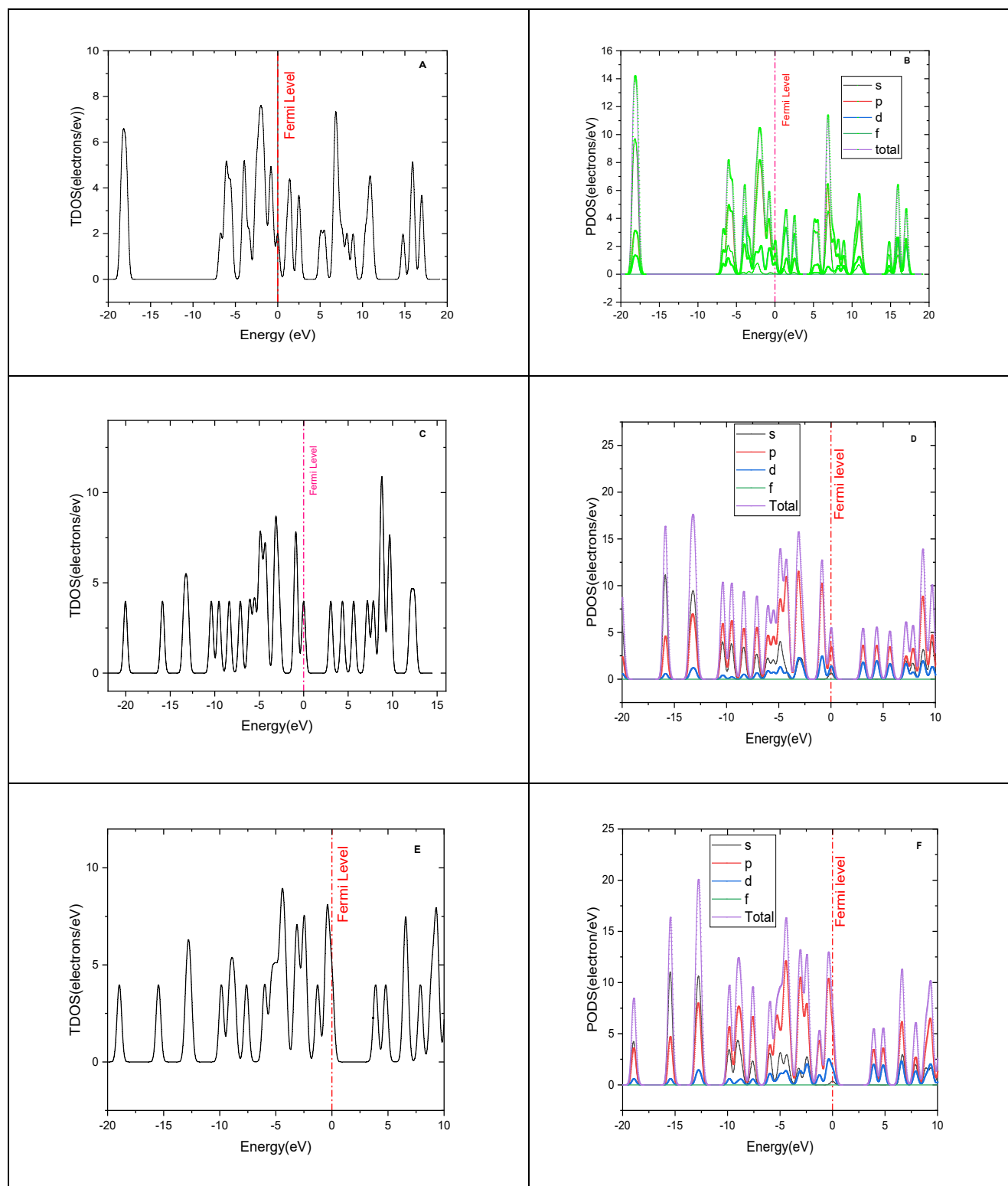


Figure 11. The TDOS of (A) Fe(OH)_3 ; (C) benzaldehyde (E) benzoic acid and the PDOS of (B) Fe(OH)_3 ; (D) benzaldehyde (F) benzoic acid

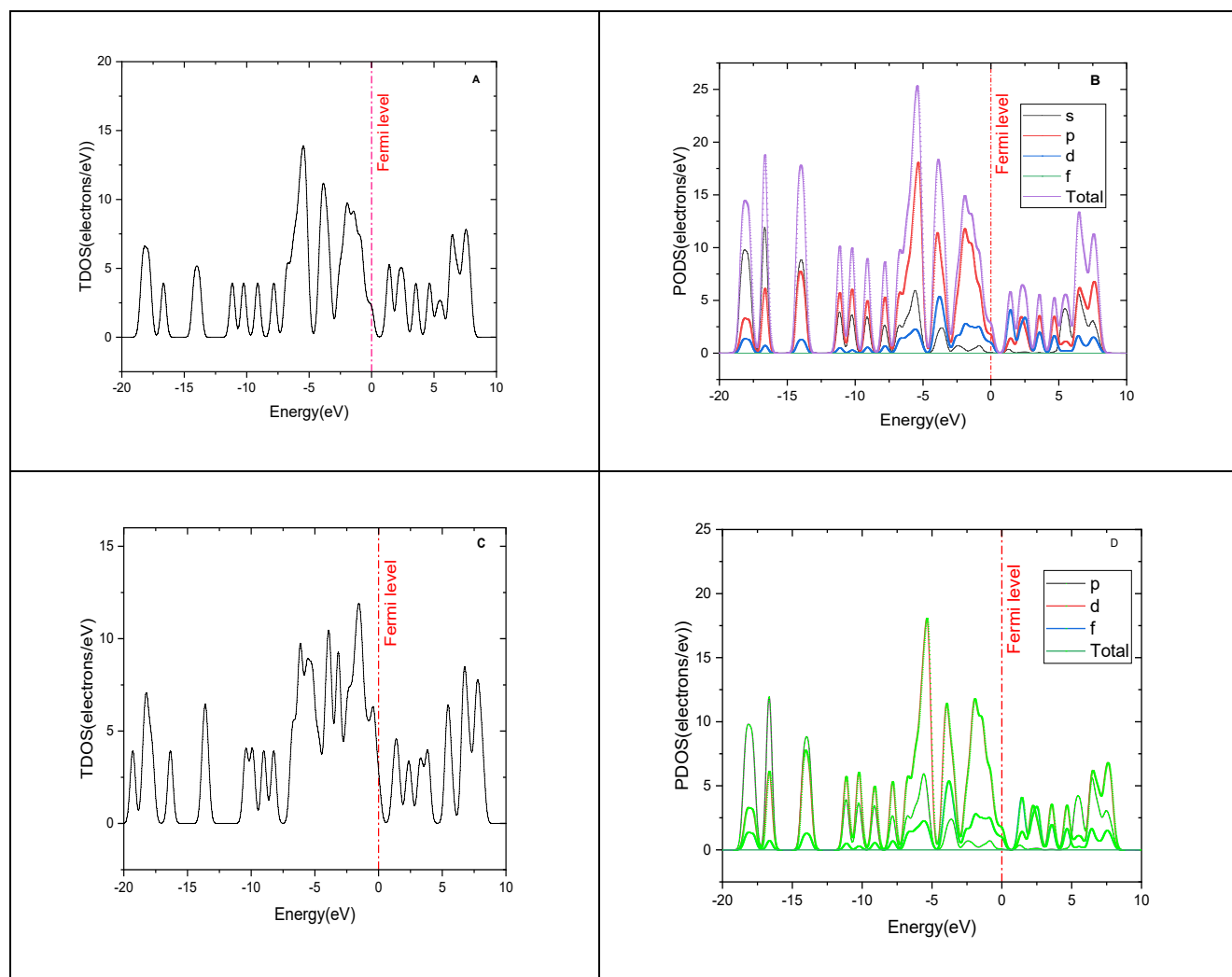
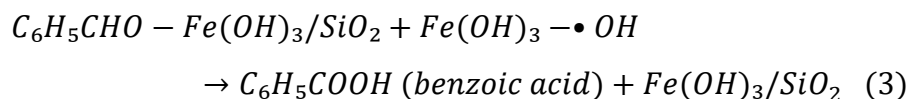
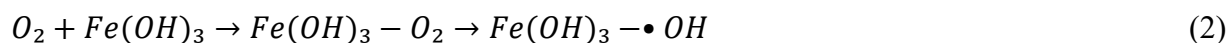
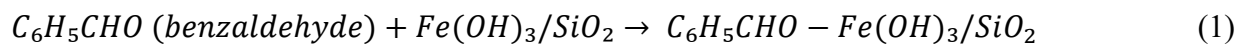


Figure 12. (A) $\text{TDOS}_{\text{Fe}(\text{OH})_3/\text{benzaldehyde}}$, (B) $\text{TDOS}_{\text{Fe}(\text{OH})_3/\text{benzoic acid}}$, (C) $\text{PDOS}_{\text{Fe}(\text{OH})_3/\text{benzaldehyde}}$ and $\text{PDOS}_{\text{Fe}(\text{OH})_3/\text{benzoic acid}}$

5. Reaction Mechanism

SiO_2 decorated with $\text{Fe}(\text{OH})_3$ acts as a heterogeneous catalyst for the oxidation of benzaldehyde to benzoic acid. The $\text{Fe}(\text{OH})_3$ catalyst has active sites for the oxidation reaction, and the SiO_2 support improves its dispersion, increasing the surface area and stability. Benzaldehyde ($\text{C}_6\text{H}_5\text{CHO}$) adsorbed on the surface of the $\text{Fe}(\text{OH})_3/\text{SiO}_2$ catalyst (eq. 1) as described by PDOS analysis. Molecular oxygen (O_2) in the air activates the $\text{Fe}(\text{OH})_3$ sites, generating reactive oxygen species (ROS) as hydroxyl radicals ($\bullet\text{OH}$) (eq.2).

The adsorbed benzaldehyde is oxidized to benzoic acid (C_6H_5COOH) by activated oxygen species, as shown in (eq. 3). The overall reaction is described in (eq. 4).



6. Conclusion

- SiO_2 increases the surface area of the catalyst, while temperature and iron content regulate the conversion yield. Higher temperatures improve the conversion rate, lower the activation energy, and improve the thermodynamics of the reaction.
- Si-Fe4 is a superior catalyst for benzaldehyde oxidation to benzoic acid with a conversion approach 96% at 08 °C.
- Computational calculation confirm the high reactivity of $Fe(OH)_3$ and its high tendency to accept electrons
- The TDOS and PDOS for $FeOH_3$, benzaldehyde, and benzoic acid show similar overall shapes but differ in peak intensities and positions. This indicates variations in the electronic structure due to the different chemical environment

References

- (1) Smith, M. *Organic synthesis*; Academic Press, **2016**.
- (2) Le Paih, J.; Frison, J.-C.; Bolm, C. Oxidation of Carbonyl Compounds. *Modern Oxidation Methods* **2004**, 253-265.
- (3) Guo, Z.; Liu, B.; Zhang, Q.; Deng, W.; Wang, Y.; Yang, Y. Recent advances in heterogeneous selective oxidation catalysis for sustainable chemistry. *Chemical Society Reviews* **2014**, 43 (10), 3480-3524.
- (4) Falletta, E.; Rossi, M.; Della Pina, C. The versatility of gold: From heterogeneous catalysis to biomedicine. *Inorganica Chimica Acta* **2022**, 537, 120959.
- (5) Sankar, M.; Nowicka, E.; Carter, E.; Murphy, D. M.; Knight, D. W.; Bethell, D.; Hutchings, G. J. The benzaldehyde oxidation paradox explained by the interception of peroxy radical by benzyl alcohol. *Nature communications* **2014**, 5 (1), 1-6.
- (6) Alonso, D. M.; Bond, J. Q.; Dumesic, J. A. Catalytic conversion of biomass to biofuels. *Green chemistry* **2010**, 12 (9), 1493-1513.

- (7) Isahak, W. N. R. W.; Al-Amiery, A. Catalysts driving efficiency and innovation in thermal reactions: A comprehensive review. *Green Technologies and Sustainability* **2024**, 100078.
- (8) El-Moselhy, M. M.; Ates, A.; Çelebi, A. Synthesis and characterization of hybrid iron oxide silicates for selective removal of arsenic oxyanions from contaminated water. *Journal of Colloid and Interface Science* **2017**, 488, 335-347.
- (9) Alotaibi, K. M.; Shiels, L.; Lacaze, L.; Peshkur, T. A.; Anderson, P.; Machala, L.; Critchley, K.; Patwardhan, S. V.; Gibson, L. T. Iron supported on bioinspired green silica for water remediation. *Chemical Science* **2017**, 8 (1), 567-576.
- (10) Kalita, A.; Kashyap, T.; Saikia, P.; Talukdar, A. K. In-situ Iron Modified Mesoporous Silica MCM-48 for Electrochemical Energy Storage. **2024**.
- (11) Din, S. U.; Mahmood, T.; Naeem, A.; Shah, N. S.; Hussain, S.; Imran, M.; Sultana, S.; Rehman, A. U. A novel insight into the adsorption interactions of arsenate with a Fe–Si binary oxide. *Colloid Journal* **2019**, 81, 469-477.
- (12) Chen, X.; Liang, C. Transition metal silicides: fundamentals, preparation and catalytic applications. *Catalysis Science & Technology* **2019**, 9 (18), 4785-4820.
- (13) Wu, X.; Xianmei, X.; Wu, Z. Oxidation of benzaldehyde to benzoic acid using heterogenous NiAl-hydrotalcite-like-compounds as the catalyst in acetic acid. *Progress in Reaction Kinetics and Mechanism* **2011**, 36 (1), 53-62.
- (14) Yan, H.; Liu, C.; Luo, G. Oxidation of benzaldehyde to benzoic acid. *Petroleum science and technology* **2005**, 23 (11-12), 1511-1516.
- (15) Yang, X.; Tang, S.; Lu, T.; Chen, C.; Zhou, L.; Su, Y.; Xu, J. Sulfonic Acid Resin–Catalyzed Oxidation of Aldehydes to Carboxylic Acids by Hydrogen Peroxide. *Synthetic Communications* **2013**, 43 (7), 979-985.
- (16) Hojo, J.-I.; Yuasa, S.; Yamazoe, N.; Mochida, I.; Seiyama, T. Liquid phase oxidation of benzaldehyde catalyzed by low-valent transition metal complexes. *Journal of Catalysis* **1975**, 36 (1), 93-98.
- (17) Zeng, L. Arsenic adsorption from aqueous solutions on an Fe (III)-Si binary oxide adsorbent. *Water Quality Research Journal* **2004**, 39 (3), 267-275.
- (18) Zeng, L. A method for preparing silica-containing iron (III) oxide adsorbents for arsenic removal. *Water research* **2003**, 37 (18), 4351-4358.
- (19) Wang, X.; Zhang, X.; Zhang, Y.; Wang, Y.; Sun, S.-P.; Wu, W. D.; Wu, Z. Nanostructured semiconductor supported iron catalysts for heterogeneous photo-Fenton oxidation: a review. *Journal of materials chemistry A* **2020**, 8 (31), 15513-15546.
- (20) Huber, D. L. Synthesis, properties, and applications of iron nanoparticles. *Small* **2005**, 1 (5), 482-501.
- (21) Lutz, W.; Täschner, D.; Kurzhals, R.; Heidemann, D.; Hübert, C. Characterization of silica gels by ²⁹Si MAS NMR and IR spectroscopic measurements. Wiley Online Library: 2009.
- (22) Ellerbrock, R.; Stein, M.; Schaller, J. Comparing amorphous silica, short-range-ordered silicates and silicic acid species by FTIR. *Scientific Reports* **2022**, 12 (1), 11708.
- (23) Gude, K.; Gun'ko, V. M.; Blitz, J. P. Adsorption and photocatalytic decomposition of methylene blue on surface modified silica and silica-titania. *Colloids and Surfaces A: Physicochemical and Engineering Aspects* **2008**, 325 (1-2), 17-20.
- (24) Zhang, F.; Lan, J.; Zhao, Z.; Yang, Y.; Tan, R.; Song, W. Removal of heavy metal ions from aqueous solution using Fe₃O₄–SiO₂-poly (1, 2-diaminobenzene) core–shell sub-micron particles. *Journal of colloid and interface science* **2012**, 387 (1), 205-212.
- (25) Ward, H.; Cooper, S. L. S. The system benzoic acid, orthophthalic acid, water. *The Journal of Physical Chemistry* **2002**, 34 (7), 1484-1493.

- (26) Schwab, F. W.; Wichers, E. Preparation of benzoic acid of high purity. *J. Res. Nat. Bur. Stand* **1940**, 25, 747-757.
- (27) Sachtler, W.; Dorgelo, G.; Fahrenfort, J.; Voorhoeve, R. Correlations between catalytic and thermodynamic parameters of transition metal oxides. *Recueil des Travaux Chimiques des Pays-Bas* **1970**, 89 (5), 460-480.
- (28) Wang, F.; Xu, J.; Li, X.; Gao, J.; Zhou, L.; Ohnishi, R. Liquid phase oxidation of toluene to benzaldehyde with molecular oxygen over copper-based heterogeneous catalysts. *Advanced Synthesis & Catalysis* **2005**, 347 (15), 1987-1992.
- (29) Guan, X.; Duan, C.; Wang, H.; Lu, B.; Zhao, J.; Cai, Q. Tuneable oxidation of styrene to benzaldehyde and benzoic acid over Co/ZSM-5. *New Journal of Chemistry* **2021**, 45 (38), 18192-18201.
- (30) Inoue, H.; Kida, Y.; Imoto, E. Organic Catalysts. V. Specific catalytic properties of copper-iron-polyphthalocyanine in the oxidation of aldehydes. *Bulletin of the Chemical Society of Japan* **1968**, 41 (3), 692-696.
- (31) Yamada, T.; Rhode, O.; Takai, T.; Mukaiyama, T. Oxidation of aldehydes into carboxylic acids with molecular oxygen using nickel (II) complex catalyst. *Chemistry letters* **1991**, (1), 5-8.
- (32) Yamazaki, S. Oxidation of benzaldehydes catalyzed by methyltrioxorhenium with hydrogen peroxide. *Chemistry letters* **1995**, 24 (2), 127-128.
- (33) Gaspar, F.; Nunes, C. D. Selective catalytic oxidation of benzyl alcohol by MoO₂ nanoparticles. *Catalysts* **2020**, 10 (2), 265.
- (34) Brink, G.-J. t.; Arends, I. W.; Sheldon, R. A. Green, catalytic oxidation of alcohols in water. *Science* **2000**, 287 (5458), 1636-1639.
- (35) Tandon, P. K.; Gayatri; Sahgal, S.; Srivastava, M.; Singh, S. B. Catalysis by Ir (III), Rh (III) and Pd (II) metal ions in the oxidation of organic compounds with H₂O₂. *Applied Organometallic Chemistry* **2007**, 21 (3), 135-138.
- (36) Zaheer, A.; Zahra, S. A.; Iqbal, M. Z.; Mahmood, A.; Khan, S. A.; Rizwan, S. Nickel-adsorbed two-dimensional Nb₂C MXene for enhanced energy storage applications. *RSC advances* **2022**, 12 (8), 4624-4634.



FTIR Characterization of Date Syrup

Abdullah Almohammed¹, Habib Bush², Saheed Popoola³, Mohamed Ibraheem⁴, Wael Elshemey¹, Tarek Omara^{5,6,*}

¹ Physics Department, Faculty of Science, Islamic University of Madinah, KSA, arda@iu.edu.sa, welshemeu@iu.edu.sa

² Science and General Studies Department, AL-Fayha Private College, Jubail, KSA habib.j@fayha.edu.sa

³ Chemistry Department, Faculty of Science, Islamic University of Madinah, KSA abiodun@iu.edu.sa

⁴ Alghad College for Applied Medical Sciences, Najran, KSA, aalrufai@gc.edu.sa

⁵ Mathematics Department, Faculty of Science, Islamic University of Madinah, KSA,

⁶ Statistics, Mathematics and Insurance Department, Faculty of Commerce, Kafrelsheikh University, Egypt, Tarek_em@iu.edu.sa

*Corresponding author: (T. Omara), Email Address: Tarek_em@iu.edu.sa

Abstract

The date syrup is a natural sweetener with significant economic and health benefits. Ensuring its quality is essential to protect consumers from adulteration and to maintain its nutritional value. This study employs Fourier Transform Infrared (FTIR) spectroscopy as a rapid and non-destructive analytical tool to characterize date syrup and explore its possible use in detecting adulteration. Date syrup samples from five different producers in Madinah, Saudi Arabia, were analyzed. Key spectral parameters, including peak positions, intensities, full width at half maximum (FWHM), and area under the peak, were extracted and statistically evaluated. Results reveal consistent spectral features across all samples, with minor variations attributed to differences in processing and composition. Multivariate statistical techniques, such as Principal Component Analysis (PCA) and Partial Least Squares Discriminant Analysis (PLS-DA), confirm the ability of FTIR to classify and authenticate date syrup samples effectively. The findings suggest that FTIR-based spectral markers can serve as reference parameters for quality assessment and adulteration detection. Integrating FTIR spectroscopy into routine quality control procedures could enhance consumer protection, improve regulatory oversight, and strengthen the economic value of date syrup products.

Keywords: FTIR spectroscopy, Date syrup, Quality control, Adulteration detection, Spectral analysis

<https://doi.org/10.63070/jesc.2025.007>

Received 05 April 2025; Revised 10 May 2025; Accepted 20 May 2025.

Available online 25 May 2025.

Published by Islamic University of Madinah on behalf of *Islamic University Journal of Applied Sciences*. This is a free open access article.

1. Introduction

Date syrup is an increasingly valued natural sweetener due to its nutritional composition and diverse applications in the food and pharmaceutical industries. Its significance extends beyond mere cooking use, as it has been recognized for its antioxidant, antimicrobial, and anticancer properties (Taleb et al., 2016). According to Hussain et al. (2020), date syrup is rich in bioactive compounds, including flavonoids, phenolic acids, and carotenoids, which contribute to its health-promoting effects. Its potential as a functional food ingredient has led to extensive research on its composition and therapeutic benefits (Alsaleem et al., 2022). The production and commercialization of date syrup play a crucial role in many Middle Eastern and North African economies, where date palm cultivation is widespread. Abdul-Hamid et al. (2018) highlights that the economic value of date syrup is increasing due to its affordability compared to other natural sweeteners, such as honey and maple syrup. As a result, it has been extensively used as a sweetener, an ingredient in fermented foods, and a base for bioactive compound extraction. In addition to its nutritional and economic value, date syrup is an essential ingredient in traditional and modern food processing. Mohamed et al. (2014) states that it enhances the texture, viscosity, and stability of various food formulations, making it a viable alternative to synthetic additives. Deepshikha et al., (2019) emphasizes its role in food preservation, as its natural sugar content acts as a microbial inhibitor.

Despite its benefits, adulteration remains a significant concern in the date syrup industry. The addition of low-cost sugars, starch-based syrups, and artificial sweeteners to enhance yield and reduce production costs has raised concerns about food authenticity and consumer safety (Alsaleem et al., 2022). Naderi-Boldaji et al. (2018) discusses how food fraud involving date syrup is a growing issue, requiring advanced analytical techniques to detect impurities. The traditional quality control methods rely on physicochemical properties, such as pH, density, viscosity, and sugar composition, but these approaches often fail to differentiate between pure and adulterated samples (Jamshidian et al., 2017). Thus, developing more reliable and rapid analytical methods is essential to maintain product integrity.

FTIR is gaining recognition as a highly efficient and non-destructive method for food analysis. According to El Darra et al. (2017), FTIR can be used to analyze chemical bonds, molecular vibrations, and functional groups in complex food matrices. Shiddiq et al. (2019) notes that FTIR offers a unique spectral fingerprint, allowing for precise differentiation between authentic and adulterated date syrup samples. While FTIR has been extensively applied in honey, dairy, and edible oil authentication, its potential in date syrup analysis remains underexplored. This study aims to fill that gap by conducting a comprehensive spectral analysis of date syrup samples from multiple producers, establishing reliable reference parameters for quality assessment. One of the main advantages of FTIR spectroscopy is its ability to integrate with multivariate statistical analysis, significantly enhancing its discriminatory power. Multivariate techniques, such as Principal Component Analysis (PCA) and Partial Least Squares Discriminant Analysis (PLS-DA), allow researchers to extract meaningful patterns from complex spectral data (Naderi-Boldaji et al., 2018). By incorporating such statistical tools, this study aims to enhance the reliability of FTIR-based quality control for date syrup. Ensuring the authenticity and purity of date syrup is not only an economic issue but also a public health priority. According to Fakhlai et al. (2020), adulteration with harmful synthetic sweeteners or low-quality syrups may introduce toxic compounds that pose health risks to consumers.

By validating FTIR spectroscopy as a rapid and reliable method for date syrup authentication, this study contributes to enhancing consumer confidence in the safety and quality of date-based products.

This study aims to evaluate the possibility of producing standard FTIR spectroscopy parameters of date syrup for future use as a reliable reference to distinguish between pure and adulterated date syrup samples via analyzing their characteristic spectral peaks. The study integrates multivariate statistical analysis to enhance the interpretation of spectral data, improving the accuracy and reliability of food authentication techniques. Ultimately, this work aspires to contribute to the development of standardized protocols for quality control in the date syrup industry, benefiting both consumers and regulatory agencies while reinforcing confidence in date syrup products.

Fourier Transform Infrared (FTIR) spectroscopy is a powerful analytical technique used to investigate the molecular composition of substances based on their infrared absorption patterns. It operates by measuring how different chemical bonds absorb infrared light at specific wavelengths, generating a unique spectral fingerprint for each sample (El Darra et al., 2017). The FTIR spectrum provides information about the functional groups present in a substance by

analyzing vibrational transitions within molecular structures (Shiddiq et al., 2019). A key advantage of FTIR is its ability to rapidly assess complex food matrices without requiring extensive sample preparation. The method is widely used in food science due to its high sensitivity, non-destructive nature, and ability to analyze multiple components simultaneously. The primary spectral parameters used for characterization include peak position, intensity, full width at half maximum (FWHM), and area under the peak, all of which help in identifying specific molecular interactions (Hamad et al., 2020). The FTIR spectroscopy has been extensively applied in food quality assessment, authentication, and adulteration detection. One of its key applications is honey authentication, where it has been used to differentiate between pure honey and adulterated samples mixed with glucose or corn syrup (Cherigui et al., 2024). Similarly, FTIR has been applied in dairy industry research to assess the composition of milk, butter, and cheese, ensuring compliance with food safety standards (Naderi-Boldaji et al., 2018). When compared to other spectroscopic methods, such as Raman spectroscopy, nuclear magnetic resonance (NMR), and UV-visible spectroscopy, FTIR stands out due to its speed, cost-effectiveness, and minimal sample preparation requirements (Khan et al., 2018). While Raman spectroscopy provides detailed structural information, it is often affected by fluorescence interference in biological samples (Deepshikha et al. 2019). Although NMR has high precision, it is expensive and requires specialized instrumentation, making it less accessible for routine food quality control (Mohamed et al., 2014). UV-visible spectroscopy, although widely used, lacks the molecular specificity of FTIR and may require additional chemical treatments for effective analysis (Kofman et al., 2018).

Despite its extensive use in food authentication, FTIR spectroscopy remains underutilized in the analysis of date syrup. Previous studies have demonstrated its potential in distinguishing authentic date syrup from adulterated or low-quality products (Alsaleem et al., 2022). The ability of FTIR to detect changes in sugar composition, moisture content, and adulterants makes it a promising tool for ensuring the authenticity of date syrup.

One of the major concerns in date syrup production is the fraudulent addition of other syrups, such as pomegranate molasses or starch-based syrups, which alter their chemical composition (Taleb et al., 2016). FTIR allows for the identification of such alterations by analyzing variations in spectral peak parameters associated with key functional groups, including O-H stretching (around 3320 cm^{-1}), C-H stretching (2930 cm^{-1}), and C-O stretching (1230 cm^{-1}) (Elshemey et al 2010, Hamad et al 2020). These spectral markers would help differentiate pure and adulterated date syrup, offering a quick and reliable method for quality control.

Given the growing global market for date syrup, it is crucial to implement advanced analytical techniques to maintain its economic value and consumer trust. By integrating FTIR spectroscopy with multivariate statistical analysis, researchers can enhance the accuracy of food authentication, providing a scientifically robust framework for standardizing date syrup quality (Nashi, 2023).

2. Materials and Methods:

To ensure accurate characterization of date syrup, a systematic approach was followed, including sample collection, FTIR spectroscopy analysis, and statistical evaluation. FTIR spectroscopy was used to identify molecular fingerprints, while multivariate statistical methods helped assess compositional differences between date syrup samples from different producers, if any. These procedures would provide a reliable framework for detecting adulteration and ensuring product quality.

2.1. Sample Collection and Preparation

Date syrup samples were obtained from five different commercial producers in Madinah, Saudi Arabia, ensuring representation from various processing techniques and ingredient sources. Each sample was collected in sterile glass containers to prevent contamination and stored at 4°C to maintain its chemical stability until analysis (El Darra et al., 2017). The samples were thoroughly homogenized before analysis to minimize inconsistencies caused by phase separation or crystallization (Hussain et al., 2020). Prior to FTIR measurements, all samples were allowed to reach room temperature, ensuring consistency in spectral acquisition.

2.2 FTIR Spectroscopy Analysis

The FTIR spectra of date syrup samples were recorded using a Nicolet 6700 Fourier Transform Infrared Spectrometer (Thermo Scientific, USA). The FTIR spectra were obtained within the range of 4000–500 cm^{-1} at a spectral resolution of 4 cm^{-1} , ensuring high sensitivity for detecting characteristic functional groups. Each spectrum was collected as the average of 32 scans, minimizing noise and improving signal clarity (Hamad et al., 2020). The recorded FTIR spectra were baseline corrected and area-normalized to allow for precise comparisons between different samples (Sarmiento et al., 2007).

2.3 Data Processing and Peak Identification

Spectral data were processed using Origin 6.0 software for peak fitting, smoothing, and baseline correction. A Savitzky-Golay smoothing algorithm (7-point window) was applied to

reduce spectral noise while preserving the integrity of characteristic peaks (Elshemey et al., 2010). Key spectral parameters, including peak position, intensity, full width at half maximum (FWHM), and area under the peak, were extracted using Gaussian peak fitting methods. The following functional groups were identified based on their characteristic absorption bands:

O-H stretching (3320 cm^{-1}) – indicative of moisture and hydrogen bonding.

C-H stretching (2930 cm^{-1}) – associated with organic hydrocarbon chains.

C=C stretching (1640 cm^{-1}) – linked to unsaturated compounds.

C-O stretching (1230 cm^{-1}) – characteristic of carbohydrate structures.

O-H bending (1060 cm^{-1}) – related to polysaccharide content (El Darra et al., 2017).

2.4 Statistical Analysis and Chemometric Techniques

To assess the variability and similarity between different date syrup samples, statistical analysis was performed using SPSS (Statistical Package for the Social Sciences) software. The correlation of spectra between samples was evaluated using Pearson's correlation coefficient, determining the extent of spectral similarity at $p < 0.01$ significance level. Additionally, Principal Component Analysis (PCA) and Partial Least Squares Discriminant Analysis (PLS-DA) were applied to classify date syrup samples and detect subtle compositional differences (Naderi-Boldaji et al., 2018). These chemometric techniques enhance FTIR analysis by extracting hidden patterns in spectral data, improving the accuracy of authentication methods. To validate the method's reproducibility, triplicate measurements were conducted for each sample, ensuring consistency in spectral outputs. Statistical comparisons of FTIR parameters, such as peak intensities and FWHM values, were performed using one-way ANOVA, identifying significant differences between samples ($p < 0.05$).

3. Results and Discussion

The FTIR spectral analysis of date syrup samples from various producers in Madinah, Saudi Arabia, reveals important insights into the chemical composition and quality of the product. This section discusses the key findings from the FTIR spectra, emphasizing the presence of characteristic functional groups and identifying any variability among the samples. Additionally, the discussion explores the statistical methods used to analyze these spectral data, highlighting the potential of FTIR spectroscopy for quality control and authentication. The

implications of these findings for the date syrup industry, including the detection of adulteration and the assurance of product consistency, are also addressed.

3.1 FTIR Spectral Analysis of Date Syrup Samples

The FTIR spectra of date syrup samples collected from five different producers in Madinah, KSA, exhibited characteristic absorption peaks corresponding to key functional groups commonly found in carbohydrates, organic acids, and phenolic compounds. Figure 1 presents the measured FTIR spectra, where the five date syrup samples display highly similar spectral profiles, suggesting consistent chemical composition across different sources.

The presence of distinct absorption bands at 3320 cm^{-1} (O-H stretching), 2930 cm^{-1} (C-H stretching), 1640 cm^{-1} (C=C stretching), 1230 cm^{-1} (C-O stretching), and 1060 cm^{-1} (O-H bending) confirms the dominance of sugar-based compounds in date syrup (El Darra et al., 2017). These peaks are indicative of hydroxyl, carboxyl, and ether groups, which are major components of monosaccharides and polysaccharides, aligning with findings in previous food authentication studies (Hussain et al., 2020).

3.2 Identification of Variability in Spectral Peaks

Despite overall spectral similarity, slight variations were observed in the intensity and position of absorption peaks between different samples. The most noticeable differences were recorded at the 1060 cm^{-1} and 3320 cm^{-1} bands, which could be attributed to differences in moisture content, processing techniques, or sugar degradation. These findings suggest that while date syrups share common structural components, subtle compositional differences exist due to variations in raw material, storage conditions, and processing methods (Mohamed et al., 2019).

Table 1 summarizes the values of peak positions, intensities, full width at half maximum (FWHM), and area under the peak for each of the five characteristic FTIR absorption bands. The statistical significance ($p < 0.05$) of peak intensity variations indicates that these minor differences could serve as potential markers for quality control and authentication. Previously published FTIR spectral data on date syrup honey adulteration confirms that minor shifts in peak intensities and broadening of the O-H stretching band may indicate the presence of foreign sugars or moisture variations. Such spectral modifications align with syrup dilution or adulteration with glucose syrups, which is a known fraudulent practice in the food industry (Nashi, 2023).

3.3 Statistical Analysis and Chemometric Evaluation

To further assess the degree of similarity and variability among the five samples, Pearson's correlation coefficient (r-values) was calculated, revealing significant correlations ($p < 0.01$) between all five spectra. These findings confirm the overall chemical consistency between the investigated date syrups, making FTIR a promising tool for quality monitoring (Shiddiq et al., 2019).

The multivariate statistical techniques, such as Principal Component Analysis (PCA) and Partial Least Squares Discriminant Analysis (PLS-DA), were employed to classify the date syrup samples based on their spectral characteristics (Naderi-Boldaji et al., 2018).

The table 2 indicates that:

1. The first Principal Component Analysis (PCA) explains approximately 99.71% of the variance in the data, while the second principal component (PC2) explains about 0.24%. Together, they account for nearly all the variance.
2. For the PLS-DA, the first PLS component (PLS1) explains a significant amount of variance (approximately 4.90), while the second PLS component (PLS2) explains a negligible amount (approximately 0.0003).

This results demonstrates a clear clustering of samples, reinforcing their chemical similarity while highlighting subtle spectral differences that differentiate one producer's syrup from another. These findings indicate that spectral markers derived from FTIR data, when combined with statistical analysis, provide a robust classification framework for distinguishing different sources of date syrup. The potential for machine learning applications in FTIR-based food authentication would further enhance its relevance in modern quality control practices.

3.4 Implications for Quality Control and Authentication

The ability of FTIR spectroscopy to rapidly and accurately detect spectral variations makes it a powerful quality control tool for the date syrup industry. The establishment of standardized spectral reference values based on peak intensities, FWHM, and area under the peak would enable manufacturers and regulators to:

1. Detect adulteration with high precision by comparing test samples against reference spectra.
2. Ensure product authenticity by identifying shifts in characteristic absorption bands.
3. Monitor batch-to-batch consistency to improve consumer trust and market value.

The findings of this study align with global food safety standards, supporting the potential regulatory adoption of FTIR spectroscopy as an official method for date syrup authentication (Abbès et al., 2013).

3.5 Comparison with Previous Studies

When compared to earlier studies, the results of this research confirm that FTIR would effectively differentiate pure date syrup from adulterated products (El Darra et al., 2017). However, previous works have primarily focused on honey, fruit syrups, and dairy products, leaving a research gap in the systematic application of FTIR for date syrup monitoring. This study contributes to filling this gap by providing quantitative spectral reference parameters that can serve as future benchmarks for quality assessment. Moreover, while Raman spectroscopy, NMR, and chromatography techniques have been explored for food authentication, they often require costly instrumentation and time-consuming sample preparation (Lotfiman et al., 2018). In contrast, FTIR offers a rapid, cost-effective, and non-destructive alternative, making it more practical for industrial applications.

3.6 Limitations and Future Directions

While this study provides strong evidence for the applicability of FTIR in date syrup quality assessment, certain limitations must be acknowledged:

1. Variability in natural composition: Date syrups can differ due to seasonal and geographical variations, necessitating a larger dataset for future reference spectrum.
2. Detection of complex adulteration: While FTIR is highly effective for detecting major compositional changes, the presence of low concentrations of adulterants may require hybrid techniques, such as FTIR combined with mass spectrometry or chromatography
3. Automation and real-time monitoring: Future research should focus on developing automated FTIR-based quality control systems, integrating machine learning algorithms for real-time classification.

Table 1. . The values of the characterization parameters (peak position, intensity, FWHM and area under peak) of each of the five peaks of interest (1060, 1230, 1640, 2930 and 3320 cm^{-1}) in the FTIR spectrum of five different date syrup samples.

Functional groups	Peak (cm^{-1})	Position (cm^{-1})	Relative Intensity	FWHM (cm^{-1})	Relative Area under peak
O-H stretching vibration	1060	1036.5 \pm 4.7	1 \pm 0.4	72.9 \pm 4.0	0.35
C-O stretching vibration	1230	1252.2 \pm 3.0	0.47 \pm 0.0	42.3 \pm 3.6	0.01
-C=C- stretching	1640	1636.1 \pm 1.5	0.45 \pm 0.0	66.9 \pm 2.6	0.04
antisymmetric stretching vibrations C-H of a -CH ₂	2930	2923.9 \pm 0.9	0.46 \pm 0.0	39.4 \pm 7.8	0.01
O-H stretching vibration	3320	3295.7 \pm 1.0	0.66 \pm 0.0	327.0 \pm 5.6	1 \pm 0.1

Table 2.. Summary of PCA and PLS-DA Results for FTIR Spectroscopy Analysis of Date Syrup Samples

Principal Component	Explained Variance	Cumulative Variance	PLS Component	Explained Variance
PC1	0.997068	0.997068	PLS1	4.895467
PC2	0.002419	0.999488	PLS2	0.000287

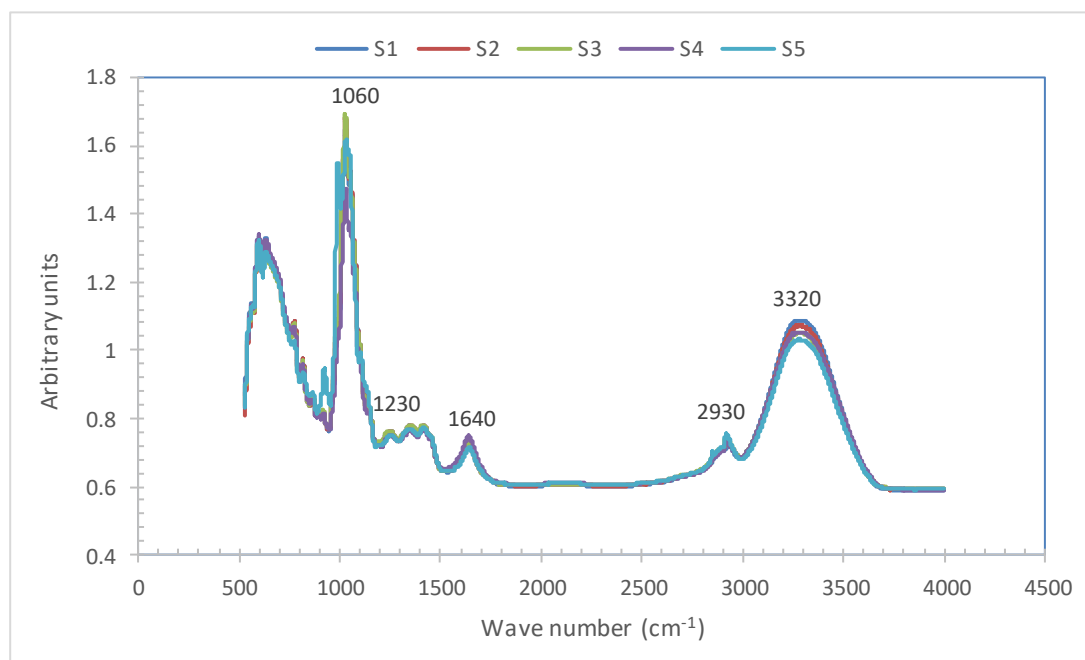


Figure 1. Measured FTIR spectra of the five investigated date syrup samples.

4. Conclusion

FTIR spectroscopy has demonstrated its effectiveness as a reliable and non-destructive method for analyzing date syrup composition and authenticity. The spectral characterization parameters established in this study—peak intensity, full width at half maximum (FWHM), and area under the peak—provide valuable markers for assessing product quality and for possible detection of potential adulteration. Minor variations in spectral peaks were observed among samples, likely due to differences in production methods, moisture content, or raw material origins. However, the overall consistency in spectral profiles confirms that FTIR spectroscopy can serve as a robust tool for distinguishing authentic date syrup from adulterated or substandard products. By integrating FTIR spectroscopy with statistical methods such as Pearson's correlation coefficient, principal component analysis (PCA), and partial least squares discriminant analysis (PLS-DA), this study has enhanced the accuracy and efficiency of quality assessment. These techniques allow for precise classification of date syrup samples, making FTIR-based analysis a promising approach for routine food authentication and regulatory compliance. The adoption of FTIR spectroscopy in the date syrup industry can strengthen consumer confidence, improve market transparency, and prevent fraudulent practices.

Given the increasing demand for natural sweeteners, implementing standardized FTIR protocols can support quality assurance efforts and regulatory frameworks. Future studies should aim to expand the spectral database by analyzing a broader range of date syrup samples from diverse geographical regions and production processes. Additionally, integrating FTIR spectroscopy with complementary analytical techniques, such as chromatography and mass spectrometry, could further improve the detection of complex adulterants. Advances in artificial intelligence and machine learning could also enhance the automation and accuracy of FTIR-based quality control systems. Ensuring the authenticity and safety of date syrup is not only a commercial priority but also a public health necessity. The findings of this study reinforce the need for innovative, science-driven approaches in food quality assessment. By leveraging FTIR spectroscopy as a primary analytical tool, food manufacturers, regulators, and researchers can uphold the integrity of date syrup products and promote sustainable industry practices.

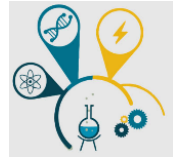
Acknowledgments: The researchers wish to extend their sincere gratitude to the Deanship of Scientific Research at the Islamic University of Madinah.

Funding and/or Conflicts of interests/Competing interests.: The authors declare that they have no conflict of interest.

References

- [1] H. Taleb, S. Maddocks, K. Morris, and A. Kanekanian, "The Antibacterial Activity of Date Syrup Polyphenols against *S. aureus* and *E. coli*," *Front. Microbiol.*, vol. 7, p. 198, 2016.
- [2] E. Rodrigues, N. Poerner, I. I. Rockenbach, L. V. Gonzaga, C. R. Mendes, and R. Fett, "Phenolic compounds and antioxidant activity of blueberry cultivars grown in Brazil," *Food Sci. Technol.*, vol. 39, no. 2, pp. 399–405, 2019.
- [3] Z. X. Tang, L. E. Shi, and S. M. Aleid, "Date fruit: Chemical composition, nutritional and medicinal values, products," *J. Sci. Food Agric.*, vol. 93, no. 10, pp. 2351–2361, 2013, [doi: 10.1002/jsfa.6154](https://doi.org/10.1002/jsfa.6154).
- [4] M. I. Hussain, M. Farooq, and Q. A. Syed, "Nutritional and Biological Characteristics of the Date Palm Fruit (*Phoenix dactylifera* L.)—A Review," *Food Biosci.*, vol. 34, pp. 1–12, 2020, [doi: 10.1016/j.fbio.2019.100509](https://doi.org/10.1016/j.fbio.2019.100509).
- [5] V. Kofman, M. J. A. Witlox, J. Bouwman, I. L. ten Kate, and H. Linnartz, "A multifunctional setup to record FTIR and UV-vis spectra of organic molecules and their photoproducts in astronomical ices," *Rev. Sci. Instrum.*, vol. 89, no. 5, p. 053111, 2018, [doi: 10.1063/1.5027079](https://doi.org/10.1063/1.5027079).
- [6] R. Fakhlaei et al., "The Toxic Impact of Honey Adulteration: A Review," *Foods*, vol. 9, no. 11, p. 1538, 2020, [doi: 10.3390/foods9111538](https://doi.org/10.3390/foods9111538).
- [7] F. Abbès et al., "Effect of concentration temperature on some bioactive compounds and antioxidant properties of date syrup," *Food Sci. Technol. Int.*, vol. 19, no. 4, pp. 323–333, 2013, [doi: 10.1177/1082013212452477](https://doi.org/10.1177/1082013212452477).
- [8] S. Cherigui, I. Chikhi, F. Dergal, et al., "Authentication of honey through chemometric methods based on FTIR spectroscopy and physicochemical parameters," *Food Biophys.*, vol. 18, pp. 4653–4664, 2024, [doi: 10.1007/s11694-024-02521-x](https://doi.org/10.1007/s11694-024-02521-x).
- [9] T. A. Alsaleem, A. A. Albalawi, T. S. Alsaleem, A. M. Alowaifeer, and S. K. Almubayedh, "A Novel Approach for Rapid Detection of Adulteration in Saudi Wild Honey with Various Types of Syrups Using FTIR-ATR and Chemometrics," *Adv. Nutr. Food Sci.*, ANAFS-245, 2022.
- [10] W. M. Elshemey, I. A. Mohammad, and A. A. Elsayed, "Wide-angle X-ray scattering as a probe for insulin denaturation," *Int. J. Biol. Macromol.*, vol. 46, no. 4, pp. 471–477, 2010.
- [11] A. M. Hamad, H. M. Fahmy, and W. M. Elshemey, "FT-IR spectral features of DNA as markers for the detection of liver preservation using irradiation," *Radiat. Phys. Chem.*, vol. 166, p. 108522, 2020, [doi: 10.1016/j.radphyschem.2019.108522](https://doi.org/10.1016/j.radphyschem.2019.108522).

- [12] N. El Darra, H. Rajha, F. Saleh, and R. Maroun, "Food fraud detection in commercial pomegranate molasses syrups by UV–VIS spectroscopy, ATR-FTIR spectroscopy and HPLC methods," *Food Control*, vol. 80, pp. 23–30, 2017, [doi: 10.1016/j.foodcont.2017.02.043](https://doi.org/10.1016/j.foodcont.2017.02.043).
- [13] A. Hussain, H. Kashif, and S. Majeed, "Bioactive compounds in date syrup: Composition and health benefits," *J. Funct. Foods*, vol. 65, p. 103733, 2020, [doi: 10.1016/j.jff.2020.103733](https://doi.org/10.1016/j.jff.2020.103733).
- [14] Deepshikha, P. Kashyap, and N. Jindal, "Effect of date syrup on physicochemical, pasting, textural, rheological, and morphological properties of sweet potato starch," *Food Biophys.*, vol. 13, pp. 2398–2405, 2019, [doi: 10.1007/s11694-019-00160-1](https://doi.org/10.1007/s11694-019-00160-1).
- [15] S. A. Khan, S. B. Khan, L. U. Khan, A. Farooq, K. Akhtar, and A. M. Asiri, "Fourier Transform Infrared Spectroscopy: Fundamentals and Application in Functional Groups and Nanomaterials Characterization," in *Handbook of Materials Characterization*, S. Sharma, Ed. Cham: Springer, 2018, [doi: 10.1007/978-3-319-92955-2_9](https://doi.org/10.1007/978-3-319-92955-2_9).
- [16] R. M. Mohamed, A. S. Fageer, M. M. Eltayeb, and I. A. Mohamed Ahmed, "Chemical composition, antioxidant capacity, and mineral extractability of Sudanese date palm (*Phoenix dactylifera* L.) fruits," *Food Sci. Nutr.*, vol. 2, no. 5, pp. 478–489, 2014, [doi: 10.1002/fsn3.123](https://doi.org/10.1002/fsn3.123).
- [17] M. Naderi-Boldaji et al., "Potential of two dielectric spectroscopy techniques and chemometric analyses for detection of adulteration in grape syrup," *Measurement*, vol. 127, pp. 518–524, 2018, [doi: 10.1016/j.measurement.2018.06.015](https://doi.org/10.1016/j.measurement.2018.06.015).



Influence of Internal Obstacle Size and Position on Magnetohydrodynamic Convection in Square Cavities

Wedad Hassan Asiri ¹, Ammar Abdulkadhim ², H.I. Elsaeedy ¹, Nejla Mahjoub Said ^{1,*}

¹ Department of Physics, College of Science, King Khalid University, Abha 61413, Saudi Arabia, 445816980@kku.edu.sa; halsayed@kku.edu.sa; nalmahjoub@kku.edu.sa

² Mechanical Engineering Department, University of Al-Qadisiyah, Al-Qadisiyah 58001, Iraq, ammar.abdulkadhim@qu.edu.iq

*Corresponding author: (N. Mahjoub), *Email Address:* nalmahjoub@kku.edu.sa

Abstract

Understanding the impact of internal obstacle configurations on magnetohydrodynamic (MHD) convection has become essential for optimizing thermal systems such as electronic cooling devices, solar enclosures, and advanced heat exchangers. This review investigates how variations in the size and placement of internal bodies within square enclosures influence natural convection performance under the presence of magnetic fields. The paper compiles and analyzes studies from 2015 to 2024, highlighting key trends in heat transfer enhancement or suppression as a function of geometric positioning. Special focus is given to works incorporating nanofluids and different Hartmann numbers, with findings synthesized to guide future research and design improvements.

Keywords: Magnetohydrodynamics, Obstacle configuration, Thermal Performance, Cavity flow, Nanofluids, Rayleigh number, Hartmann number

<https://doi.org/10.63070/jesc.2025.008>

Received 08 April 2025; Revised 12 May 2025; Accepted 21 May 2025.

Available online 25 May 2025.

Published by Islamic University of Madinah on behalf of *Islamic University Journal of Applied Sciences*. This is a free open access article.

1. Introduction

Natural convection is a pivotal mode of heat transfer that results from the inherent movement of a fluid driven by internal buoyancy forces rather than external mechanical sources. This phenomenon occurs when temperature differences within a fluid cause density gradients, resulting in fluid movement. It plays an essential role in a variety of technical systems, particularly in passive thermal control applications such as electronics cooling, architectural insulation, solar thermal collectors, drying processes and thermal storage devices [1]. Its self-sufficient nature requires no external energy input, making it a favourable solution for energy efficient design. However, the complex interplay between temperature gradients, boundary conditions and geometric constraints poses considerable challenges in predicting and optimising the behaviour of natural convection.

Among the enhancements to this mechanism is the use of nanofluids, suspensions of nanoparticles within conventional base fluids, which offer superior thermal conductivity and stability. These advanced fluids have garnered significant attention for their ability to improve heat dissipation in high-performance systems, such as microelectronic devices, solar panels, and nuclear cooling loops. Their finely tuned dispersion not only mitigates the issues of sedimentation and channel blockage commonly associated with larger particles but also leads to more uniform thermal profiles and higher operational reliability [2]. Continued innovation in nanofluid formulation is expected to unlock further improvements in thermal system compactness and efficiency.

To better understand and model the impact of complex geometries on natural convection, Abdulkadhim et al. [3] surveyed a wide range of enclosures, including rectangular, elliptical, wavy, and square configurations. Their comprehensive review of numerical methods, employing key dimensionless numbers like Rayleigh, Hartmann, and Darcy, provided insight into the thermal and fluid dynamics of these geometries. Of particular interest was the similarity observed between square and diamond-shaped cavities, the latter being simply rotated forms of the former, offering design flexibility with minimal changes in flow behavior.

Complementing this, Pandey et al. [4] conducted detailed investigations, both computational and experimental, on natural convection in cavities with internal bodies, focusing on cylinders of varying shapes and orientations. The study highlighted the significance of geometrical parameters such as aspect ratio, angular positioning, and internal body placement on convective flow patterns. Employing diverse computational techniques, including finite volume and lattice

Boltzmann methods, they demonstrated how tailored internal structures could manipulate fluid flow to enhance thermal performance.

As research in this area progresses, the synergy between nanofluid science, geometric optimization, and magnetic field manipulation continues to unlock new possibilities for improving heat transfer performance. The following section presents a curated summary of recent contributions, drawing attention to key trends and findings that shape the current landscape of natural convection research.

2. The most selected parameters in the previous publications

Natural convection, a fundamental physical phenomenon, plays a critical role in numerous engineering applications, including packed layers, nuclear power system design, geological processes, electronic equipment cooling, solar collectors, heat exchangers, building ventilation systems, and other cooling systems [3].

Furthermore, the size and location of an internal body within the cavity directly impact heat flow patterns. Larger internal bodies can either enhance or diminish heat transfer efficiency, depending on their placement. Boundary conditions, such as constant or varying temperatures, and fluid properties, including viscosity and thermal conductivity, are also crucial factors influencing heat transfer dynamics. Abdulkadhim et al. [3] demonstrated that incorporating nanoparticles into base fluids, such as water, alters thermal properties and enhances heat transfer effectiveness. The positioning of heat sources significantly affects convection patterns, as evidenced by studies from Esmail [5] and Umadevi and Nithyadevi [6], which showed that placement near cavity edges or centrally could substantially alter heat distribution and overall system efficiency.

2.1. Conventional Square enclosure in the absence of the magnetic field

Chen et al. [7] examined heat transfer by conjugating natural convection in an open square chamber that has porous material partly filled in. They introduced a novel Lattice Boltzmann (LB) approach, validating the model through three benchmark tests: the thickness of the porous layer, the ratio of thermal conductivity between the fluid and the porous medium, and the permeability of the porous layer. The parameters for their study were set as follows: $Da=10^{-3}$, $\varepsilon=0.6$, $Ra=10^5$, $\sigma_{porous} = 1$ and $R_k=1$, while the dimensionless depth-to-length ratio (d/L) varied between 0.1, 0.3, and 0.5. The findings demonstrated that the proposed model is

applicable for unsteady conjugate heat transfer problems. Figure 1 illustrates the configurations at different d/L ratios, indicating the position of the pore/liquid interface. In all scenarios, fluid enters from the lower cavity and exits through the upper orifices.

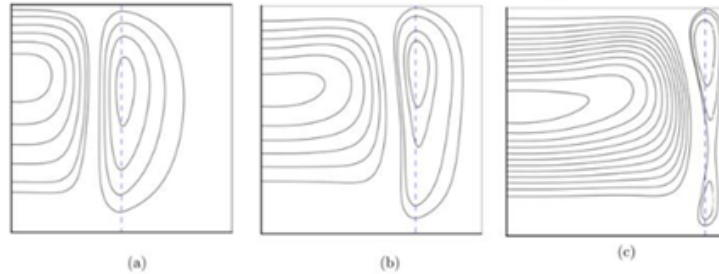


Figure 1. streamlines at the values of d/L are (a) 0.5, (b) 0.3, and (c) 0.1 [7]

Esmail [5] conducted a numerical investigation to explore the impact of thermophysical characteristics on laminar natural convection in a container with nanofluids that is differentially heated. This study was characterized by the Gasthof numbers Gr_f , ranging from 10 to 3×10^9 for pure water and from 100 to 10^9 for nanofluids. The results showed that the effective thermophysical characteristics of the nanofluids were significantly changed when nanoparticles were added to the base fluid. According to a parametric analysis of the data, the viscosity of nanofluids has a significant impact on how well they transport heat. Furthermore, the viscosity of the nanofluids plays a critical role in determining their natural heat and momentum transfer properties, whereas the thermal conductivity of the nanofluids has a comparatively lesser impact.

Mehryan et al. [8] examined, using a local thermal nonequilibrium model, the conjugate natural convection of a polar nanofluid inside a porous container. To address the coupled and nonlinear equations, they employed the Galerkin finite element method. The governing parameters included the Interface parameter ($H = 1-1000$), porosity ($\varepsilon = 0.1-0.9$), and Darcy-Rayleigh number ($Ra = 10-1000$), relative thermal conductivity ($k_r = 0.1-10$), nanofluid volume fraction ($\phi_{nf} = 0 - 0.08$), eddy viscosity parameter ($\Delta = 0 - 3$), solid wall width ($d = 0.1-0.4$), and the thermal conductivity ratio between the solid wall and base fluid ($R_k = 0.1-10$). Their findings indicated that a slight increase in microrotational force occurred with an increase in k_r , resulting from enhanced angular momentum applied to the fluid molecules. As shown in Figure 2, the stream function value increased with H , suggesting improved thermal interaction between the matrix phases of the fluid and solid, which consequently altered the Isotherm patterns in the solid and fluid phases.

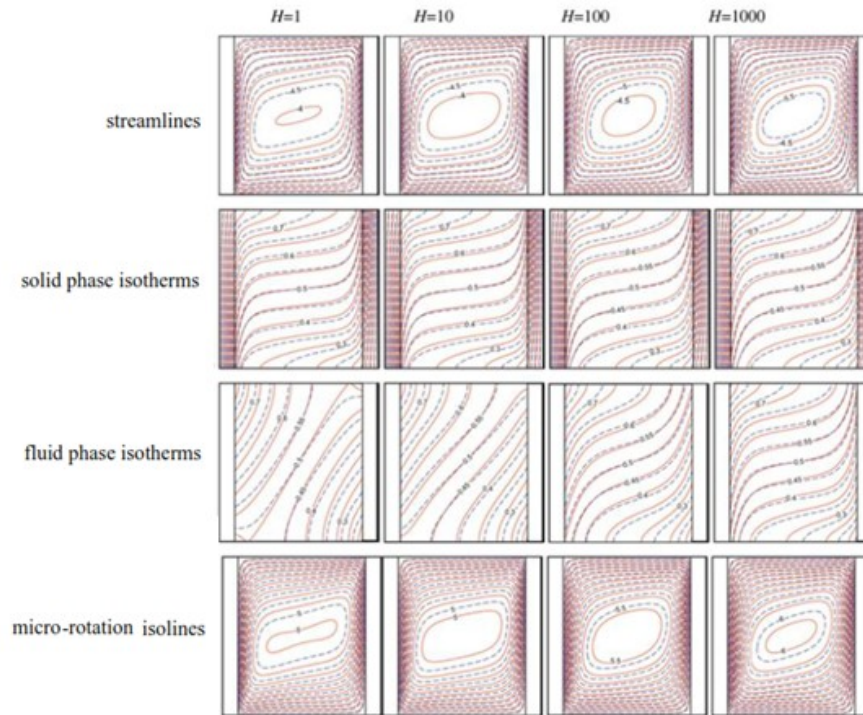


Figure 2. Dependency of streamlines, solid phase isotherms, fluid phase isotherms and micro-rotation isolines on H [8]

Reddy and Sreedevi [9] investigated the influence of thermal radiation on a nanofluid's mass transfer and natural convection heat in a square cavity, using Buongiorno's mathematical model. The study examined various parameters, including Thermophoresis number ($0.1 \leq N_t \leq 0.5$), buoyancy ratio parameter ($0.1 \leq N_r \leq 0.9$), Lewis number ($1.0 \leq Le \leq 10$), Rayleigh number ($100 \leq Ra \leq 300$), Brownian motion parameter ($0.1 \leq N_b \leq 0.9$), and radiation number ($0.1 \leq R \leq 0.9$), with results presented graphically. The findings showed that the Rayleigh number increased, an upward heat wave emerges from the left vertical heat source, while a downward heat wave forms from the right vertical heat source.

Sivarami et al. [10] examined the magnetohydrodynamic (MHD) natural convection heat transport from a heated square cylinder in a square container with uneven temperature distributions using numerical analysis. Dimensionless form was used to describe the governing equations, which were then solved using a second-order finite difference scheme using the Marker and Cell technique. In this work, the impacts of several dimensionless factors were examined, such as the eddy viscosity parameter ($0 \leq K \leq 5$), magnetic (Hartmann) parameter ($0 \leq Ha \leq 50$), and Rayleigh number ($10^3 \leq Ra \leq 10^6$). The basis fluid for all simulations was pure water, which had a Prandtl number (Pr) of 7. As shown in Figure 3, the average Nusselt

number rises as the thermal Rayleigh number grows and falls as the magnetic parameter increases.

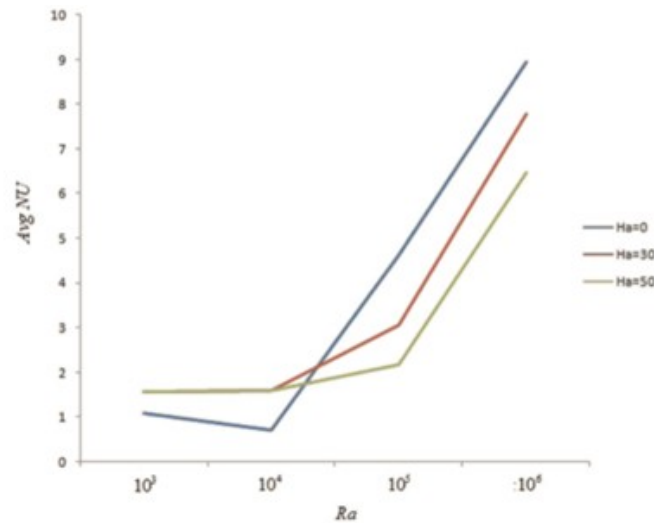


Figure 3. Average cold wall Nusselt number for various Ha values, $Pr = 7$, and $K = 1$ [10]

Charreh and Saleem [11] investigated the dynamics of fluid flow, heat transfer, and entropy generation during natural convection transients in a square cavity filled with a saturated, non-porous medium, taking into account dissipation effects and thermal radiation. They employed a direct substitution method to address the boundary and initial conditions within the porous medium. The simulations were conducted across a range of relevant dimensionless parameters, including the Rayleigh number ($10^3 \leq Ra \leq 10^6$), the Gasthof number ($10^3 \leq Gr \leq 10^7$), the Eckert number ($0 \leq Ec \leq 5 \times 10^{-5}$), the radiation parameter ($0 \leq R_d \leq 5$), the Prandtl number ($0 \leq Pr \leq 10$), and the Chheimer resistance ($0 \leq \Gamma, \gamma \leq 10$).

2.2. Conventional Square Enclosure without Inner Body in the Presence of a Magnetic Field

El Hammami et al. [12] investigated the rate of heat transfer in a square container containing an aqueous Cu nanofluid under the influence of a magnetic field using numerical analysis. They used Maxwell's model for thermal conductivity and Brinkman's model to determine the nanofluid's effective viscosity. With a focus on examining the influence of the magnetic field at a 5% nanoparticle concentration, this study sought to forecast the impacts of the Rayleigh number, Hartmann number, and volume fraction of nanoparticles. Figure 4 displays their findings, which show the local Nusselt number along the hot wall for different Rayleigh and Hartmann values ($Ha = 0, 30$, and 60). The findings indicated that the magnetic field had a negligible effect on the heat transfer performance.

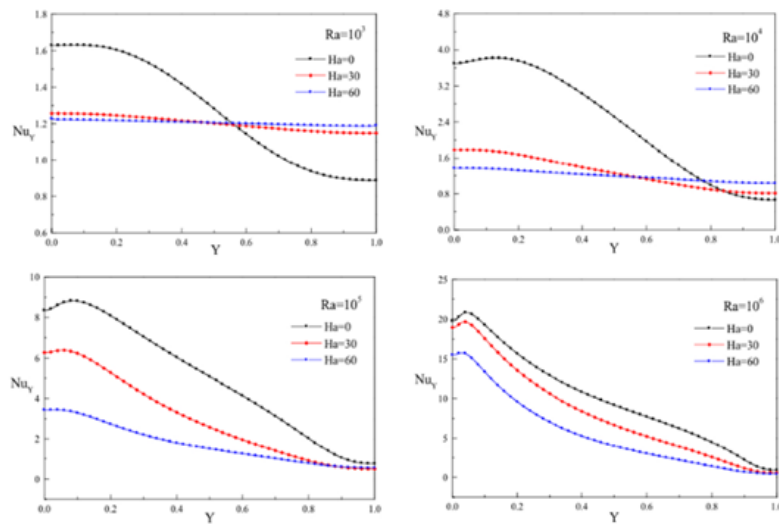


Figure 4. Local Nusselt number for different Rayleigh numbers along the cavity's left hot wall [12]

Mejri and Mahmoudi [13] conducted a comprehensive examination of natural convection in an open cavity characterized by a sinusoidal convection current. This cavity, filled with a nanofluid composed of water, was subjected to an external magnetic field. The researchers utilized the lattice Boltzmann method for numerical verification of their findings. According to their findings, the heat transfer rate and the dimensionless entropy generation number rise as the volume percentage of nanoparticles and Rayleigh number (Ra) grow, but they fall when the Hartmann number (Ha) increases. Furthermore, the study found a relationship between the volume fraction of nanoparticles and the Nusselt number (Nu). The authors investigated a broad variety of parameters, such as phase deviations ($y = 0, \pi/4, \pi/2, 3\pi/4$, and π), solid volume fractions ranging from $\phi = 0$ to 0.06, Rayleigh numbers for the base fluid ($Ra = 10^5$ to 10^6), and Hartmann numbers between 0 and 60.

Another noteworthy study by Zhang et al. [14] conducted a numerical analysis of the effects of thermal radiation on Rayleigh-Magnetohydrodynamic (R-MHD) natural convection within a square cavity, examining various levels of thermal radiation. In their research, they employed the Finite Volume Method (FVM) to solve the momentum and energy equations, while utilizing the Discrete Ordinates Method (DOM) to determine the local radiant heat flux. This comprehensive approach allowed for a detailed understanding of how thermal radiation influences the flow dynamics and heat transfer characteristics in the context of R-MHD natural convection. Their findings revealed that the influence of thermal radiation on R-MHD natural convection notably decreases with increasing Pl number, while the critical Pl_c number drops significantly with increasing Reynolds number (Re) and rises considerably with Hartmann

number (Ha). Additionally, they observed that Pl_c values increase with Ha , with Pl_c values recorded as 4.7, 4.9, 7.7, and 13.2 for Ha values of 0, 10, 50, and 100, respectively. The study highlights the crucial role of the Pl number in affecting MHD flow and temperature distribution. Figure 5 illustrates their results, showing a substantial decrease in $\overline{Nu_r}/\overline{Nu}$ at fixed Ha , indicating reduced thermal radiation effects on heat transfer, along with a notable increase in $\overline{Nu_r}/\overline{Nu}$ with fixed Ha .

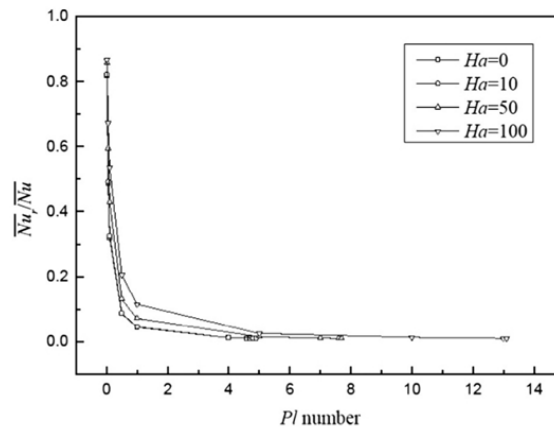


Figure 5. With $Re = 500$, $Ri = 2$, and $Pr = 0.733$, the ratio of $Nu_r = Nu$ under various heat radiation intensities: $Ha = 0$ in (a), 10 in (b), 50 in (c), and 100 in (d). [14]

Bouchair et al. [15] investigated numerically how conjugate magnetohydrodynamic (MHD) natural convection in a square cavity containing an electrically conducting fluid is affected by non-uniform volumetric internal energy production. An internal software based on the Semi-Implicit Method for Pressure-Linked Equations (SIMPLE) algorithm and the Finite Volume Method (FVM) was used to get the numerical solutions to the governing conservation equations. Their simulations, which especially examined internal Rayleigh numbers of $Ra_I = 10^4$, 10^5 , and 10^6 as well as Hartmann numbers of $Ha = 0, 50$, and 200 , showed how different controlling factors affected flow and thermal behavior. A solid-to-fluid thermal conductivity ratio of $k_r = 1$, a solid partition thickness of $\Delta = 0.2$, and a cavity tilting angle of $\alpha = 0$ were additional parameters. They also investigated three Prandtl number values: $Pr = 0.015$, 0.024 , and 0.054 . The outcomes provide insightful information about the complex relationships between these variables and how they affect the system's thermal performance.

Rashad et al. [16] investigated numerically the effects of heat sink, source location, and size on heat transfer, MHD natural convection, and entropy formation in a tilted porous cavity containing hydrated copper nanofluid. The dimensionless partial differential equations were solved using the finite difference technique, with constant values set at $Ec = 10^{-3}$, $Da = 10^{-3}$,

$Q = 1$, $\varepsilon = 0.5$, and $C_T = 0.5$. Results indicate that optimal heat transfer occurs at tilt angles between 40° - 50° and 300° - 310° across the full range of D .

Karimdoost et al. [17] employed a straightforward algorithm to solve the governing equations for temperatures ($T_c < T_h$) and conducted simulations to assess the effects of various parameters, including Rayleigh number ($Ra = 10^3$ to 10^6), nanoparticle volume fraction ($\phi = 0$ to 5%), Hartmann number ($Ha = 0$ to 60), and baffle length ($L_1 = 0$ to $0.5L$). Their results demonstrated that an increase in the Rayleigh number led to enhanced flow velocity within the enclosure by elevating the temperature difference between the hot and cold surfaces.

Li et al. [18] investigated free convective heat transfer in an alumina-water nanofluid within a square cavity inclined at angle γ with respect to the horizontal. Their results revealed that both heat transfer rate (HTR) and generated entropy increased with rising Rayleigh number. Specifically, as Ra increased from 10^3 to 10^6 , the HTR experienced a remarkable 4.5-fold increase. Figure 6 presents their findings on the flow field, temperature distribution, and local entropy generation at various angles, Rayleigh numbers, and aspect ratios.

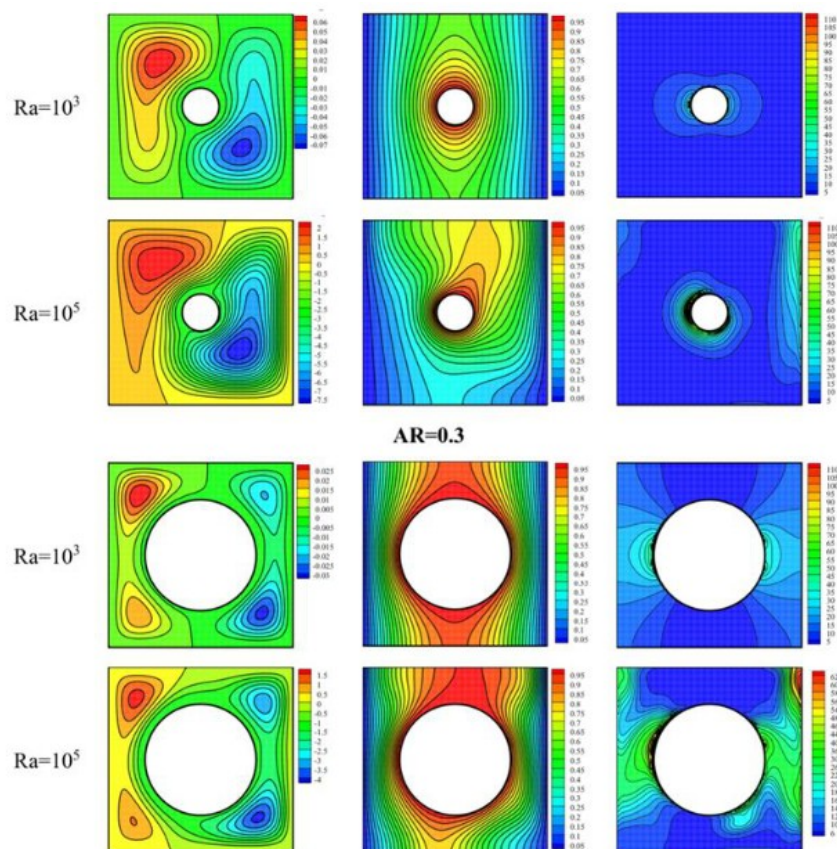


Figure 6. Temperature field, flow field and local entropy at $Ha = 20$ [18]

Dimitrienko and Li [19] examined, using computational techniques, the natural convection heat transport of a Karo fluid in a square cavity exposed to different orientations of a uniform magnetic field. For the simulation, they used a new finite difference approach. Keeping the Prandtl number constant at 0.065, the study concentrated on parameters in the following ranges: the magnetic field inclination angle (α) from 0 to π and the Rayleigh number (Ra) from 10^4 to 10^5 . The following three fluid types were examined: Newtonian fluid ($n = 1.0$ or $Ca = 0$), shear-thickening fluid ($n = 1.3$, $Ca = 2$), and shear-thinning fluid ($n = 0.7$, $Ca = 2$). They discovered that the shear-thinning fluid's convective heat transfer and flow were more noticeable than those of the Newtonian fluid when there was no magnetic field present, while the shear-thickening fluid's convective heat transfer and flow were less noticeable than those of the Newtonian fluid.

Jino and Kumar [20] explored both constant and quadratic normal heat flow of a Cu-water nanofluid over a porous square cavity subjected to an applied magnetic field. They analyzed the governing equations that describe cavity flow patterns resulting from heated thermal wall boundaries, utilizing a cascade over-relaxation method combined with an implicit algorithm to solve the dimensionless equations. Their research discusses various parameters, these include the non-linear temperature parameter λ (-1 to 1), the Darcy number (10^{-5} to 10^{-1}), the Rayleigh number (10^3 to 10^6), the Hartmann number (0 to 50), the solid volume fraction ϕ (0.01 to 0.03) of nanoparticles, and the Prandtl number (6.2).

Salma et al. [21] conducted a numerical study on unsteady natural convection flow and heat transfer within a square cavity filled with nanofluids, influenced by a periodic magnetic field. They varied the sizes and fractions of nanoparticles to enhance the physical realism of their investigation. The main dimensionless parameters examined in this study included a Rayleigh number (Ra) ranging from 10^4 to 10^6 , a Hartmann number (Ha) between 25 and 100 , a periodicity parameter (λ) from 0.1 to 1.0 , nanoparticle volume fraction (ϕ) between 0.01 and 0.05 , and a dimensionless time (τ) varying from 0.01 to 1 .

2.3. Previous studies with inner Bodies

2.3.1 Square inner Body

In a significant study, Sheremet et al. [22] conducted computational analyses to explore the effects of introducing solid isothermal bodies into a cavity filled with nanofluids that are cooled via an isothermal cooler positioned in one corner. The investigation focused on various geometric ratios of the solid mass and the isothermal coolant, in addition to factors like the

nanoparticles' solid volume fraction and Rayleigh number respectively. Using nanoparticles improves heat transfer and decreases convective flow in the cavity, according to their research. Moreover, increased entropy creation within the cavity is linked to an increase in the Rayleigh number. The results, which are shown in Figures 7 and 8, show the average Bejan number, average Nusselt numbers, entropy generation profiles, simplifications, and isotherms that correspond to various values of the important parameters that were studied.

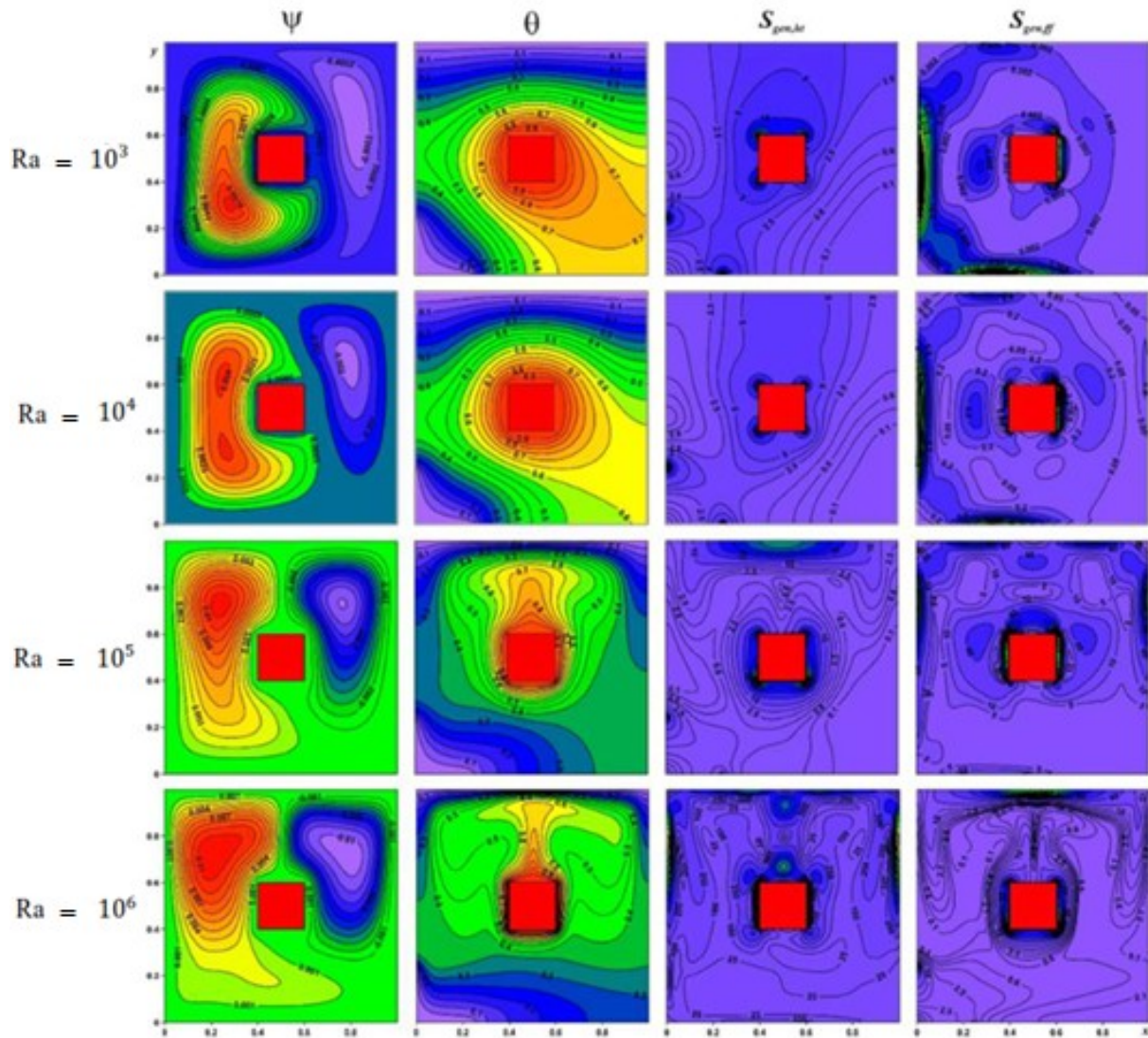


Figure 7. For $l/L=0.2$, $h/L=0.25$ and $\phi=0.03$, streamlines ψ , isotherms θ , local entropy generation from heat transfer $S_{gen,ht}$, and local entropy generation from fluid friction $S_{gen,ff}$ [22]

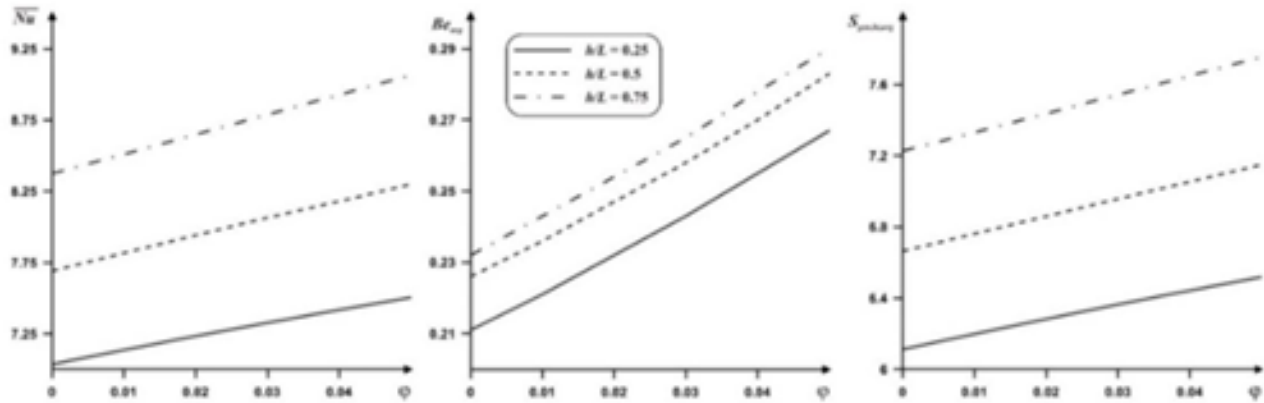


Figure 8. For $Ra = 10^5$, $l/L = 0.2$, the average Nusselt number (a), Bejan number (b), and entropy generation from heat transfer (c) are plotted against the volume % of nanoparticles and the dimensionless cooler length [22]

Bondareva and Sheremet [23] conducted a numerical study on natural convective melting in a square cavity with a localized square heat source, focusing on the effects of a tilted magnetic field. They employed a second-order finite difference method utilizing the enthalpy formulation to solve the governing equations, along with the corresponding initial and boundary conditions in both solid and liquid phases. Their results indicated that the magnetic field's inclination angle significantly influences the flow patterns, temperature distribution, and Nusselt number, particularly at a Hartmann number (Ha) of 0. Specifically, for inclination angles of $\alpha = 0$ and $\alpha = \pi/2$, they observed a symmetrical distribution of velocity and temperature within the melting zone. This study provides valuable insights into the interplay between natural convection, magnetohydrodynamics, and the Prandtl number in a square container containing an adiabatic square body.

Hussein et al. [24] conducted a numerical investigation of two-dimensional magnetic convection flow (MHD) within a square container filled with an electrically conductive fluid, employing the Lattice Boltzmann method (LBM). They explored a range of non-dimensional parameters, specifically varying the Hartmann number ($0 \leq Ha \leq 50$), the Rayleigh number ($10^3 \leq Ra \leq 10^5$), and the Prandtl number ($0.05 \leq Pr \leq 5$). Their findings revealed that as the Hartmann number increases, the magnetic field exerts a significant influence on the flow dynamics, particularly at higher Prandtl numbers. Notably, their results illustrated that the average Nusselt number decreases with an increase in the Hartmann number, as depicted in Figure 9. This study underscores the complex interplay between magnetic fields and convection phenomena in electrically conductive fluids.

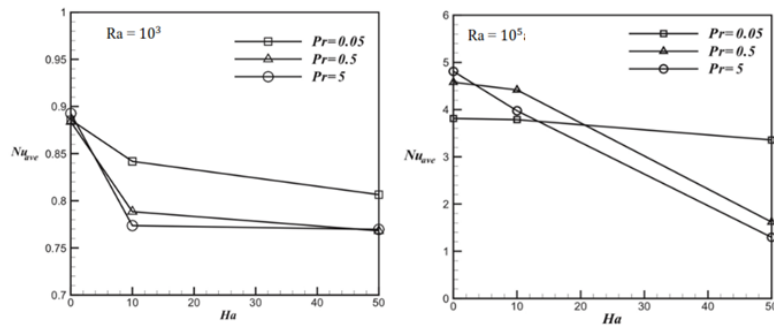


Figure 9. The Nusselt number average for different Hartmann and Prandtl numbers [24]

2.3.2 Elliptical inner body

El Moutaouakil et al. [25] performed a comprehensive two-dimensional numerical analysis to explore the interaction between natural convection and surface radiation within a horizontal toroidal region. This region is bounded by an inner heated elliptical cylinder and an outer square cavity. To investigate the natural convection phenomena quantitatively, the researchers merged the discrete arrangement approach with the finite volume method. Important factors were the ellipsoidal body's eccentricity ($00 \leq \xi \leq 0.98$) and inclination angle ($|\phi| \leq 90^\circ$). Additionally, the impacts of the interior and exterior surfaces' emissivity and Rayleigh number were examined.

2.3.3 Inner circular body and cylinder

Wang et al. [26] adopted an improved lattice Boltzmann method to simulate conjugate natural convection in a square box with a circular cylinder. They performed simulations for Rayleigh numbers in the range of $10^4 \leq Ra \leq 10^6$, with the radius of the cylinder ranging from $0.1H$ to $0.3H$, wall thickness from $0.05H$ to $0.2H$, and thermal conductivity ratio from $0.5 \leq k_s/k_f \leq 20$. Unless otherwise stated, for all cases, the Prandtl number is fixed at 0.71 , the wall-to-liquid heat capacity ratio is set to $(\rho c_p)_s/(\rho c_p)_f = 10.0$, and the inner cylinder has a radius $R=0.2H$, located at the center of the cavity. It was observed that the average Nusselt number (Nu_{av}) for a cavity with limited wall thickness is generally smaller than that for a cavity with zero wall thickness.

Mahmood et al. [27] investigated the natural convection of a horizontal cylinder placed in a square container numerically, using two different fluids as heat transfer mediums: water and air (Figure 10). They employed a 2D computational fluid dynamics (CFD) approach to predict

natural convection when using water and air as the heat transfer media. Their results showed that the surface temperature significantly affects the Nusselt number when the cylinder is surrounded by air, with maximum velocities ranging from 0.007 m/s to 0.11 m/s.

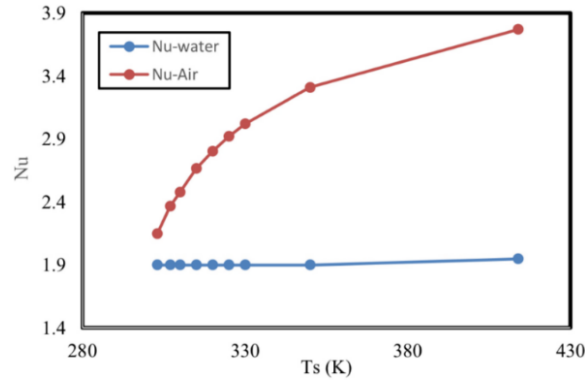


Figure 10. Nusselt number variation for air and water natural convection in relation to the horizontal cylinder's surface temperature [27]

Nammi et al. [28] numerically investigated unsteady natural convective heat transfer in a porous square container containing four heated cylinders arranged in either a square or rectangular configuration. The results are presented through simplifications, isotherms, and the time-average Nusselt number for the ranges $10^3 \leq Ra \leq 10^6$, $10^{-4} \leq Da \leq 10^{-2}$, and four different cylinder spacings of $0.3 \leq S \leq 0.6$. Pandey et al. [29] conducted A numerical study in three dimensions of buoyancy-driven heat transfer for Rayleigh numbers (Ra) = 10^4 - 10^6 and Prandtl numbers (Pr) = 0.7 in a container with four heated cylinders. Their results indicated that the average time-averaged and surface Nusselt numbers on the cylinder surface increased with increasing ε_h , regardless of Ra (Figure 11).

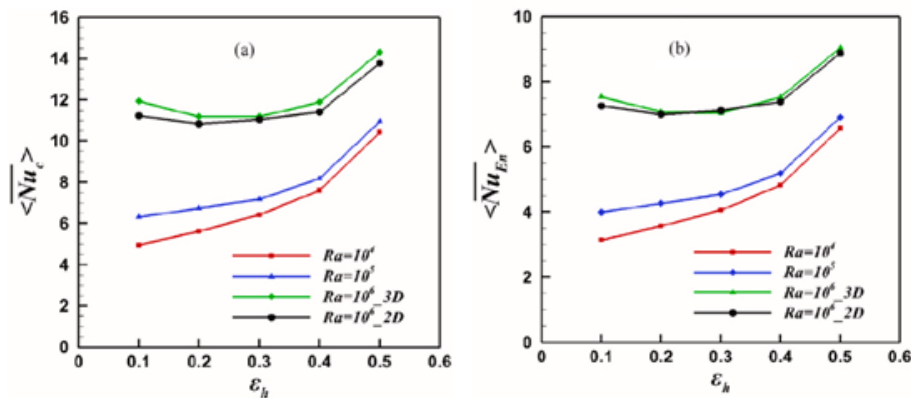


Figure 11. Nusselt number average across time and surface at (a) the cylinder and (b) the enclosure.[29]

2.3.4. Square enclosure with two wavy sided walls

Abdulkadhim et al. [30] numerically investigated natural convection heat transfer using the temperature gradient of a heated inner corrugated cylinder. Their study simulated various internal corrugation configurations within a refrigerated double-walled square container filled with two layers. They employed the Galerkin method to solve the main dimensionless equations numerically. The analysis considered several dimensionless parameters: Rayleigh number ($10^3 \leq Ra \leq 10^6$), Vertical location ($-0.2 \leq H \leq 0.2$), the number of sinusoidal internal cylinders ($3 \leq N \leq 6$), the Darcy number ($0.00001 \leq Da \leq 0.1$), the volume percentage of nanoparticles ($0 \leq \phi \leq 0.1$), and the thickness of the porous layer ($0.2 \leq X_p \leq 0.8$). Their findings suggested that when the fluid flow force increases, the inner sinusoidal cylinder should rise. A square container with a horizontal barrier at the center line of the left wall that contained water mixed with Al_2O_3 and a magnetic field was used to study natural convection heat transfer.

Alsabery et al. [31] investigated natural convective heat transfer in a porous and undulating domain filled with non-Darcian nanofluids under conditions of local thermal non equilibrium. A numerical solution of the non-dimensional transport equations was obtained by applying the Galerkin finite element differentiation method. Several parameters were taken into consideration in the investigation, including the modified conductivity ratio ($10^{-1} \leq \gamma \leq 10^{-4}$), number of ripples ($0 \leq N \leq 4$), nanoparticle volume fraction ($0 \leq \phi \leq 0.04$), and Darcy number ($10^{-6} \leq Da \leq 10^{-2}$). The heat source's dimensionless position ($0.2 \leq B \leq 0.8$) and dimensionless length ($0.2 \leq D \leq 0.8$) were also investigated.

2.4. Triangular inside a square with MHD

Mahmuda and Ali [32] investigated the effects of a magnetic field on the partial heating and cooling of vertical walls in a square cavity filled with aqueous Al_2O_3 nanofluid by numerical study of free convective flow and heat transfer. A heat-conducting triangular cylinder was positioned centrally within the cavity. Using the weighted Galerkin residual method within a finite element formulation, they solved the dimensionless governing equations. The study explored the influence of key parameters, such as Rayleigh numbers ($10^3 \leq Ra \leq 10^6$), Hartmann numbers ($0 \leq Ha \leq 100$), and nanoparticle solid volume fractions ($0\% \leq \phi \leq 5\%$), on velocity and temperature fields. Results demonstrated a notable increase in heat transfer rate with rising Rayleigh number, as the elevated Ra values intensified buoyancy forces, accelerating the rotational flow within the cavity (Figure 12).

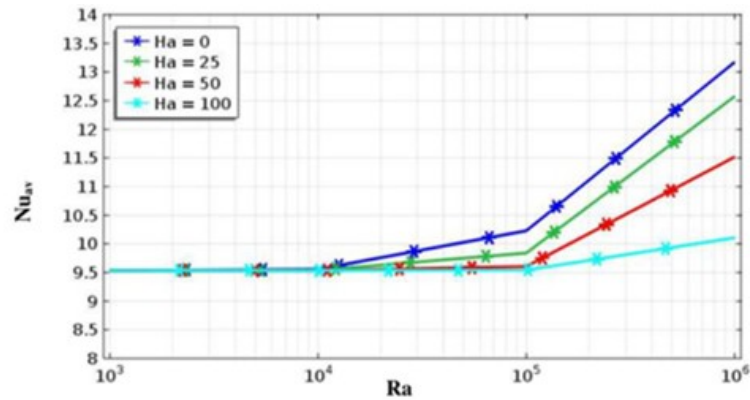
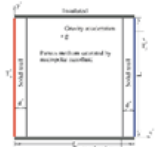
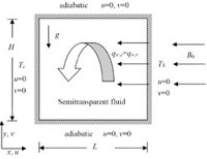

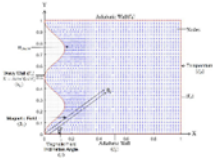
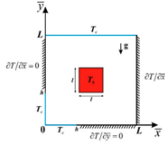
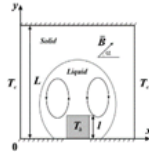
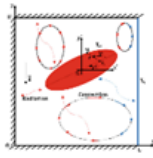

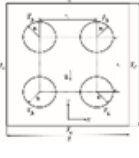
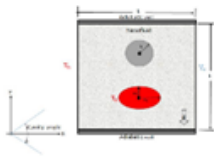
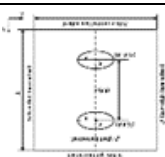
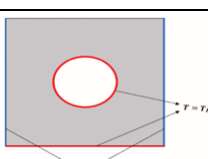


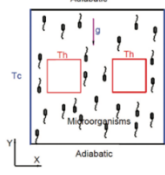
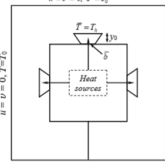
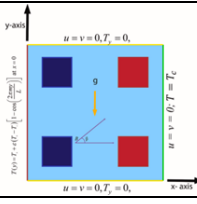
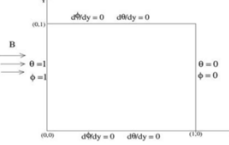
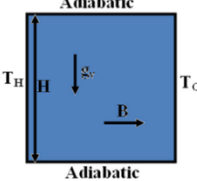
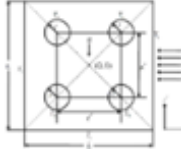
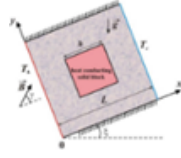
Figure 12 Effect of Hartmann number on Nusselt number average at partially heated side walls [32]

Altaee et al. [33] conducted a study on natural convection heat transfer in a square cavity containing an interior structure with an equilateral triangular cross-section. They used computational fluid dynamics (CFD) simulations with Ansys Fluent 16 to solve continuity, momentum, and energy equations. The study examined Rayleigh numbers ranging from 10^4 to 10^6 and orientation angles from 0° to 105° , with 15° increments for each case. Results revealed that the flow intensity was highly sensitive to oblique and rotational angles of the heated triangle, significantly altering both the streamline and temperature fields. When the triangle was at 0° and Rayleigh numbers were $Ra = 10^5$ and 10^6 , the top of the triangle formed two nearly symmetric convection cells, consistent with typical natural convection patterns.

Table 1. A summary of the Effect of Different Internal and external bodies in Square Containers on Natural Convection

Reference	Major topic	Enclosure shape	Results
[8]	Micropolar nanofluid in porous media	Porous square enclosure 	Thicker solid walls increase the wall stress-to-fluid volume ratio at the fluid-solid interface.
[14]	MHD natural convection with radiation	Square enclosure 	The critical parameter Plc increases exponentially with Hartmann number (Ha) and decreases exponentially with Reynolds number (Re).

[16]	MHD natural convection of nanofluid	Inclined porous square cavity 	Maximum average Nusselt number occurs at $B = 0.2$ and inclination angles between 50° and 310° .
[21]	MHD heat transfer in nanofluids	Square cavity with magnetic fields 	Both average Nusselt number and heat transfer rate increase under uniform and periodic magnetic fields.
[22]	Natural convection of nanofluids	Square cavity 	Increasing the Rayleigh number enhances convective flow and heat transfer.
[23]	Local heat source and MHD-induced melting	Square cavity 	Nusselt number decreases over the top and vertical sides of the heater over time due to increasing heating demands in those regions.
[25]	Radiative natural convection	Elliptical internal body in square cavity 	At high Rayleigh numbers, streamlines rotate clockwise with vortex formation near the top-left corner.
[26]	Natural convection with cylindrical body	Circular cylinder in square cavity 	Heat transfer rate declines as the outer wall thickness increases.
[28]	Natural convection with internal heaters	Four heated cylinders in a square cavity 	Total Nusselt number (Nu_t) increases monotonically with cylinder spacing (S) for Darcy number $Da = 10^{-4}$.
[34]	Natural convection in inclined nanofluid	Heated, inclined square cavity 	Minimum stream function values are observed at high Rayleigh numbers when the caustic angle is -30° .
[35]	Dual heated inner cylinders	Two heated elliptical cylinders 	At $Ra = 10^4-10^5$, increasing aspect ratio (AR) enhances the time-averaged Nusselt number and surface heat transfer.
[36]	Convection with a circular obstacle	Fixed circular object in nanofluid-filled cavity 	Lamina nanoparticles enhance heat transfer and thermal distribution in diamond-water systems.

[37]	Dual internal heaters	Two heaters inside square enclosure 	Sherwood number increases by 31% when thermal Rayleigh number rises from 10^3 to 10^5 for $Ra_b = 10$.
[38]	Natural convection in composite geometry	Trapezoidal cavity with a central square cylinder 	Heat transfer across cavity walls and sources is significantly enhanced with higher Rayleigh numbers.
[39]	Sinusoidal boundary conditions and blocks	Square cavity with hot/cold blocks 	Stronger magnetic fields (higher Ha) suppress flow velocity and result in weaker, more symmetrical vortices.
[40]	MHD effects on convection	Square cavity 	Buoyancy ratio has minimal effect at low Rayleigh numbers and high magnetic field strength..
[41]	Laminar vs. turbulent MHD convection	Square cavity 	Heat transfer decreases with increasing Hartmann number at $Ra = 10^5$ (laminar) and $Ra = 10^8$ (turbulent).
[42]	MHD convection with multiple obstacles	Four circular cylinders in square cavity 	Increased magnetic field strength and ϵ significantly reduce oscillation frequency.
[43]	Conductive solid block in MHD convection	Square cavity with internal conducting block 	Average Nusselt number varies nonlinearly with the angle of the applied magnetic field.

2.5. Inner body studies without MHD

Rahmati and Tahery [44] Performed a two-dimensional simulation of natural convection heat transfer surrounding a heated obstacle within a square hollow, characterized by cold side walls, an adiabatic top wall, and a heated bottom wall. Using the capillary Boltzmann method, they analyzed transfer of heat in a water- TiO_2 nanofluid, Prandtl's number is 6.2 and a Rayleigh number of 10^6 . The volume fraction of the nanofluid was 0.05. According to the study, when the volume fraction of nanoparticles rises while keeping the Rayleigh number constant, the

average Nusselt number on the cold walls also rises. Additionally, with increasing Rayleigh number, the streamlines intensify near the cavity boundaries, becoming more pronounced as the Rayleigh number grows. Figure 13 illustrates the proximity of streamlines to the cavity edges under higher Rayleigh numbers.

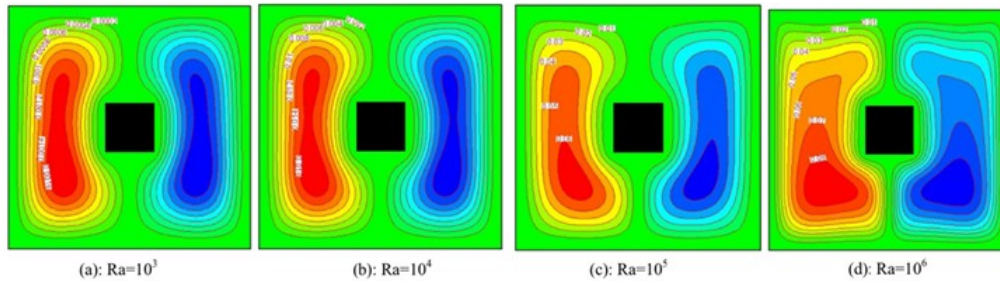


Figure 13. Streamlines for $\phi=0.04$ and various Rayleigh numbers.[44]

Ali et al. [45] conducted a numerical analysis of natural convection in saturated porous media, applying the governing equations using the finite difference approach. They provided numerical results on heat transfer behavior for a modified Rayleigh number (Ra) ranging from 100 to 1000, examining two distinct section positions: Case 1 ($X_{P_1} = \frac{1}{4}, X_{P_2} = \frac{3}{4}$) and Case 2 ($X_{P_1} = \frac{3}{4}, X_{P_2} = \frac{1}{4}$), with section lengths varying between 0.2 and 0.8. Their findings indicated that heat transfer through free convection improves with an increase in Ra values.

Rashid et al. [36] examined the influence of nanoparticle morphology on nanofluid dynamics in a lid-driven square cavity with a stationary circular obstruction at the center. The research employed the finite element technique (FEM) to resolve the linked partial differential equations that dictate the flow. They considered the Prandtl number to be constant at $Pr = 6.8$. As shown in Figure 14, their results revealed that the velocity and temperature of the water-diamond nanofluid were inversely and directly related, respectively, to the angular momentum (ϕ).

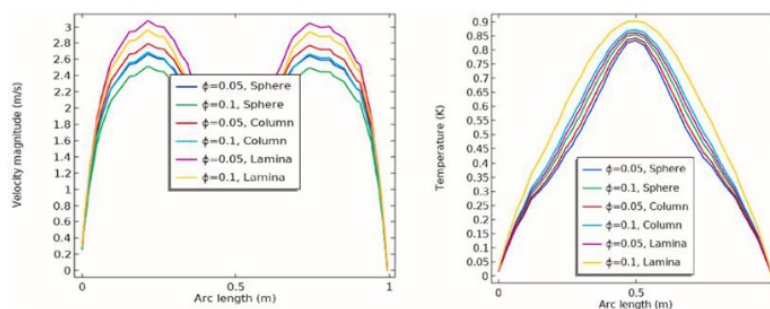


Figure 14. Variation in velocity and temperature of nanofluid with the impact of ϕ [36]

Izadpanah et al. [37] examined the natural biothermal convection of gyrotactic microorganisms in a square cavity containing two smaller square heat sources. They applied the finite element method (FEM) to assess microorganism dynamics and buoyancy-driven convection. Their research examined the impact of many parameters, including the thermal Rayleigh number (Ra_t , spanning from 10^3 to 10^5) and the biothermal Rayleigh number (Ra_b , ranging from 10 to 100). heater movement, the Peclet number (0.001–0.1), and the Lewis number (Le, between 1 and 10), on mass transport (Sherwood number) and natural convective heat transfer (Nusselt number). performance. Fixed parameters in the study included the oxygen diffusion rate ($\sigma = 1$) and the ratio of oxygen diffusion to microorganism diffusion ($\chi = 1$).

Roy et al. [38] investigated the characteristics of heat transmission and natural convection in an annulus made up of two square cylinders. By applying coordinate transformations, they developed a mathematical model for their system, which included three heat sources positioned at $\xi = 90^\circ$, 180° , and 270° with parameters of width $w = 0.10$, breadth $b = 24^\circ$, and Rayleigh number $Ra = 10,000$. Results demonstrated that increasing the number, width, and amplitude of heat sources, as well as the Rayleigh number, amplified flow strength. Figure 15 illustrates the effect of heat source width on the Nusselt number, particularly at the heat source top and on the cavity's outer walls.

Hamid et al. [46] examined the natural convection phenomenon in a square cavity with a unique curvature containing circular obstructions. They employed Galerkin weighted residuals as a numerical simulation technique, exploring the impact of three axial parameters: the Hartmann number, which ranged from 0 to 200, and the circular obstacle's radius, which systematically changed from 0.1 to 0.3 to capture various obstacle sizes. The Rayleigh number was varied between 10^2 and 10^7 , while maintaining a constant Prandtl number of 6.2.

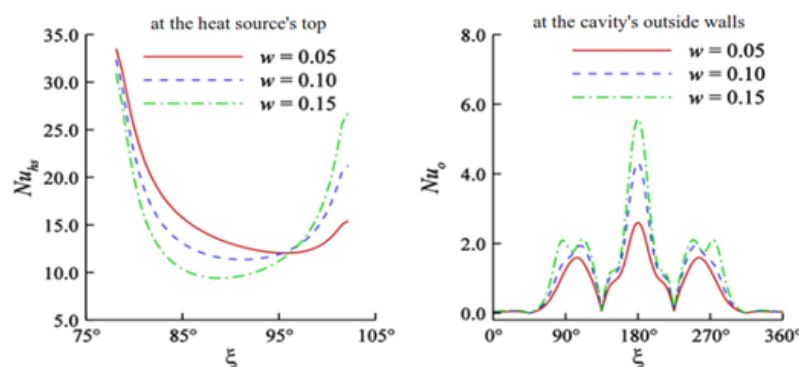


Figure 15. Effect of Nusselt number [38]

Another study [39] focused on the properties of Convection in two dimensions using magnetohydrodynamics (MHD) in a rectangular chamber containing an electrically conducting fluid. This investigation included a broad spectrum of governing parameters, such as inclination angle ($0 \leq \beta \leq 90^\circ$), porosity ($0.1 \leq \varepsilon \leq 0.9$) Rayleigh number ($10^4 \leq Ra \leq 10^7$), Hartmann number ($0 \leq Ha \leq 500$), and a parameter m ($1 \leq m \leq 6$). The findings showed that the simplification inside the cavity increased by 445% and 5284% when the inclination angle (β) was enhanced from 0° to 90° and Rayleigh number (Ra) from 10^5 to 10^7 , respectively. Conversely, simplification decreased by 1627% as Hartmann number (Ha) varied from 0 to 100. Additionally, heat transfer improved by 58% as porosity (ε) changed from 0.1 to 0.5. Overall, the findings revealed that larger inclination angles significantly enhanced heat transfer efficiency by reducing convective heat losses and improving fluid movement regulation.

2.6. Conventional Enclosure without inner body

Arjun and Rakesh [47] studied the simulation of fluid flow and natural convection heat transfer in a differentially heated square cavity that featured horizontal adiabatic walls and vertical isothermal walls, equipped with several fins. They employed the finite volume method to analyze the flow of Cu-water nanofluids containing non-uniform nanoparticles ($R = 0.007$) at an average diameter of 50 nm, maintained at a temperature of 333.15 K. The aspect ratio was set to 3, with three thin horizontal conductive fins connected to the hot wall, and the fins positioned at 0.4 of the height of the cavity. Their simulations, conducted under a Hartmann number of 10 and a Rayleigh number of 10^6 , showed that the configuration achieved optimal heat transfer enhancement, maximizing the cold wall's average Nusselt number. They concluded that using three fins provided the best enhancement for heat transfer performance.

Reddy and Murugesan [40] conducted a numerical study on natural dual-diffusion convection in a square cavity subjected to an external magnetic field, employing the weighted Galerkin residual finite element method with a vortex velocity formulation. Their simulations covered a range of parameters: Hartmann number ($0 < Ha < 200$), Rayleigh number ($10^4 < Ra < 10^6$), and field inclination angles from 0° to 360° . The study explored various fluid systems, including gas, water, and liquid gallium.

Their results indicated that increasing the Hartmann number from 0 to 30 resulted in a significant decrease in the Nusselt number and Sherwood number by approximately 72% and 78%, respectively. Figures 16 and 17 illustrate the simplified profiles, isothermal lines, and

concentration lines for Rayleigh numbers of 10^4 , 10^5 , and 10^6 when the magnetic field is applied horizontally at $N = 0.75$, $Pr = 1$, and $Le = 2$.

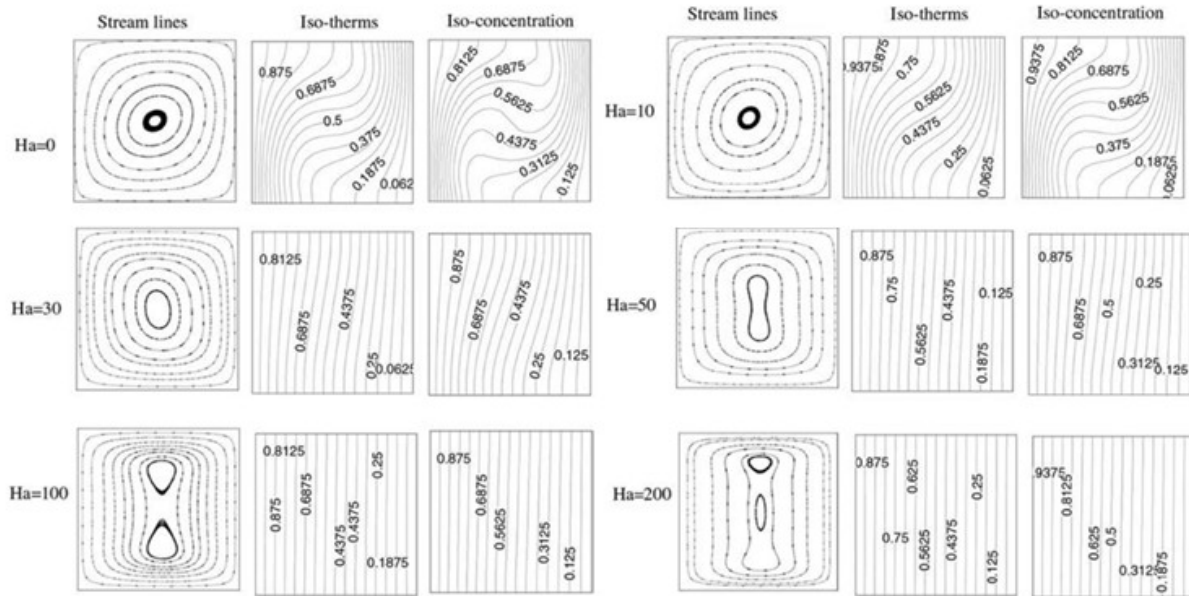


Figure 16. Hartmann number's impact on streamlining, isotherms, and isoconcentration

lines at $Ra = 10^4$ for $N = 0.7$. [40]

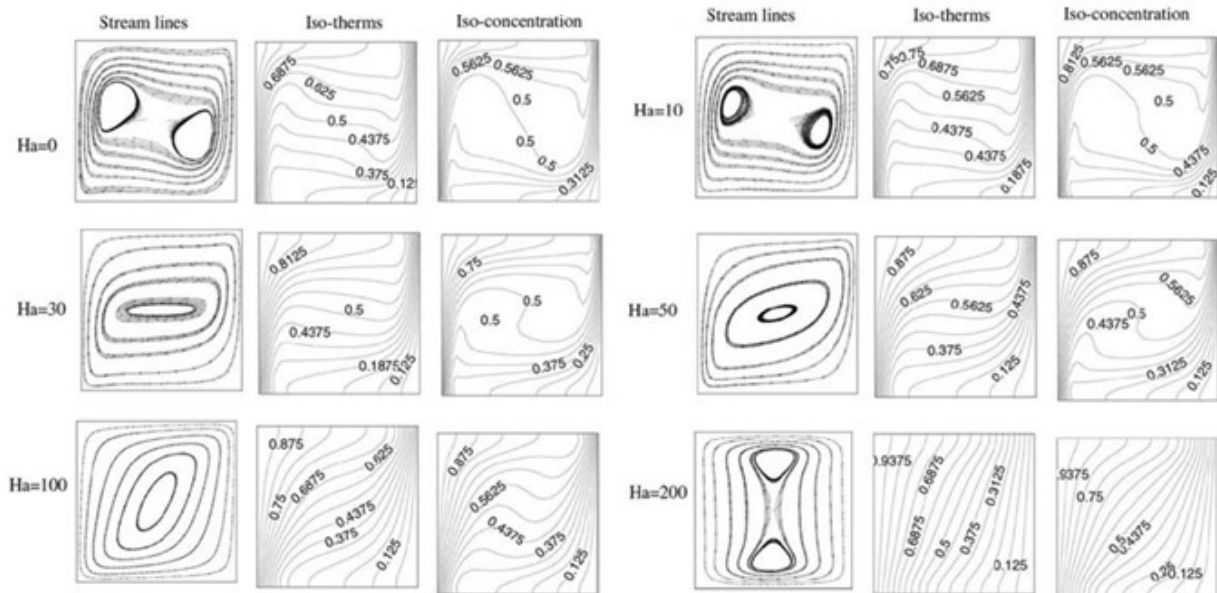


Figure 17. Hartmann number's impact on streamlining, isotherms, and isoconcentration

lines at $Ra = 10^6$ for $N = 0.75$. [40]

Sajjadi and Kefayati [41] applied the lattice Boltzmann method to analyze both turbulent and laminar natural convection within a square cavity containing water ($Pr = 6.2$). Their study considered Rayleigh numbers in the ranges $Ra = 10^3 - 10^5$ for laminar flow and $Ra = 10^7 - 10^9$ for turbulent flow, along with Hartmann numbers ($H = 0 - 100$). They observed that the magnetic field had a significant influence on heat transfer, especially at $Ra = 10^5$, where increasing Ha from 0 to 100 led to a notable reduction in heat transfer. Figure 18 illustrates the local Nusselt number distributions on the hot and cold walls under various Rayleigh and Hartmann numbers.

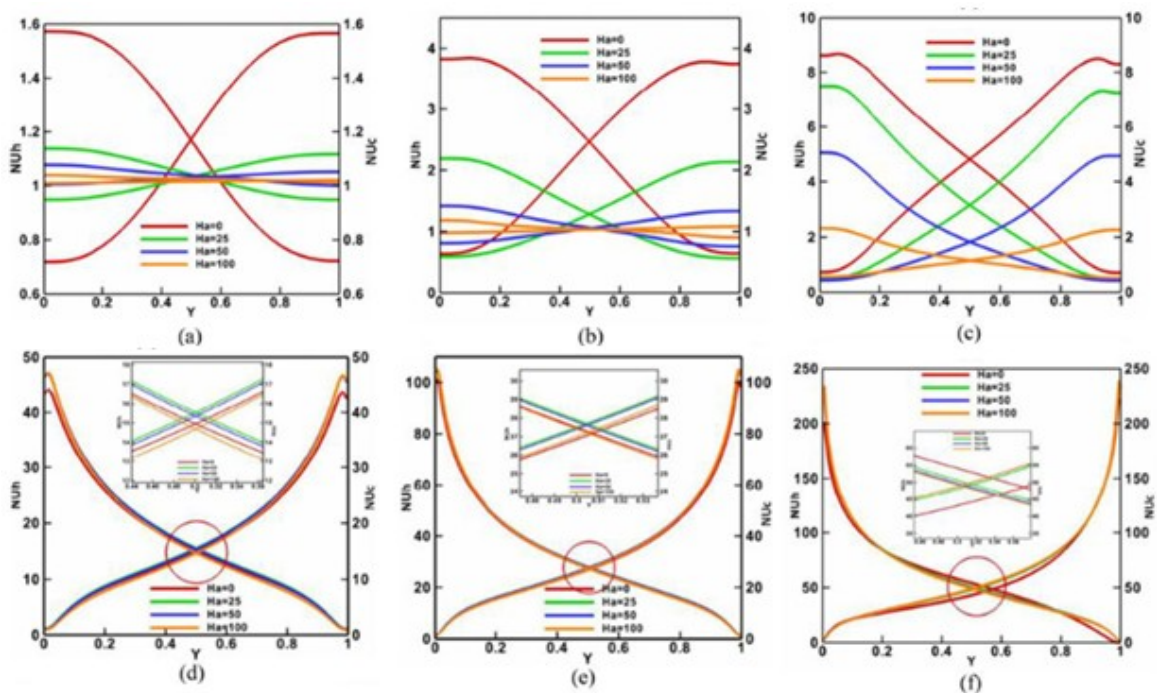


Figure 18. Effect of Rayleigh and Hartmann values on the Nusselt number on the hot and cold walls ($Ra = 10^3, 10^4, 10^5, 10^7, 10^8$ and 10^9) [41]

2.6.1. Inner body studies with MHD

Chatterjee and Kumar [42] conducted a finite-volume numerical study to explore two-dimensional hydromagnetic natural convection in a cooled square container containing four uniformly shaped, heated inner circular cylinders. They assumed all solid walls were electrically insulated. The simulations covered various control parameters, including Rayleigh numbers from 10^3 to 10^6 , Hartmann numbers from 0 to 50, and dimensionless distances between cylinder centers ranging from 0.3 to 0.7. The study's primary goal was to analyze how

the placement of the cylinders along the case's diagonals influences magnetic heat transfer within the cavity.

Tayebi and Chamkha [48] studied natural convection of an AL_2O_3 -Cu/water hybrid nanofluid in a cavity containing a centrally positioned corrugated conductive cylinder under a constant horizontal magnetic field. They utilized the finite volume method (FVM) to solve the governing transport equations. Parameters were analyzed based on various factors, specifically the average Nusselt number (Nu_{avg}) for different thermal conductivity ratios (k^*) at a nanoparticle volume fraction (ϕ) of 0.06, corrugation amplitude (A) of 0.2, and Hartmann number (Ha) of 25, with Rayleigh numbers of $Ra = 10^3$ and $Ra = 10^5$. Their findings revealed that alumina nanoparticles in water enhanced heat transfer significantly, especially under convection-dominated conditions.

2.6.2. Previous studies without inner body and Without MHD

Khalili et al. [49] investigated natural convection heat transfer of a nanofluid in a two-dimensional square cavity using the lattice Boltzmann method with constant heat flow boundary conditions. They explored parameters such as Rayleigh numbers ($Ra = 3.5 \times 10^5$, 3×10^6), constant streamline, velocity, average Nusselt number, and temperature throughout volume fractions of nanoparticles ($\phi = 0.05, 0.1, 0.2$). According to their findings, the Nusselt number rose as the volume fraction of nanoparticles increased, indicating improved heat transmission in the nanofluid as opposed to the pure fluid, even with a fixed Grashof number. The dimensionless temperature distribution, velocity profiles, and simplifications for water at $Ra^* = 3.5 \times 10^5$ and $Ra^* = 3 \times 10^6$ are shown in Figure 19 of their paper.

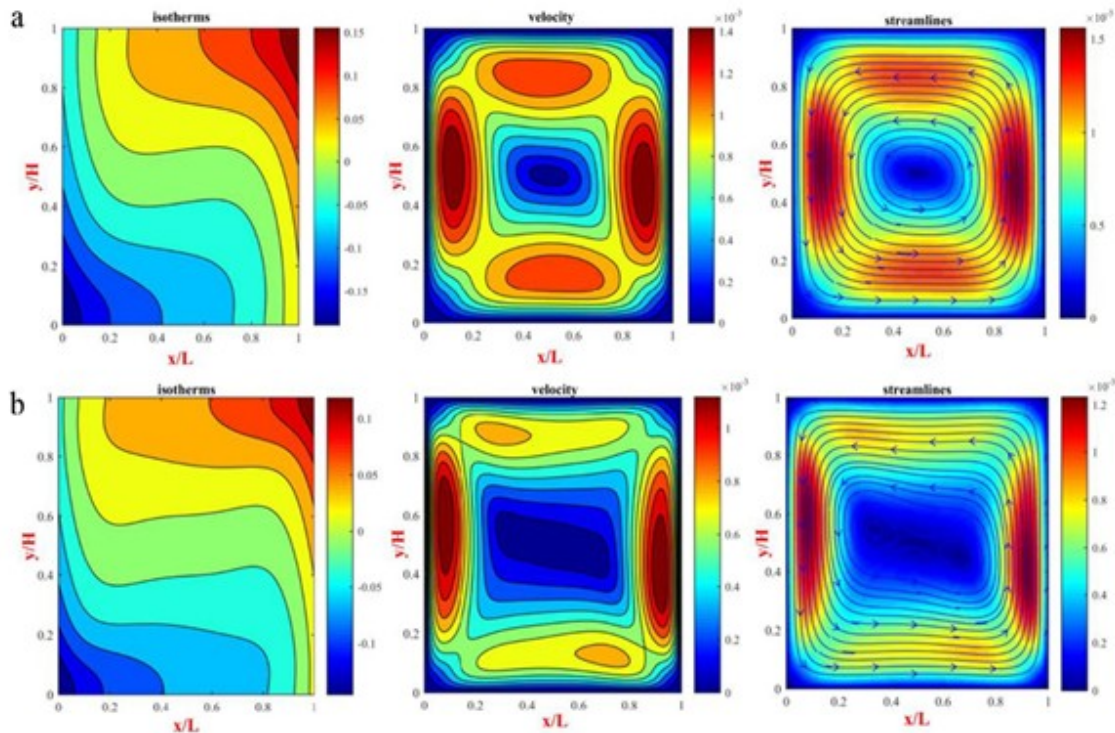


Figure 19. Water temperature distribution, velocity, and streamlines Ra^* values for a and b are 3.5×10^5 and 3×10^6 , respectively.[49]

3. Conclusion

The reviewed studies clearly show that the size and position of internal bodies within square enclosures play a pivotal role in influencing natural convective heat transfer. Variations in these parameters significantly alter the flow circulation and heat distribution patterns, affecting the overall heat transfer performance. Future research should focus on systematically analysing how incremental changes in size and position can be optimised to improve thermal efficiency. The influence of internal body size and positioning is evident across various studies, demonstrating its critical role in enhancing or suppressing heat transfer depending on the configuration. Optimizing these parameters, in combination with factors like nanofluid application and magnetic field strength, can significantly improve thermal performance. These insights can be useful in designing more effective thermal management systems in engineering applications.

References

- [1].Tasnim, S., A. Mitra, H. Saha, M.Q. Islam, and S. Saha, MHD conjugate natural convection and entropy generation of a nanofluid filled square enclosure with multiple heat-generating elements in the presence of Joule heating. *Results in Engineering*, 17 (2023) :100993.

- [2] Wang, X.-Q. and A.S. Mujumdar, A review on nanofluids-part I: theoretical and numerical investigations. *Brazilian journal of chemical engineering*, 25 (2008) 613-630.
- [3] Abdulkadhim, A., I. mejbel Abed, and N. mahjoub Said, An exhaustive review on natural convection within complex enclosures: Influence of various parameters. *Chinese Journal of Physics*, 74 (2021) 365-388.
- [4] Pandey, S., Y.G. Park, and M.Y. Ha, An exhaustive review of studies on natural convection in enclosures with and without internal bodies of various shapes. *International Journal of Heat and Mass Transfer*, 138 (2019) 762-795.
- [5] Esmaeil, K.K., Thermophysical properties-based evaluation of nanofluids laminar natural convection inside square enclosure. *Journal of Thermophysics and Heat Transfer*, 29(1) (2015) 102-116.
- [6] Umadevi, P. and N. Nithyadevi, Convection in a sinusoidally heated square enclosure utilizing Ag– water nanofluid with heat generating solid body. *International Journal of Mechanical Sciences*, 131 (2017) 712-721.
- [7] Chen, S., W. Gong, and Y. Yan, Conjugate natural convection heat transfer in an open-ended square cavity partially filled with porous media. *International Journal of Heat and Mass Transfer*, 201 :124 .8p. 368-380.
- [8] Mehryan, S., M. Izadi, and M.A. Sheremet, Analysis of conjugate natural convection within a porous square enclosure occupied with micropolar nanofluid using local thermal non-equilibrium model. *Journal of Molecular Liquids*, 250 (2018) 353-368.
- [9] Reddy, P.S. and P. Sreedevi, Buongiorno's model nanofluid natural convection inside a square cavity with thermal radiation. *Chinese Journal of Physics*, 72 (2021) 327-344.
- [10] Sivarami Reddy, C., V. Ramachandra Prasad, and K. Jayalakshmi, Numerical simulation of natural convection heat transfer from a heated square cylinder in a square cavity filled with micropolar fluid. *Heat Transfer* ,(6)50(2021:) 5267-5285.
- [11] Charreh, D. and M. Saleem, Entropy generation and natural convection analyses in a non-Darcy porous square cavity with thermal radiation and viscous dissipation. *Results in Physics*, 52 (2023) 106874.
- [12] El Hammami, Y., M. El Hattab, R. Mir, and T. Mediouni, Numerical study of natural convection of nanofluid in a square enclosure in the presence of the magnetic field. *Int. J. Eng. Adv. Tech.(IJEAT)*, 4 (2015)4 .
- [13] Mejri, I. and A. Mahmoudi, MHD natural convection in a nanofluid-filled open enclosure with a sinusoidal boundary condition. *Chemical Engineering Research and Design*, 98 (2015) 1-16.
- [14] Zhang, J.-K., B.-W. Li, Y.-Y. Chen, H.-L. Li, and X.-Y. Tian, Critical parameter research on natural convection of radiation-magnetohydrodynamics in a square cavity. *International Communications in Heat and Mass Transfer* ,68(2015) 114-121.
- [15] Bouchair, R., A. Bourouis, and A. Omara, Conjugate MHD natural convection in a square cavity with a non-uniform heat source thick solid partition. *International Journal for Computational Methods in Engineering Science and Mechanics*, (5)23 (2022) 396-411.
- [16] Rashad, A., T. Armaghani, A.J. Chamkha, and M. Mansour, Entropy generation and MHD natural convection of a nanofluid in an inclined square porous cavity: effects of a heat sink and source size and location. *Chinese journal of physics*, 56(1) (2018) 193-211.
- [17] Karimdoost Yasuri, A., M. Izadi, and H. Hatami, Numerical study of natural convection in a square enclosure filled by nanofluid with a baffle in the presence of magnetic field. *Iranian Journal of Chemistry and Chemical Engineering*, 38(5) (2019) 209-220.
- [18] Li, Z., A.K. Hussein, O. Younis, M. Afrand, and S. Feng, Natural convection and entropy generation of a nanofluid around a circular baffle inside an inclined square cavity under thermal radiation and magnetic field effects. *International Communications in Heat and Mass Transfer*, 116 (2020) 104650.
- [19] Dimitrienko, Y.I. and S. Li ,Numerical simulation of MHD natural convection heat transfer in a square cavity filled with Carreau fluids under magnetic fields in different directions. *Computational and Applied Mathematics*, 39(4) (2020) 252.
- [20] Jino, L. and A.V. Kumar, Cu-water nanofluid MHD quadratic natural convection on square porous cavity. *International Journal of Applied and Computational Mathematics*, 7(4) (2021) 164.

- [21] Salma, U., M.M. Haque, and M. Alam. Convective heat transfer in a square cavity filled with nanofluids under the influence of periodic magnetic field. in AIP Conference Proceedings. (2021) AIP Publishing.
- [22] Sheremet, M.A., H.F. Oztop, I. Pop, and N. Abu-Hamdeh, Analysis of entropy generation in natural convection of nanofluid inside a square cavity having hot solid block: Tiwari and Das' model. *Entropy*, 18(1) (2015) 9.
- [23] Bondareva, N.S. and M.A. Sheremet, Effect of inclined magnetic field on natural convection melting in a square cavity with a local heat source. *Journal of Magnetism and Magnetic Materials*, 419 (2016) 476-484.
- [24] Hussein, A.K., H. Ashorynejad, S. Sivasankaran, L. Kolsi, M. Shikholeslami, and I. Adegun, Modeling of MHD natural convection in a square enclosure having an adiabatic square shaped body using Lattice Boltzmann Method. *Alexandria Engineering Journal*, 55(1) (2016) 203-214.
- [25] El Moutaouakil, L., M. Boukendil, Z. Zrikem, and A. Abdelbaki. Conjugate natural convection-surface radiation in a square cavity with an inner elliptic body. in *The Proceedings of the Third International Conference on Smart City Applications*. (2019). Springer.
- [26] Wang, L., Y. Zhao, X. Yang, B. Shi, and Z. Chai, A lattice Boltzmann analysis of the conjugate natural convection in a square enclosure with a circular cylinder. *Applied Mathematical Modelling*, 71 (2019) 31-44.
- [27] Mahmood, R.A., A.K. Ibrahim, A.G.M. Kamilxy, and R.I. Saeed. Natural convection from a horizontal cylinder placed in a square enclosure: CFD simulations. in *AIP Conference Proceedings*. (2023) AIP Publishing.
- [28] Nammi, G., D.K. Deka, S. Pati, and L. Baranyi, Natural convection heat transfer within a square porous enclosure with four heated cylinders. *Case Studies in Thermal Engineering*, 30 (2022) 101733.
- [29] Pandey, S., P.S. Jakkareddy, Y.M. Seo, and M.Y. Ha, Direct numerical simulation of natural convection between an enclosure and multiple circular cylinders: an influence of horizontal arrangement of cylinders. *Case Studies in Thermal Engineering*, 36 (2022) 102205.
- [30] Abdulkadhim, A., H.K. Hamzah, F.H. Ali, A.M. Abed, and I.M. Abed, Natural convection among inner corrugated cylinders inside wavy enclosure filled with nanofluid superposed in porous–nanofluid layers. *International Communications in Heat and Mass Transfer*, 109 (2019) 104350.
- [31] Alsabery, A.I., T. Tayebi, A.J. Chamkha, and I. Hashim, Natural convection of Al₂O₃-water nanofluid in a non-Darcian wavy porous cavity under the local thermal non-equilibrium condition. *Scientific Reports*, 10(1) (2020) 18048.
- [32] Mahmuda, S. and M.M. Ali, MHD free convection flow of nanofluids inside a flush mounted heated square cavity containing a heat conducting triangular cylinder. (2024.)
- [33] Altaee, A.H., F.H. Ali, and Q.A. Mahdi, Natural convection inside square enclosure containing equilateral triangle with different orientations. *Journal of University of Babylon*, 25(4) (2017) 1194-1205.
- [34] Ibrahim, M.N.J., K.A. Hammoodi, A.D. Abdulsahib, and M.A. Flayyih, Study of natural convection inside inclined nanofluid cavity with hot inner bodies (circular and ellipse cylinders). *International Journal of Heat and Technology*, 40(3) (2022) 699-705.
- [35] Cho, H.W., M.Y. Ha, and Y.G. Park, Natural convection in a square enclosure with two hot inner cylinders, Part II: The effect of two elliptical cylinders with various aspect ratios in a vertical array. *International Journal of Heat and Mass Transfer*, 135 (2019) 962-973.
- [36] Rashid, U., D. Lu, and Q. Iqbal, Nanoparticles impacts on natural convection nanofluid flow and heat transfer inside a square cavity with fixed a circular obstacle. *Case Studies in Thermal Engineering*, 44 (2023) 102829.
- [37] Izadpanah, F., M. Sadegh Sadeghi, M. Ghodrati, and M. Behnia, Natural thermo-bio convection of gyrotactic micro-organisms in a square cavity with two heaters inside: application to ocean ecosystems. *International Journal of Environmental Studies*, 81(3) (2024) 1390-1412.
- [38] Roy, N.C., M.A. Hossain, and R.S.R. Gorla, Natural convection in a cavity with trapezoidal heat sources mounted on a square cylinder. *SN Applied Sciences*, 2 (2020) 1-11.
- [39] Hamid, M., M. Usman, W.A. Khan, R.U. Haq, and Z. Tian, Natural convection and multidirectional magnetic field inside a square shaped cavity with sinusoidal temperature and heated/cold blocks. *International Communications in Heat and Mass Transfer*, 152 (2024) 107291.

- [40] Reddy, N. and K. Murugesan, Magnetic field influence on double-diffusive natural convection in a square cavity—A numerical study. *Numerical heat transfer, part A: Applications*, 71(4) (2017) 448-475.
- [41] Sajjadi, H. and G.R. Kefayati, MHD turbulent and laminar natural convection in a square cavity utilizing lattice Boltzmann method. *Heat Transfer—Asian Research*, 45(8) (2016) 795-814.
- [42] Chatterjee, D. and S. Kumar Gupta, Magnetohydrodynamic natural convection in a square enclosure with four circular cylinders positioned at different rectangular locations. *Heat Transfer Engineering*, 38(17) (2017) 1449-1465.
- [43] Sivaraj, C. and M.A. Sheremet, MHD natural convection in an inclined square porous cavity with a heat conducting solid block. *Journal of Magnetism and Magnetic materials*, 426 (2017) 351-360.
- [44] Rahmati, A. and A. Tahery, Numerical study of nanofluid natural convection in a square cavity with a hot obstacle using lattice Boltzmann method. *Alexandria engineering journal*, 57(3) (2018) 1271-1286.
- [45] Ali, r.a., analysis of the natural convection heat transfer inside square enclosure partially divided by non-conductive partitions s.
- [46] Hamid, M., M. Usman, W.A. Khan, R.U. Haq, and Z. Tian, Characterizing natural convection and thermal behavior in a square cavity with curvilinear corners and central circular obstacles. *Applied Thermal Engineering*, 248 (2024) 123133.
- [47] Arjun, K. and K. Rakesh, MHD natural convection heat transfer in a nanofluid filled finned square cavity. *Journal of Mechanical Engineering Research & Developments*, 40 (2017) 481-489.
- [48] Tayebi ,T. and A.J. Chamkha, Effects of various configurations of an inserted corrugated conductive cylinder on MHD natural convection in a hybrid nanofluid-filled square domain. *Journal of Thermal Analysis and Calorimetry*, 143(2) (2021) 1399-1411.
- [49] Khalili, R., E. Tavousi, R.B. Kazerooni, A. Noghrehabadi, and S. Taheripour, Lattice Boltzmann method simulation of nanofluid natural convection heat transfer in a square cavity with constant heat flux at walls. *Iranian Journal of Science and Technology, Transactions of Mechanical Engineering*, (2024) 1-16.



Chua Chaotic System Parameters Estimation using PSO Algorithm to increase its Dynamics

Hadda Ouguissi¹, Slami Saadi², Hibat errahmane Benmessaoud¹, Abdelaziz Rabehi^{3,*}

¹ Exact Sciences and Informatics Faculty, Djelfa University, Algeria,

ouguissi@gmail.com, hibaking@gmail.com

² Technology Faculty, Laghouat University, Algeria, s.saadi@univ-djelfa.dz

³ Telecommunications and Smart Systems Laboratory, University of Djelfa, PO Box 3117, 17000, Djelfa, Algeria, rab_ghi@hotmail.fr

*Corresponding author: (A. Rabehi), Email Address: rab_ghi@hotmail.fr

Abstract

In this article, we estimate the parameters of the Chua system using PSO optimization algorithm by exploiting the property of chaotic synchronization; in order to increase the chaotic dynamics and this is done by the modifications of the parameters of a nonlinear dynamical system to obtain optimal parameter values that result in the most chaotic system. Parameter estimation is formulated as a multidimensional optimization problem that aims to minimize the synchronization error between two chaotic systems. To verify the accuracy and robustness of the proposed algorithm in parameter estimation, a Chua system is simulated and comparison experiments are performed. Through the results obtained, the efficiency of the algorithm was efficient in the estimation of the parameters, where we obtained a more chaotic system at the estimated values.

Keywords: Chaos; Chua system; Estimation; PSO; Synchronization

<https://doi.org/10.63070/jesc.2025.009>

Received 02 April 2025; Revised 05 May 2025; Accepted 15 May 2025.

Available online 25 May 2025.

Published by Islamic University of Madinah on behalf of *Islamic University Journal of Applied Sciences*. This is a free open access article.

1. Introduction

The term "chaos" defines a particular state of a system whose behavior never repeats itself. There are several possible definitions of chaos [1], [2]. Due to the properties of chaotic systems, such as the very sensitivity of nonlinear systems to initial conditions and their parameters, a small change in the parameters of chaotic systems can lead to another system [3], [4]. Chaotic systems have been applied in various fields such as communication systems [4], assurance of a communication system increases with the high chaotic system randomness caused through the increase of the chaotic dynamics.

Parameter estimation for chaotic systems has become an important problem in last decades with the aim of increasing the dynamics of chaos. There are many parameter estimation methods, some researches have also estimated chaotic system parameters using synchronization based methods like feedback-based synchronization method and adaptive synchronization [6], [7].

Parameter estimation can be formulated as a multi-dimensional. Genetic Algorithm (GA) and Particle Swarm Optimization (PSO) algorithm are used to estimate the parameters of the chaotic Lorenz system [8], [9], [10], and Differential Evolution (DE) [11], and the Gravity Search Algorithm (GSA) [12] are adopted to estimate the parameters of the chaotic Lorenz system. PSO has been applied to estimate chaotic Lorenz systems parameters in a wide research range [13]. The parameter estimation method is based on the hybridization between the synchronization error and optimization algorithms, because the synchronization error is very sensitive to the chaotic system parameters. The smaller the synchronization error, the better is the parameters estimation. For this purpose, we minimize the synchronization error considered as an optimization problem.

In this article, we will apply the PSO algorithm to estimate parameters of the chaotic Chua system to minimize the synchronization error. This paper is organized as follows: In the first part, we address a brief introduction to the proposed PSO algorithm. In the second part, we present the problem of the estimation of the parameters by giving the mathematical formula. In the third part, we estimate the parameters of the Chua circuit, and in the fourth part, we present and discuss the simulation results, and finally we conclude this work by some deductions.

2. PSO Algorithm

PSO is a technique proposed by Kenndy and Aberhard in 1995 [14], which is inspired by the social behavior of animals moving in swarms. Authors in [15] have also given recent insight about PSO. This algorithm was found to be effective in solving the optimization problems characterized by their non-linearity and non-differentiation, multi-optima and high dimensionality through adaptation.

The PSO optimizes an objective function by performing a search based on the population P. The population is composed of potential solutions, called p-particles, initialized randomly and flying freely

in the multidimensional search space E . During the flight, the particles change their own positions $p(t)$ and speed $v(t)$ according to their own experiments where the cost of the function is optimal $f(t)$. Eventually, all the particles will gather around the global optimal solution \vec{G}_{best} . The motion of the particles between iteration t and $t+1$ is calculated using equations (1) and (2).

$$v_i(t+1) = wv_i(t) + c_1r_1(p_i(t) - x_i(t)) + c_2r_2(p_i(t) - x_i(t)) \quad (1)$$

$$x_i(t+1) = x_i(t) + v_i(t+1) \quad (2)$$

Where: w : Inertia Coefficient

c_1 et c_2 : correlation coefficients

r_1 et r_2 : uniformly distributed random numbers in $[0,1]$

3. Parametric Estimation Problem

Parameters estimation can be formulated as a nonlinear multidimensional optimization problem to minimize the objective function J for the parameter decision vector θ . The general scheme is shown in Fig.1. Consider the dynamical system of dimension n and parameters m :

$$\dot{x} = f(x, x_0, \theta) \quad (3)$$

Where:

$x \in R^n$ is the state vector with dimension n , x_0 initial state and $\theta \in R^m$ is the m dimension vector of system parameters. To estimate the following system parameters:

$$\hat{x} = f(\hat{x}, x_0, \hat{\theta}) \quad (4)$$

Where :

$\hat{x} \in R^n$: the state estimation vector with dimension n

x_0 : the initial state and $\hat{\theta} \in R^m$ is the system parameters estimation vector with dimension m .

The parameter estimation method is based on the synchronization error between the transmitter and the receiver because the synchronization error is very sensitive to the parameters of the chaotic system. For this reason, we minimize the synchronization error, which we consider as the objective function J representing the root mean square of the synchronization error.

$$J = \frac{1}{M} \sum_{k=1}^M \|x_k - \hat{x}_k\|^2 \quad (5)$$

M : the number of states

x_k : states of the master system

\hat{x}_k : states of the slave system

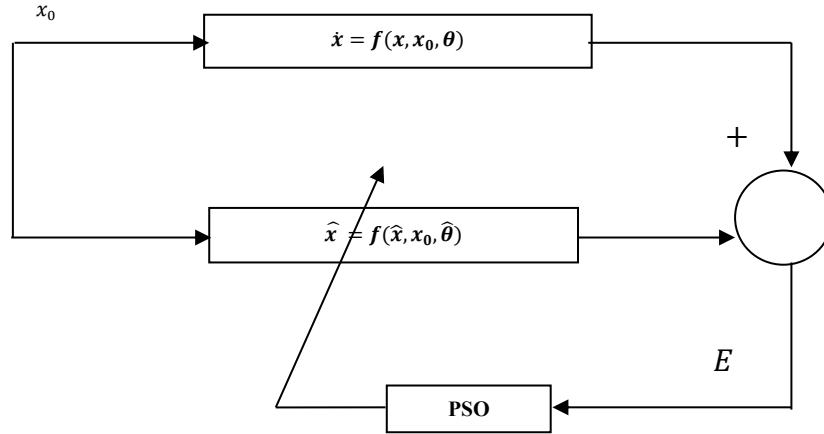


Figure 1. General Scheme of parameters estimation in chaotic systems

4. Application example

In this section, we apply PSO Algorithm in order to estimate the Chua Chaotic system parameters.

4.1 Chua System

Chua circuit is a simple electrical circuit that shows the classical behavior of Chaos theory [16], [17] and [18]. It has been presented by Leon O. Chua, an invited Professor at Waseda University in Japan. The proposed model is shown in figure Fig.2:

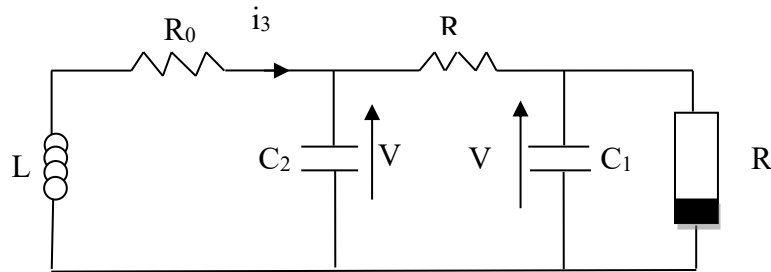


Figure 2. Chua Circuit

Chua system is represented by the set of differential equations:

$$\begin{cases} \dot{x} = \alpha(y - x - f(x)) \\ \dot{y} = x - y + z \\ \dot{z} = -\beta(x - R_0 z) \end{cases} \quad (6)$$

$$\text{Where: } f(x) = m_1 x + \frac{m_0 - m_1}{2} (|x + 1| - |x - 1|) \quad (7)$$

We will estimate the parameters α and β by the PSO optimization algorithm using the synchronization error between the transmitter and the receiver, because the synchronization error of chaotic systems is very sensitive to the parameters of the chaotic system. In this section we apply the synchronization technique theory of Pécora and Carroll between the two identical chaotic systems [19]. This

synchronization is based on the "Master-Slave" concept. A Slave signal is intended to faithfully reproduce the Master signal. The "Master" system is also called transmitter and the "Slave" system is called receiver.

The receiver is a system identical to the transmitter in addition to be a simple sub-tractor in order to successfully remove the chaotic masking. This scheme is based on sending a driving signal X_m , which is a simple addition between the transmitter output signal $y(t)$ and the message $m(t)$. The signal $s(t)$ is transmitted to the receiver through the transmission channel, assuming that only this channel is ideal, see Fig.3.

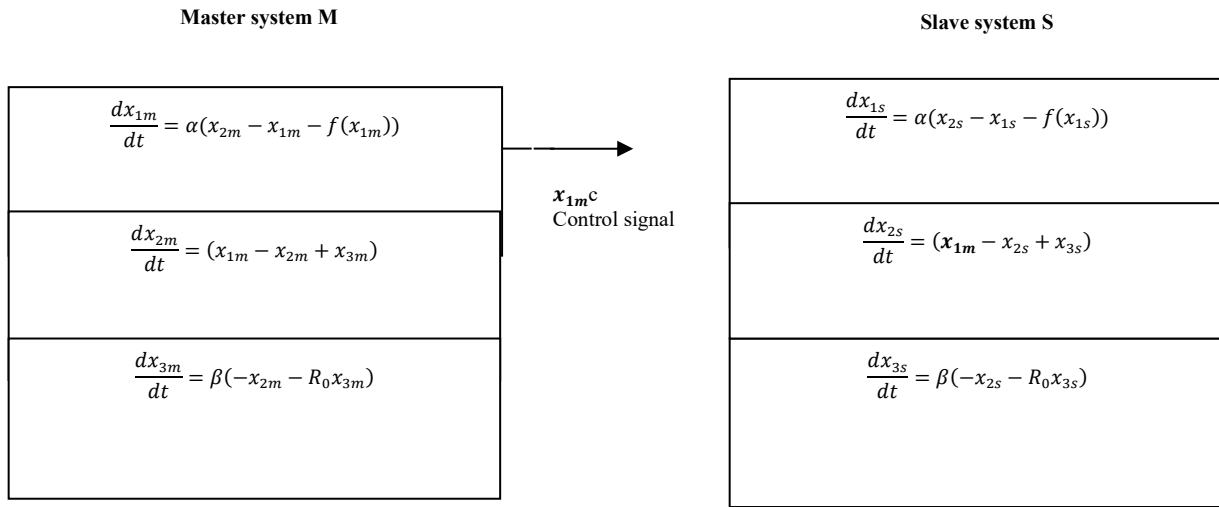


Figure 3. Pecora and Carroll synchronization method

Where:

x_m, y_m, z_m : master system state variables

x_s, y_s, z_s : slave system state variables

The synchronization is obtained when the error converges to zero in function with time tends to infinity, i.e.:

$$\lim_{t \rightarrow \infty} e(t) \quad \text{where} \quad e(t) = x_{s(k)}(t) - x_{m(k)}(t)$$

k is the state number

PSO Algorithms is used to optimize this objective function defined, as follows in (8), by the summation of the squared errors between master and slave systems [20-25]:

$$J = \frac{1}{M} \sum_{k=1}^M \|x_{sk} - x_{mk}\|^2 \quad (8)$$

5. Simulation Results

In this part, the performances of the proposed method will be evaluated by experimental tests using a computer PC with Windows 7, 32 bits and the Matlab-13 software. We estimate the Chaotic Chua system parameters by the PSO optimization algorithm and we will check the efficiency of this method by a comparison with GA and GOW algorithms.

In order to study the various modes or the different behaviors that can be shown by the Chua circuit, it is enough to modify one of the Chua circuit parameters values, where we take the parameter α as a bifurcation parameter. We performed simulations by varying the parameter α from 0 to 19, with an iteration step of 0.01, $28m_0 = -1.27$, $m_1 = -0.68$, and the initial conditions $(x_0, y_0 \text{ and } z_0) = (0.5, 1 \text{ and } -0.5)$. These presents different behaviours :

- ❖ For $\alpha = [0 \ 13]$, we notice that the behavior of the Chua circuit converges towards a periodic solution. In this case, the trajectory converges towards a cycle of order 2, see Fig.4(a).
- ❖ By increasing values of $\alpha = [13.5 \ 14]$, a new behavior converges to a periodic double solution with period doubling, see Fig.4(b).
- ❖ By increasing values of $\alpha = [14.3 \ 14.9]$, a new behavior converges to a quasi-periodic solution with period doubling, see Fig.4(b)
- ❖ For $\alpha = [15 \ 19]$, Chua's circuit behavior no longer represents an ordered structure. So, the system becomes chaotic as shown in Fig.4 (d).

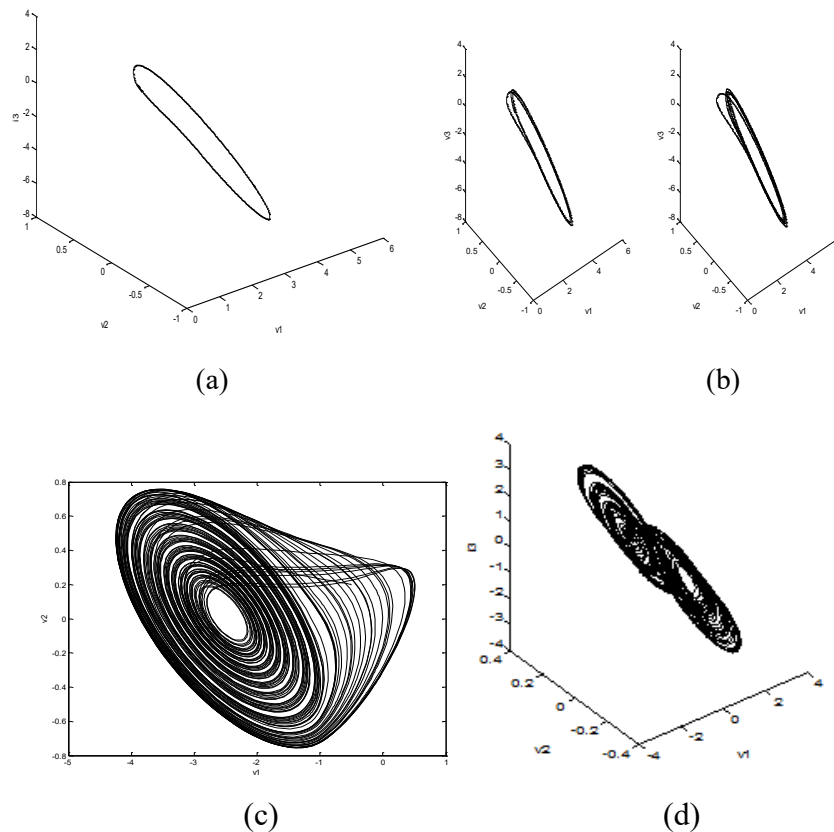


Figure 4. Chua circuit behaviour for different values of α

The different choices of PSO simulation parameters are given in Table.2, with time laps of 0.02 for 1000 steps. From the above, we will conclude that the Chua circuit parameters α and β which give the chaotic behavior of the Chua circuit lie in the approximate range of values $15 \leq \alpha \leq 19$ and $24 \leq \beta \leq 30$. From this and in order to increase the dynamics of chaos, we will estimate these parameters by the PSO algorithm. We choose PSO simulation algorithm parameters given in Table.2, with a time step of 0.02 for 1000 steps.

PSO is used to estimate the parameters $\theta = (\alpha, \beta)^T$ in a range around the real values of the parameters in a chaotic regime, the search ranges of the parameters are defined as follows:

$$14 \leq \alpha \leq 17 \text{ and } 26 \leq \beta \leq 30$$

- ❖ To estimate the parameter α , it is considered that the parameter β is known in advance with the original value. The initial assumptions for the control parameter α are in the range [14, 17].
- ❖ As before, and to estimate β parameter, we will only consider the variation on the parameter β and we assume α constant. Initial assumptions for the control parameter β are in the range [26,30].

The θ parameters were estimated using the PSO algorithm, where in each time we take three fine domains from the search range of α, β parameter values in a chaotic regime and we will make a comparison for the three versions of PSO.

We will run each algorithm 20 times and note the results obtained from the objective function J with the smallest population size. For each particle position (x) consists of m real numbers in the corresponding range, each individual of the population represents the possible solution of the objective function J minimization problem, which corresponds to the synchronization error of two master and slave systems in the chaotic mode as shown in Fig.3.

Tables 1 and 2 show the statistical values (best, maximum and minimum) of the estimated parameters α and β for each model of the PSO and GA algorithms.

Table 1. Statistical values of α parameter

Algorithm	α parameters		
	Best	Max	Min
PSO1/GA1	15.352	16.830	14.590
PSO2/GA2	15.800	16.530	14.550
PSO3/GA3	15.400	16.641	15.020

Table 2. Statistical values of β parameter

Algorithm	β parameters		
	Best	Max	Min
PSO1/GA1	27.820	29.513	26.950
PSO2/GA2	28.230	30.000	27.670
PSO3/GA3	27.950	28.130	26.653

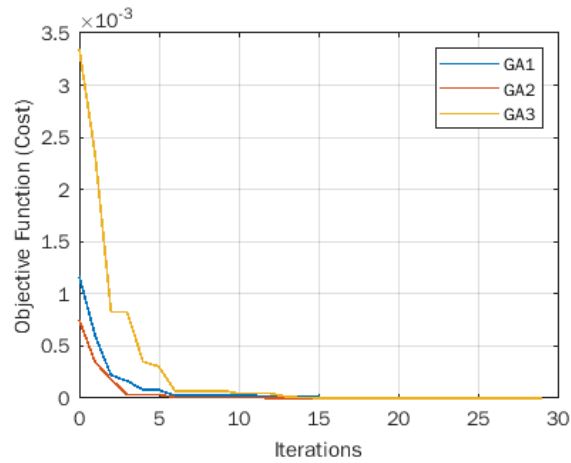


Figure 5. Objective function J evolution for α using GA (1-3) models

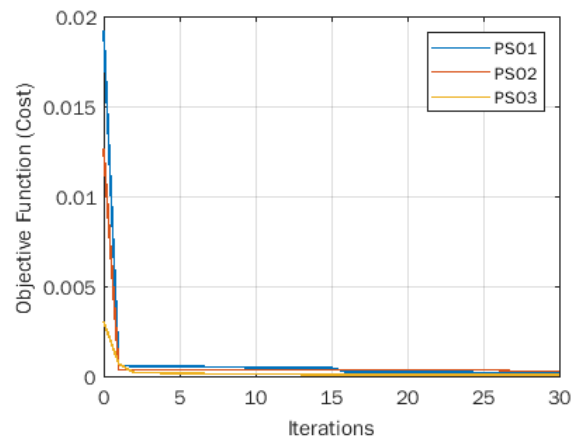


Figure 6. Objective function J evolution for α using PSO (1-3) models

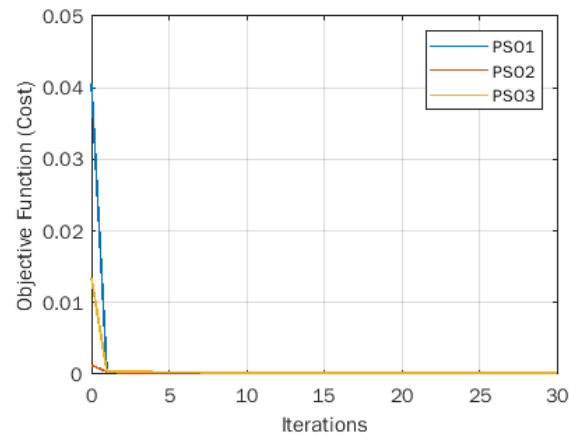


Figure 7. Objective function J evolution for β using PSO (1-3) models

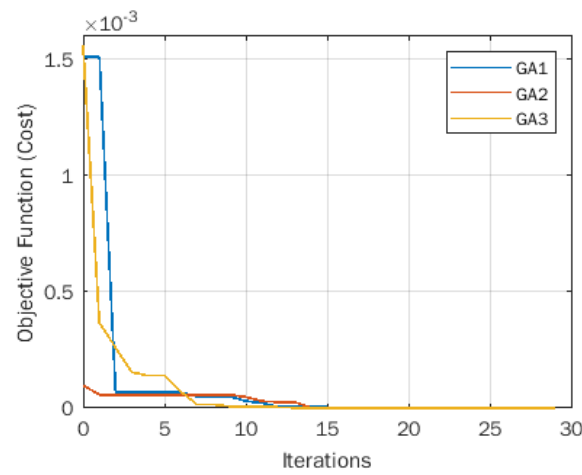


Figure 8. Objective function J evolution for β using GA (1-3) models

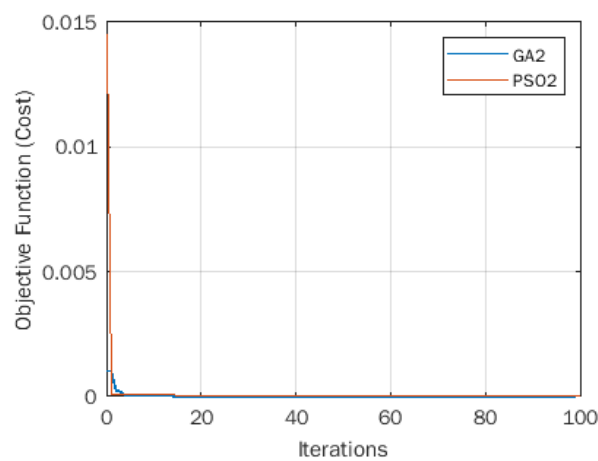


Figure 9. Objective function J evolution for $\alpha = 15.8, \beta = 28.23$

Figures: Fig.5, Fig.6, Fig.7, Fig.8 and Fig.9 show the objective function J evolution for the typical execution of the PSO(1-3) and GA(1-3) models with the values of the parameters α and β respectively.

We note that after few iterations, the best results (estimated values) are given by the PSO-2 model which offers the best values of the objective function quickly approaches the lowest value that tends to zero.

From the values estimated by PSO-2, $\alpha = 15.8, \beta = 28.23$, we notice that the chaotic dynamics is increased compared to the chaotic dynamics of the Chua system with the real parameters as shown in Fig.10.

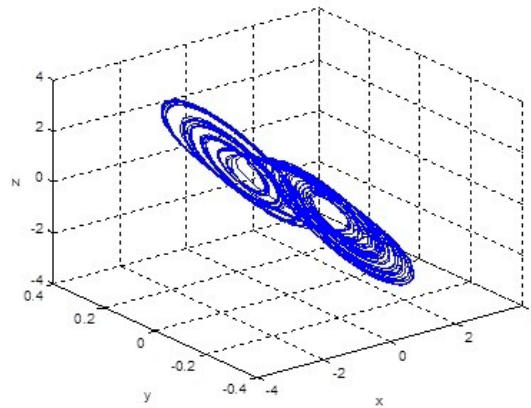


Figure 10. The new Chua chaotic system using the resultant estimated: $\alpha = 15.8, \beta = 28.23$

6. Conclusion

In this paper we have proposed and applied a PSO optimization algorithm to estimate the parameters of a chaotic Chua system. We considered the synchronization error between the master system and the slave system as an optimization problem, the performance of the PSO algorithm is compared to GA. The results of the simulation demonstrated that the proposed algorithm performs better than others in estimating the chaotic system parameters of Chua which increase the dynamics of chaos, in order to increase the security of communication systems in the event of chaos.

References

- [1] Lakshmanan, Muthusamy, and Shanmuganathan Rajaseekar. *Nonlinear dynamics: integrability, chaos and patterns*. Springer Science & Business Media, 2012.
- [2] Layek, G. C. *An introduction to dynamical systems and chaos*. Vol. 1. West Bengal, India: Springer India, 2015.
- [3] Shivamoggi, Bhimsen K. *Nonlinear dynamics and chaotic phenomena: An introduction*. Vol. 103. Springer, 2014.
- [4] Strogatz, Steven H. *Nonlinear dynamics and chaos: with applications to physics, biology, chemistry, and engineering*. Chapman and Hall/CRC, 2024.
- [5] Kaddoum, Georges. "Wireless chaos-based communication systems: A comprehensive survey." *IEEE access* 4 (2016): 2621-2648.

- [6] Nathasarma, Rahash, and Binoy Krishna Roy. "Parameter estimation of nonlinear systems with stable, chaotic and periodic behaviours at different initial conditions-a new approach." *2022 4th International Conference on Energy, Power and Environment (ICEPE)*. IEEE, 2022.
- [7] Li, Guohui, Ruiting Xie, and Hong Yang. "Dynamic analysis of the fractional-order Duffing-Van der Pol oscillator and its application extension." *Nonlinear Dynamics* 112.20 (2024): 17709-17732.
- [8] Gharehchopogh, Farhad Soleimanian, Isa Maleki, and Zahra Asheghi Dizaji. "Chaotic vortex search algorithm: metaheuristic algorithm for feature selection." *Evolutionary Intelligence* 15.3 (2022): 1777-1808.
- [9] Sattar, D., & Braik, M. S. (2023). Metaheuristic methods to identify parameters and orders of fractional-order chaotic systems. *Expert Systems with Applications*, 228, 120426.
- [10] Rizk-Allah, Rizk M., et al. "A Memory-Based Particle Swarm Optimization for Parameter Identification of Lorenz Chaotic System." *Proceedings of International Conference on Computing and Communication Networks: ICCCN 2021*. Singapore: Springer Nature Singapore, 2022.
- [11] Peng B, Liu B, Zhang FY, et al. "Differential evolution algorithm based parameter identification for chaotic systems". *Chaos, Solitons & Fractals* 2009;39(5):2110–8.
- [12] Kumar, Deepak, and Mamta Rani. "Alternated superior chaotic variants of gravitational search algorithm for optimization problems." *Chaos, Solitons & Fractals* 159 (2022): 112152.
- [13] B. Samanta, Senior Member , IEEE and C. Nataraj "particle Swarm Optimisation For Chaotic System Parameter Estimastion" 978-1-4244-2762-8/09/\$25.00 ©2009 IEEE.
- [14] Kano, Takeshi. "Review of interdisciplinary approach to swarm intelligence." *Journal of Robotics and Mechatronics* 35.4 (2023): 89
- [15] Sadiku, Matthew NO, et al. "Swarm intelligence." *A Primer on Multiple Intelligences* (2021): 211-222.
- [16] Sambas, Aceng, et al. "A novel chaotic system with two circles of equilibrium points: multistability, electronic circuit and FPGA realization." *Electronics* 8.11 (2019): 1211.
- [17] Corinto, Fernando, and Mauro Forti. "Memristor circuits: Bifurcations without parameters." *IEEE Transactions on Circuits and Systems I: Regular Papers* 64.6 (2017): 1540-1551.
- [18] Romero, Francisco J., et al. "Memcapacitor and meminductor circuit emulators: A review." *Electronics* 10.11 (2021): 1225.
- [19] Battiston, Federico, et al. "Networks beyond pairwise interactions: Structure and dynamics." *Physics reports* 874 (2020): 1-92.
- [20] Bentegri, Houcine, et al. "Assessment of compressive strength of eco-concrete reinforced using machine learning tools." *Scientific Reports* 15.1 (2025): 5017.
- [21] Mehallou, Abderrahmane, et al. "Optimal multiobjective design of an autonomous hybrid renewable energy system in the Adrar Region, Algeria." *Scientific Reports* 15.1 (2025): 4173.
- [22] Ladjal, Boumediene, et al. "Hybrid models for direct normal irradiance forecasting: A case study of Ghardaia zone (Algeria)." *Natural Hazards* 120.15 (2024): 14703-14725.
- [23] Belaid, Abdelfetah, et al. "High-Resolution Mapping of Concentrated Solar Power Site Suitability in Ghardaia, Algeria: A GIS-Based Fuzzy Logic and Multi-Criteria Decision Analysis." *IEEE Access* (2024).
- [24] Tibermacine, Ahmed, et al. "Comparative Analysis of SVM and CNN Classifiers for EEG Signal Classification in Response to Different Auditory Stimuli." *2024 International Conference on Telecommunications and Intelligent Systems (ICTIS)*. IEEE, 2024.
- [25] Mostefaoui, Mohammed, et al. "Enhanced Detection of EVA Discoloration Defects in Solar Cells Using Vision Transformers and Contrastive Learning." *2024 International Conference on Telecommunications and Intelligent Systems (ICTIS)*. IEEE, 2024.



Synergy of (L1, H2, H ∞) Norms for Nonlinear Optimal PEMFC Dynamic MIMO Model Reduction using a Novel ANN-BBO Approach

Zohra Touati ¹, Slami Saadi ², Hibat errahmane Benmessaoud ¹, Abdelaziz Rabehi ^{3,*}

¹ Exact Sciences and Informatics Faculty, Djelfa University, Algeria,

ztouati@gmail.com, hibaking@gmail.com

² Technology Faculty, Laghouat University, Algeria, s.saadi@univ-djelfa.dz

³ Telecommunications and Smart Systems Laboratory, University of Djelfa, PO Box 3117, 17000, Djelfa, Algeria, rab_ghi@hotmail.fr

*Corresponding author: (A. Rabehi), *Email Address:* rab_ghi@hotmail.fr

Abstract

In this work, we present an optimal reduced order nonlinear dynamic model for proton exchange membrane fuel cell (PEMFC) using the minimization of error between original and reduced order models via (L1, H2, H ∞) norms synergy optimized with biogeography-based optimization (BBO) Algorithm. The data necessary to form the autoregressive exogenous (ARX) artificial neural network (ANN) model are generated by the simulation of the dynamic model of the nonlinear PEMFC500w differential equations to extract space state matrices values. This approach is compared with Balanced Truncation (BT) model reduction method and illustrated through simulation results.

Keywords: Norms (L1, H2, H ∞); ANN; PEMFC; Order reduction; Balanced Truncation; Biogeography-based optimization.

<https://doi.org/10.63070/jesc.2025.010>

Received 24 March 2025; Revised 28 April 2025; Accepted 14 May 2025.

Available online 25 May 2025.

Published by Islamic University of Madinah on behalf of *Islamic University Journal of Applied Sciences*. This is a free open access article.

1. Introduction

Model order reduction intends to decrease the calculation difficulty such as reproduction of significant dynamical and control systems at the same time maintaining major performances of the original system. Specifically, the use of low order models lead to the following desired properties like simple design and analysis, computational advantage and simplicity of simulation. The first technique of model reduction is the model study by state space procedures presented by Davison in 1966 [1]. Moore in 1981 designed the theory of balancing, that directed to the well known technique of estimate by unbiased truncation [2]. Though, Moore's advance still endure from stability. Wilson in [3-4] employs an H_2 norm model reduction approach based on the minimization of the integral squared impulse response error among the complete and reduced order models. In 2006, Gugercin et al. [5] suggested an iterative rational Krylov approach (IRKA) for optimal H_2 model reduction. In 2010, Bunse-Gerstner et al. [6] proposed an H_2 optimal interpolation used for big size discrete dynamical multiple input, multiple output (MIMO) systems. Lately, Panda et al. [7] applied a particle swarm optimization Algorithm to achieve a reduced-order model of SISO complex linear structures. Also, Du et al. [8] employed a Genetic Algorithm to constrain H_2 model reduction technique intended to MIMO delay models. Fuel cells have become a very large field of research to be a new source of energy for several uses, varying from power generators to mobile applications due to their viability, efficiency and robustness. The proton exchange membrane fuel cell (PEMFC) technology is rapidly being developed. In this work, we want to make a complete assessment and comparison of ANN-BBO based approach and standard BT method for optimal model reduction of PEMFC500w system as a discrete MIMO complex model. Moreover, we consider hybrid (L_1 , H_2 and H_∞) criteria of our model reduction problems being studied to get a better compromised reduced model.

2. PEMFC 500W State-space Modelling

The fuel cell output voltage is an important part of its modeling. It is the potential of the cell obtained in an open circuit thermodynamic balance (without load). At normal conditions of pressure and temperature, the Nernst equation of the electrochemical reaction potential E_{cell} of one cell is given by [9]:

$$E_{cell} = E_0^{cell} + \frac{RT}{2F} \ln \left(\frac{P_{H_2} (P_{O_2})^{0.5}}{P_{H_2O}} \right) \quad (1)$$

where:

E_0 : Reference potential

R : Gas constant (8.3143 J/[mol K])

T : Fuel cell temperature (K)

F : Faraday constant (96487 C/mol)

P_{H₂} : hydrogen pressure (atm)

P_{O₂} : Oxygen pressure (atm)

P_{H₂O} : Water pressure (atm)

The open-circuit output voltage of the PEMFC is given as:

$$E_{o,FC} = n_s \cdot E_0^{Cell} + n_s \frac{RT}{2F} \ln \left(\frac{P_{H_2} (P_{O_2})^{0.5}}{P_{H_2O}} \right) \quad (2)$$

n_s is the number of cells

The PEMFC dynamics is characterized by non-linear differential equations converted into state-space representation [9]. The net mole flow of oxygen, hydrogen and water at the cathode and at anode correspondingly is given by [10]:

Let : $x_1 = (m_{O_2})_{net}$, $x_2 = (m_{H_2})_{net}$ and $x_3 = (m_{H_2O})_{net}$

$$\dot{x}_1 = \left(\frac{-1}{\lambda_c} \right) x_1 + \left(\frac{1}{4\lambda_c F} \right) I \quad (3)$$

$$\dot{x}_2 = \left(\frac{-1}{\lambda_A} \right) x_2 + \left(\frac{1}{4\lambda_A F} \right) I \quad (4)$$

$$\dot{x}_3 = \left(\frac{-1}{\lambda_c} \right) x_3 + \left(\frac{1}{4\lambda_c F} \right) I \quad (5)$$

The dynamic equations of the partial pressure of hydrogen and oxygen, and the rate of change of the fractional pressure of water is written based on an ideal gas law $P.V = n.R.T$ as [11]:

Let: $x_4 = T$, $x_5 = P_{H_2}$, $x_6 = P_{O_2}$ and $x_7 = P_{H_2O}$

$$\frac{dP_{H_2}}{dt} = \left(\frac{RT}{V_a} \right) (m_{H_2})_{in} - \left(\frac{RT}{V_a} \right) \cdot (m_{H_2})_{out} - \left(\frac{RT}{V_a} \right) \frac{I}{2F} \quad (6)$$

Therefore, we have:

$$\dot{x}_5 = 2 \cdot \theta_1(x_4) u_{pA} - 2\theta_1(x_4) \cdot x_5 - \theta_2(x_4) \cdot I \quad (7)$$

Where:

$$\theta_1(x_4) = \left(\frac{R \cdot (m_{H_2O}) \cdot x_4}{V_a \cdot (P_{H_2O})} \right) \theta_2(x_4) = \left(\frac{R x_4}{2V_a F} \right)$$

Similarly, the partial pressure of oxygen dynamic equation can expressed as: $n_s \cdot E_0^{Cell}$

$$\dot{x}_6 = 2 \cdot \theta_3(x_4) u_{pC} - 2\theta_3(x_4) \cdot x_6 - \theta_4(x_4) \cdot I \quad (8)$$

Where:

$$\Theta_3(x_4) = \left(\frac{R \cdot (m_{H_2O})_m^c \cdot x_4}{V_c \cdot (P_{H_2O})_m^c} \right) \Theta_4(x_4) = \left(\frac{R x_4}{2V_c F} \right)$$

Similarly The rate of water partial pressure variation is given as:

$$\dot{x}_7 = 2 \cdot \Theta_5(x_7) x_4 + 2 \Theta_4(x_4) \cdot I \quad (9)$$

Where :

$$\Theta_5(x_7) = \left(\frac{R \cdot (m_{H_2O})_{in}^c (P_{H_2O}^{in} - x_7)}{V_c \cdot (P_{H_2O})_n^c} \right)$$

The net raise in the PEMFC temperature of the assembly is given by:

$$\dot{x}_4 = \frac{1}{M_{fc} C_{fc}} (\dot{x}_8 - \dot{x}_9 - \dot{x}_{10}) \quad (10)$$

Where: M_{fc} is Total mass of PEMFC stack (kg)

C_{fc} is Specific heat capacity of PEMFC stack [J/(mole.K)]

$$\dot{x}_8 = \Theta_6(x_4, x_5, x_6, x_7) \cdot I \quad (11)$$

Where:

$$\begin{aligned} \Theta_6(x_4, x_5, x_6, x_7) &= \left[n_s \frac{\Delta G^0}{2F} - \frac{n_s R x_4}{2F} \ln \left(\frac{x_5 \cdot x_6^{0.5}}{x_7} \right) \right] \\ \dot{x}_9 &= \Theta_7(x_4, x_5, x_6, x_7) \cdot I \end{aligned} \quad (12)$$

With I is stuck current:

$$\begin{aligned} \Theta_7(x_4, x_5, x_6, x_7) &= n_s \left[E_0^{Cell} + \frac{R x_4}{2F} \ln \left(\frac{x_5 \cdot x_6^{0.5}}{x_7} \right) - V^{Act} - V^{Conc} - V^0 \right] \\ \dot{x}_{10} &= [h_s n_s A_s] \cdot x_4 - [h_s n_s A_s] \cdot u_{TR} \end{aligned} \quad (13)$$

Replacing equations (2.11), (2.12) and (2.13) into equation (2.10), we can get :

$$\dot{x}_{11} = \left[\frac{-h_s n_s A_s}{M_{fc} C_{fc}} \right] \cdot x_4 - \Theta_7(x_4, x_5, x_6, x_7) I + \left[\frac{-h_s n_s A_s}{M_{fc} C_{fc}} \right] \cdot u_{TR} \quad (14)$$

$$\text{Where: } \Theta_8(x_4, x_5, x_6, x_7) = n_s \left[\frac{2}{M_{fc} C_{fc}} E_0^{Cell} + \frac{R x_4}{F M_{fc} C_{fc}} \ln \left(\frac{x_5 \cdot x_6^{0.5}}{x_7} \right) - V^{Act} - V^{Conc} - V^0 \right]$$

In general, the state space model of the PEMFC system is given as:

$$\begin{cases} \dot{x}(t) = A(\theta) \cdot x(t) + B(\theta) \cdot u(t) + K(\theta) \cdot w(t) \\ y(t) = C(\theta) \cdot x(t) + v(t) \\ x_0(t) = x_0 \end{cases} \quad (15)$$

$\dot{x}(t)$ are states of system, $u(t)$ and $y(t)$ are input, output of system correspondingly, $w(t)$ is the disturbance input, $v(t)$ is the measurement noise, A the state matrix, B the input matrix, C the output matrix and K the disturbance matrix.

3. PEMFC ARX -ANN Modelling

For modeling the nonlinear states equations of a PEM500W fuel cell using ANN, we propose an identification approach for identifying dynamic system model from measured input-output data. To represent nonlinear system dynamics, we can estimate nonlinear autoregressive exogenous (ARX) models with tree-partition network. ARX models describe nonlinear structures using a parallel combination of nonlinear and linear blocks [12]. The nonlinear and linear functions are expressed in terms of variables called regressors. Several nonlinear estimators can be used such as wavelet network, sigmoid network, tree partition, custom network, and neural network. In this study, the performance of tree partition estimators is chosen due to the simplicity of its structure.

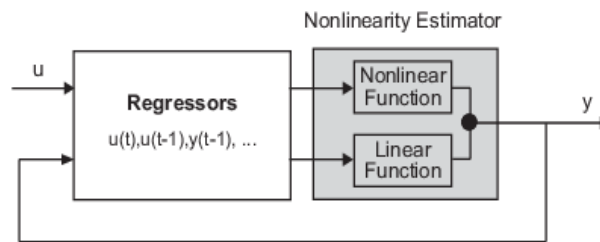


Figure 1. Structure of Nonlinear ARX Models

The output of the nonlinear model was computed by regressor values from the past and current input and past output data such as $u(t), u(t-1), \dots, y(t), y(t-1)$. In Figure 1, the block of nonlinearity estimator can include linear and nonlinear blocks in parallel as:

$$F(x) = L^T(x - r) + d + g(Q(x - r)) \quad (16)$$

Where x is the regression vector, r is the mean of the regressor x . $(L^T(x) + d)$ is the block linear function output and d is a scalar offset. $g(Q(x - r))$ represents the output of the nonlinear function block. Q is a projection matrix that makes the calculations well conditioned. The exact form of $F(x)$ depends on the choice of the nonlinearity estimator.

4. Optimal hybrid (L_1 , H_2 , H_∞) norms-based model reduction

4.1 Problem statement

The purpose of model order reduction is to replace a large model by a smaller one, which preserves the essential behavior of the original model. For the systems considered in this work, it can be stated as follows: we have a state space model with identifiable coefficients (a disturbance element) given by the matrix K with initial state values given by the vector x_0 and with sample time T_s .

The discrete time state-space model of a system with input vector u , output vector y , and disturbance e takes the following equation [13]:

$$\Sigma_N: \begin{cases} x_N(k+1) = A_N x(k) + B_N u(k) + K_N e(k) \\ y(k) = C_N x(k) + D u(k) + e(k) \\ x(o) = x_0 \end{cases} \quad (17)$$

Where $A_N \in \mathbb{K}^{N \times N}$ is the state matrix, $B_N \in \mathbb{K}^{N \times m}$, $C_N \in \mathbb{K}^{p \times N}$ and $K_N \in \mathbb{K}^{N \times m}$. The vectors $x(k) \in \mathbb{K}^N$, $u(k) \in \mathbb{K}^m$ and $y(k) \in \mathbb{K}^p$ represent the state, the input and the output of the discrete-time dynamical system, respectively. Often, the order N of the system is too big for solving various control, simulation and optimization problems. The aim of model order reduction is to construct a reduced order system:

$$\Sigma_n: \begin{cases} x_n(k+1) = A_n x(k) + B_n u(k) + K_n e(k) \\ y(k) = C_n x(k) + D u(k) + e(k) \\ x(o) = x_0 \end{cases} \quad (18)$$

Where $A_n \in \mathbb{K}^{n \times n}$, $B_n \in \mathbb{K}^{n \times m}$, $K_n \in \mathbb{K}^{n \times m}$, $C_n \in \mathbb{K}^{p \times n}$ and $n \ll N$,

The quality of this estimation is measured by the error between original system and reduced order system, i.e.:

$$\|\Sigma_N - \Sigma_n\| < \varepsilon \quad (19)$$

For a specified precision and a appropriate norm.

4.2 Biogeography Based Optimization (BBO)

The biogeography based optimization (BBO) Algorithm is a new evolutionary algorithm originated by biogeography. As its name involves, the BBO algorithm has been inspired by biogeography [14-20]. The BBO algorithm imitates relations linking diverse types (habitants) situated in diverse habitats in terms of migration, evacuation, and transformation. In reality, this algorithm reproduces the progress of environment, considering movement and transformation among diverse physically alienated areas towards a stable state.

Commonly talking, the ideas of the explore procedure of BBO are the same to those of further evolutionary algorithms, in which a set of arbitrary solutions is initially created. Subsequently, the

primary arbitrary solutions are assessed through a fitness function and after that progresses over a predefined number of iterations. The BBO algorithm is extremely like GA. Exploration agents in BBO, labeled habitats, work equally to chromosomes in GA.

These regulation habitats, labeled habitants, are comparable to genes in GA. The related fitness cost for every habitat in BBO is called the Habitat Suitability Index (HSI). Depending on the HSI of habitats, the habitants are capable to travel starting from a location to another one. In other terms, habitats can progress based on their HSI as:

1. Habitants existing in habitats with elevated HSI are further probable to immigrate to habitats with small HSI.
2. Habitants situated in low-HSI habitats are further flat to let movement of new habitants from habitats with high HSI.

In the BBO algorithm, every habitat is given three rates: immigration (λ_k), emigration (μ_k), and mutation. These rates are determined based on the number of habitants as below:

$$\mu_k = \frac{E \times n}{N} \lambda_k = I \times \frac{1 - n}{N}$$

Where n is the habitant number, N is the highest amount of habitants, E is the greatest emigration speed, and I designates the greatest immigration speed. Figure.2 shows emigration and immigration rates. It demonstrates that the probability of emigration is in relation with the number of habitats. Also, the immigration probability is inversely relative to the number of habitats. The mutation rate of BBO is furthermore a function of the number of habitants and given by:

$$m_n = M \times \left(1 - \frac{p_n}{p_{max}}\right) \quad (20)$$

Where M is an initial value for mutation defined by the user, p_n is the mutation probability of the n -th habitat, and $p_{max} = \arg \max(p_n)$, $n=1,2,\dots,N$ and $p_{max} = \arg \max(p_n)$, $n=1,2,\dots,N$.

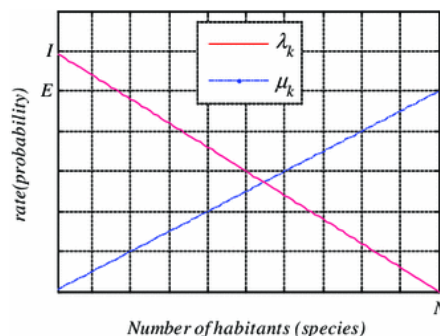


Figure 2. Emigration (μ_k) and immigration (λ_k) curves

To resume, the BBO algorithm can be presented as follows:

1. Define the migration probability and mutation probability;
2. population initialization;
3. R_i and R_e calculation of all candidate through the population;
4. Modification of the selected islands based on the immigration rate;
5. Choice of the island from which the HSI is to be emigrated based on the emigration rate.
6. Randomly select an HSI from the chosen island at step5.
7. Mutation based on each island mutation probability;
8. The objective function computation for each individual island. If the objective function is not fulfilled, go to step three.

4.3 BBO based model order reduction

In this paper, PEMFC500w model reduction problem is investigated using BBO Algorithm, minimizing the hybrid (L_1 , H_2 , H_∞) norm.

$$\text{Let: } E(z) = G_N(z) - G_n(z) \quad (21)$$

Using different norms leads to diverse approximations since diverse norms desire diverse characteristics of the system. Though, it is sometimes attractive to get a decreased order model by means of some attractive characteristics that might not be attainable through using a particular norm only. Hence, we propose the next hybrid norm condition to get improved compromised reduced order models [21]:

$$\|E\|_{\text{hybrid}} = \alpha \|E\|_2 + \beta \|E\|_\infty + \gamma \|E\|_{L1} \quad (22)$$

where β and γ are constants

Then the H_2 norm is defined as:

$$\|E\|_2 = \left\{ \frac{1}{2\pi} \sum_1^\infty |E(k)|^2 \right\}^{1/2} \quad (23)$$

And the H_∞ norm is defined as:

$$\|E\|_\infty = \max |E(k)| \quad (24)$$

The H_{L1} norm is given by:

$$\|e\|_{L1} = \sum_0^\infty |y_N(k) - y_n(k)| \quad (25)$$

Where $e(k)$ is the impulse response difference between the original system and the reduced system:

$$e(k) = y(k) - y_n(k) \quad (26)$$

5. Simulation Results

The parameters of the used PEMFC model are specified in the following Table 1. A nonlinear state space model of the PEMFC, developed previously, is simulated in MATLAB software.

Table 1. Parameters of the PEMFC Model [10]

$A_s = 3.2.10^{-2} \text{ m}^2$	$M_f = 44 \text{ kg}$
$a = -3.0810^{-3} \text{ V/K}$	$(m_{H_2O})_{in}^a = 8.614.10^{-5} \text{ mol/s}$
$a_0 = 1.3697 \text{ V}$	$(m_{H_2O})_{in}^c = 8.614.10^{-5} \text{ mol/s}$
$b = 9.72410^{-5} \text{ V/K}$	$n_s = 48$
$C_k = 500 \text{ J(moLK)}$	$(P_{H_2O})_{in} = 2 \text{ atm}$
$C = 10 \text{ F}$	$R = 8.31 \text{ J/(mol/K)}$
$E_0^{\text{Cell}} = 1.23 \text{ V}$	$R_c^0 = 0.28\Omega$
$e = 2$	$V_a = 10^{-3} \text{ m}^3$
$F = 96487 \text{ C/mol}$	$V_c = 10^{-3} \text{ m}^3$
$\Delta G^0 = 2372.10^3 \text{ J/mol}$	$\lambda_A = 60 \text{ s}$
$h_s = 37.5 \text{ W/(m}^2\text{K)}$	$\lambda_c = 60 \text{ s}$
$K_I = 1.87.10^{-3} \Omega/\text{A}$	$(P_{H_2O})_{in}^a = 1 \text{ atm}$
$K_T = -237.10^{-3} \Omega/\text{K}$	$(P_{H_2O})_{in}^c = 1 \text{ atm}$

In order to find the V - I characteristics of the PEMFC, the model is simulated via nonlinear state space equations with input variables: $u_{pa} = 60 \text{ atm}$, $u_{pc} = 30 \text{ atm}$ and $u_T = 308 \text{ K}$. Figures 3 and 4 show the results close match to simulation results obtained by the experimental results of the *Avista Labs SR-12* (500W) PEMFC stack in [11]. The output voltage response of the PEMFC model is presented in Figure 3. The output voltage diminishes from about 38.43 to 25.88 volts.

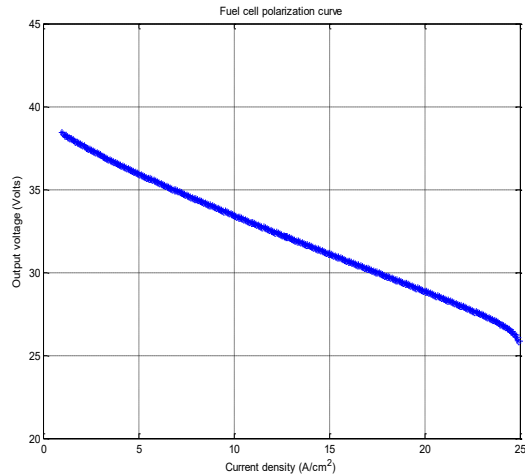


Figure 3. V-I Characteristics of the PEMFC Model

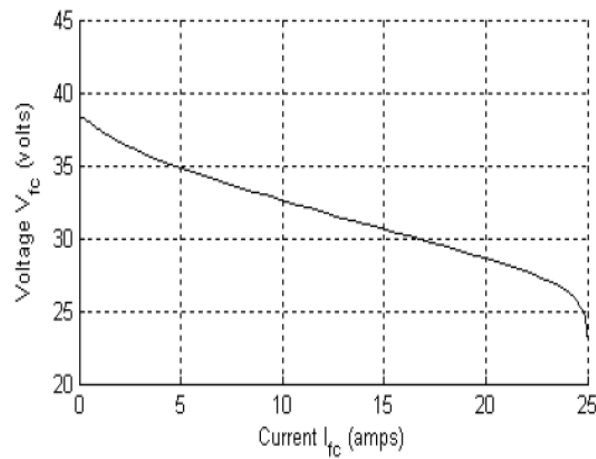


Figure 4. Experimental results of the Avista Labs SR-12 (500W)

The P - I characteristics of the PEMFC model are given in Figure 5. The maximum output power is attained at a position near to the rated current of the fuel cell (25A), but not precisely at the rated current. The PEMFC leaves in the concentration area close to the rated current value, where the output power decreases with the rising load current owing to the potential decline in the PEMFC's output voltage.

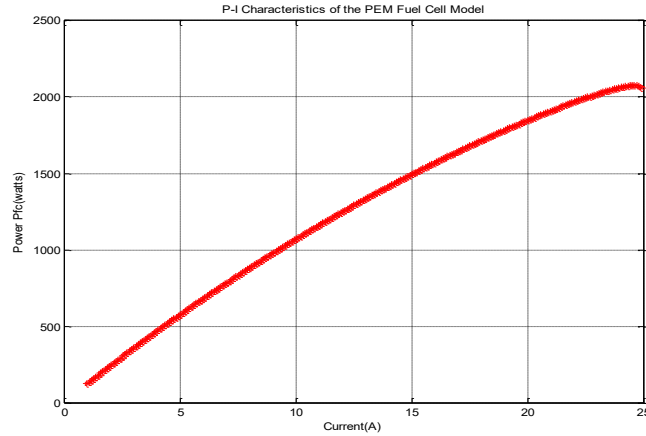


Figure 5. P-I Characteristics of the PEM Fuel Cell Model

After nonlinear equations simulation step of a 500-W proton exchange membrane (PEM) fuel cell, in order to get the voltage and current outputs, we identified a dynamic system model from measured input-output data using nonlinear ARX models with tree-partition network. Then we linearized this model to get a state space model with identifiable coefficients (a disturbance element) given by the matrix K with initial state values given by the vector X and with sample time $T_s = 0.2$.

$$A_d = \begin{bmatrix} 0.9004 & 0 & -0.2470 & 0 & -0.5076 & -0.5076 & 0.3498 & 0.3498 \\ 0.2859 & 0 & -0.4406 & 0 & 1.1560 & 1.1560 & -0.7268 & -0.7268 \\ 10 & 0 & 0 & 0 & 0 & 0 & 0 & 0 \\ 0 & 1 & 0 & 0 & 0 & 0 & 0 & 0 \\ 0 & 0 & 0 & 0 & 0 & 0 & 0 & 0 \\ 0 & 0 & 0 & 0 & 0 & 0 & 0 & 0 \\ 0 & 0 & 0 & 0 & 10 & 0 & 0 & 0 \\ 0 & 0 & 0 & 0 & 0 & 10 & 0 & 0 \end{bmatrix}$$

$$B_d = [0 \ 0; 0 \ 0; 0; 0; 0; 1 \ 0; 0 \ 1; 0 \ 0; 0 \ 0];$$

$$C_d = [0.9004 \ 0 \ -0.2470 \ 0 \ -0.5076 \ -0.5076 \ 0.3498 \ 0.3498; \\ 0.2859 \ 0 \ -0.4406 \ 0 \ 1.1560 \ 1.1560 \ -0.7268 \ -0.7268]$$

$$D_d = [0 \ 0; 0 \ 0]$$

$$K_d = [1 \ 0; 0 \ 1; 0 \ 0; 0 \ 0 \ 0; 0 \ 0; 0; 0 \ 0]$$

$$X_d = [0; 0; 0; 0; 0; 0; 0; 0]$$

$$\text{Eigen values: } \lambda_1 = 0, \lambda_2 = 0, \lambda_{3,4} = 0.4502 \pm 0.2104i, \lambda_5 = 0, \lambda_6 = 0, \lambda_7 = 0, \lambda_8 = 0$$

With the parameters of the BBO Algorithm utilized are: population size=100, the initial population of candidate solutions is generated randomly, mutation probability is set to 0.04, the number of nodes HSI is 20, the maximum immigration (λ) and emigration (μ) rates are 0.75 and 0.75. The termination

criterion is a function evaluation limit set at 10^{-20} attained at 600 runs; the temporary population is so that all emigrating variables may initiate from the population that is put at starting of the generation.

Hence, the results of (L_1, H_2, H_{inf}) hybrid norm model reduction with $\alpha = \beta = \gamma = 1$:

Ar = [0.21106 0.044441 0.14361; 1.3189 -0.3388 0.89948; -0.36742 -0.19781 -0.089514]

Br = [0.60513 0.96219; 0.0028169 -0.052779; 0.72425 -0.013944]

Cr = [-0.54119 -0.04784 -0.20932; 1.1679 -0.67317 0.62251]

Dr = [-0.014372 -0.0018601; 0.0086205 -0.011826]

Kr = [0.12484 2.5473; 0.71806 -2.6324; 0.16301 -0.68393]

xr(0) = [3.0308; -1.6829; 0.18331]

Eigenvalues: $\lambda_1 = -0.1938$, $\lambda_{2,3} = -0.0117 \pm 0.3276i$

Table 2 shows the results comparison of the different the relative norms of model error obtained by ANN-BBO and BT approaches with model order reduction $n=3$:

Table 2. Comparison of the relative norms of error systems obtained by ANN-BBO and BT approaches

norms	ANN-BBO	BT method
H ₂ norm	0.0587	0.0837
H _{inf} norm	0.0493	0.0656
L ₁ norm	L ₁ _Norm(:,1) = [0.2862 0.0456]	L ₁ _Norm(:,1) = [0.2282 0.0786]
(L ₁ , H ₂ , H _{inf})	L ₁ _Norm(:,2) = [0.2306 0.3942 0.1536]	L ₁ _Norm(:,2) = 0.2282
hybrid norm	hybrid norm(:,1) = [0.3776 0.2279]	hybrid norm(:,1) = [0.3776 0.2279]
	hybrid norm(:,2) = [0.3385 0.1626]	hybrid norm(:,2) = [0.3776 0.2279]

To better evaluate the quality of approximants, we trace the temporal responses in Figures 6-9 blow, and the frequency responses in Figures 10-11 for PEMFC500W original system and the reduced order model by the ANN-BBO approach and BT method of dimension $n=3$.

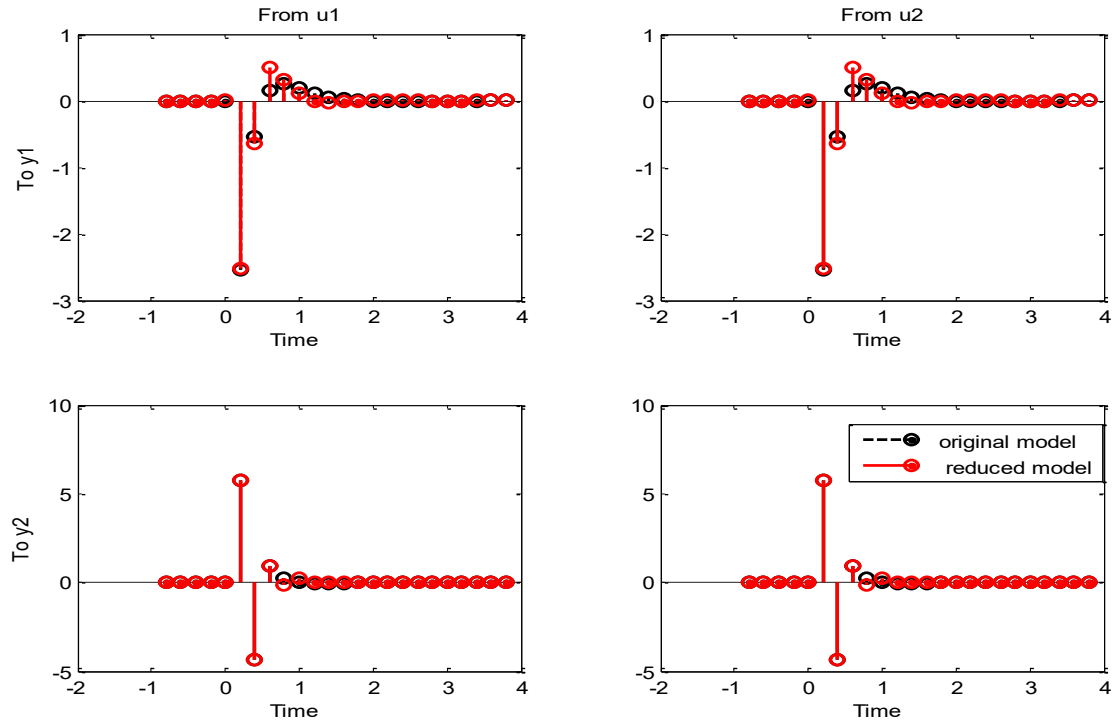


Figure 6. Impulse response by BT approach

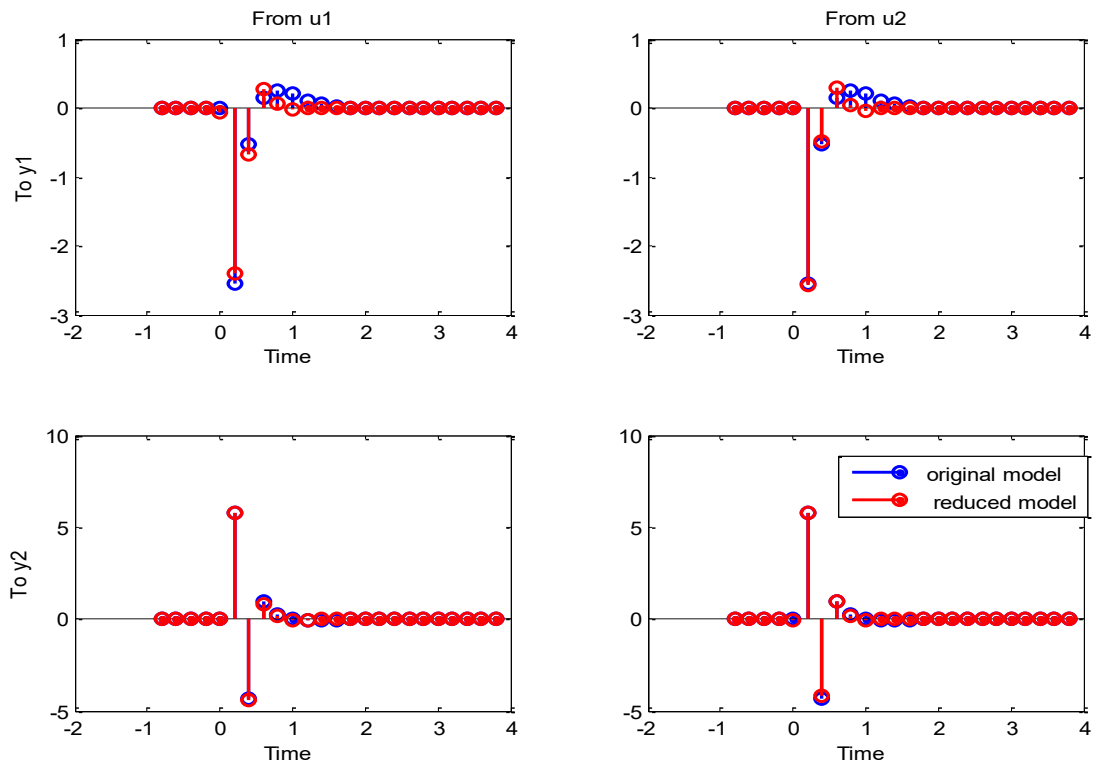


Figure 7. Impulse response by ANN-BBO approach

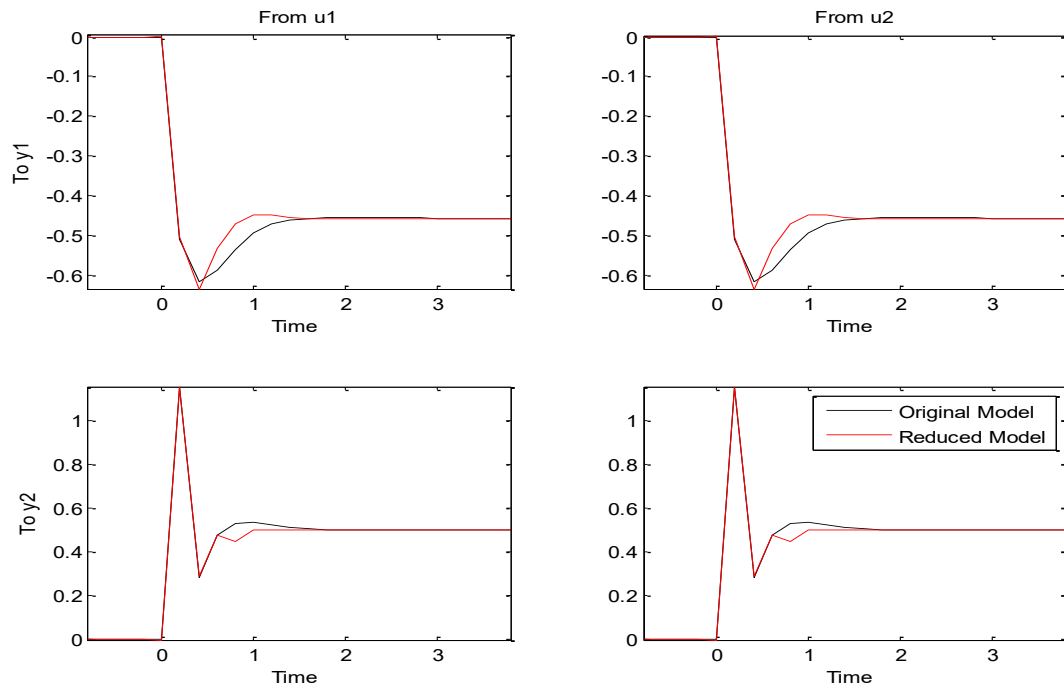


Figure 8. Step response by BT approach

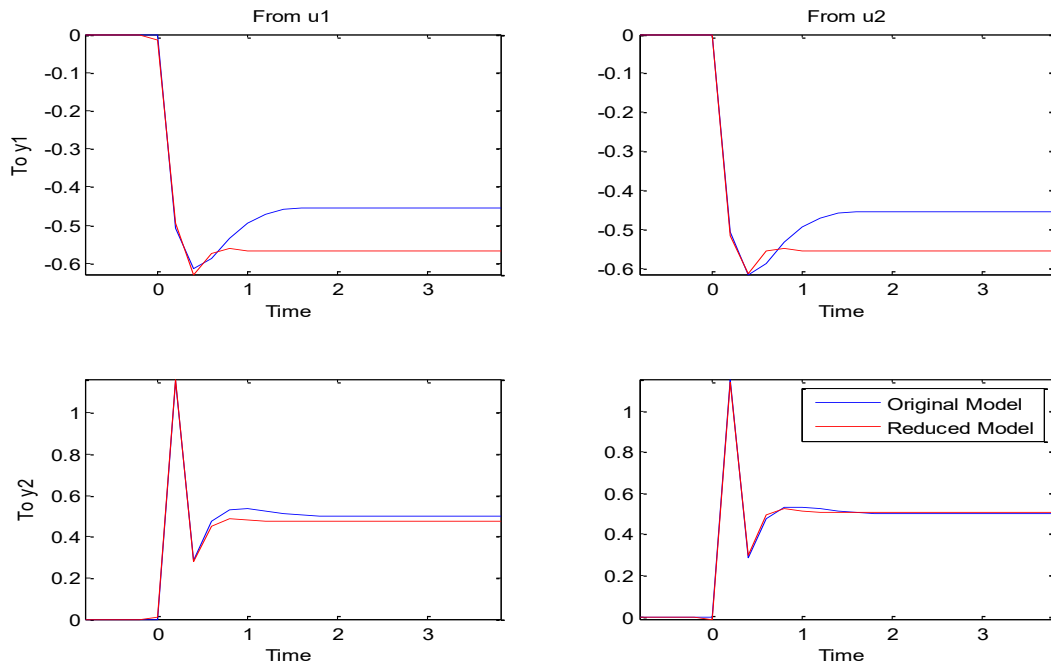


Figure 9. Step response by ANN-BBO approach

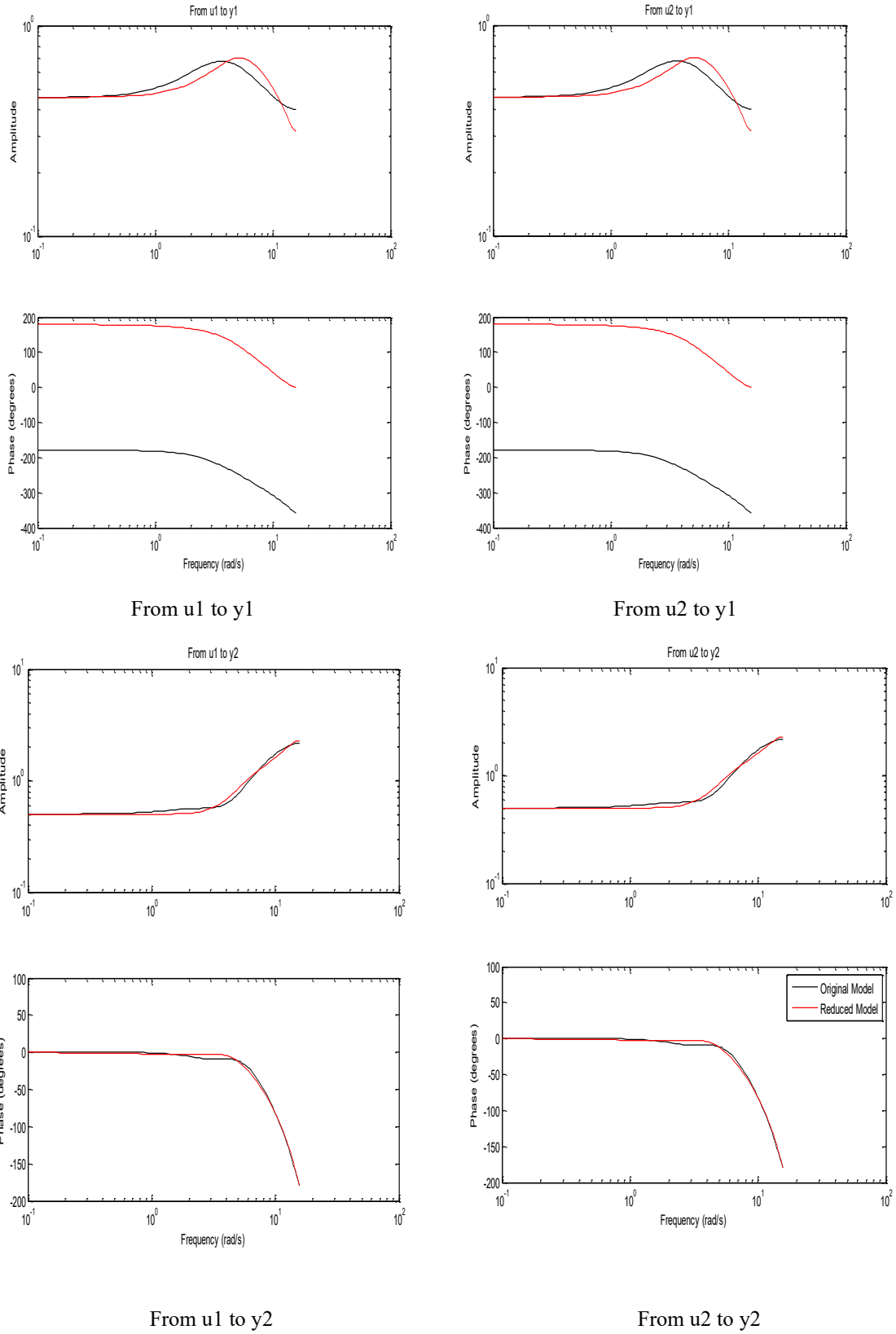


Figure 10. Frequency response by BT approach

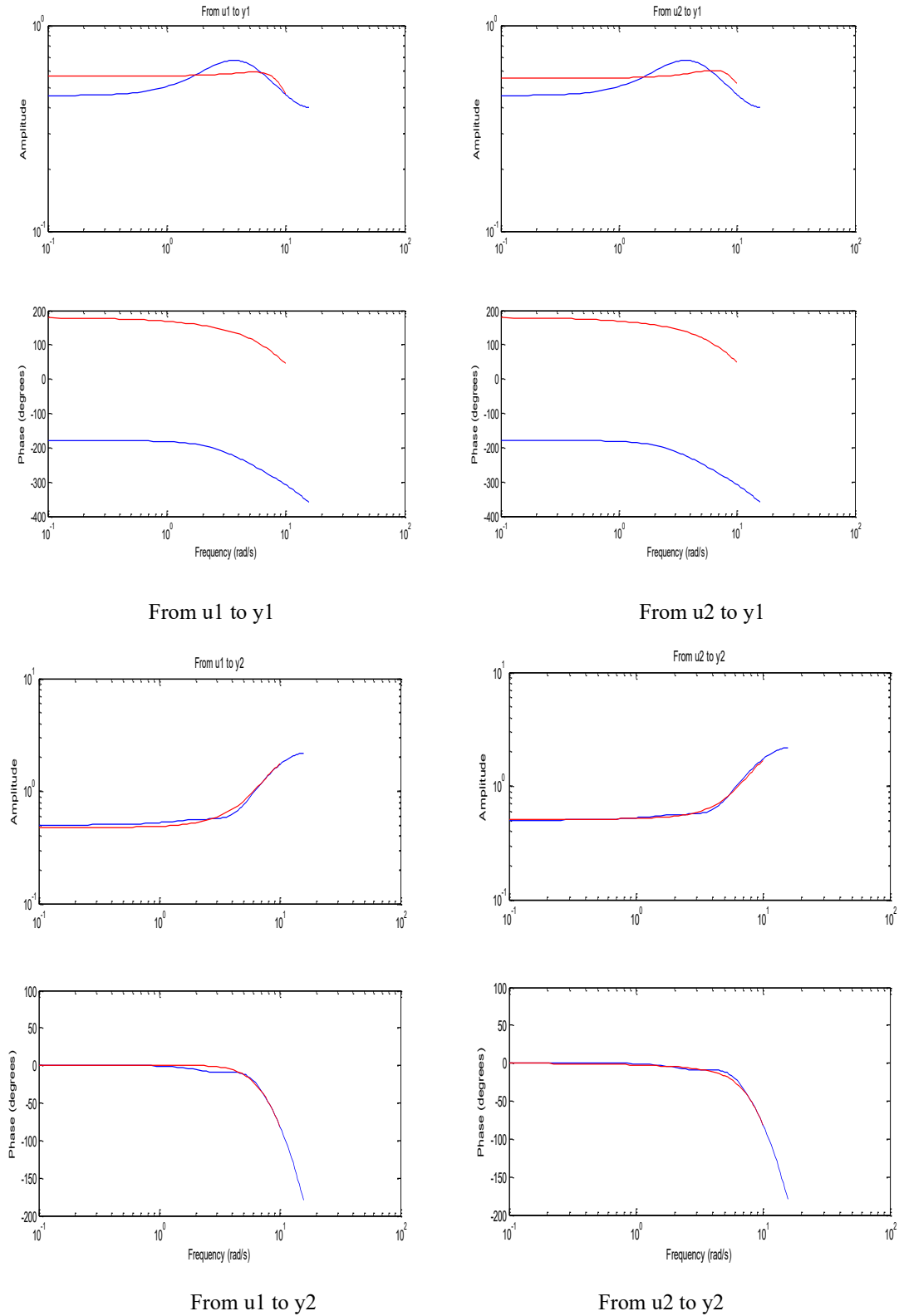


Figure 11. Frequency response by ANN-BBO approach

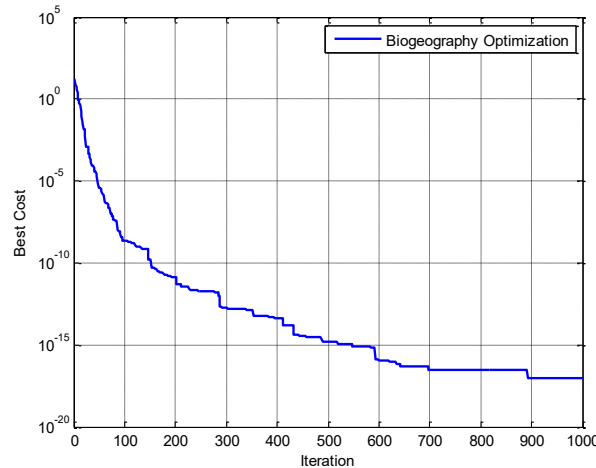


Figure 12. Objective function evolution with runs

We observe in Table.2 that the relative error norms of H_2 -norm and H_{inf} - norm systems obtained by ANN-BBO approach are better than those obtained by BT method. But results are different in cases: L_1 -norm and hybrid (L_1, H_2, H_{inf}) norms, in which, we find BT method in first output with inputs of hydrogen and oxygen pressures better than ANN-BBO approach. In the contrary, results in the second output show better performance of ANN-BBO approach compared to BT method.

Figures. 6–11 illustrate the impulse responses, step responses and frequency responses of all models, correspondingly. Notice that the impulse responses of the reduced-order model via ANN-BBO is greatly close to those of the original model than using BT method for all outputs. While in step responses, the first output of the reduced-order model by BT method match those of the original model than ANN-BBO approach. The frequency response comportment of the reduced-order model by BT method strictly look like that of the original model than ANN-BBO approach with a little error at elevated frequencies. On the other hand, because the majority of physical systems function at low frequencies, this elevated frequency error can be unobserved. Evolution of system error represented by an objective function minimized by BBO algorithm is illustrated in Figure 12.

6. Conclusion

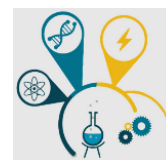
We have studied in this paper an optimal order reduction of complex MIMO nonlinear dynamic model of PEMFC via (L_1, H_2, H_{∞}) norms synergy optimized with biogeography based optimization (BBO) Algorithm. The system is modeled using an autoregressive (ARX) model simulated by an artificial neural network (ANN). A comparison is accomplished among BT approach. The results shows us the use of this novel optimal approach in models reduction to the best solution. But it has one drawback

found in its long time achieving the best solution or optimum solution compared to BT approach. The future goal is to realize this optimal controller in hardware implementation. Then, interface to a DC/AC converter for our laboratory research experiments.

References

- [1] E.J. Davison, "A Method for Simplifying Linear Dynamic Systems", IEEE. Transaction on Automatic Control, vol. AC-11, pp.93-101, January 1966.
- [2] B.C. Moore, "Principal Component Analysis in Linear Systems: Controllability, Observability and Model Reduction", IEEE Transaction on Automatic Control, vol. AC-26, pp. 17-32, 1981.
- [3] D.A. Wilson, "Optimal Solution of Model Reduction Problem", Proc. IEE, vol. 117, June 1970.
- [4] D.A. Wilson, "Model Reduction for Multivariable Systems", Int. J. Contr., vol. 20, pp.57-64, 1974.
- [5] S. Gugercin, A. C. Antoulas, C. Beattie "A Rational Krylov Iteration for optimal H2 model reduction",
Proceedings of the 17th international Symposium on Mathematical Theory of Network and Systems, Kyoto, Japan, July 24-28, 2006
- [6] A. Bunse-Gerstner, D. Kubalinska, G. Vossen, D. Wilczek, "h2-norm optimal model reduction for large scale discrete dynamical MIMO systems", Journal of Computational and Applied Mathematics 233 (2010) 1202–1216.
- [7] S. Panda, J.S. Yadav, N.P. Padidar, and C. Ardil, "Evolutionary Techniques for Model Order Reduction of Large Scale Linear Systems", World Academy of Science, Engineering and Technology International Journal of Electrical and Computer Engineering Vol:6, No:9, 2012
- [8] H. Du, J. Lam and B. Huang, "Constrained H2 Approximation of Multiple Input–Output Delay Systems Using Genetic Algorithm", ISA Transaction, vol.46, no. 2, pp. 211-221, March 2007.
- [9] A. Haddad, R. Bouyekh, A. El Moudni, M. Wack, "Non-linear dynamic modeling of proton exchange membrane fuel cell", Journal of Power Sources 163 (2006) 420–432.
- [10] Sachin Puranik, M.S. "Control of fuel cell based green energy systems for distributed generation application", dissertation presented in Partial Fulfillment of the Requirements for the Degree Doctor of Philosophy in the Graduate School of The Ohio State University 2009.
- [11] Caisheng Wang, Nehrir, M.H., Shaw S.R., "Dynamic Models and Model Validation for PEM Fuel Cells Using Electrical Circuits", IEEE Transactions on Energy Conversion, Vol. 20, Issue 2, pp. 442-451, June 2005.
- [12] M. A. Ayob, W.N.W. Zakaria, "Estimation of Nonlinear ARX Model for Soft Tissue by Wavenet and Sigmoid Estimators", ISSN: 2180-1843 e-ISSN: 2289-8131 Vol. 8 No. 7, January 2016.
- [13] L. Ljung, "System Identification Toolbox", User's Guide R2015a. www.mathworks.com
- [14] Dan Simon, Biogeography-Based Optimization, IEEE Transactions on Evolutionary Computation (Volume: 12, Issue: 6, Dec. 2008), Page(s): 702–713, DOI:10.1109/TEVC.2008.919004.
- [15] Chennana, A., Megherbi, A. C., Bessous, N., Sbaa, S., Teta, A., Belabbaci, E. O., ... & Agajie, T. F. (2025). Vibration signal analysis for rolling bearings faults diagnosis based on deep-shallow features fusion. *Scientific Reports*, 15(1), 9270.
- [16] Bentegri, H., Rabehi, M., Kherfane, S., Nahool, T. A., Rabehi, A., Guermoui, M., ... & El-Kenawy, E. S. M. (2025). Assessment of compressive strength of eco-concrete reinforced using machine learning tools. *Scientific Reports*, 15(1), 5017.

- [17] Mehallou, A., M'hamdi, B., Amari, A., Tegar, M., Rabehi, A., Guermoui, M., ... & Khafaga, D. S. (2025). Optimal multiobjective design of an autonomous hybrid renewable energy system in the Adrar Region, Algeria. *Scientific Reports*, 15(1), 4173.
- [18] Tibermacine, A., Akrou, D., Khamar, R., Tibermacine, I. E., & Rabehi, A. (2024, December). Comparative Analysis of SVM and CNN Classifiers for EEG Signal Classification in Response to Different Auditory Stimuli. In *2024 International Conference on Telecommunications and Intelligent Systems (ICTIS)* (pp. 1-8). IEEE.
- [19] Mostefaoui, M., Belfedhal, A. E., Larbi, A. A., Rabehi, A., Abderrezzaq, Z., & Dabou, R. (2024, December). Enhanced Detection of EVA Discoloration Defects in Solar Cells Using Vision Transformers and Contrastive Learning. In *2024 International Conference on Telecommunications and Intelligent Systems (ICTIS)* (pp. 1-6). IEEE.
- [20] Tibermacine, A., Tibermacine, I. E., Zouai, M., & Rabehi, A. (2024, December). EEG Classification Using Contrastive Learning and Riemannian Tangent Space Representations. In *2024 International Conference on Telecommunications and Intelligent Systems (ICTIS)* (pp. 1-7). IEEE.
- [21] R. Salim, M. Bettayeb, "H2 and Hinf optimal model reduction using genetic algorithms", Electrical and Computer Engineering Department, University of Sharjah, P.O. Box 27272, Sharjah, UAE.



Photovoltaic Cells Fed a Dual Open-End Winding Induction Motor Driven by Fuzzy Field-Oriented Control

Mourad Sellah^{1,*}, Ahmed Lamine Dourari², Hakim Bagua³

¹ Faculty of Science and Technology, University of Ghardaïa, Algeria, mourad.sellah@yahoo.fr

² Faculty of Science and Technology, University of Sidi Bel Abbès, Algeria,
lamine.dourari@gmail.com

³ Faculty of Science and Technology, University of Ouargla, Algeria, hakim90mahi@gmail.com

*Corresponding author: (M. Sellah), Email Address: mourad.sellah@yahoo.fr

Abstract

The study presented in this article focuses on photovoltaic solar panels (PV) powering a Dual Open-End Winding Induction Motor (DOEWIM) fed by four three-phase inverters. Field Oriented Control (FOC) is adopted to regulate the stator current, rotor flux and rotation speed of the proposed machine, and Maximum Power Point Tracking (MPPT) technique is used to maximize power output from the solar panel. In order to achieve high performances in terms of fast dynamic speed response and best disturbance rejection, Fuzzy Logic Controller (FLC) is used for speed regulation. The main objective of this work is to introduce renewable energies into the drive of induction motors, especially those with open windings, in order to obtain several advantages, such as obtaining more robust performance towards external and internal disturbances, reduction of torque and flux ripples, minimization of stator current harmonics, and elimination of common mode voltage (CMV). The results obtained demonstrated the realization of the main advantages mentioned above, which confirms the validity of the proposed control on the topology of the induction motor studied.

Keywords: Photovoltaic, Maximum power point tracking, Field oriented control, Open-end winding, Fuzzy logic controller

<https://doi.org/10.63070/jesc.2025.011>

Received 25 April 2025; Revised 21 May 2025; Accepted 25 May 2025.

Available online 28 May 2025.

Published by Islamic University of Madinah on behalf of *Islamic University Journal of Applied Sciences*. This is a free open access article.

1. Introduction

Over the past century, global energy consumption has grown irrationally and continues to rise across all regions. As energy demand is expected to keep increasing, it is crucial to reassess our resource use to achieve truly sustainable and environmentally friendly development [1]. The depletion of fossil fuels and the associated greenhouse gas emissions highlight the urgent need to develop alternative energy sources. Among these, renewable energy stands out as a viable, eco-friendly substitute for fossil and nuclear energy, offering advantages such as being natural, inexhaustible, and well-suited for decentralized generation. Photovoltaic (PV) energy is one of the most promising forms of renewable energy, converting sunlight into electricity using solar panels composed of interconnected solar cells. PV systems have minimal environmental impact—they operate silently, discreetly, and without visual pollution [2]. A key feature of most PV systems is the implementation of a technique known as Maximum Power Point Tracking (MPPT), which continuously adjusts system parameters to ensure the panel operates at its maximum power output.

In recent years, multi-phase machines have gained significant attention from researchers, manufacturers, and industry professionals due to their ability to overcome several limitations associated with conventional three-phase machines. By increasing the number of phases, these machines distribute power and current more evenly, reducing stress on switches and windings. This design also leads to lower torque ripple, improved torque smoothness, and enhanced reliability enabling continued operation even when one or two non-adjacent phases fail [3, 4]. These benefits make multi-phase machines robust, low-maintenance, and scalable, supporting their growing use in high-power applications such as railway traction, naval propulsion, compressors, and cement mills [4, 5]. A prominent example is the Dual Star Induction Machine (DSIM), a six-phase machine consisting of two offset three-phase stator windings in the fixed part. This configuration combines the advantages of traditional induction machines with the added benefits of multi-phase operation [6]. To further enhance its performance and reliability, the DSIM can be modified into a Dual Open-End Winding Induction Machine (DOEWIM) by separating the connections of both stator windings [7]. This topology requires control via four three-phase voltage sources with carefully calculated phase shifts to eliminate common-mode voltage—thereby mitigating issues like bearing currents and shaft voltages, which are major contributors to premature machine failures [8-9].

Advancements in power electronics and modern control strategies have enabled AC drives to achieve dynamic performance levels comparable to those of DC drives—without the drawbacks associated with brushes and commutators. The main challenge in controlling asynchronous (AC) machines lies in the complex coupling between torque and magnetic flux. Field-Oriented Control (FOC) addresses

this by decoupling torque and flux control, effectively emulating the behavior of a separately excited DC motor. With FOC and the integration of powerful microprocessors, precise control of speed and torque in AC machines is now possible, matching the performance traditionally associated with DC machines [10].

To achieve high performance and robustness under varying operating conditions, advanced control methods like fuzzy logic controllers (FLC) have been proposed as alternatives to traditional PI controllers. FLCs offer several advantages over PI and PID controllers [11]. They allow the integration of human expertise through linguistic rules and can implement nonlinear control strategies without requiring an exact mathematical model of the system. Additionally, FLCs exhibit strong robustness, though their response may vary significantly with changes in system parameters.

This article is organized into five main sections. The first introduces the photovoltaic system and the MPPT technique used to optimize panel output. The second section describes the DOEWIM, highlighting its dual stator winding configuration. The third section outlines the indirect field-oriented control strategy and its key features. In the fourth section, the conventional IFOC is enhanced by replacing the traditional speed controller with a fuzzy logic-based regulator to improve system robustness. The fifth section presents simulation results, offering a detailed performance analysis under various practical scenarios. The article concludes with future perspectives and potential directions for further research.

2. Photovoltaic system and MPPT technique

2.1 Equivalent diagram of a solar cell

A single-diode equivalent circuit is the most commonly used model for representing a solar cell. In this model, the short-circuit current generated by illumination is represented as a current source, while the photovoltaic effect is modeled by a diode. Additionally, a series resistance and a parallel (shunt) resistance are included to account for the losses in the system. Figure 1 shows the equivalent circuit of the photovoltaic cell model [12,13].

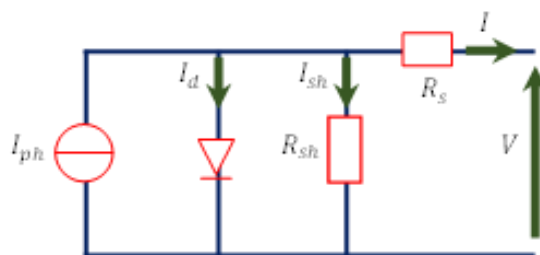


Figure 1. Equivalent PV cell circuit.

The characteristic equations of a solar cell are given by:

$$\begin{cases} I = I_{ph} - I_d - I_{sh} \\ I_d = I_0 \left(e^{\left[\frac{q(V+R_s I)}{kAT} \right]} - 1 \right) \\ I_{sh} = \frac{V+R_s I}{R_{sh}} \end{cases} \quad (1)$$

2.2 Perturb and Observe algorithm (P&O)

Due to its simplicity and ease of implementation, the Perturb and Observe (P&O) method is one of the most widely used MPPT techniques. Its principle is based on introducing a small disturbance in the DC voltage of the PV array and observing the resulting variation in the output power.

If the power increases following the disturbance, the system continues perturbing in the same direction. Otherwise, the direction of the disturbance is reversed. When a power increase is observed, the operating point lies to the left of the maximum power point (MPP). Conversely, if the disturbance causes a decrease in power, it indicates that the MPP has been crossed and the operating point is now on the right side of the MPP [14].

In such cases, the algorithm reverses the perturbation direction to track the MPP more effectively. Once the MPP is reached, the operating point stabilizes at the maximum power output.

3. Description and modelling of DOEWIM

The DOEWIM is a DSIM with open stator windings and, therefore, consists of twelve stator terminals six for each winding forming two identical star configurations that share the same stator and are electrically shifted by an angle of $\pi/6$ radians.

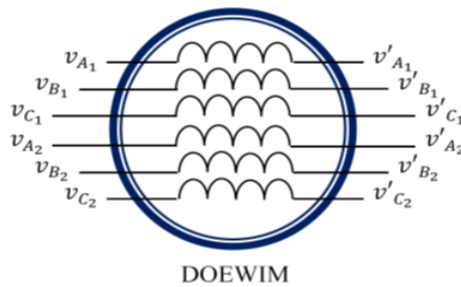


Figure 2. Voltage supply dual open-end winding induction motor.

Hence, four groups of three terminals are obtained, which require four three-phase converters to ensure powering and controlling the studied machine.

Consider $v_{a1}, v_{b1}, v_{c1}, v'_{a1}, v'_{b1}$ and v'_{c1} are respectively the pole voltages at the six outputs of the first two converters that are feeding the first ends of the two-stator winding, and $v_{a2}, v_{b2}, v_{c2}, v'_{a2}, v'_{b2}$ and v'_{c2} are respectively the pole voltages at the six outputs of the second two converters that are feeding the second ends of the two previous stator winding, as shown in the Figure 2.

The voltage across each phase winding among the six phases of the studied motor can be obtained based on the difference between the corresponding terminal voltages applied to its ends, as follows:

$$\text{First stator: } \begin{cases} V_{A_1} = v_{A_1} - v'_{A_1} \\ V_{B_1} = v_{B_1} - v'_{B_1} \\ V_{C_1} = v_{C_1} - v'_{C_1} \end{cases} \quad (2)$$

$$\text{Second stator: } \begin{cases} V_{A_2} = v_{A_2} - v'_{A_2} \\ V_{B_2} = v_{B_2} - v'_{B_2} \\ V_{C_2} = v_{C_2} - v'_{C_2} \end{cases} \quad (3)$$

Based on these assumptions, the DOEWIM model in the (d, q) frame can be presented as follows:

The stator and rotor voltages equations

$$\begin{cases} V_{ds_1} = R_{s_1} i_{ds_1} + \dot{\phi}_{ds_1} - \omega_s \phi_{qs_1} \\ V_{qs_1} = R_{s_1} i_{qs_1} + \dot{\phi}_{qs_1} + \omega_s \phi_{ds_1} \\ V_{ds_2} = R_{s_2} i_{ds_2} + \dot{\phi}_{ds_2} - \omega_s \phi_{qs_2} \\ V_{qs_2} = R_{s_2} i_{qs_2} + \dot{\phi}_{qs_2} + \omega_s \phi_{ds_2} \\ V_{dr} = R_r i_{dr} + \dot{\phi}_{dr} - (\omega_s - \omega_r) \phi_{qr} = 0 \\ V_{qr} = R_r i_{qr} + \dot{\phi}_{qr} + (\omega_s - \omega_r) \phi_{dr} = 0 \end{cases} \quad (4)$$

$$\text{With: } \begin{cases} V_{ds_1} = v_{ds_1} - v'_{ds_1} \\ V_{qs_1} = v_{qs_1} - v'_{qs_1} \\ V_{ds_2} = v_{ds_2} - v'_{ds_2} \\ V_{qs_2} = v_{qs_2} - v'_{qs_2} \end{cases}$$

The stator and rotor flux equations

$$\begin{cases} \phi_{ds_1} = L_{s_1} i_{ds_1} + L_m (i_{ds_1} + i_{ds_2} + i_{dr}) \\ \phi_{qs_1} = L_{s_1} i_{qs_1} + L_m (i_{qs_1} + i_{qs_2} + i_{qr}) \\ \phi_{ds_2} = L_{s_2} i_{ds_2} + L_m (i_{ds_1} + i_{ds_2} + i_{dr}) \\ \phi_{qs_2} = L_{s_2} i_{qs_2} + L_m (i_{qs_1} + i_{qs_2} + i_{qr}) \\ \phi_{dr} = L_r i_{dr} + L_m (i_{ds_1} + i_{ds_2} + i_{dr}) \\ \phi_{qr} = L_r i_{qr} + L_m (i_{qs_1} + i_{qs_2} + i_{qr}) \end{cases} \quad (5)$$

The mechanical equation

$$\frac{J}{P} \frac{d\omega_r}{dt} = T_{em} - T_L - \frac{K_f}{P} \omega_r \quad (6)$$

4. Field oriented control

Indirect Field-Oriented Control (IFOC) eliminates the need for flux sensors by using known motor parameters to calculate the appropriate slip frequency, thereby determining the desired flux position [15,16]. In this method, rotor flux is estimated based on the stator current vector, voltage vector, and rotor speed, and this estimation is then provided to the flux and torque controllers [17]. This approach is simpler to implement than the direct FOC method and can operate effectively across the full speed range from zero to high speed in both directions. As a result, the indirect vector control method is gaining increasing popularity.

The equations system for stator voltages is given by:

$$\begin{cases} v_{ds1} = R_{s1} i_{ds1} + L_{s1} \dot{i}_{ds1} - \omega_s^* (L_{s1} i_{qs1} + \tau_r \varphi_r^* \omega_{gl}^*) \\ v_{qs1} = R_{s1} i_{qs1} + L_{s1} \dot{i}_{qs1} - \omega_s^* (L_{s1} i_{ds1} + \varphi_r^*) \\ v_{ds2} = R_{s2} i_{ds2} + L_{s2} \dot{i}_{ds2} - \omega_s^* (L_{s2} i_{qs2} + \tau_r \varphi_r^* \omega_{gl}^*) \\ v_{qs2} = R_{s2} i_{qs2} + L_{s2} \dot{i}_{qs2} - \omega_s^* (L_{s2} i_{ds2} + \varphi_r^*) \end{cases} \quad (7)$$

The electromagnetic torque expression is as follows:

$$T_{em}^* = P \frac{L_m}{L_m + L_r} [(i_{qs1} + i_{qs2}) \varphi_r^*] \quad (8)$$

The rotor flux is regulated by a defluxing block, where, in general, the flux is maintained at its nominal value during operation at or below the machine's nominal speed. In cases where the operating speed exceeds the nominal speed, the flux is reduced to limit the machine's voltage. The reference flux is defined as follows:

$$\begin{cases} \varphi_r^* = \varphi_n & \text{si } |\Omega| \leq \Omega_n \\ \varphi_r^* = \frac{\varphi_n \Omega_n}{|\Omega|} & \text{si } |\Omega| > \Omega_n \end{cases} \quad (9)$$

Defluxing allows optimal exploitation of the machine's magnetic capabilities at under speed ($|\Omega| \leq \Omega_n$) and overspeed ($|\Omega| > \Omega_n$).

5. Fuzzy logic controller

5.1 Fuzzy logic controller and its main steps

The fuzzy logic controller uses a set of fuzzy rules that represent a decision-making mechanism to adjust the system's response to various stimuli. The primary goal of using an FLC is to replace a skilled human operator with a rule-based fuzzy system. Fuzzy logic provides a convenient method for mapping input variables to output responses [18–23] and is conceptually straightforward to understand [24–28].

A typical fuzzy logic controller consists of three main steps:

Fuzzification

The most common controller has two inputs, error and the derivative of the error with respect to a defined reference signal and one output, which is usually the control command.

Fuzzy inference engine

The fuzzy rule consists of an antecedent–consequent pair, expressed as IF-THEN rules encoded in a lookup table (Table 1). The input-output mapping is performed using an inference mechanism based on Zadeh's logic.

Table 1. Inference rules table.

ce	e	NB	NM	NS	ZE	PS	PM	PB
	NB	NB	NB	NB	NB	NM	NVS	ZE
	NM	NB	NB	NB	NM	NVS	ZE	PVS
	NS	NB	NB	NM	NVS	ZE	PVS	PM
	ZE	NB	NM	NVS	ZE	PVS	PM	PB
	PS	NM	NVS	ZE	PVS	PM	PB	PB
	PM	NVS	ZE	PVS	PM	PB	PB	PB
	PB	ZE	PVS	PM	PB	PB	PB	PB

Fuzzy inference engine

The center of area defuzzification method is used to calculate the crisp output value.

5.2 Computational cost of the fuzzy logic controller

The computational cost of a fuzzy logic controller can be relatively high, especially in real-time control scenarios, due to the complexity of fuzzification, inference, and defuzzification operations. Unlike conventional controllers such as PI, a fuzzy controller requires the evaluation of multiple linguistic rules and the execution of nonlinear calculations at each sampling cycle. This computational load can be a challenge for embedded systems or applications requiring very fast response times. However, with advancements in microcontrollers and digital signal processors (DSPs), it is now possible to efficiently implement fuzzy controllers in real-time systems, provided the algorithms are optimized and the number of rules is kept within reasonable limits.

Figure 3 shows the general diagram of the control structure using the fuzzy field-oriented control technique for a DOEWIM supplied by two photovoltaic solar panels, with speed, rotor flux, and stator currents controlled in a nonlinear control plane.

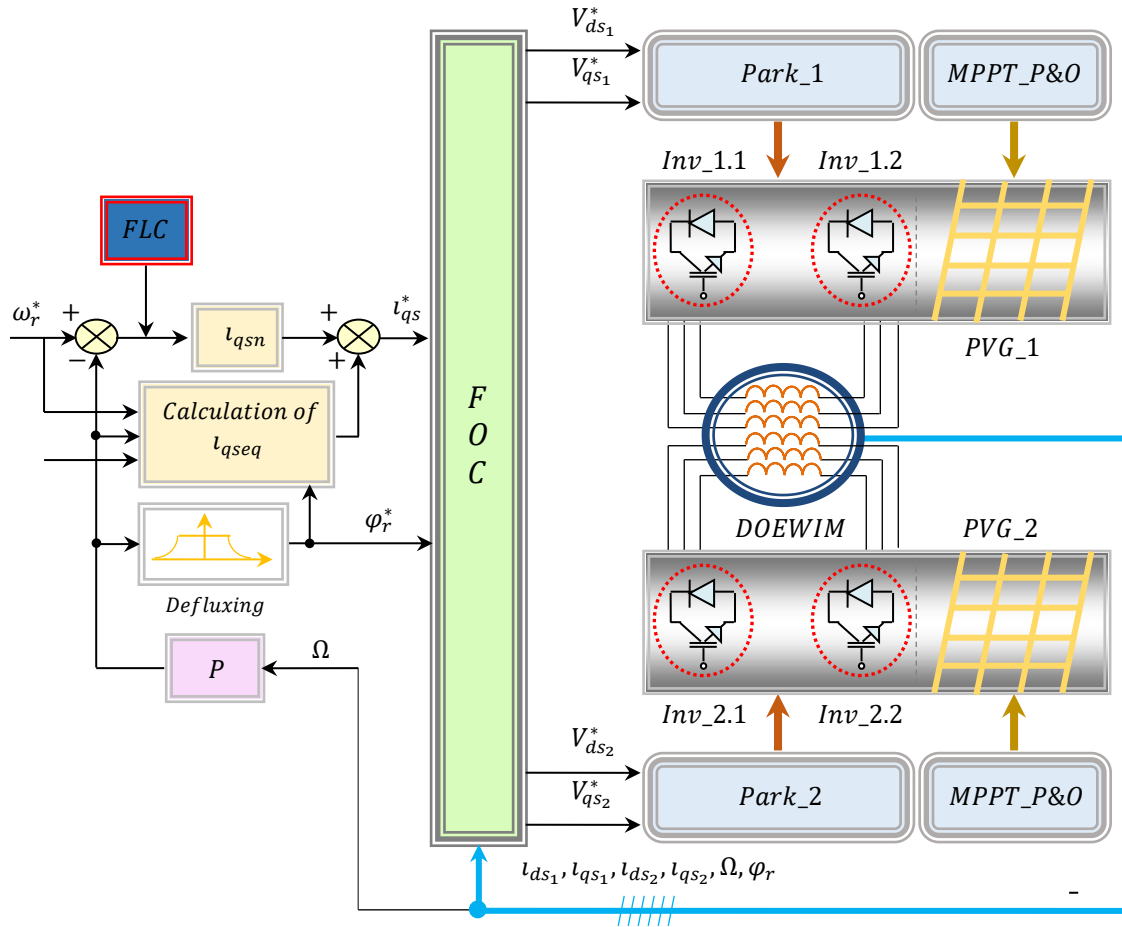


Figure 3. Fuzzy field-oriented control scheme applied on DOEWIM powered by photovoltaic cells.

6. Simulation results and discussions

In this section, the application of fuzzy field-oriented control for the operation of the DOEWIM powered by photovoltaic cells is examined through simulation tests.

The main objective is to present a detailed analysis of the performance of this control technique by studying the dynamic behavior of key electrical, electromagnetic, and mechanical variables, such as stator current, electromagnetic torque, stator flux, and rotor speed. Additionally, tests were conducted for different reference speed values, considering start-up under no load, load torque application, and speed reversal.

Indeed, these simulations include a sequence of steps that can imitate the practical cases in industrial applications. The machine starts up at $t = 0s$ with no load following an imposed reference speed profile of $150rad/s$, at $t = 1s$ a load torque of $T_L = 5N.m$ is applied which is considered as an external perturbation, at $t = 1.5s$ the reference speed value is increased to $200rad/s$ then at $t = 2s$

the applied load torque is increased to $T_L = 10 \text{ Nm}$, then at $t = 3\text{s}$ the applied load torque is removed which means that $T_L = 0 \text{ N.m}$.

The second part of these simulations present the dynamic behaviour of the proposed control technique against the speed revers, where at $t = 3\text{s}$ the reference speed is inverted to a value of -150 rad/s without the application of any load torque, then at $t = 5\text{s}$ another value of the inverted reference speed is applied to become -200 rad/s .

Figure 4 shows the rotor speed and its reference for the fuzzy field-oriented control applied to the DOEWM. Note that the four passages from 0 rad/s to 150 rad/s then from 150 rad/s to 200 rad/s on the one hand, and from 200 rad/s to -150 rad/s , then from -150 rad/s to -200 rad/s on the other hand are carried out by the rotor speed in a linear manner without any overshoot, completely identical to the practical case. In the steady state, the rotor speed perfectly follows the reference speed without showing a real influence for different load applications, moreover the error representing the difference between the two speeds is very low. Overall, the rotor speed response is very satisfactory at all stages of operation, indicating the robustness and accuracy of the fuzzy logic controller.

Figure 5 gives the electromagnetic torque developed by the machine studied. The electromagnetic torque exhibits high dynamics characterized by minimal fluctuations. The width of the torque fluctuation band appears very small, which confirms the precision of the proposed control by eliminating fluctuations. The torque response to the application of loads and to the reversal of direction of rotation is carried out with great precision and without any overshoot thanks to the great robustness of the field-oriented control.

The stator phase currents of the first DOEWM star are shown in Figure 6. At start-up, the currents are unequal due to the induction of the circuit, then in the equilibrium state the amplitude of these currents is constant, then, when the load is introduced or the direction of rotation is reversed, the amplitudes currents increase, which suggests a strong performance of the field-oriented control.

The components of the direct and quadratic rotor flux for the DOEWM powered by photovoltaic cells are represented by Figure 7. We note that the two components φ_{dr} and φ_{qr} pass a very short-term transient regime then reach perfect stability successively at the values 1 Wb and 0 Wb in steady state, which proves that the complete decoupling between the torque and the flux is maintained by field-oriented command.

Figure 8 clearly shows the chosen irradiation (E) values, which varied between 600 W/m^2 and 800 W/m^2 . Observation of Figure 9 and Figure 10, which represent the voltage and the power of photovoltaic generator respectively, confirms that the irradiation value is directly proportional to the

voltage and the power of photovoltaic generator, since as the irradiation increases, the voltage and the power of photovoltaic generator increase, and vice versa.

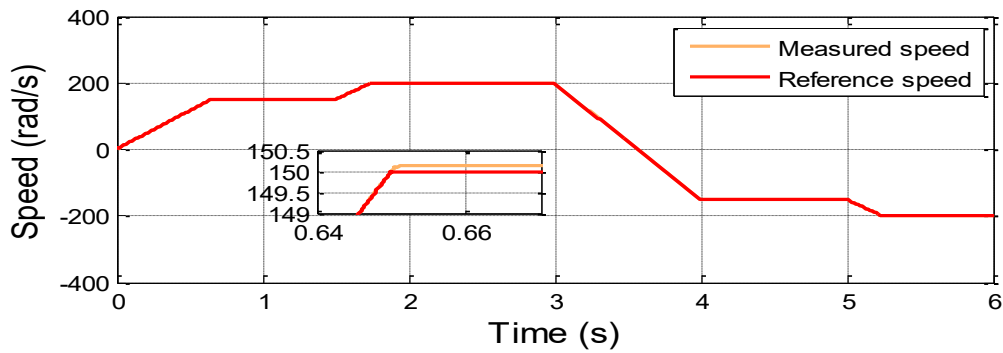


Figure 4. Rotor speed of the DOEWIM.

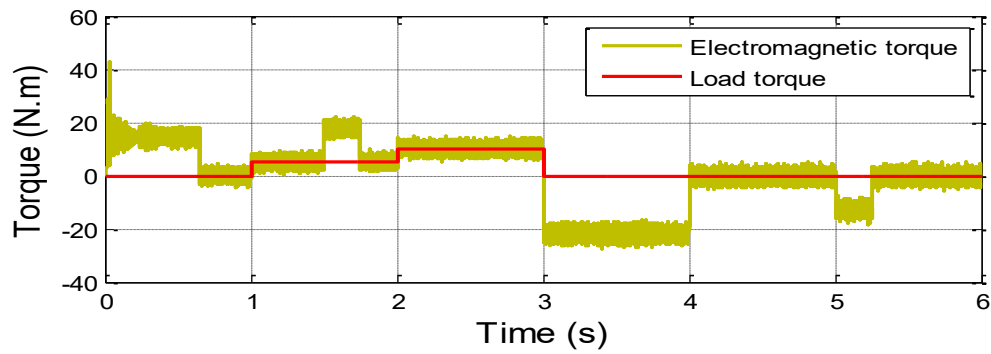


Figure 5. Electromagnetic torque developed by the DOEWIM.

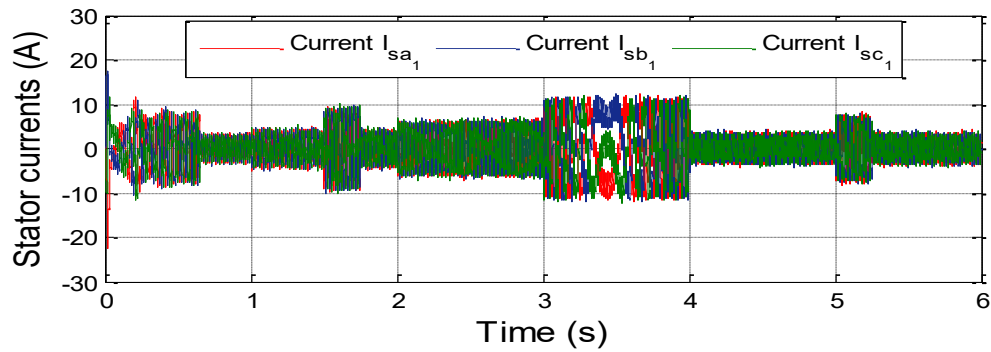


Figure 6. Stator phase currents.

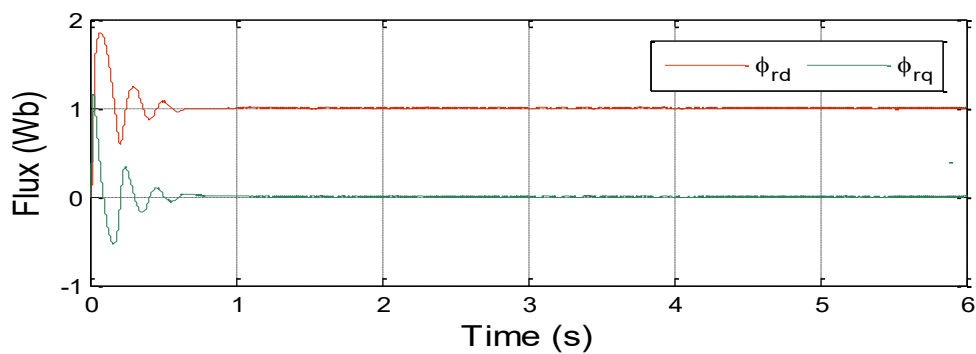


Figure 7. Components of the rotor flux.

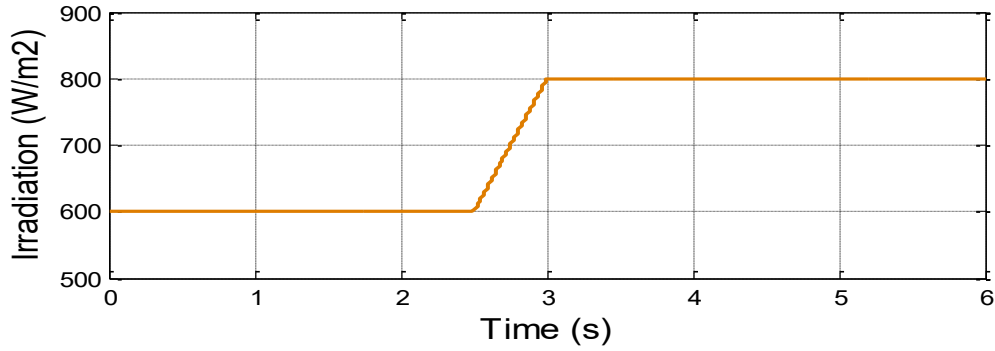


Figure 8. Solar irradiation.

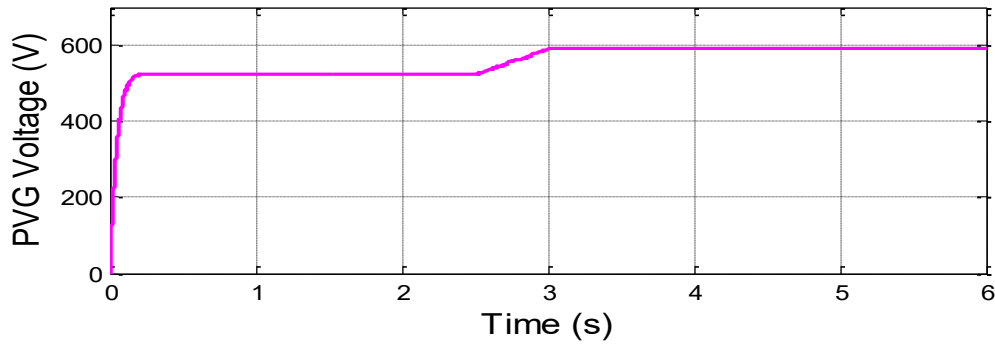


Figure 9. PVG Voltage.

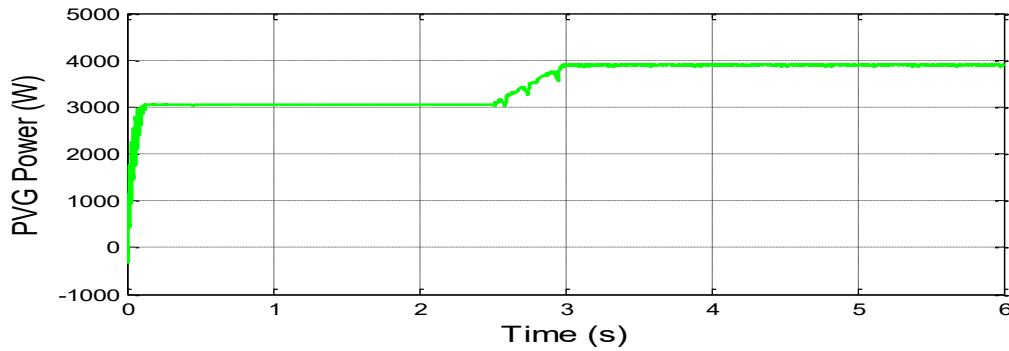


Figure 10. PVG Power.

7. Conclusion

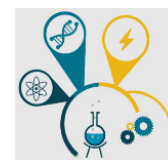
In conclusion, the proposed control technique proves to be a highly competitive and promising solution for the control of multiphase machines, particularly those with open stator winding topologies. Notably, the application of this control strategy to the DOEWIM powered by photovoltaic energy represents a novel contribution, as such integration has not been thoroughly explored in existing literature. The simulation results obtained using the artificial intelligence-based control method developed in this study highlight significant improvements in system performance, demonstrating both enhanced dynamic response and high operational efficiency under various demanding conditions.

This control approach effectively addresses many of the key challenges typically encountered in multiphase machine control such as complexity, nonlinearity, and fault tolerance making it especially suitable for high-power industrial applications where system reliability, minimal maintenance, and uninterrupted operation are critical. Therefore, the proposed technique holds strong potential for future deployment in real-world scenarios requiring robust, intelligent, and energy-efficient control systems.

References

- [1] Onyinyechukwu C., Cosmas Dominic D., and All. “Control systems in renewable energy: A review of applications in Canada, USA, and Africa “. *World Journal of Advanced Engineering Technology and Sciences*, 2024, 11(01), 029–036.
- [2] Malhar K., Muhammad Amir R., Muhammad F., and All.” Conventional and artificial intelligence based maximum power point tracking techniques for efficient solar power generation “, *Engineering Reports*, Wiley. June 2024.
- [3] Kali, Y.; Saad, M.; Doval-Gandoy, J.; Rodas, J. Discrete Terminal Super-Twisting Current Control of a Six-Phase Induction Motor. *Energies* 2021, 14, 1339.
- [4] Kali, Y.; Ayala, M.; Rodas, J.; Saad, M.; Doval-Gandoy, J.; Gregor, R.; Benjelloun, K. Current Control of a Six-Phase Induction Machine Drive Based on Discrete-Time Sliding Mode with Time Delay Estimation. *Energies* 2019, 12, 170.
- [5] Marouani, K.; Baghli, L.; Hadiouche, D.; Kheloui, A.; Rezzoug, A. A New PWM Strategy Based on a 24-Sector Vector Space Decomposition for a Six-Phase VSI-Fed Dual Stator Induction Motor. *IEEE Trans. Ind. Electron.* 2008, 55, 1910–1920.
- [6] Rahali, H.; Zeghlache, S.; Benyettou, L.; Benalia, L. Backstepping Sliding Mode Controller Improved with Interval Type-2 Fuzzy Logic Applied to the Dual Star Induction Motor. *Int. J. Comput. Intell. Appl.* 2019, 18, 1950012.
- [7] Nirsha, K.I.; Rajeevan, P.P. A direct torque control scheme for dual inverter fed induction motor drive with a common DC voltage source. In *Proceedings of the IECON 2017—43rd Annual Conference of the IEEE Industrial Electronics Society*, Beijing, China, 29 October–1 November 2017.
- [8] Ranjit, M.; Gowtami, S.; Babu, B.G. Reduction of zero sequence voltage using multilevel inverter fed open-end winding induction motor drive. *Acta Electrotech. Inform.* 2016, 16, 52–60.
- [9] Foti, S.; Testa, A.; De Caro, S.; Scimone, T.; Scelba, G.; Scarcella, G. Multi-level open end windings multi-motor drives. *Energies* 2019, 12, 861.
- [10] Ansari, S.; Chandel, A. Simulation based comprehensive analysis of direct and indirect matrix converter fed asynchronous motor drive. In *Proceedings of the 2017 4th IEEE Uttar Pradesh Section International Conference on Electrical, Computer and Electronics (UPCON)*, Mathura, India, 26–28 October 2017.
- [11] Benachour, A.; Berkouk, E.M.; Mahmoudi, M.O. Study and comparison between two DTC strategies of induction machine fed by direct matrix converter. *J. Renew. Sustain. Energy* 2017, 9, 55501.
- [12] Van Huynh, V.; Nguyen, T.D.; Dao, V.-T.; Tran, Q.-H. An Efficient Carrier-Based Modulation Strategy for Five-Leg Indirect Matrix Converters to Drive Open-End Loads with Zero Common-Mode Voltage. *Electr. Power Compon. Syst.* 2019, 47, 1303–1315.
- [13] Lavanya, N.; Rao, M.V.G. Control of indirect matrix converter by using improved SVM method. *Int. J. Power Electron. Drive Syst.* 2015, 6, 370–375.
- [14] A. Levant, “Higher-order sliding modes, differentiation and output-feedback control”, *International Journal of Control*, vol. 76, no. 09-10, pp. 924-941, 2003.
- [15] Laszlo Gyugyi, “Static Power Frequency Changers: Theory, Performance and Applications”, Book, New York: Wiley, c76, 1976.

- [16] Marco Matteini, "Control Techniques for Matrix Converter Adjustable Speed Drives", PhD thesis, Department of Electrical Engineering, University of Bologna, 2001.
- [17] François Gruson, "Modulation Naturelle Généralisée des Convertisseurs Matriciels pour la Variation de Vitesse", Thèse de doctorat, Ecole centrale de Lille, 2010.
- [18] Arie Levant, "Higher Order Sliding Modes and Their Application for Controlling Uncertain Processes", PhD theses, Institute for System Studies of the USSR Academy of Science, Moscow, 1987.
- [19] Chennana, A., Megherbi, A. C., Bessous, N., Sbaa, S., Teta, A., Belabbaci, E. O., ... & Agajie, T. F. (2025). Vibration signal analysis for rolling bearings faults diagnosis based on deep-shallow features fusion. *Scientific Reports*, 15(1), 9270.
- [20] Bentegri, H., Rabehi, M., Kherfane, S., Nahool, T. A., Rabehi, A., Guermoui, M., ... & El-Kenawy, E. S. M. (2025). Assessment of compressive strength of eco-concrete reinforced using machine learning tools. *Scientific Reports*, 15(1), 5017.
- [21] Mehallou, A., M'hamdi, B., Amari, A., Teguvar, M., Rabehi, A., Guermoui, M., ... & Khafaga, D. S. (2025). Optimal multiobjective design of an autonomous hybrid renewable energy system in the Adrar Region, Algeria. *Scientific Reports*, 15(1), 4173.
- [22] eddine Boukredine, S., Mehallel, E., Boualleg, A., Baitiche, O., Rabehi, A., Guermoui, M., ... & Tibermacine, I. E. (2025). Enhanced Performance of Microstrip Antenna Arrays through Concave Modifications and Cut-Corner Techniques. *ITEGAM-JETIA*, 11(51), 65-71.
- [23] Belaid, A., Guermoui, M., Riche, A., Arrif, T., Maamar, H., Kamel, C. M., ... & Al Rahhal, M. M. (2024). High-Resolution Mapping of Concentrated Solar Power Site Suitability in Ghardaïa, Algeria: A GIS-Based Fuzzy Logic and Multi-Criteria Decision Analysis. *IEEE Access*.
- [24] Tibermacine, A., Akrou, D., Khamar, R., Tibermacine, I. E., & Rabehi, A. (2024, December). Comparative Analysis of SVM and CNN Classifiers for EEG Signal Classification in Response to Different Auditory Stimuli. In *2024 International Conference on Telecommunications and Intelligent Systems (ICTIS)* (pp. 1-8). IEEE.
- [25] Mostefaoui, M., Belfedhal, A. E., Larbi, A. A., Rabehi, A., Abderrezzaq, Z., & Dabou, R. (2024, December). Enhanced Detection of EVA Discoloration Defects in Solar Cells Using Vision Transformers and Contrastive Learning. In *2024 International Conference on Telecommunications and Intelligent Systems (ICTIS)* (pp. 1-6). IEEE.
- [26] Tibermacine, A., Tibermacine, I. E., Zouai, M., & Rabehi, A. (2024, December). EEG Classification Using Contrastive Learning and Riemannian Tangent Space Representations. In *2024 International Conference on Telecommunications and Intelligent Systems (ICTIS)* (pp. 1-7). IEEE.
- [27] Ladjal, B., Tibermacine, I. E., Bechouat, M., Sedraoui, M., Napoli, C., Rabehi, A., & Lalmi, D. (2024). Hybrid models for direct normal irradiance forecasting: A case study of Ghardaia zone (Algeria). *Natural Hazards*, 120(15), 14703-14725.
- [28] Belaid, A., Guermoui, M., Khelifi, R., Arrif, T., Chekifi, T., Rabehi, A., ... & Alhussan, A. A. (2024). Assessing Suitable Areas for PV Power Installation in Remote Agricultural Regions. *Energies*, 17(22), 5792.



Associated Use of Design of Experiments in Numerical Energy Simulation for Energy Use Optimization in Residential Buildings

Dalia Dahbia Yaici¹, Abdelouahab Bouttout^{2,*}

¹ Institute of Architecture and Urbanism, Saad Dahlab University. Blida, Algeria,
dalia.yaici@gmail.com

² National Center of Studies and Integrated Research of Building, Souidania, 16097, Algeria,
Bouttout@gmail.com

*Corresponding author: (A. Bouttout), Bouttout@gmail.com

Abstract

This article investigates the optimization of energy consumption in residential buildings. The research begins by modelling a representative building configuration (F3) aligned with the Technical Regulatory Document (DTR C3.2/4) standards for heating and cooling. Dynamic thermal simulations assess its performance; while key input factors and their variation ranges are identified. A Design of Experiments (DOE) matrix streamlines simulations, and Analysis of Variance (ANOVA) identifies critical parameters. These parameters inform polynomial models to predict energy demands under various conditions. The findings reveal that in Algeria's hot-summer Mediterranean climate, roof and wall U-values and operative temperature significantly influence heating loads, while operative temperature, wall U-value, and Solar Heat Gain Coefficient (SHGC) are the dominant factors affecting cooling loads. Optimal solutions could reduce heating demand by 37–59.6% and cooling demand by 10–26%. These results suggest that the proposed methodology could be effectively integrated into the 2025–2030 national housing program to enhance energy performance and support CO₂ emissions reduction in alignment with the country's Nationally Determined Contributions (NDCs).

Keywords: Design of experiment (DOE), U-value, Heating, Cooling, National Determined Contributions (NDCs).

<https://doi.org/10.63070/jesc.2025.012>

Received 03 April 2025; Revised 04 May 2025; Accepted 23 May 2025.

Available online 28 May 2025.

Published by Islamic University of Madinah on behalf of *Islamic University Journal of Applied Sciences*. This is a free open access article.

1. Introduction

Being a major consumer of energy worldwide, the building sector accounts for approximately 40% of final energy consumption compared to other sectors. This sector is responsible for 31% of total emissions, with residential buildings emitting 26 million tons (MT) of CO₂ out of the global 1936 MT, representing 1.34% of the world's residential gas emissions [1]. In Algeria, the 2021 national energy balance report shows that the residential and tertiary sectors account for 47% of final energy consumption and 36% (34 MT CO₂) of GHG emissions. This 47% share is dominant, followed by the transport and industrial sectors with 29% and 24%, respectively. This data highlights a 6.20% increase in demand from the «household and others" sector (which includes residential, agriculture, tertiary, and others) from 22.1M TEP in 2020 to 23.4M TEP in 2021, with the residential sub-sector growing by 4.4%. Such demand threatens non-renewable energy resources amidst economic and demographic growth and the housing construction pace [2].

Algeria's greenhouse gas emission mitigation policy is part of the global fight against climate change. This policy is evident in Algeria's active participation in international agreements, such as the Paris Agreement, and through actions like the Framework of the Nationally Determined Contribution (NDC). Since 2015, NDC actions have outlined objectives and measures for mitigation and energy transition. For the housing and urban planning sector, the NDC proposes emission projections and measures under several scenarios by 2030, considering the significant potential of existing and under-construction housing stock, investment opportunities to reduce energy consumption, and the diversity of possible measures in the housing sector, such as building envelope improvements and performance of electrical appliances and systems [3]. The graph below (Figure 1) provides a summary of mitigation measures in the residential sector, with thermal insulation identified as a key action by 2030. Scenario S1 (45 Mt) and scenario S3 (40 Mt) suggest promising options to explore with emission reduction of 67.8% and 53% for S3 and S1, respectively. These projections are correlated with the evolution of the number of dwellings from 1999 to 2024, presented in Figure 2 [3]. The collective housing program projections for the two five-year periods, 2029 and 2034, are confronted with new strategic challenges, including housing demand, demographic growth, energy demand per dwelling, and CO₂ emissions from energy consumption during the operational phase [3].

Energy efficiency in buildings is a major action to address these challenges, offering passive measures like thermal insulation, natural ventilation and architectural solutions, as well as active measures including heating, air conditioning, home automation and building management systems. The current challenge is to create practical decision-support tools for effectively introducing these measures at the

building level, optimizing energy performance to control consumption and associated costs. Optimization involves actions such as reducing thermal losses, selecting efficient equipment, and eliminating waste under three pillars: Efficiency, Renewable and Adequacy. This research focuses on the thermal design of collective housing, emphasizing building envelope elements and occupant thermal comfort factors. The goal is to develop a practical decision-support tool for optimizing building energy performance, thereby controlling consumption and associated costs. By applying the Design of Experiments (DOE) method along with numerical simulation and regulatory compliance with the DTR C3.2/4, this paper aims to identify optimal solutions for energy efficiency in residential buildings, contributing to Algeria's sustainable development goals. The paper has two objectives:

- Develop a practical and fast energy optimization tool for collective housing.
- Identify the most influential factors on heating and cooling loads.

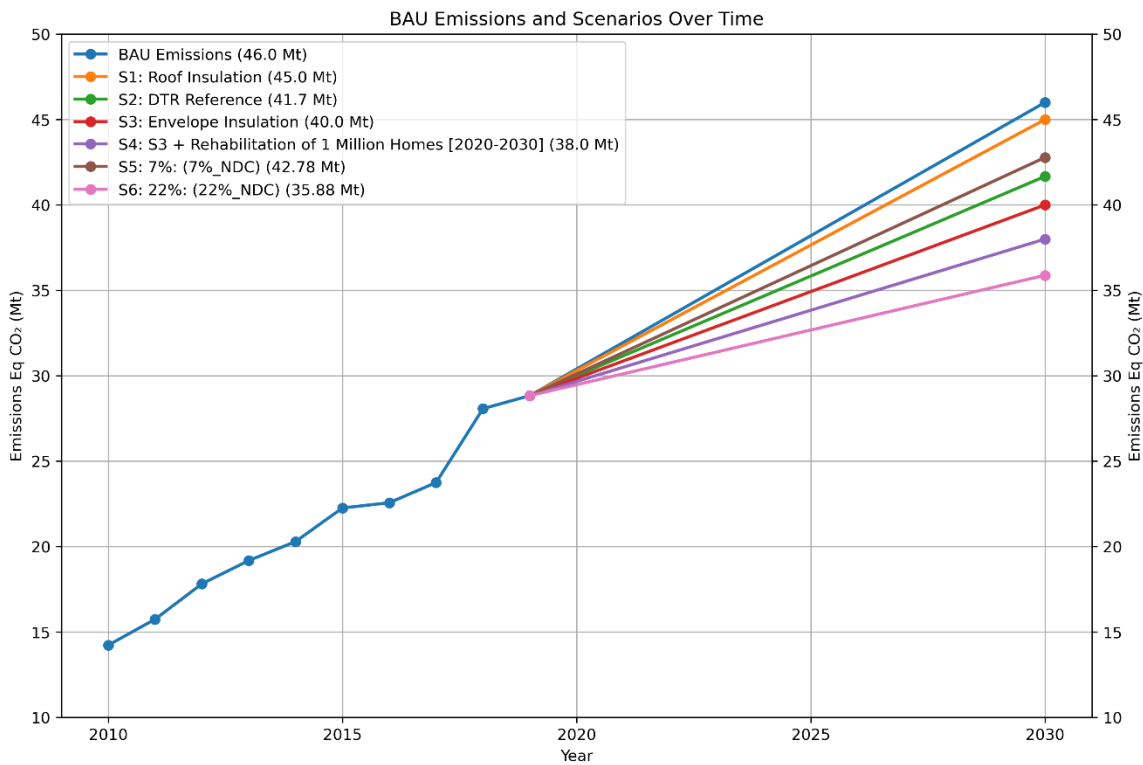


Figure 1. Mitigation measures and CO2 emission scenarios by 2030.

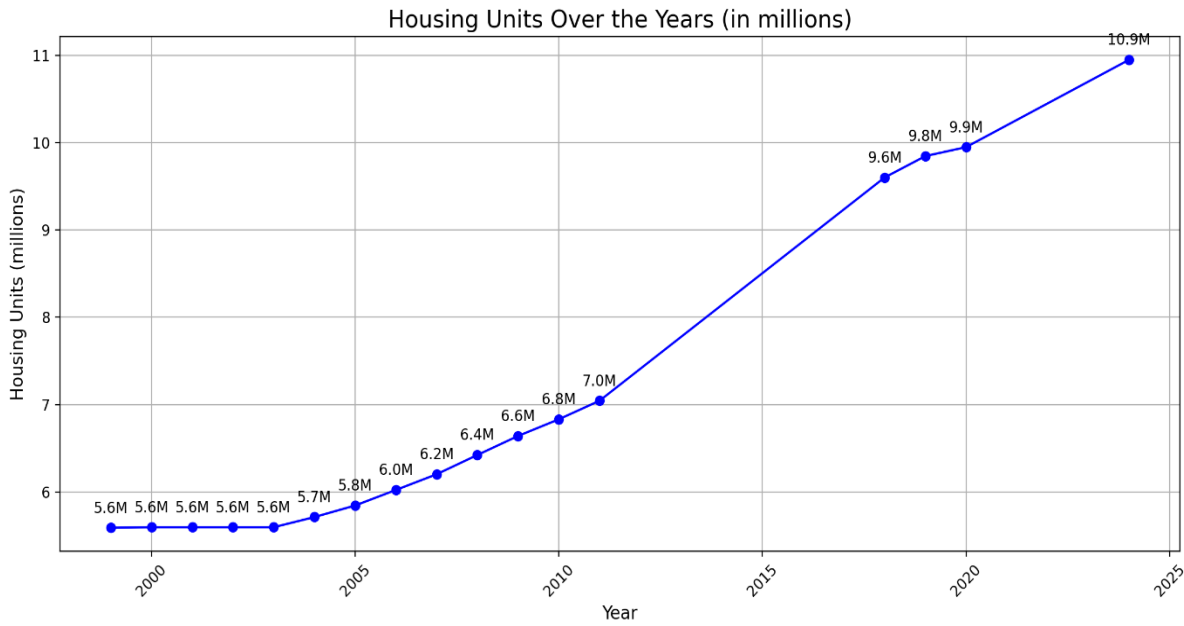


Figure 2. Evolution of the number of dwellings in Algeria (1999-2024).

Figure 3 shows the historical energy consumption of the residential sector according to the energy reports of the Ministry of Energy and Mines (MEM). Two projections are presented in this graph: the first considers the construction of 2 million non-insulated housing units, while the second envisions the same number of housing units with thermal insulation by 2030. These projections are part of the 2025–2030 five-year plan. The total energy consumption savings can be estimated at 45.43% by 2030, based on the thermal insulation of the building envelope in the housing program over five years.

The remainder of this paper is structured as follows. Section 2 provides an overview of the theoretical background of the Design of Experiments method and its relevance to energy efficiency in buildings. Section 3 introduces the case study involving AADL residential buildings in Algeria. Section 4 outlines the parametric analysis, including the identification of key factors and the determination of their variation ranges. Section 5 discusses the main findings, including regulatory verification results according to DTR C3.2/4, dynamic thermal simulation outcomes, DOE results, and recommendations for improving model accuracy. Finally, Section 6 concludes the study with a summary of key insights and future perspectives.

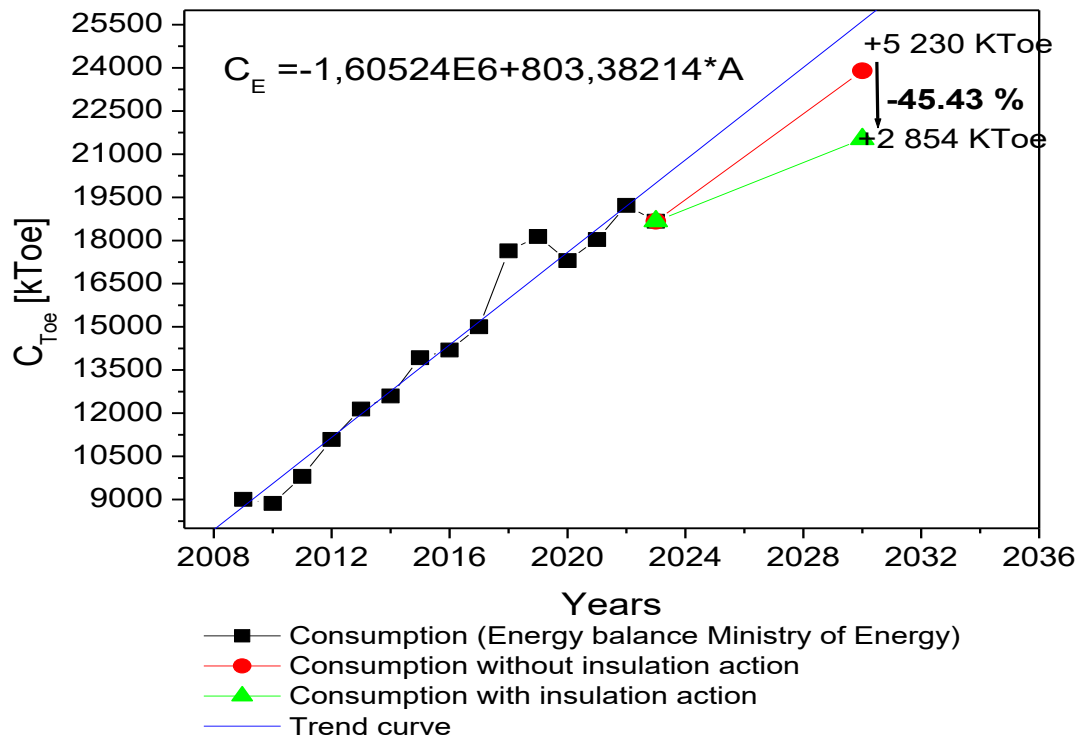


Figure 3. Historical energy consumption of the residential sector according to thermal insulation projection actions.

2. Literature Review

The DOE method is a multi-criteria decision-making method for conducting, analysing, and interpreting experiments. This mathematical methodology has been applied for a long time in several scientific fields. It is based on simultaneously modifying input variables (referred to as factors, denoted by X) to reveal their effects on one or more output variables (referred to as responses, denoted by Y). Reference [4] explains the uses of DOE for screening many factors and discerning interactions among them for optimization purposes or characterizing processes or products. Moreover, in this article we focus on the application of the DOE method along with dynamic thermal simulation (DTS) in the field of energy efficiency in residential buildings.

The literature review focused on decision-making approaches has led us to explore the DOE method as a consistent procedure to apply, given its previous uses in building's energy field.

For example, it has been used for predicting energy consumption or for sensitivity analysis of factors specifically influencing the implementation of energy efficiency measures in buildings [5]. Additionally, the flexibility of the method allows for testing a large number of factors with a reduced number of experiments simultaneously. A design of experiment that was employed to evaluate and identify optimal combinations of building elements (walls, ceilings, window and temperatures) and

how they contribute in efficient building design, especially in achieving optimal cooling load savings in a tropical residential setting [6]. The findings revealed that, for tropical regions, the most significant elements in reducing energy consumption efficiently are ceiling materials, followed by wall materials and indoor temperatures.

Expanding on the topic, authors developed a systematic approach aimed at minimizing building heating and cooling loads for efficient building design factors optimization [7]. They utilized a subset of all possible combinations of factors (fractional factorial design) and evaluated ten factors, such as wall and window insulation, ceiling height, solar heat gain coefficient, orientation...etc. to run experiments using dynamic thermal simulation software. Firstly, the study conducted a screening experiment designed to filter a shortened list of important factors, where factors related to window performance and air leakage were the most significant ones. Next, the Pareto front was used for optimization after dropping insignificant factors, where authors explain that optimization becomes quite challenging when there are factors that affect the response in contradictory ways on top of using main effects graphs to also detect the same contradictory factors such as window insulation and SHGC (Solar Heat Gain Coefficient). The Pareto front was plotted using the NSGA-2 algorithm in R language to identify the optimal values of the factors in the forms of equations for each segment of the Pareto front for minimum heating and cooling loads. The researchers consolidated their findings by incorporating the coefficient of performance COP of HVAC systems as active factors to include both passive and active factors that must be simultaneously considered and associated to achieve the best responses in terms of energy needs [7].

Polynomial models were developed using DOE method with dynamic thermal simulation software to predict heating and cooling loads, final energy needs and summer thermal comfort [5]. Following this, a parametric study of these polynomial functions was conducted using Pareto chart to identify optimal solutions for the design of new buildings in different climatic zones in Morocco, which has a similar climate to Algeria. This study established best practices such as enhancing building envelope performance, integrating economic study and life cycle analysis to manage energy consumption.

Whereas, in a local context (Ouargla, southern Algeria), characterized by an arid desert climate, researchers applied DOE approach for individual housing [8]. The study aimed to recommend a polynomial model to minimize seasonal energy consumption due to air conditioning. The focus is limited to the evaluation of parameters and geometric envelope properties for an individual house, such as: thermal transmission through walls U-wall, U-roof, U-ground, U-window, window to wall ratio North WWR-N, WWR-S-W-E, ceiling height, area floor, factor form, absorption coefficient of the solar radiation of the wall and roof. Surface area and solar radiation absorption were identified as primary factors influencing cooling and heating loads, with a square shape recommended as the

optimal building form. U-wall significantly reduced heating consumption by 10 kW/m² per year but had limited impact on cooling, while U-ground notably reduced heating consumption by approximately 8 kW/m² per year yet increased the cooling load. In addition, several experimental studies conducted in Algeria have confirmed the significant impact of thermal insulation on reducing energy consumption in residential buildings. One study carried out in northeastern Algeria (Mila) involved both experimental measurements and numerical simulations, assessing the effect of adding polystyrene insulation to the ceiling and floor. Following the renovation, experimental results showed a 55% reduction in heating energy demand during winter and an 18% reduction in cooling power, compared to 42% and 17% respectively in the simulation results [9]. In another experimental study conducted in Constantine (eastern Algeria), the potential for energy savings was evaluated in a top floor apartment through various retrofit strategies, including wall and roof insulation, and window replacement. The findings revealed that such measures could lead to energy savings ranging from 13% to 50% [10]. Similarly, a study conducted in Algiers (northern Algeria) focused on the thermal behaviour of a single-story house with an attic. A numerical model, validated using indoor air temperature data, was used to assess different configurations of attic insulation and ventilation. The results showed that, across Algeria's diverse climates, the presence of an attic weather insulated or not, contributed to a reduction in cooling energy demand [11].

Besides, the state of art reveals that the DOE is widely used in the field of energy efficiency in residential buildings. Its main advantages include the ability to simultaneously study the influence of multiple factors on one or several responses while reducing the number of experiments. This flexibility allows for the optimization of designs by identifying the optimal combinations of factors and revealing their interactions. However, some limitations exist. Notably, the optimization becomes challenging when there are contradictory factors affecting the responses in opposing ways. Most studies focus on factors related to the building envelope without considering other comfort parameters for occupants, such as indoor comfort temperature and minimum fresh airflow rate. Furthermore, very few studies on this topic have been applied in Algeria, a country with significant climatic diversity, offering a unique opportunity for development and application of optimization strategies for collective housing. This also includes the potential for comparing model results with other regulatory methods such as DTR C3.2/4 where researchers have examined the impact of thermal insulation on thermal comfort and energy consumption in existing houses within Algeria's cold climatic zone that did not comply with building regulation [9]. Therefore, it is essential to address this gap by developing models that incorporate both passive and active factors as well as occupant comfort factors, specifically adapted to the context of Algiers (Mediterranean climate) where a significant portion of the national housing

programs has been implemented in this climatic context. Additionally, exploring the relevance of these models by comparing them against regulatory calculations and compliance that could be beneficial and may lead to the creation of a general framework of recommendations and practical implementation scenarios for designing collective housing. This would combine regulatory requirements with optimized calculation models for predicting heating and cooling needs for residential buildings.

3. Case Study

The national collective housing program in Algeria is developed by the National Agency for the Improvement and Development of Housing (AADL). The selected building for the study is an F3 AADL apartment, F3 is a residential unit consists of two bedrooms and a living room with a typical construction configuration. It is located in Ouled Fayet, Algiers, Algeria with a total area of 80.62 m² (71.92 m² Net area), and six stories (R+5) with a focus on the apartment on the top floor. This choice is relevant because this apartment features a larger surface area exposed to the external environment, leading to higher losses in winter and heat gains in summer compared to a reference apartment. In contrast, the reference apartment typically benefits from thermal influence from adjacent units, reducing its heating and cooling demands. The selection of this unit aligns with the objectives of this research, which aims to analyse the energy consumption patterns of a representative building, as described in this study. The facades are oriented to the south and east. The floor plan (Figure 4) and the 3D model (Figure 5) provide more details. Thermal properties of building's envelope and space areas are presented in tables 1 and 2.

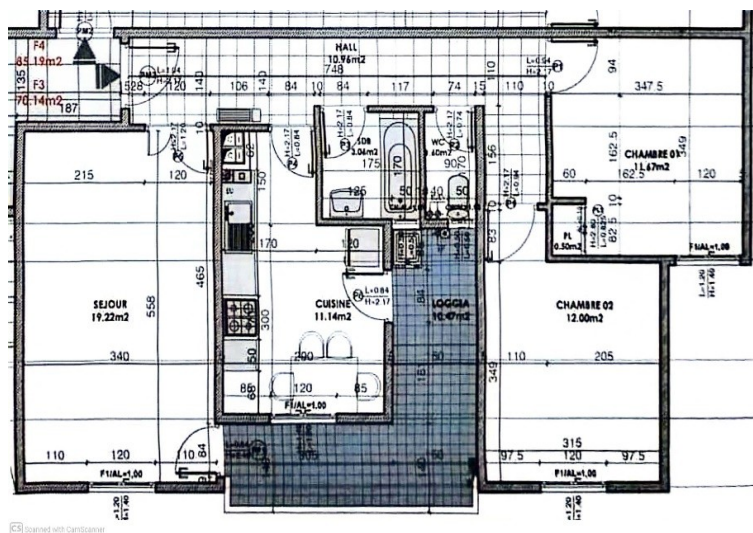


Figure 4. Floor plan of F3 apartment

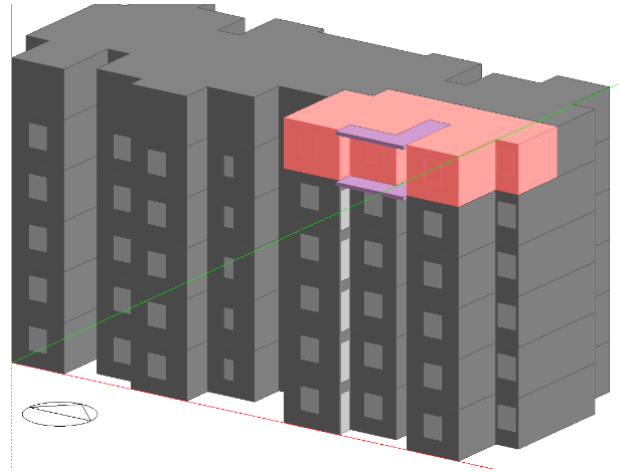


Figure 5. 3D model of the F3 apartment

Table 1. Space areas of the F3 apartment

Space	Living room	Kitchen	Hall	Loggia	Bedroom 1	Bedroom 2	WC	Bathroom
Area (m ²)	19.22	11.14	10.96	10.47	11.67	12.00	1.6	3.06

Table 2. Thermal properties of building's envelope

N	Element	Composition	thickness (m)	Thermal conductivity (W/m-K)	U value (W/m ² -K)
1	Exterior wall	Cement coating	0.03	1.40	2.99
		Concrete	0.15	1.75	
		Plaster render	0.02	0.35	
2	Roof	Plaster render	0.01	0.35	0.48
		Concrete	0.15	1.75	
		Expanded polystyrene	0.08	0.046	
		Mortar render	0.01	1.15	
		Waterproofing (bitumen felt)	0.01	0.23	
3	Interior partitions	Plaster render	0.02	0.35	2.55
		Concrete	0.10	1.75	
		Plaster render	0.02	0.35	
4	Window				2

4. Parametric Analysis

The research approach begins with modelling the representative building configuration (F3) that incorporates essential characteristics and relevant scenarios, providing a realistic basis for analysing parameters affecting energy consumption. The model undergoes regulatory verification to ensure alignment with DTR C3.2/4 standards for heating and cooling, followed by dynamic thermal simulation to evaluate thermal performance and energy efficiency. Next, influential input factors are identified, and their variation ranges are established. A DOE matrix is then constructed to streamline the simulations, reducing the number of experiments while maintaining comprehensive analysis. The resulting data are analysed using Analysis of Variance (ANOVA) to determine the most impactful parameters, which are subsequently used to develop polynomial models that predict energy demands under various conditions. These models facilitate the identification of optimal solutions for heating and cooling, balancing efficiency and thermal comfort. The methodology concludes with a comparative analysis across DTR C3.2/4 standards, DTS simulations, and DOE-derived models to ensure accuracy and regulatory compliance. Based on these insights, general recommendations are proposed for improving energy efficiency in collective housing in Algiers, with statistical software supporting data analysis and model formulation throughout the process.

4.1 Selection of factors and their variation ranges

The chosen design factors and their minimum and maximum variation ranges for applying the experimental design are presented in table 3. Each parameter's range is indicated by its levels (-1) and (+1) in standardized, centred coordinates.

Table 3 – Variation ranges for experimental design factors

Factor	(-1)	(+1)	Unit	Reference
U wall	0.35	3.286	W/m ² . K	[10]
U roof	0.349	1.895	W/m ² . K	[10]
U window	1.2	5	W/m ² . K	[11], [13]
WWR_ E	25	50	%	[8], [11]
WWR_ S	25	50	%	[8], [11]
SHGC glass	0.372	0.949	/	[8]
Minimum fresh air flow rate (F3 dwelling)	4.14 75	8.28 150	l/s-person m ³ /h	[10], [12]

Air infiltration rate	0.36	1.15	V/h	[5]
COP heating	0.88	3.73	/	[14]
EER cooling	1.1	3.5	/	[14]

5. Results and discussions

5.1 Regulatory verification Results according to DTR C3.2/4

The regulatory Technical Document DTR C3.2/4 CNERIB 2016 defines the general building regulations for thermal design (heating and cooling) and energy needs assessment for winter and summer periods [10]. Appendix 1 summarizes calculation and verification method. Results are presented in table 4.

Table 4. Regulatory verification Results according to DTR C3.2/4

Heating calculation	
Climatic and building data	Multi-family Housing Climatic zone : A
Regulatory verification: $A1 + A2 + A3 + A4 \leq 1.05 \times D_{ref}$	Heat loss: $D_{transmission} = 437 \text{ W/}^\circ\text{C}$ Total heat losses: $D_{total} = 561.74 \text{ W/}^\circ\text{C}$ Installed heating power: $Q = 11,685 \text{ W}$ Reference heating power = 9285.18 W The housing does not meet the regulatory verification requirements
Heating demand	$Q = 11,685 \text{ W}$
Cooling calculation	
Climatic and building data	Latitude = 36.00 Calculation Month : July
Regulatory verification	$A_{ref} = 2597.13 \text{ W}$ $APO_{POA_15h} + AVT_{PVE_15h} + AVT_{t_15h} + AVE_{15h} = 3571.54 \text{ W}$ The housing does not meet the regulatory verification requirements
Cooling demand	3571.54 W

5.2 Dynamic thermal simulation Results

Following the modelling of the baseline F3 apartment under various real-life scenarios, the results regarding heating and cooling demands are presented in table 5. The results of the dynamic thermal

simulation closely align with those of the regulatory calculations (table 4). The heating capacity is estimated at 11.68 kW and 13 kW respectively. For cooling, the regulatory calculation estimates are 3.57 kW and 4.63 kW. The baseline model fails to meet regulatory verification due to excessively high thermal coefficients of the envelope, particularly, in the exterior walls.

Table 5 – Dynamic thermal simulation results

	Energy	Value
Heating demand	Thermal losses	10.43 kW
	Heating capacity to be installed	13 kW
	Annual consumption	7057.39 kWh
	Heating demand/m ²	101.44 kW/m ² .an
Cooling demand	Gains	4 kW
	Cooling power	4.63 kW
	Annual consumption	2940.25 kWh
	Cooling demand/m ²	40.88 kW/m ² .an

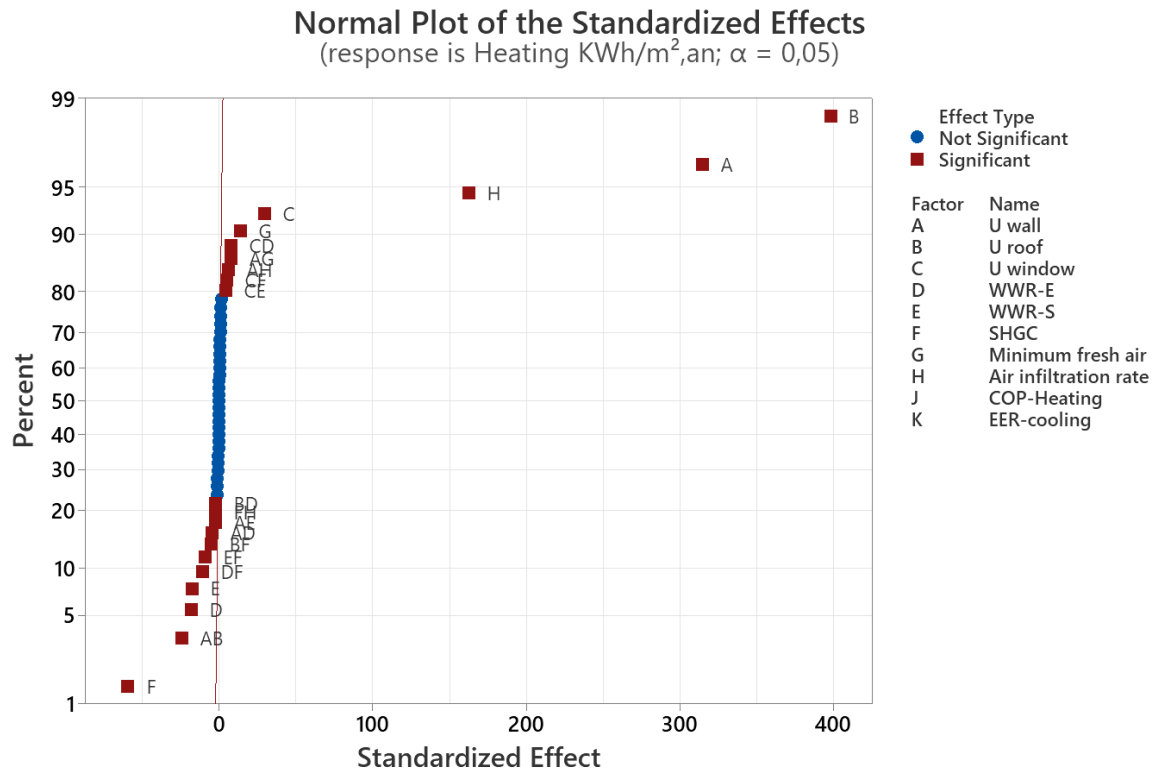
5.3 DOE methodology: results of the experiments

Conducting the experiments begins with a significant reduction in the number of experiments by using a fractional factorial design of resolution IV. This approach allows for the analysis of all factors while limiting the number of tests to a fraction of 1/16, enabling effective selection and screening of the factors being studied. The results of the 64 simulations are presented in Appendix 2.

5.3.1 Selection of influential parameters

In this initial selection for heating loads, significant factors were chosen based on analysis of variance for linear effects and two-way interactions. Summarized results are presented in figures 6 and 7. The probability of each effect is shown in the standardized effects plot (figure 6), where negligible effects align along the red line, and significant effects deviate from it. Important effects include B (U value roof), A (U wall), H (infiltration rate, and F (SHGC). The Pareto chart (figure 7) confirms this classification, with the red dashed line at 2.10 marking the threshold for statistical significance. The graph highlights that factors B,A,H, and F indicate their effects on the response “Heating demand in kWh/m².year.” Thermal coefficients of the roof (top floor location of the apartment) and walls are key factors impacting heating demand, underscoring the importance of the building envelope in the winter. Factor H (infiltration rate) also significantly influences the response, highlighting the role of

airtightness in conjunction with these elements. SHGC has a moderate effect, likely due to the model's



southeast orientation and its location in Algiers.

Figure 6 . Normal standardized effects plot for heating loads

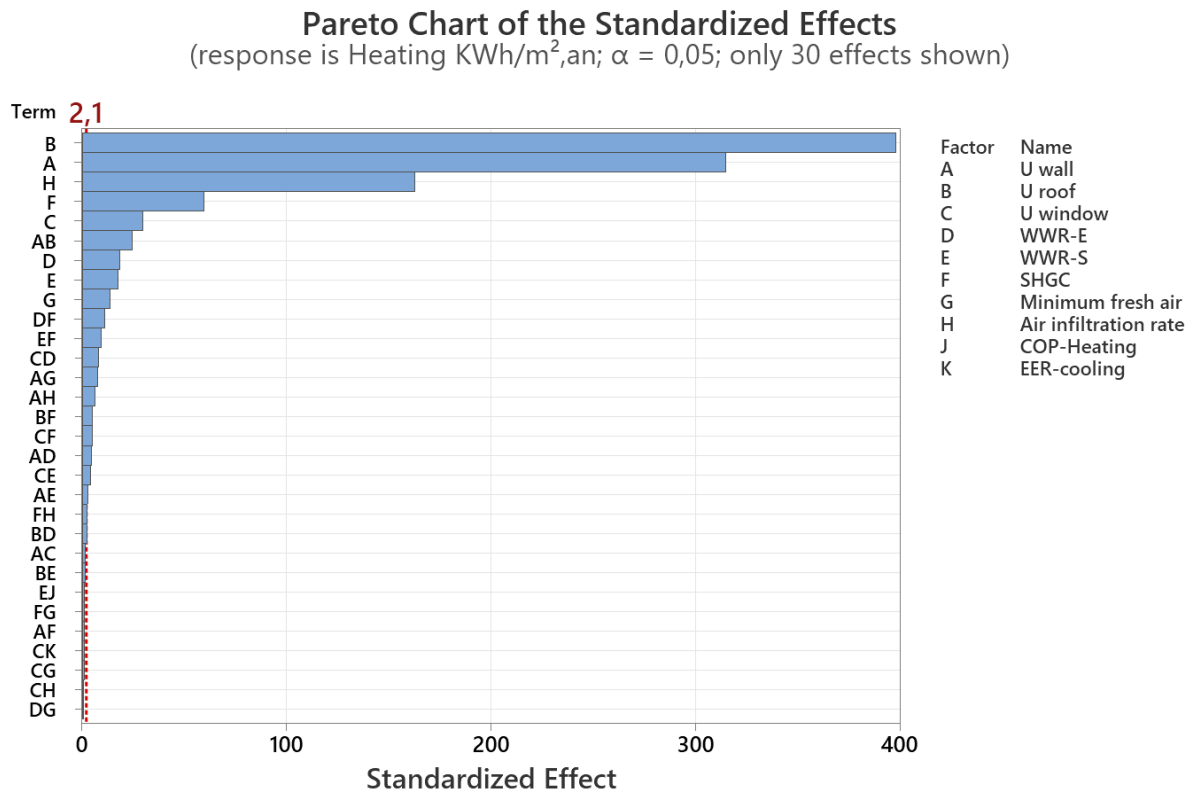


Figure 7. Pareto chart of the standardized effects for heating loads.

For cooling loads, important factors were identified through analysis of variance focusing on linear effects and two-way interactions. The summarized findings are shown in figures 8 and 9. The probability of effects on “Cooling demand in kWh/m² per year” is shown in the effects plot (figure 8), where factors F (SHGC), B (U roof), A (U wall), and D (WWR-E) are all significant. The Pareto front (figure 8) is used for final classification of factors F,B,A, and D based on their standardized effects, along with other combinations such as DF, AB, and BF. The SHGC factor, along with WWR-E, is the most influential, highlighting the importance of glazing properties in thermal performance. It defines the portion of solar radiation admitted through windows as heat, directly impacting cooling loads in simulations. Optimizing SHGC in east and west-facing facades significantly lowers cooling energy demand in hot climates [17]. The WWR-E, which ranges from 25% to 50%, is particularly significant on the east due to the rectangular shape of the house. This configuration allows higher WWR distributions in the east facade, leading to larger glazed areas. Factors B and A have a substantial impact on cooling demand. The COP and EER factors are non-significant, likely due to simplified HVAC modelling, which limits the scope of this study.

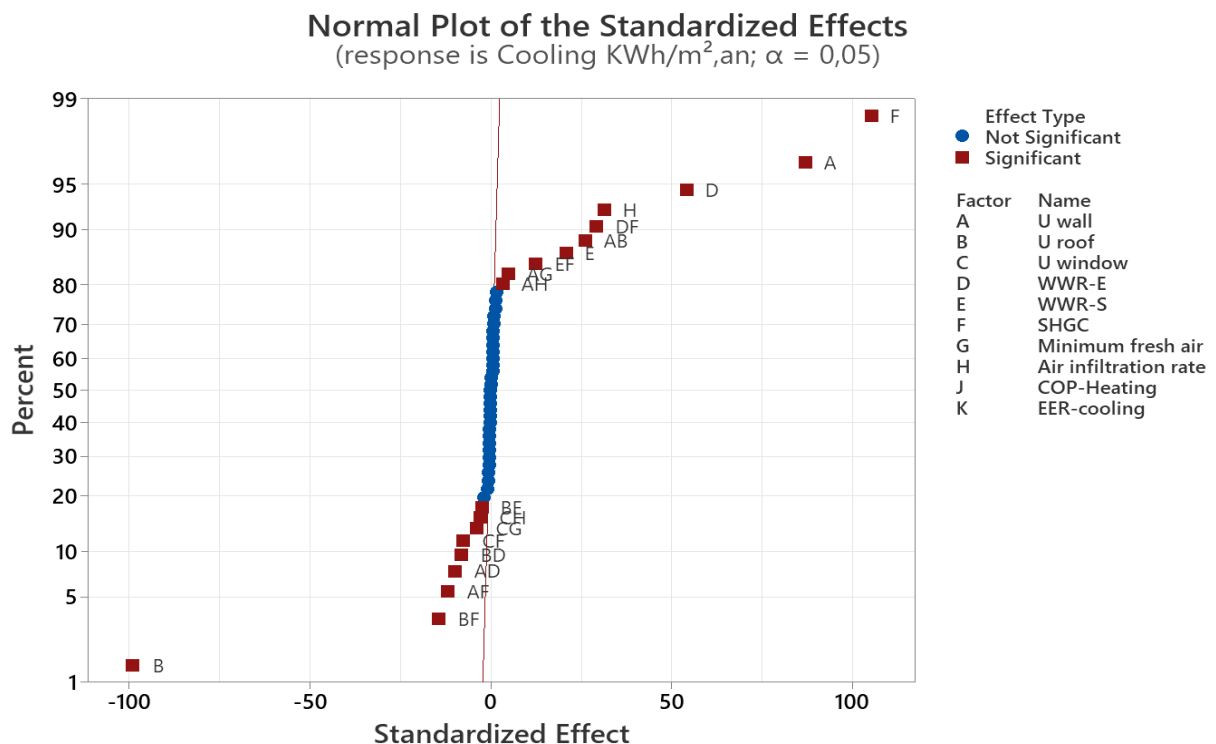


Figure 8. Normal standardized effects plot for cooling loads

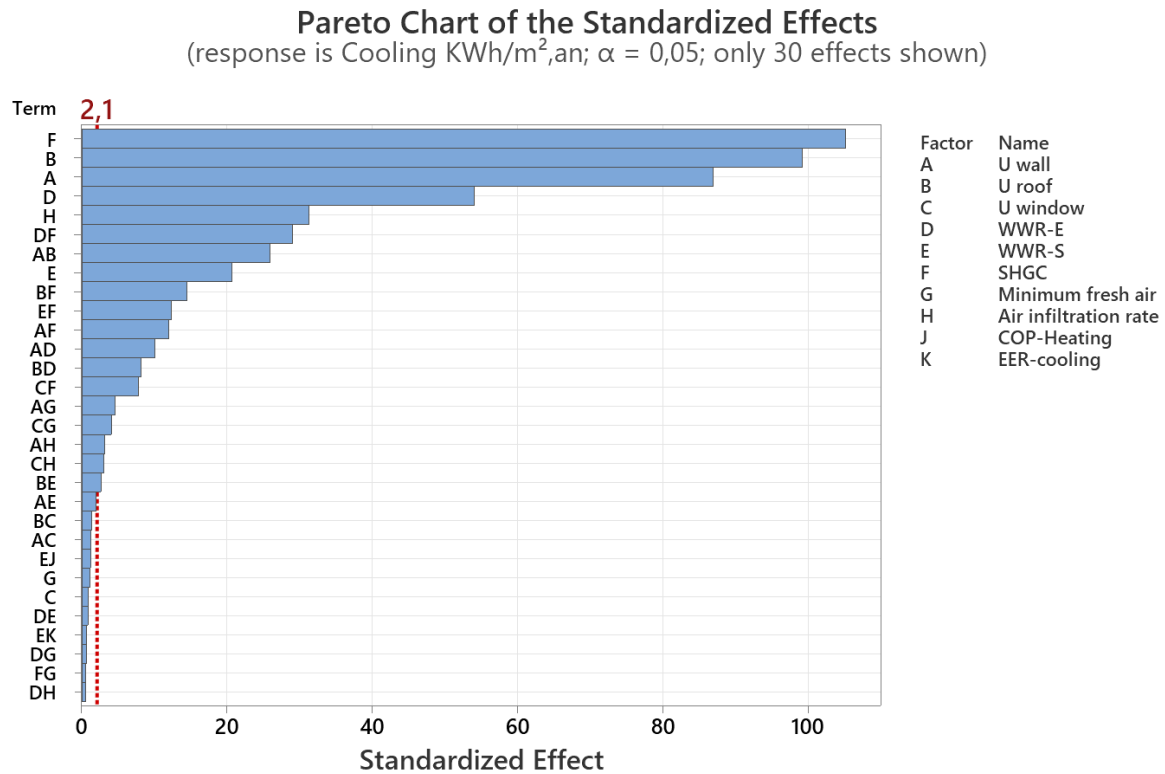


Figure 9. Pareto chart of the standardized effects for cooling loads

5.3.2 Determination of polynomial models

This section focuses on factors of: U roof, U wall, and infiltration rate for heating analysis, as well as on SHGC, U roof, and U wall for cooling. To enhance precision, separate full factorial and response surface designs are implemented, with the introduction of operative temperature as a key factor to examine its impact on occupant comfort. The objective is to identify mathematical models for optimizing heating and cooling responses.

For heating, a full factorial design is created with a reduced set of four factors, resulting in 22 experiments to test all possible combinations (16 experiments plus 6 center points). The main effects plot (figure 10) illustrates the influence of the four factors on heating loads, showing a significant increase in response with higher roof and wall U-values (represented by blue lines at extreme factor levels). A similar pattern is observed for the operative temperature, while infiltration rate has a less impact on the response. The main effects plot also shows that the center points (in red) deviate from the linear response for all factors, indicating a quadratic response curve and prompting further experiments with a response surface matrix to identify the mathematical models for optimization.

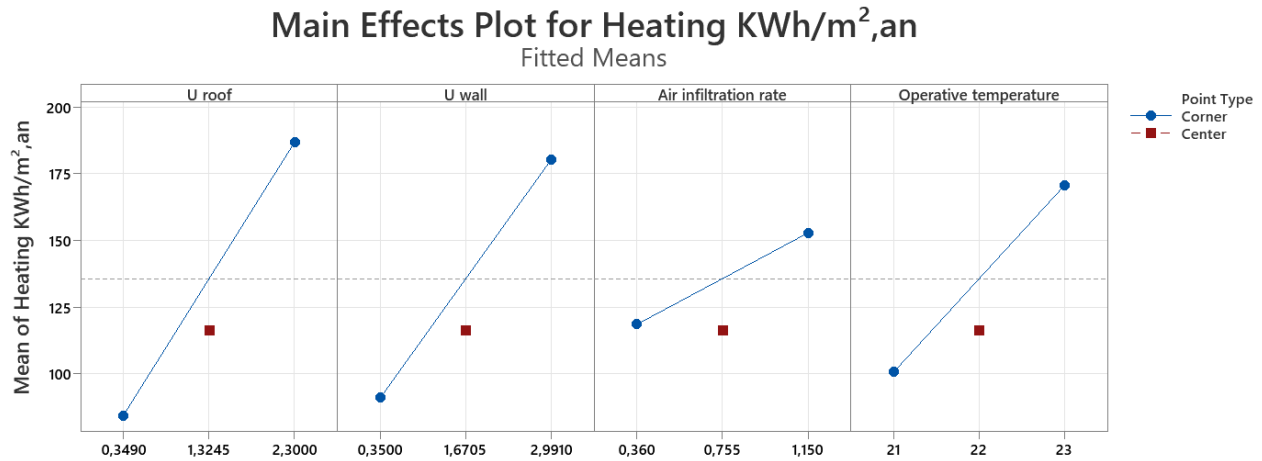


Figure 10. Main effects plots for heating loads

To proceed with this, the factors: U- roof, U- wall and operative temperature are used to develop a central composite response surface design (20 experiments central composite plan). For optimization purposes, two responses are presented throughout regression equations: heating demand and heating capacity. Detailed tables for the polynomial models are shown in appendix 3. The Pareto chart (figure 10) for the full quadratic model ranks the factors by their effect: roof U-value (A) has the most significant impact, followed by wall U-value (B) and the operative temperature respectively. The analysis of the second response, “heating capacity” (figure 10), ranks the primary effects as B,A, and C. The two contour plots (figure 11) illustrate heating demand as a function of two variables: wall U value (ordinate axis) and roof U value abscissa axis). Different color gradients indicate heating demand ranges in kWh/m².year. Expectedly, heating demand increases as U-values for walls and roof rise, reflecting poor thermal insulation and, consequently, greater heat loss. The operative temperature is set at 22°C for the first plot and 21°C for the second (figure 11), representing the heating requirements needed to maintain these indoor temperatures, with heat loss through walls and roof factored in according to their transmission coefficients. The parabolic shape of the curves illustrates the relationship between the response and the two variables, indicating quadratic modeling with second-degree polynomial functions, as confirmed by the response surface equations. These mathematical models and the contour plots enable the identification of optimal heating demand solutions and a commemorative evaluation of the DOE, DTS, and DTR models.

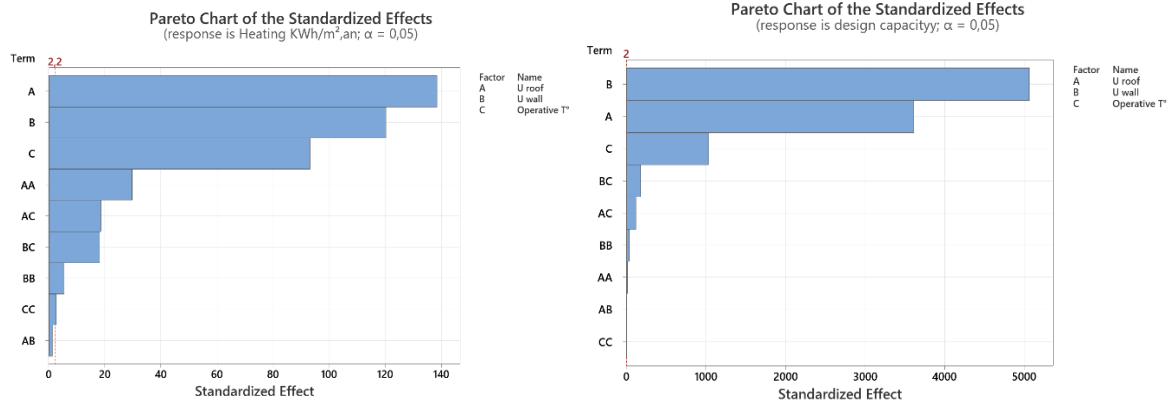


Figure 11. Pareto charts for heating loads and design capacity

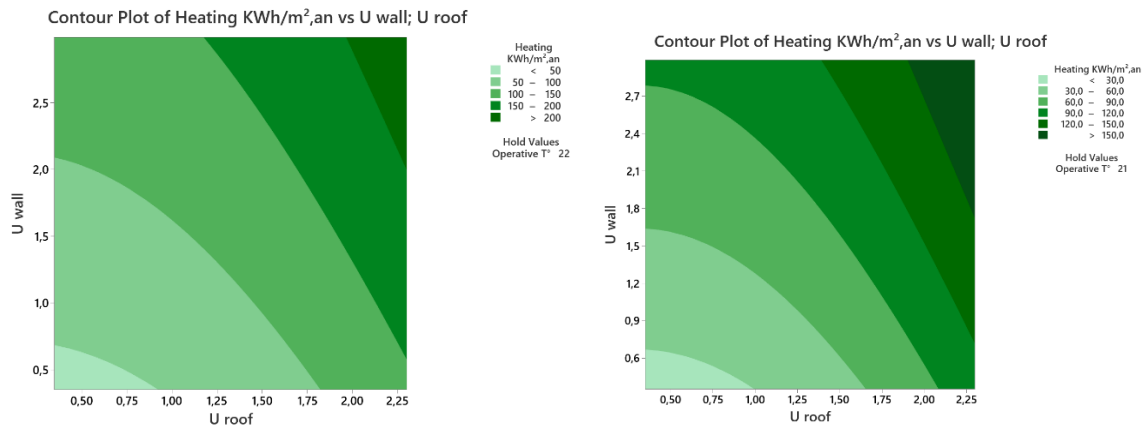


Figure 12. Contour plots for heating loads

Following the approach used for heating loads, a full factorial design was necessary to test all possible combinations for cooling loads. In the main effects plot (figure 12), a significant increase in the response is observed with a rise in operative temperature, followed by wall U-value and the SHGC. The response is less influenced by the U-roof factor. In the same plot, the central points lie outside the linear response line for all factors, suggesting a curve in the response (quadratic). Therefore, a response surface design is needed to identify the models for optimization. For this, three factors (Op. temperature, U wall, and SHGC) are selected to create a central composite design with 20 experiments. The Pareto chart (figure 13) of the full quadratic model classified factors as following: A (Op. temperature) has the most significant effect on both responses, followed by B (U wall), which influences “design capacity” more than the first response, and the AB interaction is notable in the second response. The SHGC factor ranks last in both plots. The operative temperature is identified as the primary determinant for both installed cooling capacity and annual cooling demand, particularly within the range of 24°C to 27°C. This is also confirmed in the contour plot (figure 14), with optimal results achieved when the variable ranges between 25.7°C and 26.7°C. Figure 14 (plot 2) presenting cooling capacity to install, shows a greater range (color diversity) than the first plot. Detailed tables for the polynomial models are shown in appendix 4.

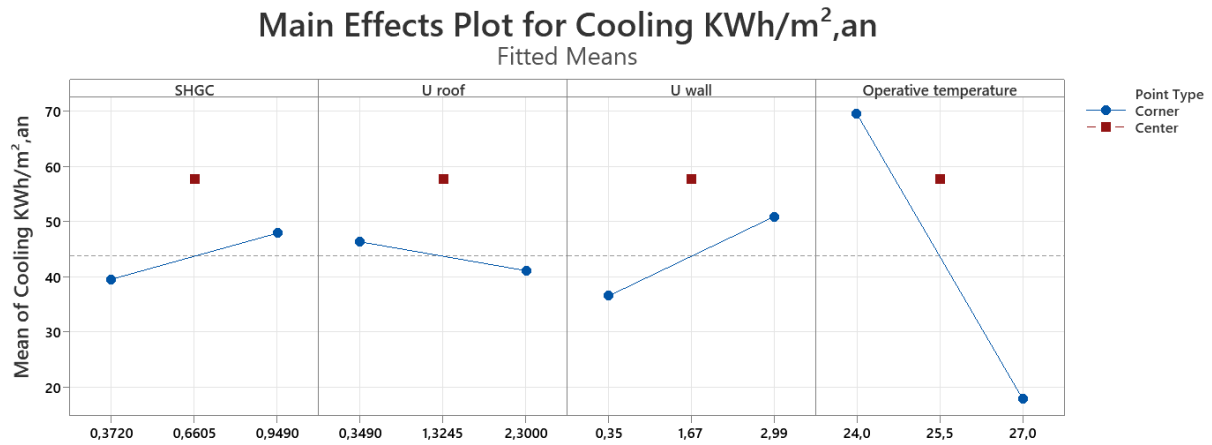


Figure 13. Main effects plots for cooling loads

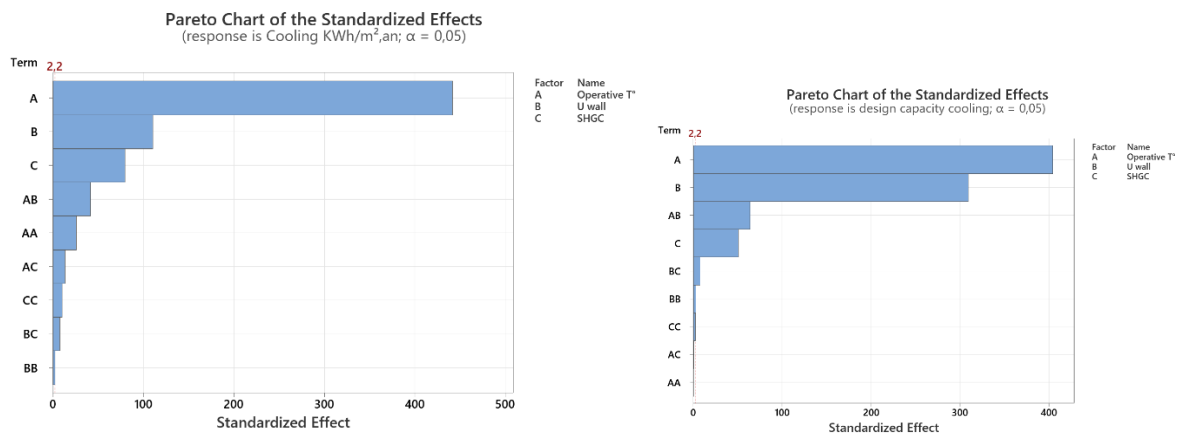


Figure 14. Pareto charts for cooling loads and design capacity

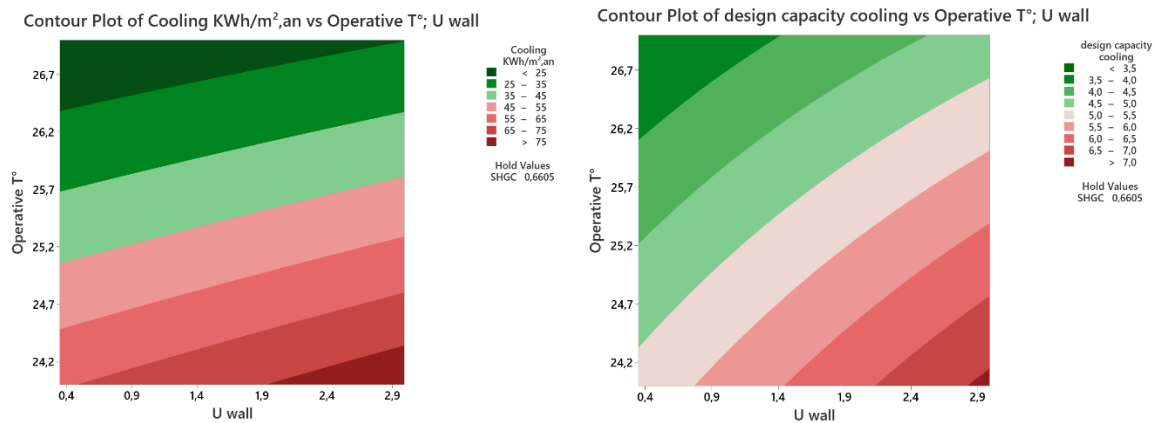


Figure 15. Contour plots for cooling loads and cooling design capacity

5.3.3 Optimal solutions for heating and cooling loads

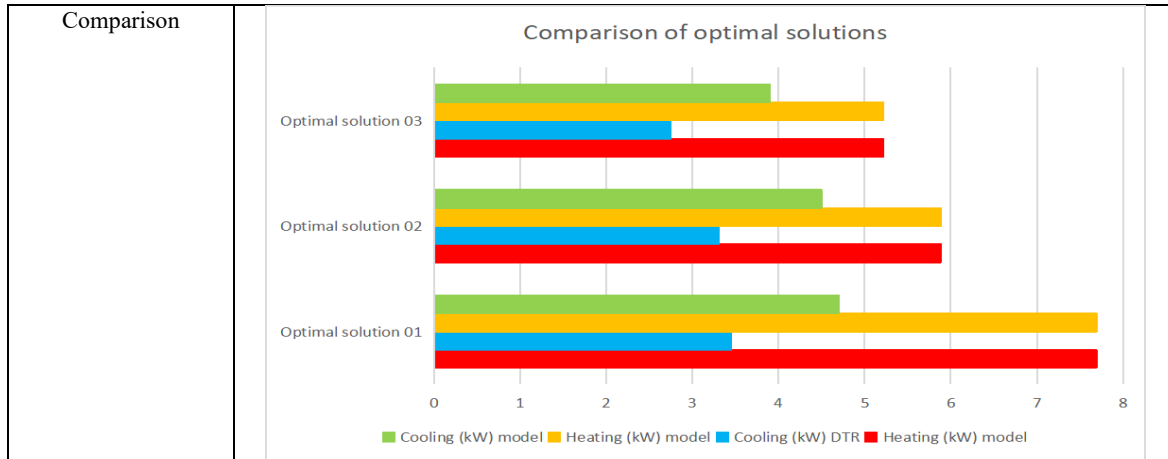
This section presents three scenarios that consolidate the most influential factors affecting heating and cooling loads, with comparative analysis between regulatory calculations, DOE models, and dynamic thermal simulations. Based on this comparison, optimal solutions are identified using contour plots for

each scenario, meeting both regulatory compliance and the optimal values derived from the models. The scenarios are outlined in table 6. Optimal solutions are determined by screening for responses that meet regulatory requirements for thermal transmission coefficients and required indoor seasonal temperatures. Selected factors optimize heating and cooling responses based on defined constraints. The graph (table 6) illustrates the comparison, where Solution 1 achieves a 37% optimization in heating, with 4.6 kW reduction and 10.5% optimization for cooling. Solution 2 reaches an optimization of 6 kW (52%) for heating and 13.2% for cooling. Solution 3 provides the highest optimization (59.6%) for heating and 26% in cooling loads, and while it's optimized primarily for heating, Solution 3 is suitable for cases where higher heating capacity is essential but allows for moderate cooling efficiency. The model is adjusted as necessary to meet or minimize the target values, ensuring an optimal balance between regulatory compliance DTR C3.2/4 and energy performance.

While this study is based on simulation results without direct empirical calibration, the findings align closely with experimentally validated research conducted in Algeria. Several studies using monitored real data [9-11] reported comparable energy savings following the application of thermal insulation and passive design strategies. For example, reduction in heating demand ranging from 37% to 59,6% and cooling demand from 10% to 26% observed in this study are consistent with the experimental outcomes documented in these works. This consistency supports the relevance of the present model outputs for informing energy-efficient strategies in the Algerian residential sector.

Table 6. Optimal solutions results

Optimal Solution	Optimal values	Results
01	U roof= 0.75 U wall =0.815 SHGC= 0.372 T° winter= 21°C T° summer= 27°C	Heating. DTR=7.70 kW Heating. model= 7.69 kW Cooling. DTR= 3.45 kW Cooling. Model= 4.6 kW
02	U roof= 0.586 U wall=0.35 SHGC= 0.372 T° winter= 21°C T° summer= 24°C	Heating. DTR=5.89 kW Heating. Model= 5.88 kW Cooling. DTR= 3.31 kW Cooling. Model= 4.50 kW
03	U roof= 0.349 U wall=0.35 SHGC= 0.372 T° winter= 21°C T° summer= 26°C	Heating. DTR=4.74 kW Heating. Model= 5.22 kW Cooling. DTR= 2.75 kW Cooling. Model= 3.90 kW



5.4 Recommendations for enhancing model accuracy

In this study, a linear regression model (figure 16) was applied to all cumulative data, evaluating heating loads results based on heating design capacity. Results depicted in the fitted line plot show an R^2 value of 88.2%, meaning that 88.2% of the variance in heating demand is explained by the predictor, indicating a strong explanatory model. The normal probability plot of residuals (figure 17) suggests that most residuals align with a normal distribution (illustrated by the red line), with some deviations at the extremes. This indicates that further data processing may be required. To improve model predictive accuracy, the recommendations include expanding experimental data to increase robustness and adopting a hybrid approach that combines experimental design data with machine learning algorithms, thereby maximizing predictive power while maintaining the rigorous framework of experimental design.

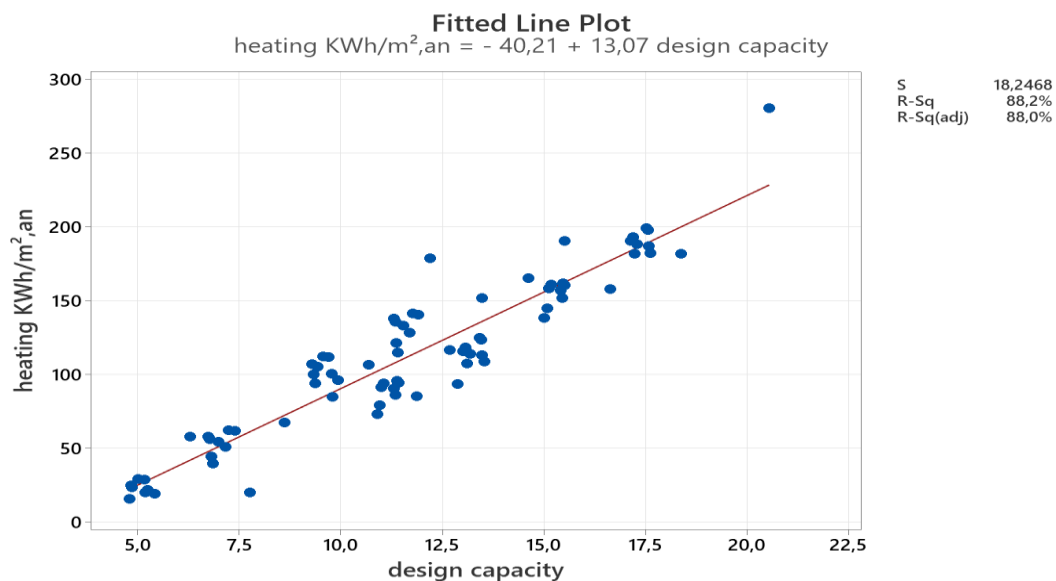


Figure 16. Fitted line plot for cumulative data (heating loads)

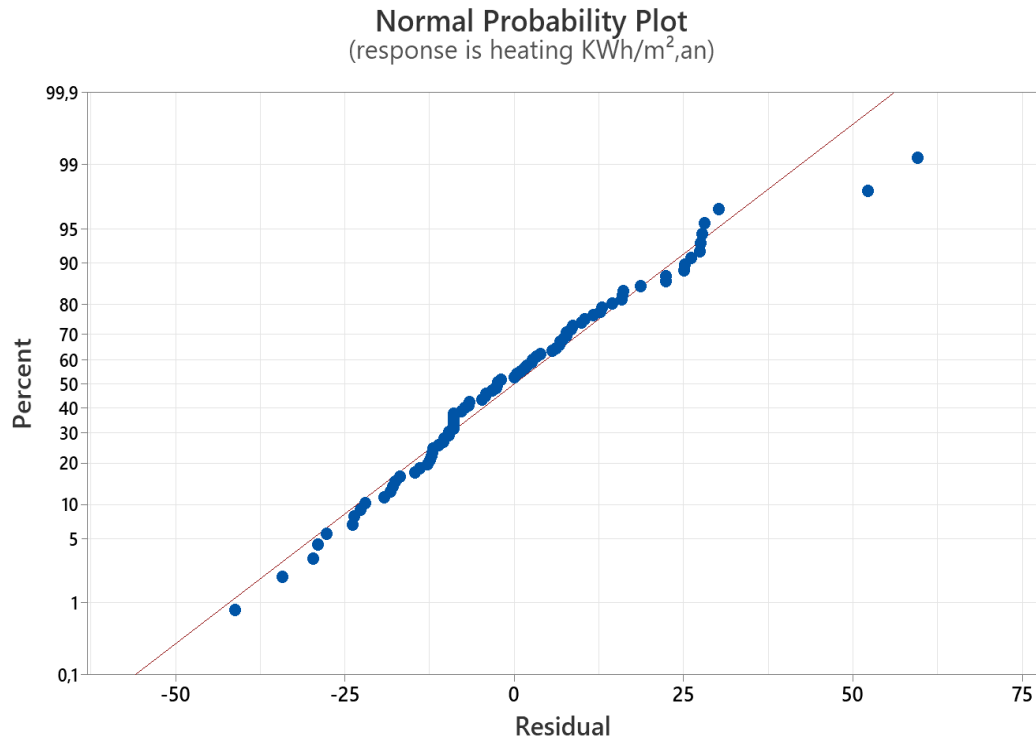


Figure 17. Normal probability plot for residuals.

6. Conclusion

This aforementioned research underscores the importance of optimizing building envelope parameters to reduce energy consumption in residential buildings within Algiers hot-summer Mediterranean climate. Results revealed that U-values for the roof and walls, as well as operative indoor temperature, are key drivers for heating loads, while operative temperature, wall U-value and SHGC influence cooling demands. Optimized solutions offer substantial energy savings, with potential reductions ranging from 37% to 59.6% for heating and 10% to 26% for cooling, while remaining compliant with the Algerian regulatory standards (DTR C3.2/4). These results align with Algeria's Nationally Determined Contribution (NDC) toward the UNFCCC Climate Convention, particularly through Strategy 01 (target 230 kWh/m² per year by roof insulation) and Strategy 03 (target 205 kWh/m² per year by envelope insulation), reinforcing the relevance of passive design strategies in both retrofitting existing buildings and guiding future residential projects through 2030.

Despite the strength of the findings, some limitations remain. In particular, HVAC systems were modelled in a simplified manner. This limitation constrained the evaluation of active system performance within the optimization framework. To enhance accuracy, future work should integrate more detailed HVAC modelling. Additionally, although economic aspects were not addressed in this study, incorporating cost-benefit analyses of insulation strategies would improve decision-making for

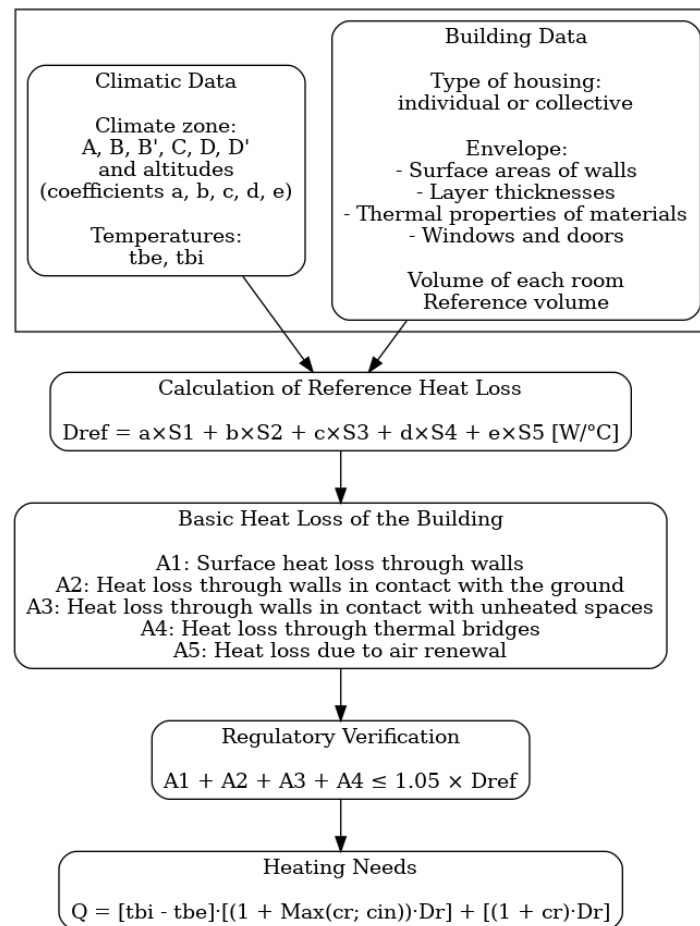
real world implementation. Further research should also consider the integration of active renewable energy systems, such as PV and solar thermal solutions, to support a more comprehensive approach to energy efficient residential design.

References

- [1] International Energy Agency IEA, Buildings - Energy System, <https://www.iea.org/energy-system/buildings>, (accessed 1 Dec. 2024).
- [2] Ministère de l'énergie, <https://energy.gov.dz>, (accessed 31 Oct. 2024).
- [3] Programme De Développement Des Nations Unies, Elaboration de la Troisième Communication Nationale et du Premier Rapport Biennal de l'Algérie auprès de la CCNUCC, <https://www.undp.org/fr/algeria/projets/elaboration-de-la-troisieme-communication-nationale-et-du-premier-rapport-biennal-de-lalgerie-aupres-de-la-ccnucc>, (accessed 20 May 2024).
- [4] J.K. Telford, A brief introduction to design of experiments, Johns Hopkins APL Tech. Dig. 27 (2007) 224–232.
- [5] Z. Romani, Développement d'une méthode d'aide à la décision multicritère pour la conception des bâtiments neufs et la réhabilitation des bâtiments existants à haute efficacité énergétique, PhD Thesis, Université de La Rochelle, Université Abdelmalek Essaâdi, 2015.
- [6] A.N. Sadeghifam, S.M. Zahraee, M.M. Meynagh, I. Kiani, Combined use of design of experiment and dynamic building simulation in assessment of energy efficiency in tropical residential buildings, *Energy Build.* 86 (2015) 525–533.
- [7] J. Xu, J.H. Kim, H. Hong, J. Koo, A systematic approach for energy efficient building design factors optimization, *Energy Build.* 89 (2015) 87–96.
- [8] H. Belahya, A. Boubekri, A. Kriker, A fast evaluation method for energy building consumption based on the design of experiments, *IOP Conf. Ser.: Earth Environ. Sci.*, IOP Publishing, 2017.
- [9] L. Bentoumi, T. Bouacida, R. Bessaih, A. Bouttout, Impact of thermal insulation on energy consumption in buildings, *J. Therm. Eng.* 10 (2024) 924–935.
- [10] The Algerian Regulatory Technical Document C3.2/4.
- [11] N. Meftah, Z.L. Mahri, Analysis of Algerian energy efficiency measures in buildings for achieving sustainable development goals, *J. Renew. Energ.* (2021) 37–44.
- [12] S. Semahi, M.A. Benbouras, W.A. Mahar, N. Zemmouri, S. Attia, Development of spatial distribution maps for energy demand and thermal comfort estimation in Algeria, *Sustainability* 12 (2020) 6066.
- [13] S. Rahmouni, R. Smail, A design approach towards sustainable buildings in Algeria, *Smart Sustain. Built Environ.* 9 (2020) 229–245.
- [14] K.E.B. Djebbar, S. Salem, A. Mokhtari, A multi-objective optimization approach of housing in Algeria. A step towards sustainability, *Urban. Arhit. Constr.* 9 (2018) 131.

Appendix 1: Calculation and verification method according to DTR C3.2/4

The following schemes summarize the calculations and verification for heating and cooling needs during the winter and summer periods. The equations are taken from the regulatory document (9, 10). For heating:



With:

Tbe: Base outdoor temperature [°C]

Tbi: Base indoor temperature [°C]

Dref: Reference heat loss [W/°C]

Cr: is an estimated ratio of heat losses due to the possible piping network.

Cin: represents an overpower coefficient.

Q: Required heating power Q [W]

For cooling:

The sum of the thermal gain through the glazed walls and the overhead opaque walls must be verified in July at 3 p.m. (15h), for an interior dry temperature of 27°C.

With:

Aref: Reference heat gain

APO: Heat gains through an opaque wall

AV: Heat gains through glazed surfaces

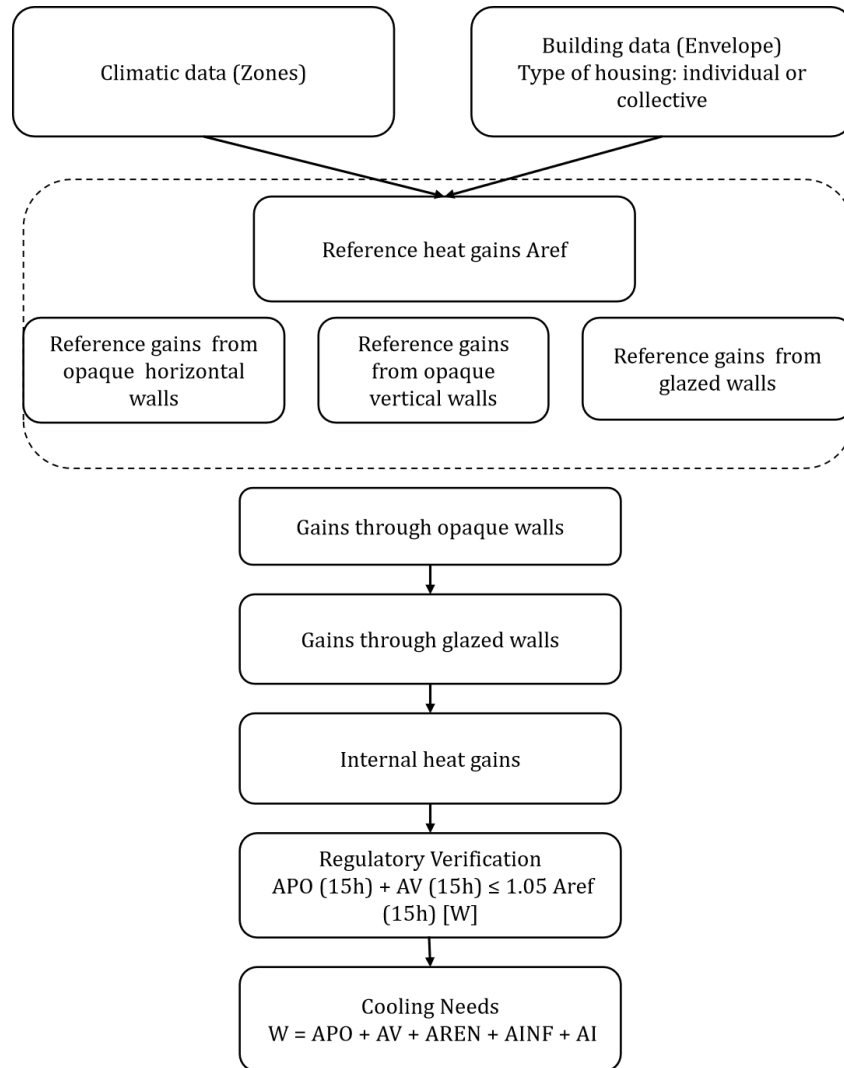
AREN: Heat gains due to air renewal

AINF: Heat gains due to outdoor air infiltration

AI: Internal heat gains

AVT: Heat gains by transmission through glazed surfaces

AVE: Solar radiation heat transfer through glazed surfaces



Appendix 2: fractional factorial design results

U wall	U roof	U window	WW R-E	WW R-S	SHG C	Minimum fresh airflow	Infiltrati on Rate	CO P-H	EE R-C	Heating (kWh/ m ²)	Cooling (kWh/ m ²)
1	1	1	-1	-1	1	-1	-1	1	-1	156.81	36.43
1	1	-1	1	1	-1	1	1	1	-1	190.47	36.81
1	-1	-1	-1	1	-1	1	-1	1	1	91.31	37.38
-1	-1	-1	-1	1	-1	1	1	-1	-1	56.1	34.38
-1	-1	-1	1	-1	-1	-1	-1	-1	1	24.93	34.57
1	-1	1	-1	1	-1	-1	1	1	-1	123.3	39.56
-1	-1	-1	-1	1	1	-1	-1	-1	-1	15.74	39.99
-1	1	-1	1	-1	-1	1	-1	1	-1	107.19	27.99
1	-1	-1	-1	-1	-1	1	-1	-1	-1	93.97	37
-1	1	-1	1	1	1	-1	1	-1	1	114.91	38.58
1	-1	1	1	-1	-1	1	-1	1	1	95.58	38.54
-1	-1	1	1	-1	-1	1	1	-1	-1	62.14	36.15
1	1	1	1	-1	1	1	1	-1	-1	186.91	41.8
1	-1	-1	1	-1	-1	-1	1	1	-1	118.39	39.87
1	-1	1	-1	-1	-1	-1	1	-1	1	124.68	39.10
1	-1	-1	1	1	-1	-1	1	-1	1	115.7	40.26
1	-1	-1	1	1	1	1	-1	-1	1	73.16	47.28
-1	-1	-1	1	1	-1	-1	-1	1	-1	23.49	35.135
-1	-1	-1	-1	-1	-1	1	1	1	1	57.81	33.84
-1	1	1	1	1	-1	-1	1	-1	-1	140.57	30.79
-1	1	-1	-1	1	1	1	-1	1	1	93.79	32.10
1	-1	1	1	1	1	-1	1	-1	-1	108.78	48.78
1	1	-1	1	1	1	-1	-1	1	-1	138.33	41.46
-1	1	1	-1	-1	-1	1	-1	-1	1	112.18	26.85
-1	-1	1	-1	-1	1	1	1	1	-1	54.4	38.24
-1	1	-1	1	1	-1	1	-1	-1	1	105.31	28.43
1	-1	1	-1	-1	1	1	-1	-1	1	90.55	40.51
-1	-1	1	-1	1	-1	-1	-1	-1	1	28.91	33.35
-1	1	-1	-1	1	-1	-1	1	1	1	135.88	28.8
-1	-1	1	-1	-1	-1	-1	-1	1	-1	29.09	32.75
1	-1	-1	-1	-1	1	-1	1	-1	-1	114.07	42.61
-1	-1	1	1	1	-1	1	1	1	1	61.97	36.76
1	-1	1	1	1	-1	1	-1	-1	-1	94.25	39.10
1	-1	-1	1	-1	1	1	-1	1	-1	79.21	45.28
-1	-1	1	1	-1	1	-1	-1	-1	-1	21.82	43.16
-1	-1	1	1	1	1	-1	-1	1	1	19.33	45.28
-1	1	1	1	-1	-1	-1	1	1	1	141.1	30.23
-1	1	-1	1	-1	1	-1	1	1	-1	121.19	36.69
1	1	-1	-1	-1	1	1	1	1	1	188.36	38.79
1	-1	-1	-1	1	1	-1	1	1	1	107.41	44.44
1	1	-1	-1	1	1	1	1	-1	-1	181.55	40.23

1	1	-1	-1	1	-1	-1	-1	-1	-1	158.27	33.86
-1	1	1	-1	-1	1	-1	1	-1	1	133.02	31.78
-1	1	1	1	-1	1	1	-1	1	1	100.37	34.46
1	1	1	1	1	1	1	1	1	1	182.15	43.2
-1	-1	-1	1	1	1	1	1	1	-1	39.52	47.32
1	1	-1	-1	-1	-1	-1	-1	1	1	160.89	33.59
1	1	1	-1	1	1	-1	-1	-1	1	151.93	37.76
-1	1	-1	-1	-1	1	1	-1	-1	-1	100.22	30.24
1	-1	1	1	-1	1	-1	1	1	1	113.27	46.38
-1	1	-1	-1	-1	-1	-1	1	-1	-1	137.81	28.37
-1	1	1	-1	1	1	-1	1	1	-1	128.45	33.43
1	1	1	-1	-1	-1	1	1	1	-1	199.04	36.07
1	1	-1	1	-1	-1	1	1	-1	1	193.09	36.53
1	-1	1	-1	1	1	1	-1	1	-1	85.98	42.14
-1	-1	1	-1	1	1	1	1	-1	1	50.78	40.26
1	1	1	-1	1	-1	1	1	-1	1	197.58	36.48
1	1	-1	1	-1	1	-1	-1	-1	1	144.86	39.93
-1	-1	-1	1	-1	1	1	1	-1	1	44.52	44.91
-1	1	1	-1	1	-1	1	-1	1	-1	111.59	27.42
-1	-1	-1	-1	-1	1	-1	-1	1	1	19.94	37.68
1	1	1	1	-1	-1	-1	-1	-1	-1	161.91	34.78
-1	1	1	1	1	1	1	-1	-1	-1	96.22	36.16
1	1	1	1	1	-1	-1	-1	1	1	160.45	35.18

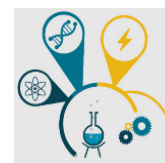
Appendix 3: polynomial models for heating loads and design capacity

Type	Equation	R ²
Linear	Regression equation in uncoded units Heating KWh/m ² = -764.3 + 52.91 U roof + 33.92 U wall + 34.71 operative T°	95.2%
Linear +quadratic	Heating KWh/m ² .year = 174 – 5.8 U roof + 41.5 U wall - 48 T° + 22.18 (U roof) ² - 2,26 (U wall) ² + 1.89 (operative T°) ²	98.47%
Linear+ interactions	Heating KWh/m ² .year = -325 – 120.4 U roof- 90.9 U wall + 14.72 T° - 0.41 U roof*U wall + 7.91 U roof*T° + 5.70 U wall*T°	96.7%
Full quadratic	Heating KWh/m ² = 612 – 179.10 U roof – 83.36 U wall – 68.4 T° operative + 22.178 (U roof) ² - 2.260 (U wall) ² + 1.890 (T° operative) ² - 0.408 U roof*U wall + 7.906 U roof*T° operative + 5.699 U wall*T° operative	99.98%
Type	Equation	R ²
Linear	Design capacity = -14.225 + 2.9288 U roof + 3.0345 U wall + 0.8140 operative T°	98.2%
Linear +quadratic	Design capacity = -13.9 + 2.996 U roof + 3.138 U wall + 0.77 operative T° - 0.0253 (U roof) ² - 0.0310 (U wall) ² + 0.0009 (T° operative) ²	98.47%
Linear+ interactions	Design capacity = -6.631 + 0.557 U roof + 0.366 U wall + 0.4690 T° operative + 0.0019 U roof*U wall + 0.1076 U roof*T° operative + 0.1212 U wall*T° operative	99.9%
Full quadratic	Design capacity = -6.284 + 0.6246 U roof + 0.4699 U wall + 0.4290 T° operative – 0.02532 (U roof) ² - 0.031020 (U wall) ² + 0.00091 (T° operative) ² + 0.001941 U roof*U wall + 0.107637 U roof*T° operative + 0.121166 U wall*T° operative	99.99%

Appendix 4: polynomial models for cooling loads and design capacity

Type	Equation	R ²
Linear	Cooling KWh/m ² = 472.6 – 17.468 Temperature + 4.958 U wall + 16.38 SHGC	96.10%

Linear +quadratic	Cooling KWh/m ² = 1323 – 83.8 Temperature + 4.50 U wall – 1.9 SHGC + 1.301 (Temperature) ² + 0.136 (U wall) ² + 13.8 (SHGC) ²	97.32%
Linear+ interactions	Cooling KWh/m ² .year = 377.4 – 13.79 Temperature + 41.3 U wall + 70.7 SHGC – 1.394 Temperature*U wall – 2.05 Temperature*SHGC – 1.27 U wall*SHGC	96.7%
Full quadratic	Cooling KWh/m ² .year = 1227.6 – 80.14 Temperature + 40.889 U wall + 52.37 SHGC + 1.3010 (Temperature) ² + 0.1362 (U wall) ² + 13.84 (SHGC) ² - 1.3939 Temperature*U wall – 2.045 Temperature*SHGC – 1.274 U wall*SHGC	99.96%
Type	Equation	R²
Linear	Design capacity cooling = 21.308 – 0.6847 Temperature + 0.5955 U wall + 0.447 SHGC	96.31%
Linear +quadratic	Design capacity cooling = 21.7 – 0.72 Temperature + 0.622 U wall + 0.27 SHGC + 0.0006 (Temperature) ² - 0.0078 (U wall) ² + 0.14 (SHGC) ²	95.40%
Linear+ interactions	Design capacity cooling = 17.520 – 0.53370 Temperature + 2.8929 U wall + 0.280 SHGC – 0.09154 Temperature*U wall + 0.00289 Temperature*SHGC + 0.05580 U wall*SHGC	99.97%
Full quadratic	Design capacity cooling = 17.95 – 0.565 Temperature + 2.9190 U wall + 0.100 SHGC + 0.00061 (Temperature) ² - 0.00783 (U wall) ² + 0.1365 (SHGC) ² - 0.09154 Temperature*U wall + 0.00289 Temperature*SHGC + 0.05580 U wall*SHGC	99.99%



Power Optimization in MIMO-NOMA VLC Systems Using Fractional and Dynamic Frequency Reuse

Nesrine Titi, Sofiane Haddad *, Ammar Soukkou

Department of Electronics, Faculty of Sciences and Technology, MSB Jijel University, Algeria

*Corresponding author: (S. Haddad), Email Address s_haddad@univ-jjel.dz

Abstract

This paper investigates power allocation strategies for enhancing the achievable sum rate in indoor Multi-User Visible Light Communication (MUVLC) systems using Multiple-Input Multiple-Output Non-Orthogonal Multiple Access (MIMO-NOMA). Two frequency reuse methods—Fractional Frequency Reuse (FFR) and Dynamic Frequency Reuse (DFR)—are proposed and evaluated against the existing Normalized Gain Difference Power Allocation (NGDPA) technique. Simulation results for a (2×2) MIMO-NOMA-VLC system show that while FFR can offer substantial performance improvements under favorable conditions, its effectiveness diminishes and may even underperform in specific scenarios. In contrast, DFR consistently outperforms NGDPA across a range of network conditions, demonstrating robust and reliable sum rate enhancement. This consistent adaptability makes DFR a more effective and preferred solution for optimizing power allocation and maximizing spectral efficiency in indoor VLC environments.

Keywords: Multiple-input, Multiple-output, Non-orthogonal multiple access, Visible light communication systems, Power allocation methods, Fractional Frequency Reuse, Dynamic Frequency Reuse.

<https://doi.org/10.63070/jesc.2025.013>

Received 05 April 2025; Revised 10 May 2025; Accepted 23 May 2025.

Available online 28 May 2025.

Published by Islamic University of Madinah on behalf of *Islamic University Journal of Applied Sciences*. This is a free open access article.

1. Introduction

VLC has gained significant attention as an emerging technology for advancing 5G and B5G (beyond 5G) wireless systems. One of the key advantages of VLC is that it operates in a wide license-free spectrum, which makes it an attractive option for wireless communication. The use of VLC technology allows for the exploitation of the visible light spectrum, which is typically not used for communication purposes, thus offering a vast and unutilized resource for wireless data transmission. Moreover, VLC can potentially offer high-speed data transmission, low latency, and high security, making it a strong contender for the upcoming generation of wireless networks.

In the last years, there has been a growing focus on optimizing the allocation of transmit power values to users in combined NOMA-VLC networks. This involves determining the appropriate power values to be assigned to each user by the LED transmitter. NOMA is a technique designed to enable several users to be served using the same resource. VLC systems, on the other hand, offer the advantage of a channel condition that typically stays consistent and only changes with the movement of users. Thus, VLC can be a particularly effective approach for enhancing the effectiveness of NOMA-based systems. By leveraging the stability of the VLC channel, it becomes possible to optimize the transmit power values assigned to each user in the NOMA-VLC network, thereby improving the overall system performance. In [1], a power allocation method named NLGRPA (Normalized Logarithmic Gain Ratio Power Allocation) has been suggested for NOMA-assisted MIMO-VLC networks. This method efficiently allocates power by utilizing optical channel information from all LEDs on the transmitter. The authors have indicated that the suggested NLGRPA method has achieved a substantial enhancement in terms of the achievable sum rate compared to conventional power allocation approaches. In [2], a 2-user 2×2 MIMO-NOMA-VLC system using OOK (On-Off Keying) and L-PPM (L-pulse position modulation) is proposed, and the authors derived the BER (Bit Error Rate) formulas for the system. The authors observed that increasing the number of photo-detectors at the receiver fails to substantially enhance the system's error performance. To enhance the error performance of the OOK and L-PPM modulated MIMO-NOMA-VLC system, two dynamic field of view (FOV) strategies are proposed. These strategies outperform the existing fixed FOV receivers in a MIMO environment.

Moreover, [3] provides a thorough overview of user pairing and power allocation techniques for NOMA-based VLC systems. The authors have discussed various user pairing schemes and power allocation strategies, highlighting that high channel gain difference is a significant concern when implementing

NOMA effectively. In [4], a secure NOMA VLC system with OFDM modulation is proposed and experimentally demonstrated. In which chaotic phase rotations in the selected mapping has been used to decrease the PAPR ratio (Peak-to-Average Power Ratio) of the transmitted OFDM-NOMA signal. The proposed scheme provides two-fold protection against eavesdroppers with a large key space and guarantees the privacy between legitimate users while minimizing the PAPR. Besides, in [5], NOMA has been combined with VLC to create a high-speed and error-free network. The authors have used OOK and L-PPM in a 2-user downlink NOMA VLC-based system, and evaluated the system's performance with perfect and imperfect channel state information (CSI). As findings, giving at least 60% of the power to the far user resulted in significantly better performance for that user, and L-PPM modulation with $L > 2$ has outperformed OOK modulation. Additionally, increasing the order of modulation has improved the performance for both users. However, if the far user shifts away from the fixed location of the near user and toward the corner of the room, their error performance suffers. The performance of both users also has been improved with a smaller FOV, with the close user performing better with a FOV of less than 35° than the far user with a FOV of 60° . Both OOK and L-PPM modulated NOMA-VLC systems have performed poorly with channel estimation error, and this effect is worsened with more complex modulation techniques. In [6], a NOMA VLC network that can serve 2, 3, or 4 clients simultaneously using NHS-OFDM IFFT/FFT size efficient (SE) OFDM format has been proposed and developed. The authors conducted a numerical analysis of the impact of signal amplitude on bit error rate (BER) performance for various users, and compared the suggested system with a common HS OFDM modulation example, termed DCO-OFDM NOMA-VLC system.

Furthermore, the authors in [7] have employed NOMA in VLC systems and proposed a simplified gain ratio power allocation method (S-GRPA) as a low-complexity power allocation method for indoor NOMA-based VLC systems. The authors found that the suggested S-GRPA system used a look-up table to obtain channel gains, and although users with stronger channel quality experienced some performance variations during a single trial, the average data rate over multiple trials was higher than that achieved using the conventional GRPA method. Besides, the suggested S-GRPA system has minimal feedback overhead and computational complexity, suggesting a promising future for high-speed VLC systems. An effective framework for a combined power line communication (PLC) and VLC system has been explored in [8], with a focus on its potential applications in smart grids. The work has explored NOMA as a means of growing the capacity of the integrated system, given the opportunistic features of both the VLC and PLC systems, which focus primarily on lighting and power delivery. The paper [9] provided a

comprehensive review of previous studies on 5G and B5G, and compared them to various paper's contributions, distinctiveness, and advantages. It covered various topics, including the prerequisites and technologies for 5G and B5G, channel analysis, and NOMA's significance in these networks, different types of NOMA, the architecture of the NOMA network, mobility management (MM), asynchronous and synchronous operations in NOMA, energy and green aspects of NOMA in 5G and B5G, challenges faced by NOMA, solutions for these challenges, and NOMA's performance indicators. Also, in [10] the authors have demonstrated the feasibility of using NOMA in optical MIMO-VLC systems. They showed that the NOMA scheme provided a good trade-off balancing throughput and fairness, and increased system capacity for a higher number of users. The authors proposed utilizing channel estimation techniques, specifically ISFA and MMSE, to remove inter-user interference, along with effective channel equalization for MIMO demultiplexing.

Challenges and limitations of integrating NOMA with 5G and future wireless technologies were highlighted in [11], including signaling, practical implementation, resource allocation, and security issues. Various analytical, matching theory, game theory, graph theory, and machine learning approaches have been proposed to address these challenges. The authors have conducted an in-depth investigation and comparison of different options, and provided insights into the operability and usability of NOMA for qualitative study. They also suggested intriguing research paths and challenges for applying PD NOMA to current and next-generation wireless networks. In [12], the authors have recommended a framework for user connection and power distribution in a 2-tier heterogeneous network using non-orthogonal multiple access. They took into consideration channel uncertainties and real-world wireless communication environments by presenting them as probability constraints. The non-convex objective function that regulated intra-cell and inter-cell interference was solved using the logarithmic approximation approach, and a method for dispersed user association was developed based on Lagrangian dual analysis. The authors concluded that their proposed approach outperformed both the FTPA algorithm and the conventional OMA algorithm in a dynamic communication environment. Further, in [13] the authors have presented a literature survey that highlights the need to shift from the current RF band to VLC due to its limitations. They have proposed a mathematical model that considers reflection from various reflectors and suggest approaches such as Bragg grating, adaptive beam shifting, and hybrid access technology to enhance signal strength.

An investigation of a unique problem of blind source separation in communication systems using observed magnitude-only measurements of its convolutive mixing has been presented in [14]. In which a blind

receiver architecture that is capable of reconstructing signals from their recorded phaseless convolutive mixture with the trade-off of requiring more measurements has been introduced. Both deterministic and stochastic subspaces can be used with the given strategy, and the experimental results and theoretical findings are in agreement. In [15], scientists have reviewed current publications on 6G, covering its introduction, core technologies, basic architecture, challenges, and relevant factors. The study included several applications and architectural descriptions, clarifying the current state-of-the-art and the direction of future research. Moreover, in [16], the authors have presented a comprehensive perspective on a number of OWC enabling technologies and survey probable OWC system problems. They have studied FSO and VLC as prospective OWC system implementation strategies and examined potential characteristics and categorizations of OWC systems, critical allowing technologies, connection design specifications and modulation techniques, main impairments and strategies to address them, and security concerns and methods to secure OWC. The work in [17], explored the use of multi-level AM modulation combined with trellis coding in a NOMA's downlink channel for VLC. The authors used a trellis decoder to implement non-orthogonal transmission through successive interference cancellation and superposition coding. They have compared two maximum likelihood signal detection levels for related 4 and 8 trellis-coded modulations. In [18], the authors discussed the application of NOMA technique to increase the attainable sum rate of MIMO-based multi-user VLC systems. They have proposed an NGDPA method to guarantee efficient and low-complexity power allocation in indoor MIMO-NOMA-based VLC systems. Through numerical simulations, they have demonstrated that NOMA with NGDPA attains a significantly higher sum rate than NOMA with GRPA in an indoor 2×2 MIMO-VLC system. They also found that applying NOMA with NGDPA in the 2×2 MIMO-VLC system with 3-users can boost the sum rate by up to 29.1%. The authors have suggested that MIMO-NOMA using the suggested NGDPA approach is potential for next high-speed multi-user VLC systems.

Furthermore, a broad-based multi-user MIMO-NOMA-VLC framework that uses OOK modulation and $M \times N$ LOS links for each user, to create a resilient, high-performance, and error-free network designed for multi-user environments, has been proposed in [19]. The authors have developed a closed form expression to calculate the error probability for the suggested system, taking into account a real-world example of imperfect SIC. Also, a thorough analysis of a 2×2 MIMO-NOMA-VLC system with three users, generating a precise closed-form formula of the system's error probability from this analysis has been presented. In [20], a HPD-LACO-OFDM (Hierarchical Pre-Distorted Layered Asymmetrically Clipped Optical) system for NOMA, providing excellent optical power efficiency and spectrum efficiency has

been developed. The experiment showed that the three layers HPD-LACO-OFDM based NOMA-VLC network outperformed the DCO-OFDM based NOMA-VLC network in terms of BER while requiring just half as much DC power. In [21], the authors have analyzed the performance of short-packet communication (SPC) within a downlink NOMA-VLC system. The SPC-NOMA VLC system was found to offer greater reliability and lower latency compared to LPC-NOMA VLC systems. Besides, the SPC-NOMA-VLC system outperformed the SPC-OMA VLC system in terms of throughput, latency, and dependability. In [22], researchers have proposed a NOMA-OFDM-VLC system based on non-Hermitian symmetry (NHS) inverse-fast Fourier-transform (IFFT)/FFT size efficient (SE), which was experimentally tested. The proposed strategy outperformed the HS based on DCO-OFDM NOMA-VLC system. A demodulator for NOMA-VLC based on convolutional neural networks (CNNs), which simultaneously performed signal recovery and compensation has been proposed in [23]. The proposed CNN-based receiver effectively corrects both linear and nonlinear distortions caused by multipath dispersion, limited modulation bandwidth, and LED nonlinearity, outperforming SIC and JD-based receivers. In [24], a development of a joint PLC-VLC power allocation (JPA) technique to maximize the sum throughput, which was found to outperform the SPA and NGDPA benchmarks under various minimum rate requirements and user densities has been presented. However, in the proposed PLC-VLC network, several problems related to multiple users power allocation and subcarrier allocation still need to be addressed.

Additionally, in [25], researchers proposed an OQAM/OFDM-NOMA modulation strategy, combining offset QAM/OFDM and non-orthogonal access, applicable to a multi-user, non-synchronized multi-cell VLC system. The optimal power ratio between the cell-center user and the cell-edge user was investigated, and the OQAM/OFDM-NOMA was found to be promising to increase user connectivity, stronger reliability, and enhanced user fairness for the multi-cell VLC system. Also, in [26], the authors conducted a theoretical analysis of errors in a downlink power-domain NOMA-based VLC system utilizing higher-order modulation schemes, considering the potential impact of imperfect SIC. The SER in NOMA-based systems was found to decrease when an appropriate PA was selected based on the users' modulation orders. In [27], the use of NOMA in VLC networks is investigated to enhance the sum rate performance and overcome the limitations of narrow modulation bandwidth. The authors have focused on power control for indoor downlink NOMA-VLC systems with a single LED and multiple users, and they found that the MFOPA scheme performed better in terms of sum rate and user fairness compared to existing SPA and GRPA schemes. Moreover, in [28], the authors have examined a downlink multiuser VLC

network with fluctuating vertical orientation and location of users, and they found that NOMA transmission with practical feedback methods generated optimal sum-rate performance. The authors in [29], have proposed a hybrid VLC-RF system using NOMA technology with imperfect channel-state information, and they found that the performance of both NOMA and OFDMA systems is affected by the quantity of CSI error, but the hybrid VLC-RF system with NOMA outperformed the VLC-Only System with NOMA in imperfect CSI scenarios. These findings are useful for the development of hybrid VLC-RF systems.

Recently, several techniques based on frequency reuse are proposed to optimize communication system's performance. Among these techniques are fractional frequency reuse (FFR) and dynamic frequency reuse (DFR) schemes. Both FFR and DFR work by dividing the entire bandwidth into multiple sub-bands, which are strategically allocated within the system to optimize power distribution. The authors in [30] have introduced a generalized FFR model for Ultra Dense Networks (UDNs), enabling better performance without increasing Base Station (BS) power usage. It addressed challenges in frequency band reuse caused by ultra-high BS densities, providing analytical solutions for user coverage probabilities. The work in [31] discussed FFR to manage interference in cellular networks, employing dynamic thresholding techniques like Otsu's and entropy methods. Furthermore, [32] introduced an approach to assess the uplink cellular spectral efficiency of MC-CDMA systems with fractional and soft frequency reuse. In [33], the authors proposed a coordination scheme for D2D communications, leveraging LTE's FFR to reuse uplink spectrum. Their approach adjusts transmissions to minimize interference with cellular uplinks, ensuring effective peer discovery while conserving radio resources. Evaluation demonstrates minimal impact on cellular transmissions and sufficient D2D discovery. Also, in [34], DFR and Weighted-DFR algorithms have been proposed to address inter-cell interference in indoor optical attocell networks utilizing LEDs for visible light communication. Also, the study in [35] explored the use of NOMA techniques MUVLC systems with MIMO technology. A power allocation technique based on the Water-Filling Algorithm is proposed and compared to NGDPA. Simulation results for a 2x2 indoor MIMO-NOMA-VLC system showed that the Water-Filling technique outperforms NGDPA, achieving a 3% higher sum rate gain at higher offsets.

In this work, we propose two methods to optimize power allocation in MIMO-NOMA VLC systems utilizing frequency reuse schemes. The rest of the paper is structured as follows: Section 2 details the system model of the indoor VLC network, including its characteristics and problem formulation. Section

3 introduces power allocation techniques and the developed models related to FFR and DFR. Section 4 presents the simulation results. Finally, Section 5 provides the conclusions.

2. System Model

This section presents a mathematical model for a 2x2 indoor MIMO-NOMA-VLC system, where each user has two photodiodes for enhanced signal reception and utilizes the full LED modulation bandwidth (**Figure 1**). The system uses DCO-OFDM modulation for high spectral efficiency and interference resilience, with potential for extension to more complex setups.

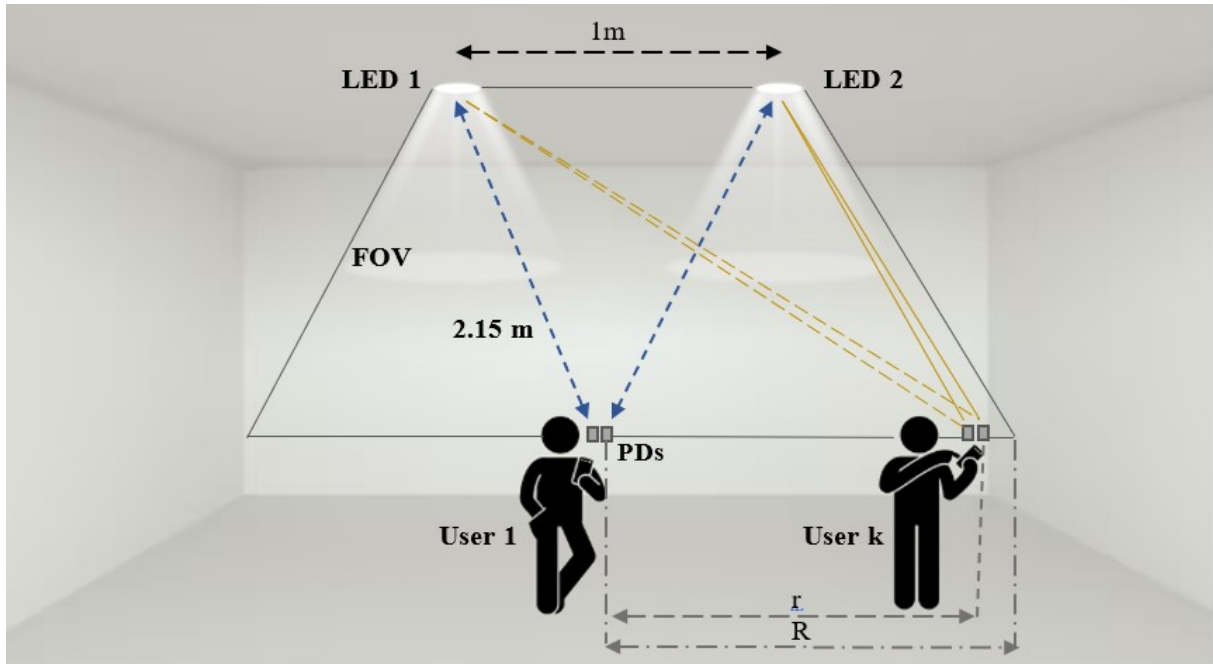


Figure 1. Graphic of a 2x2 MIMO-NOMA-VLC system.

Figure 2 illustrates the 2x2 MIMO-NOMA-VLC system using DCO-OFDM modulation. Input signals $x_1(t)$ and $x_2(t)$ are applied to LEDs 1 and 2, respectively. After DCO-OFDM modulation and DC polarization, the input signal $x_i(t)$ for the i -th LED is represented as [18]:

$$x_i(t) = \sum_{k=1}^K \sqrt{\rho_{i,k}} s_{i,k}(t) + I_{DC} \quad (1)$$

The signal $s_{i,k}(t)$ is the signal for the k -th user from the i -th LED, with $\rho_{i,k}$ being the electrical power allocated to the k -th user by the i -th LED, and I_{DC} representing the DC bias for each LED to ensure the signal $x_i(t)$ remains non-negative, as required for intensity modulation in VLC systems. $s_{i,k}(t)$ Encodes user data and

is orthogonal to other subcarriers to minimize interference. Upon modulation, the signal is emitted by the LED and captured by the users' photodiodes. The reception process utilizes MIMO-NOMA to separate signals from various LEDs, followed by demodulation to retrieve the original data, with further details provided below.

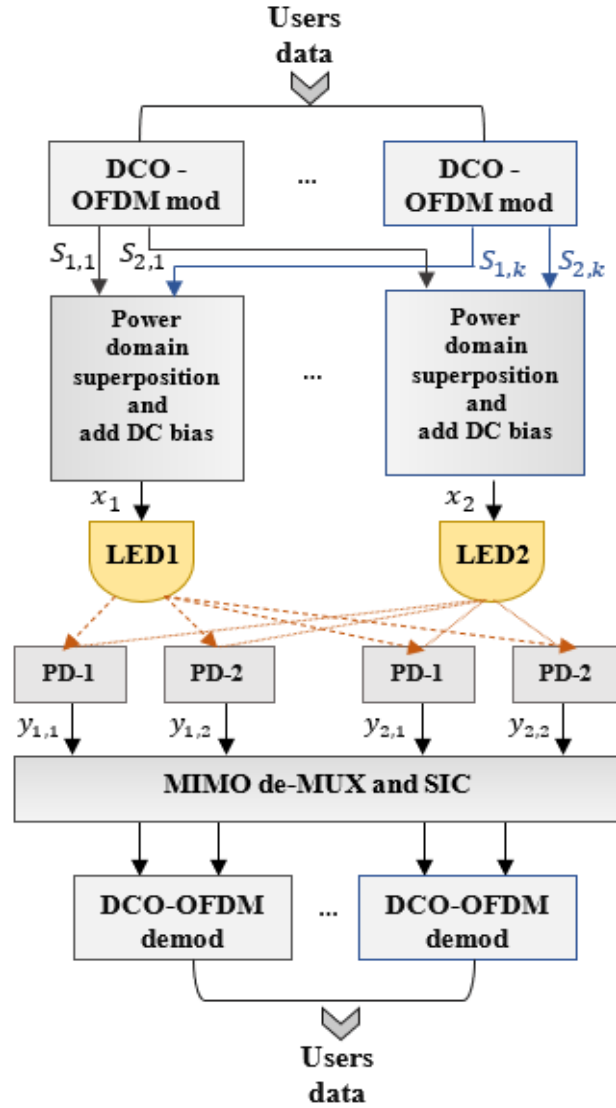


Figure 2. Functional diagram of a VLC system using DCO-OFDM modulation, based on 2x2 MIMO-NOMA [18].

To maintain consistent electrical power (P_{elec}) per LED, the following power constraint is applied:

$$\sum_{k=1}^K \rho_{i,k} = P_{elec} \quad (2)$$

For simplicity, P_{elec} per LED is set to 1. The received electrical signal by the k -th user after transmission is represented by the following vector:

$$\mathbf{y}_k = \gamma P_{opt} \zeta \mathbf{H}_k \mathbf{x} + \mathbf{n}_k \quad (3)$$

The received signal by the k -th user considering the responsivity γ of the photodetector and the LED optical output P_{opt} is characterized by a modulation index ζ , a channel matrix $H_K(2 \times 2)$, and an electrical signal vector $\mathbf{x} = [x_1 \ x_2]^T$. The additive noise is denoted by the vector \mathbf{n}_k .

This paper, as in [18], considers the Lambertian radiation pattern for each LED, focusing solely on LOS component. The LOS optical channel gain between the i -th LED ($i = 1, 2$) and the j -th user ($j = 1, 2$) is then calculated as follows:

$$h_{ji,k} = \frac{(m+1)A_{PD}}{2\pi d^2} \mu \eta \cos^m(\varphi) \cos(\theta) \quad (4)$$

The LOS optical channel gain from the i -th LED to the j -th user depends on factors like the LED's half-power angle, Lambertian order m , A_{PD} active area, optical filters, lenses, LED-user distance, emission angle φ , and incidence angle θ . If the incident light is outside the receiver's FOV, the gain is zero. MIMO demultiplexing and a low-complexity zero-forcing (ZF) method are used for data recovery. After demultiplexing and power normalization, the electrical signal vector for the j -th user is represented by the following formula:

$$\tilde{\mathbf{x}}_k = \mathbf{x} + \frac{1}{\gamma P_{opt} \zeta} \mathbf{H}_k^{-1} \mathbf{n}_k \quad (5)$$

The MIMO-NOMA-VLC system uses multiple LEDs and DCO-OFDM modulation. The input signal $x_i(t)$ for the i -th LED is derived from DCO-OFDM modulation, power superposition in the frequency domain, and addition of DC bias. The signal $s_{i,k}(t)$, meant for the k -th user from the i -th LED, has electrical power $\rho_{i,k}$ and DC bias I_{DC} . To maintain constant total electrical power P_{elec} for each LED, a power constraint is applied. After free-space propagation, the received electrical signal vector at user k is $\mathbf{H}_k [x_1 \ x_2]^T + \mathbf{n}_k$, where γ is the responsivity, P_{opt} is the optical output of the LED, ζ is the modulation index, \mathbf{H}_k is the 2×2 channel matrix of user k , and \mathbf{n}_k is the additive noise vector. Optical channel gains are calculated using the Lambertian radiation pattern and direct visibility component. Decoding uses MIMO demultiplexing with ZF and basic channel inversion. User decoding order for each LED is based

on the optical channel gains' sum for every user, sorted in descending order. SIC decoding is performed for every LED and user using the inverse of the channel matrix \mathbf{H}_k .

$$h_{1i,1} + h_{2i,1} > h_{1i,2} + h_{2i,2} > \dots > h_{1i,K} + h_{2i,K} \quad (6)$$

The order of the decoding for the i-th LED is then established as follows:

$$O_{i,1} < O_{i,2} < \dots < O_{i,K}. \quad (7)$$

This study assumes perfect SIC without error propagation in the signal, and the two users' data is gotten through DCO-OFDM demodulation.

3. Power allocation methods

3.1. Power Allocation with Normalized Gain Difference (NGDPA)

The NGDPA method optimizes power allocation in MIMO-NOMA VLC systems by efficiently distributing emission power among users sharing the same resource. It calculates the normalized gain difference by estimating transmitter-receiver channels, computing the gain difference between user pairs with mutual interference considered, and dividing this difference by the total sum of gains. Power is then allocated to maximize the normalized gain difference, with users having better channels receiving less power. The allocation for users k and k+1 on the i-th LED is based on the optical channel gain difference [18].

$$\rho_{i,k} = \left(\frac{h_{1i,1} + h_{2i,1} - h_{1i,k+1} - h_{2i,k+1}}{h_{1i,1} + h_{2i,1}} \right)^k \rho_{i,k+1} \quad (8)$$

3.2. Power Allocation using Fractional Frequency Reuse

FFR enhances spectral efficiency in MIMO-NOMA-VLC systems by dividing the frequency spectrum into fractions and allocating them to different users or cells. The power allocation scheme based on FFR is modeled as follows:

$$\Delta h_{i,k}^{FFR} = \alpha \cdot \Delta h_{i,k} \quad (9)$$

Where $\Delta h_{i,k}^{FFR}$ is the modified optical channel gain difference incorporating FFR for user k in the i-th LED, $\Delta h_{i,k}$ is the original optical channel gain difference for user k in the i-th LED, and α represents the FFR factor (α equal to 0.5 in our case study). Using the modified optical channel gain differences, the power allocation for the k-th user in the i-th LED incorporating FFR becomes:

$$\rho_{i,k}^{FFR} = \left(\frac{\Delta h_{i,k}^{FFR}}{h_{1i,1} + h_{2i,1}} \right)^k \rho_{i,k+1} \quad (10)$$

In this equation, we use $\Delta h_{i,k}^{FFR}$ to reflect the impact of FFR on the optical channel gain differences. This adjusted power allocation considers the modified channel conditions due to FFR while maintaining the same power allocation relationship between consecutive users within the LED.

3.3. Power Allocation with Dynamic Frequency Reuse

DFR is an algorithm for power allocation in MIMO-NOMA-VLC systems, where multiple users share the same transmission resource. DFR dynamically allocates frequency resources based on traffic and channel conditions. The DFR factor, denoted as β , represents the dynamic allocation factor for optical channel gain differences, which are then modified accordingly.

$$\Delta h_{i,k}^{DFR} = \beta_k \cdot \Delta h_{i,k} \quad (11)$$

Where $\Delta h_{i,k}^{DFR}$ is the modified optical channel gain difference incorporating DFR for the k-th user in the i-th LED, $\Delta h_{i,k}$ is the original optical channel gain difference for the k-th in the i-th LED and β_k is the DFR factor for the k-th user. The DFR factor is the ratio of power allocated to each LED based on channel gains. Power allocation for user k on the i-th LED incorporating DFR is then:

$$\rho_{i,k}^{DFR} = \left(\frac{\Delta h_{i,k}^{DFR}}{h_{1i,1} + h_{2i,1}} \right)^k \rho_{i,k+1} \quad (12)$$

The term $\Delta h_{i,k}^{DFR}$ is used to reflect the impact of DFR on the optical channel gain differences. This adjusted power allocation incorporates dynamic frequency allocation based on channel conditions and traffic demands while preserving the power allocation relationship between consecutive users within the LED. Including DFR enhances the adaptability and efficiency of the MIMO-NOMA-VLC system, especially under varying traffic loads and channel conditions.

4. Results and Discussion

4.1. System configuration

We evaluate a 2×2 MIMO-NOMA-VLC system using various power allocation techniques through simulations, based on the configuration in [18]. The system features LEDs spaced 1 meter apart and 2.15 meters vertically from users. Each LED has a 10 W output power with a 60° beam angle, a 10 MHz modulation bandwidth, and a 0.5 modulation index. Detectors have a 1 cm² active area, a 0.53 A/W responsivity, and are spaced 4 cm apart. Optical filter and lens gains are 0.9 and 2.5, respectively (see Table 1). We assess performance with a fixed user 1 at the center between LEDs 1 and 2, 2 meters from the coverage edge. Other users, denoted as K, are uniformly distributed with distances defined by r/R , where R is the distance from user 1 to the edge of the coverage. Furthermore, the normalized offset of user k regarding user 1 is calculated as $\frac{(k-1)r}{(K-1)R}$, which determines the position of each user relative to user 1, Table 2.

Table 1. System configuration.

Parameter	Value
LED Spacing	1 m
Vertical Distance (LEDs-Users)	2.15 m
LED Output Power	10 W
LED Beam Angle (half-power)	60°
Modulation Bandwidth	10 MHz
Modulation Index	0.5
Photodetector Area	1 cm ²
Photodetector Responsivity	0.53 A/W
Detector Spacing (per User)	4 cm
Optical Filter Gain	0.9
Optical Lens Gain	2.5

Table 2. User's description for performance evaluation.

Parameter	Description
User 1	Fixed user, center between LEDs 1 & 2, 2 m from system edge.
Users K	K users uniformly distributed around User 1 at distance r .
Normalized Offset (r/R)	Relative distance of User k to User 1 (R = distance between User 1 and system edge).
Normalized Offset ($\frac{(k-1)r}{(K-1)R}$)	User k position relative to User 1 (k = user number).

4.2. Comparison of achievable sum rates for different power allocation techniques

Based on **Figure 3** and the numerical results presented in Table 3, the achievable sum rate varies with the normalized offset (r/R) for the power allocation methods. The NGDPA method shows a decreasing sum rate with increasing offset due to higher interference. FFR has a sharper decline in sum rate as the offset increases, especially in the LED1+LED2 scenario, indicating higher sensitivity to offset changes. DFR maintains the highest sum rates among the methods but also shows a rapid decline with increasing offset. Overall, while NGDPA offers stable performance, DFR provides the highest sum rates but is more sensitive to offset variations, outperforming both NGDPA and FFR. **Figure 3** shows the mean performance of NGDPA, FFR, and DFR across different normalized offsets, with bars representing LED1+LED2, LED1, and LED2 configurations. Error bars indicate standard deviation, reflecting performance variability. Statistical comparisons reveal that DFR significantly outperforms NGDPA and FFR, with p-values of 0.0010071 (NGDPA vs. FFR), 9.2691×10^{-9} (NGDPA vs. DFR), and 5.6372×10^{-7} (FFR vs. DFR), confirming the superior performance of DFR over both NGDPA and FFR. **Figure 4** and **Figure 5** compare the Average Bit Error Rate (ABER) and Average Signal to Noise Ratio (ASNR) for various methods using 4-QAM modulation. NGDPA consistently provides the best ASNR across all offsets but shows significant ABER beyond an offset of 0.5. FFR maintains low ABER up to an offset of 0.5 but experiences a progressive decline in ASNR. DFR also has low ABER up to 0.5 but follows with a decrease in ASNR. NGDPA is ideal for applications prioritizing high signal quality, while FFR and DFR are better for maintaining low error rates at moderate offsets.

Table 3. Comparison of NGDPA, FFR, and DFR methods (Sum rate Mbits/s vs. Normalized Offset r/R).

Normalized Offset r/R	Sum rate Mbits/s								
	NGDPA method			FFR method			DFR method		
	LED1+LED2	LED1	LED2	LED1+LED2	LED1	LED2	LED1+LED2	LED1	LED2
0.1	113.6799	56.4781	57.2018	151.7281	75.2768	76.4513	279.2620	138.5732	140.6888
0.2	113.4502	56.5029	56.9473	150.2587	73.9810	76.2777	276.2659	136.3171	139.9487
0.3	112.1914	56.5035	55.6878	147.8315	72.2551	75.5763	271.2661	133.4380	137.8281
0.4	110.1434	56.4908	53.6526	144.4697	70.1275	74.3422	264.2201	129.9806	134.2394
0.5	106.3947	56.4595	49.9352	140.1866	67.6138	72.5727	255.0162	125.9234	129.0927
0.6	111.8666	56.3902	55.4764	134.9635	64.7073	70.2563	243.4436	121.1567	122.2869
0.7	112.1559	56.2273	55.9286	128.7119	61.3604	67.3514	229.1520	115.4680	113.6840
0.8	111.6286	55.8034	55.8252	121.1891	57.4470	63.7421	211.5407	108.4984	103.0423
0.9	109.8027	54.6114	55.1914	111.7640	52.6538	59.1103	189.3764	99.5615	89.8150

1	104.4413	51.8753	52.5659	98.4930	46.1082	52.3848	159.5254	86.9561	72.5693
---	----------	---------	---------	---------	---------	---------	----------	---------	---------

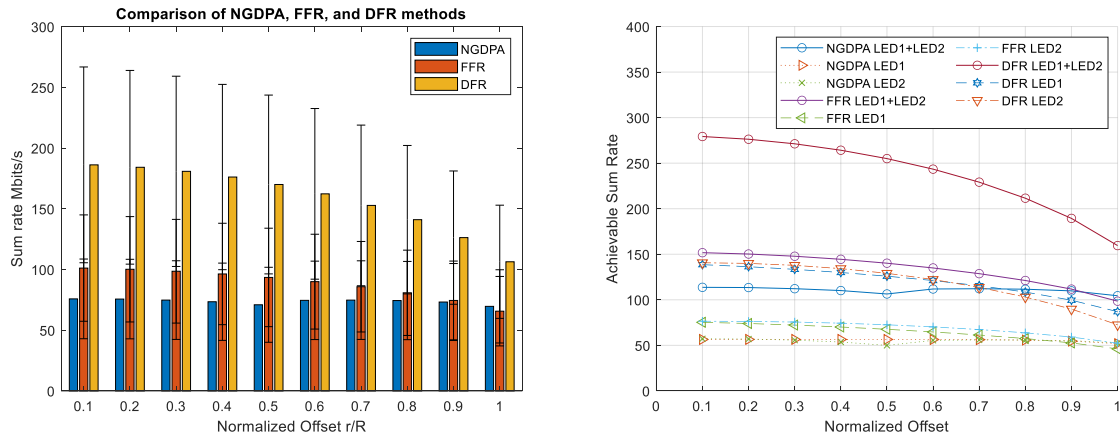


Figure 3. Achievable sum rate vs. normalized offset using NGDPA, FFR, and DFR techniques for NOMA-VLC system.

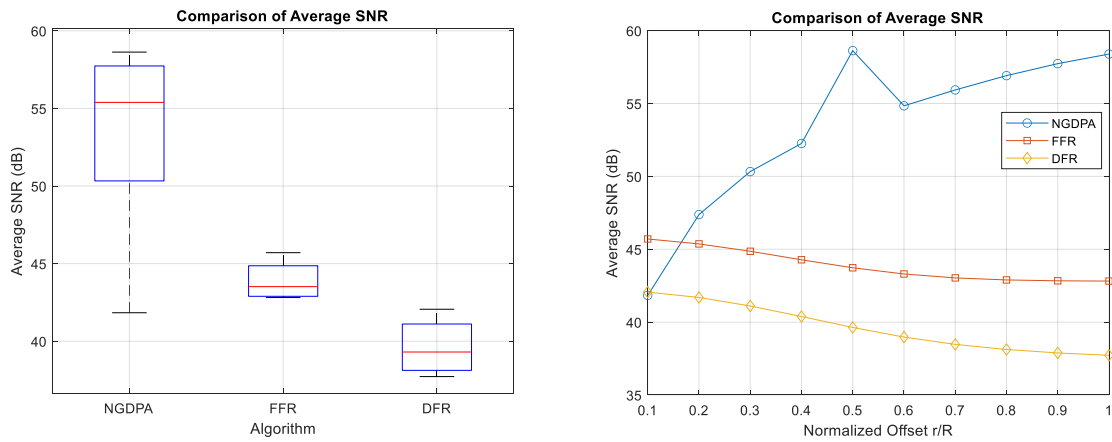


Figure 4. Average SNR using NGDPA, FFR, and DFR techniques for NOMA-VLC system.

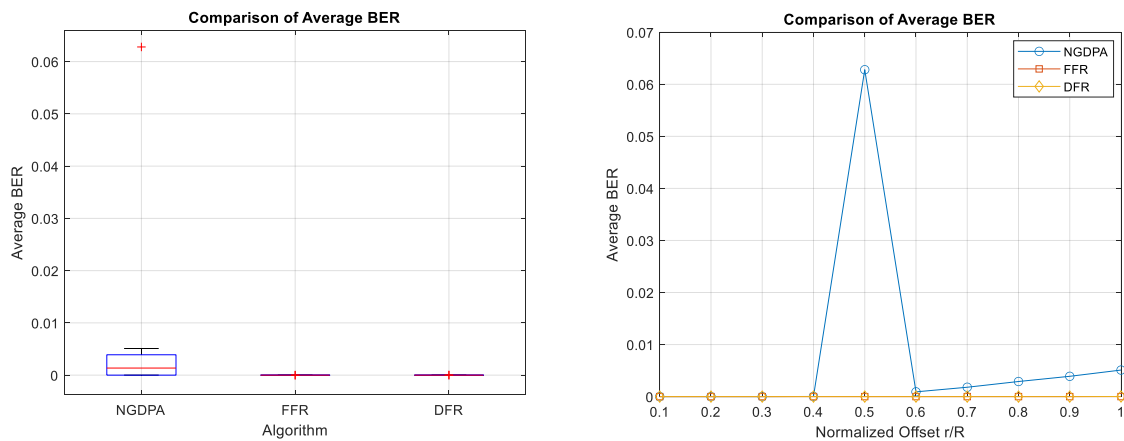


Figure 5. Average BER using NGDPA, FFR, and DFR techniques for NOMA-VLC system.

Figure 6 shows that both FFR and DFR outperform NGDPA, though their gains vary. FFR starts with a gain of over 30% but decreases and becomes negative (around -5%) as the normalized offset (r/R) increases, indicating worse performance than NGDPA under certain conditions. In contrast, DFR consistently offers a higher gain in sum rate compared to NGDPA across all offsets, with only a slight reduction in gain as conditions change. This suggests that DFR is more effective in optimizing sum rate, making it the preferred method for most network scenarios.

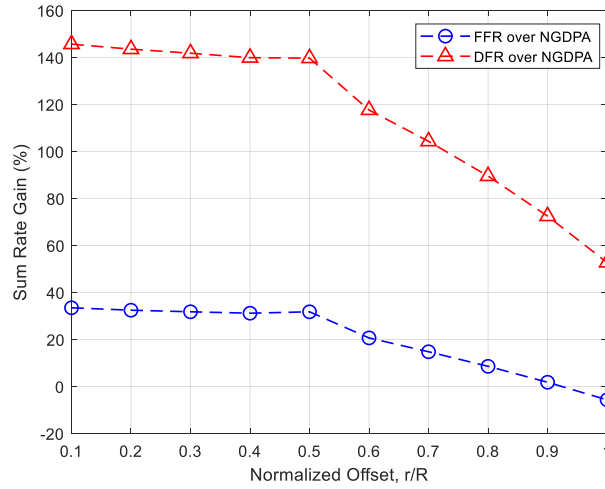


Figure 6. Percentage Gain of sum rate based FFR & DFR techniques over NGDPA method.

5. Conclusion

In this paper, we have studied the multi-user system based on MIMO-NOMA in VLC. We analyzed the performance of three different power allocation methods, including the NGDPA method, the FFR method, and the DFR method. Results have shown that these power allocation methods can improve system performance. The DFR algorithm demonstrated the highest achievable sum rate, followed by the FFR method and the NGDPA method. FFR optimally allocates frequency resources by dividing the cell into multiple zones with different reuse factors, thereby effectively reducing interference and enhancing spectral efficiency. Meanwhile, DFR dynamically adjusts frequency allocation based on the traffic load, allowing for more flexible and efficient spectrum utilization. In contrast, the NGDPA method, while theoretically promising, falls short in practical implementation due to its limited adaptability to dynamic network conditions and its inability to effectively mitigate interference. The choice of power allocation method in MIMO-NOMA-VLC systems depends on the specific application requirements, with key considerations including computational complexity, accuracy, and overall system performance. Techniques such as Fractional Frequency Reuse (FFR) and Dynamic Frequency Reuse (DFR) can enhance spectral efficiency and adaptability, though FFR may suffer from rigidity while DFR can introduce significant computational overhead. These trade-offs underscore the need for adaptive or hybrid

approaches tailored to deployment scenarios. This work paves the way for future research aimed at further optimizing system performance, including the exploration of machine learning-based dynamic reuse factor adjustment and hybrid FFR/DFR frameworks to meet the real-time demands of advanced communication environments.

Conflict of interest statement:

On behalf of all authors, the corresponding author states that there is no conflict of interest.

Data availability

All data underlying the results are available as part of the article and no additional source data are required.

Author Contributions

All authors contributed to the study and all authors read and approved the final manuscript.

References

- [1] H. Wang, F. Wang, and R. Li, "Enhancing power allocation efficiency of NOMA aided-MIMO downlink VLC networks," *Opt. Commun.* **454**, 124497 (2020).
- [2] V. Dixit and A. Kumar, "BER analysis of dynamic FOV based MIMO-NOMA-VLC system," *AEU-Int. J. Electron. Commun.* **142**, 153989 (2021).
- [3] T. Dogra and M.R. Bharti, "User pairing and power allocation strategies for downlink NOMA-based VLC systems: An overview," *AEU-Int. J. Electron. Commun.* **149**, 154184 (2022).
- [4] Y. Wu, Y. Hu, Z. Wan, *et al.*, "Joint security enhancement and PAPR mitigation for OFDM-NOMA VLC systems," *Opt. Commun.* **508**, 127719 (2022).
- [5] V. Dixit and A. Kumar, "An exact BER analysis of NOMA-VLC system with imperfect SIC and CSI," *AEU-Int. J. Electron. Commun.* **138**, 153864 (2021).
- [6] A. Adnan, Y. Liu, C.-W. Chow, *et al.*, "Analysis of non-Hermitian symmetry (NHS) IFFT/FFT Size Efficient OFDM for multiple-client Non-Orthogonal Multiple Access (NOMA) visible light communication (VLC) system," *Opt. Commun.* **472**, 125991 (2020).
- [7] Q. Zhao, J. Jiang, Y. Wang, *et al.*, "A low complexity power allocation scheme for NOMA-based indoor VLC systems," *Opt. Commun.* **463**, 125383 (2020).
- [8] A. Naz, S. Baig, and H.M. Asif, "Non Orthogonal Multiple Access (NOMA) for broadband communication in smart grids using VLC and PLC," *Optik* **188**, 162–171 (2019).
- [9] U. Ghafoor, M. Ali, H.Z. Khan, *et al.*, "NOMA and future 5G & B5G wireless networks: A paradigm," *J. Netw. Comput. Appl.* **204**, 103413 (2022).
- [10] B. Lin, Z. Ghassemlooy, X. Tang, *et al.*, "Experimental demonstration of optical MIMO NOMA-VLC with single carrier transmission," *Opt. Commun.* **402**, 52–55 (2017).
- [11] A. Akbar, S. Jangsher, and F.A. Bhatti, "NOMA and 5G emerging technologies: A survey on issues and solution techniques," *Comput. Netw.* **190**, 107950 (2021).
- [12] Z. Liu, G. Hou, Y. Yuan, *et al.*, "Robust resource allocation in two-tier NOMA heterogeneous networks toward 5G," *Comput. Netw.* **176**, 107299 (2020).
- [13] H. Sharma and R.K. Jha, "VLC enabled hybrid wireless network for B5G/6G communications," *Wirel. Pers. Commun.* **124**, 1741–1771 (2022).
- [14] H. Hameed, A. Ahmed, and U.U. Fayyaz, "Single-channel phaseless blind source separation," *Telecommun. Syst.* **80**, 469–475 (2022).
- [15] P. Meena, M.B. Pal, P.K. Jain, *et al.*, "6G communication networks: introduction, vision, challenges, and future directions," *Wirel. Pers. Commun.* **125**, 1097–1123 (2022).
- [16] S.A.H. Mohsan, A. Mazinani, H.B. Sadiq, *et al.*, "A survey of optical wireless technologies: Practical considerations, impairments, security issues and future research directions," *Opt. Quantum Electron.* **54**, 187 (2022).

- [17] D. Astharini, M. Asvial, and D. Gunawan, "Performance of signal detection with trellis code for downlink non-orthogonal multiple access visible light communication," *Photonic Netw. Commun.* **43**, 185–192 (2022).
- [18] C. Chen, W.-D. Zhong, H. Yang, *et al.*, "On the performance of MIMO-NOMA-based visible light communication systems," *IEEE Photonics Technol. Lett.* **30**, 307–310 (2017).
- [19] V. Dixit and A. Kumar, "An exact error analysis of multi-user RC/MRC based MIMO-NOMA-VLC system with imperfect SIC," *IEEE Access* **9**, 136710–136720 (2021).
- [20] H. Li, Z. Huang, Y. Xiao, *et al.*, "A power and spectrum efficient NOMA scheme for VLC network based on hierarchical pre-distorted LACO-OFDM," *IEEE Access* **7**, 48565–48571 (2019).
- [21] G.N. Tran and S. Kim, "Performance analysis of short packets in NOMA VLC systems," *IEEE Access* **10**, 6505–6517 (2022).
- [22] A. Adnan, Y. Liu, C.-W. Chow, *et al.*, "Demonstration of non-hermitian symmetry (NHS) IFFT/FFT size efficient OFDM non-orthogonal multiple access (NOMA) for visible light communication," *IEEE Photonics J.* **12**, 1–5 (2020).
- [23] B. Lin, Q. Lai, Z. Ghassemlooy, *et al.*, "A machine learning based signal demodulator in NOMA-VLC," *J. Light. Technol.* **39**, 3081–3087 (2021).
- [24] S. Feng, T. Bai, and L. Hanzo, "Joint power allocation for the multi-user NOMA-downlink in a power-line-fed VLC network," *IEEE Trans. Veh. Technol.* **68**, 5185–5190 (2019).
- [25] J. Shi, J. He, K. Wu, *et al.*, "Enhanced performance of asynchronous multi-cell VLC system using OQAM/OFDM-NOMA," *J. Light. Technol.* **37**, 5212–5220 (2019).
- [26] E.M. Almohimmah, and M.T. Alresheedi, "Error analysis of NOMA-based VLC systems with higher order modulation schemes," *IEEE Access* **8**, 2792–2803 (2019).
- [27] Q. Li, T. Shang, T. Tang, *et al.*, "Optimal power allocation scheme based on multi-factor control in indoor NOMA-VLC systems," *IEEE Access* **7**, 82878–82887 (2019).
- [28] Y. Yapıcı and I. Güvenç, "NOMA for VLC downlink transmission with random receiver orientation," *IEEE Trans. Commun.* **67**, 5558–5573 (2019).
- [29] A. Al Hammadi, P.C. Sofotasios, S. Muhaidat, *et al.*, "Non-orthogonal multiple access for hybrid VLC-RF networks with imperfect channel state information," *IEEE Trans. Veh. Technol.* **70**, 398–411 (2020).
- [30] S.C. Lam and X.N. Tran, "Fractional frequency reuse in ultra dense networks," *Phys. Commun.* **48**, 101433 (2021).
- [31] A. Onim, S. Musyoki, and P. Kihato, "Selection of optimal SINR threshold in fractional frequency reuse by comparing Otsu's and entropy method," *Heliyon* **8**, e11736 (2022).
- [32] H.C. Mora, N.O. Garzón, and C. de Almeida, "On the cellular spectral efficiency of MC-CDMA systems with MMSE multiuser detector employing fractional and soft frequency reuse," *AEU-Int. J. Electron. Commun.* **84**, 34–45 (2018).
- [33] D. Tsolkas, N. Passas, and L. Merakos, "Enabling device discovery transmissions in LTE networks with fractional frequency reuse," *Comput. Netw.* **88**, 149–160 (2015).
- [34] H. Liu, P. Xia, Y. Chen, *et al.*, "Interference graph-based dynamic frequency reuse in optical attocell networks," *Opt. Commun.* **402**, 527–534 (2017).
- [35] N. Titi, S. Haddad, A. Soukkou, F. Aknouche and H. E. Djema, "Power Allocation Optimization Using Water-Filling Technique for MIMO-NOMA-Based Visible Light Communication Systems," 2024 International Conference on Advances in Electrical and Communication Technologies (ICAECOT), Setif, Algeria, 2024, pp. 1-6, doi: 10.1109/ICAECOT62402.2024.10829012.



Application of Machine Learning to Developing an Internet Community Model

Ozoh Patrick ^{1, *}, Musibau Ibrahim ¹, Oyinloye Olufunke ²

¹ Faculty of Computing and Information Technology, Osun State University, Nigeria

patrick.ozoh@uniosun.edu.ng, ibrahima@uniosun.edu.ng

² Department of Computer Science, University of Ilesa, Nigeria

*Corresponding author: (O. Patrick), *Email Address:* patrick.ozoh@uniosun.edu.ng

Abstract

This study will assist in determining the types of elements and occasions that influence people's opinions. It aims to implement a social media sentiment Social Media Sentiment Analysis using machine learning techniques. The objectives of this study are as follows: (i) To combine natural language processing, machine learning, and financial modeling to analyze the different impacts of sentiments on social media. (ii) To implement the developed model in (i) (iii) To evaluate the performance of the developed model in (ii). The method used in this study includes the application downloads of tweets from Tweeter and inserts the data into the MongoDB database. The Natural Language Toolkit corpus called Twitter samples is available for the training dataset, the application extracts features from the training dataset. The insights would help the people for example in the National Security Department and Emergency Response Teams to understand the public emotional behaviors towards certain events and people, take appropriate actions with informed decisions, and perform situational analysis regarding public safety and security. Pymongo retrieved the text driver from the Tweets. The classifier model assigned polarity to each tweet and displayed the Tweet. Data visualization was successful for the retrieved system for Twitter user followers, friends, status counts, and charts to visualize the data. The application displayed exploratory visualization using line charts, bar charts, and tweets on a map using coordinates.

Keywords: Online social media, Sentiment analysis, Supervised learning, Natural language processing, Behavioral analysis

<https://doi.org/10.63070/jesc.2025.014>

Received 23 March 2025; Revised 12 May 2025; Accepted 26 May 2025.

Available online 28 May 2025.

Published by Islamic University of Madinah on behalf of *Islamic University Journal of Applied Sciences*. This is a free open access article.

1. Introduction

Due to social media's rising prominence in contemporary culture, its use has increased. They are now used by internet users for more purposes than just exchanging private information or corresponding with peers, co-workers, or relations. These subjects cover a broad range, including goods, individuals, occasions, trends, and societal problems. Customers' input is beneficial in helping businesses improve since it allows them to learn what the public thinks about their products or services [19]. The government, organizations, and prominent figures would like to learn more about how the public perceives them. From the viewpoint of the consumer, opinions, and feelings about goods are also useful as a guide when making decisions about those specific products. Numerous studies have been done to examine attitudes and feelings on social networking sites, and they cover a variety of topics, including finance and, particularly, share markets. The stock markets are extremely unpredictable, and social media reports or news frequently have a significant impact on a company's share price. Some of the variations in the stock market are hypothesized in [17].

The advancements in communication tools, made possible by the Internet, have recently brought people closer together. With the aid of the Internet, the lengthy process of contact that previously involved mail and telegraph has been transformed into an instantaneous one. People can now connect with anyone thanks to social media; one of the application software programs that appeared alongside smartphone technology. All individuals and organizations were impacted by this. Sharing a space, like a theatre, shop, or cafe, or voicing a favourable or unfavourable opinion about it, for instance, everyone and the entire community in every aspect. Social media is viewed by many as the primary setting for conversation. Through social media, people exchange news, sports, movies, personal emotions, and ideas. This has changed significant data for many different entities, such as companies marketing or selling their goods and researchers looking at thoughts and emotions.

Sentiment analysis has been made possible as a necessary instrument whom frequently share their opinions about social, economic, health, and brand-related problems. Expressions of emotion in texts are anticipated by sentiment analysis research. People's messages are evaluated for their positivity, negativity, or indifference. The advent of the internet has changed how people express their opinions. It is now carried out through blog entries, online discussion groups, product review websites, and other channels. They essentially contend that certain market disruptions can affect the equity markets. A famous news outlet's news report, speculative news, changes to market rules, or any of these things can cause a market jolt. These effects are explained by [17]. Large negative share returns are more probable than large positive share returns, according to the volatility feedback. Although the volatility

feedback helps to explain some of the effects of market changes, how these news items are interpreted is of utmost significance.

The goal of this research is to combine natural language processing, machine learning, and financial modeling to examine the various effects that social media opinions have on shared values. People rely on this user-generated material in huge numbers. When looking for merchandise, a person will first look up reviews online before making a decision. A typical consumer cannot possibly investigate the volume of user-produced material. The two key strategies used in mood analysis are symbolic strategies, also known as understanding basis approaches, and machine mastering methods. The expertise-based method necessitates a sizable collection of pre-set emotions and a green expertise example for sentiment analysis. An emotional classifier that categorizes feelings is expanded using machine learning techniques using a training set. System learning is significantly simpler than the knowledge-based approach because it contains a predefined database of all feelings.

In the period of machine learning, machines are left to think and solve problems by finding the patterns in every data set on their own. Examination of secret trends and patterns helps predict and know precisely how to fit the correct algorithm with a particular learning process or resources.

The focus of this research paper is on the evaluation of online content for a variety of websites, in terms of numbers and volumes. These websites are devoted to particular types of stock and have experience with storing customer reviews from various websites, including Amazon and a great deal more. Google Play Store/Twitter is primarily where polls are communicated through tweets, but it can take a lot of time to gather a general understanding of these unorganized records. Customers view those unstructured evaluations on a specific website, developing an opinion of the goods or services and ultimately deciding. This can be very helpful for companies and cast light on how rumours or news spreading online may favour or harm the company in the short and long term. It can also assist in determining the types of elements and occasions that influence people's opinions and confidence in the goods that a company sells. Businesses can conduct an early analysis of new goods, films, etc. thanks to sentiment analysis. Data classification is used for sentiment analysis, and done with different methods. Text is pre-processed using text extraction techniques before being classified. To illustrate these procedures, a collection of terms is created by removing symbols, commas, word stems, and stop words. This study is achieved with a categorization procedure.

This study consists of five sections. Section one contains the background and contribution to knowledge. Section two includes a review of fundamental concepts and related works. Section three

showcases the presentation of the methodology and describes the techniques, technologies, and tools to be used. Section four discusses the results obtained. Section five includes the summary.

The contributions of this study are as follows:

- 1 To have an insight on how news or rumours circling on the internet might benefit or disadvantage the business
- 2 To combine natural language processing, machine learning, and financial modelling to analyse the different impacts of sentiments on social media
- 3 To understand factors that affect the opinion of people toward products.

2. Literature Review

[2] assess the classification performance of transformer-based pre-trained language models to correctly classify tweets dependent on heat stroke, a significant health effect as true or false. The study evaluates combining social networks with artificial intelligence for public health monitoring. The study visualizes data on classified tweets and heat stroke occurrences in animated videos. The results from the study indicate that the pre-trained language models are reliable in classifying the tweets. The animated video visualizations revealed a positive correlation. [20] Ullah et al. (2025) applied computational models to identify individuals with depression dependent on Twitter posts—feature extraction using Natural Language Processing (NLP) techniques retrieved and cleaned 1.6 million tweets. The methodology involves applying the Grey Relational Grade (GRG) to study the association between likes and shares of Twitter posts. As a result, different machine learning models were used to classify user tweets into "stressed" or "not stressed" categories. The findings suggest the importance of social media and computational models in mental health detection.

[11] presented an automated deep-learning model for identifying malicious activities. The data was collected from the social media platforms using Formspring, Instagram, and MySpace for observing cyberbullying behavior—the preprocessing processes involved removing stop words, and punctuations, and converting comments to lowercase. The study used Feature Density (FD) to compute intricate natural language datasets using the linguistically backed preprocessing model. The dataset is then input to the feature selection process that identifies important features for the predictive model. The identified features are investigated for cyberbullying behaviour detection. The Matlab software is applied for simulation. The study yielded outcomes with values of 99.12%, 94.73%, 97.45%, and 93.91% respectively for accuracy, precision, recall, and F1-Score.

The relevance of conversations and microblogs has grown due to the development of social media platforms like online reviews [8]. Because the internet has such a massive amount of opinionated data, if it is correctly examined, it may greatly aid corporations and policymakers in their decision-making. It is simple to classify attitudes even in real time.

Due to its user-friendly API and the social effect of certain powerful individuals, including politicians and celebrities, Twitter has emerged as the leading social media analytics platform. There are more than 15 billion Application Programming Interface (API) calls and over 3 billion tweets sent each day [3]. The increasing number of social media analytic applications are archived data. According to [18], a significant amount of data from users' tweets is required for opinion mining. Unstructured tweets are used. The Twitter dataset uses performance metrics. These methods are assessed. For classification approaches, the accuracy indicated SVM outperformed all others in the Twitter Sentiment assessment [7].

[15] analyses the affective content of the writings in different groups. [14] used patient remarks on Twitter about drug adverse effects to perform a sentiment analysis. [12] investigated whether the distribution of the data among groups affected the classification algorithm's success rate. [16] proposed a technique for autonomously gathering data from Twitter for opinion. In the study, N-grams and POS tags were used as features in the classifier. [1] used machine-learning techniques on movie evaluations. The paper extracted the features using TF-IDF. The support vector machine has produced superior outcomes. [5] applied sentiment analysis study. [6] proposed the sentiment analysis to classify comments using the feature vector. [9] present actions considered in the study.

3. Methodology

This section discusses the study methods used in predicting fuel consumption using machine learning. It provides details of data collection, data pre-processing, and the models used.

3.1 Data collection

Data is collected from Google Play Store and some other social media platforms like Twitter, Google Play Store, etc. (Figure1).

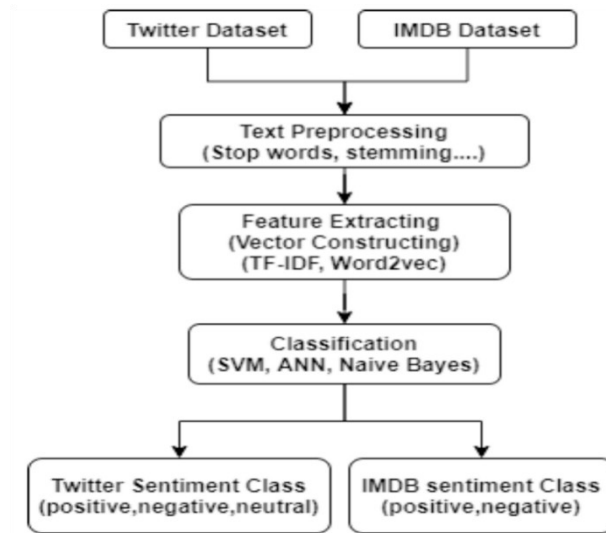


Figure 1. Flowchart of the study.

The Google Play Store/Twitter (Application Programming Interface) API was used to gather tweets. A Python program was used to pre-process the data and calculate sentiment ratings. 1680 of the tweets that were collected, and classified as neutral, 1220 as positive, and 1600 as unfavorable. The characteristics of the tweets collected by the API using Python are displayed in Table 1.

Table 1. Characteristics of tweets dataset.

Dataset Attribute	Explanation of Attribute
Id	Order of tweet data frame
Text	Tweet
created at	Date and time the Tweet was posted
Retweeted	Tweet rerun status (bool)
retweet count	Number of retweets
User screen name	Username
user followers_count	Number of followers
user location	Followers location
Hashtags	Tweet tag
sentiment score	Sentiment score
sentiment class	positive, negative, neutral

The same models were also applied to the dataset of 500 positive and 500 negative opinions, shown in Table 2.

Table 2. Dataset of opinion of users .

Dataset Attribute	Explanation of Attribute
Text	Reviews
sentiment class	positive, negative

The application accesses the Twitter messages called tweets shared by users while sharing their views, emotions, and opinions on the Twitter Social Network.

3.2 Data Pre-processing

The application pre-processes the Twitter data to remove symbols like @ mentions and # hashtags before it performs feature extraction. The words known as stop-words in the sentiment analysis context, include words such as in, on, at, it, if, is, and so on. The diagram in Figure 2 shows the overall interactions between application modules from data acquisition to classification. The application downloads the tweets posted by the users and stores in the database, then accesses the stored data for pre-processing the text and passes it to the feature extractor function using the model built from the training dataset.

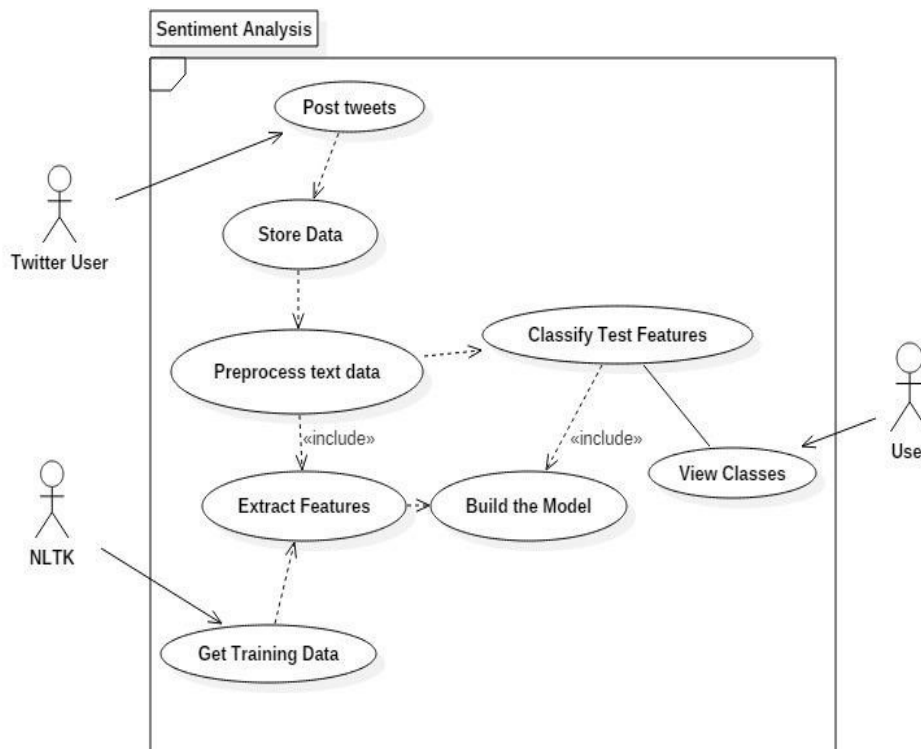


Figure 2. Use case diagram for sentiment analysis system.

3.3 Model Descriptions

This section includes the algorithms for the models and is described.

3.3.1 Naïve Bayes Algorithm

It is given as follows.

Step 1: Choose a training set.

Step 2: Train the classification algorithm using the training data.

Step 3: Use a classification algorithm to classify sample data.

Step 4: Compare the results against the known results set.

3.3.2 Bayes theorem

The Bayes theorem as given by [3] is represented in Equation 1.

$$P(c \setminus x) = \frac{P(x \setminus c)P(c)}{P(x)} \quad (1)$$

Where

$P(c \setminus x)$ = Posterior Probability function

$P(x \setminus c)$ = Likelihood function

$P(c)$ = Class Prior Probability function

$P(x)$ = Predictor Prior Probability function

3.3.3 Maximum Entropy Algorithm

The algorithm is defined as the log-likelihood of the model p concerning the empirical distribution p , with x number of iterations derived in Equation (2) [13].

$$\log_{\vec{p}}(p) = \log \prod_{x \in X} p(x)^{\vec{p}(x)} = \sum_{x \in X} p(x) \log p(x) \quad (2)$$

3.3.4 Support Vector Machines

It is represented as in Equation 3 [20].

$$\begin{aligned} TS_i &= \max \left\{ \left| \frac{\bar{x}_{ik} - \bar{x}_i}{m_k s_i} \right|, \quad k = 1, 2, \dots, K \right\} \\ \bar{x}_{ik} &= \sum_{j \in C_k} \bar{x}_{ij} / n_k \\ \bar{x}_i &= \sum_{j=1}^n x_{ij} / n \\ s_i^2 &= \frac{1}{n - K} \sum_k \sum_{j \in C_k} (x_{ij} - \bar{x}_{ik})^2 \\ m_k &= \sqrt{1/n_k + 1/n} \end{aligned} \quad (3)$$

There are k classes, $\max \{y_k, k=1,2, 3,\dots,K\}$ is the maximum of all y_k . C_k refers to class k which includes n_k samples. x_{ij} is the expression value of I in sample j . \bar{x}_{ik} is the mean expression value in k . n is the total number of samples. \bar{x}_i is the general mean expression value for i . s_i is the pooled within-class standard deviation.

3.3.5 K-Means Clustering

Given a dataset $X=[x_1,\dots,x_n]$, $x_n \in \mathbb{R}^d$. The dataset is partitioned into M disjoint subsets C_1,\dots,C_m . The algorithm is given as in Equation 4 [9].

$$\frac{1}{m_k} \sum_{i=1}^{m_k} \|x^i - \mu_{c_k}\|^2 \quad (4)$$

3.3.6 Term Frequency

This technique gives the significance of a given textual context. This method involves assigning weights [10]. The weights are assigned as in Equation 5.

$$W_{i,j} = TF_{t,d} \left(\frac{N}{D_t} \right) \quad (5)$$

where TF_t , D_t has the term t .

3.3.7 Predicting Users' Actions from Sentiment

1. "Share positive: Fracking topic: "Fracking saves us money; fracking creates jobs; fracking reduces greenhouse gas emissions."
2. "Spread negative vaccination topic: "Vaccination has never been proven to have saved one single life"
3. "Call for oppose action: Protect our kids and families from £10 fracking. Pls RT!"

The appendix code for the implementation of this study is displayed in Appendix A.

4. Implementation and Testing

This section explains the system development designs specified in previous sections. It highlights the algorithms that present the results for social media sentiment analysis using machine learning. The proposed system was successfully tested to denote its effectiveness and achievability. It makes possible expressions of emotion in texts as they are anticipated by sentiment analysis research. People's messages are evaluated for their positivity, negativity, or indifference.

As a purposeful goal achieved, businesses can conduct an early analysis of new goods, films, etc. The system has been fully built and is ready to be used. Figure 4 shows data exploration. In Figure 5, the data pre-processing was analyzed by loading the Google Play Store review dataset.

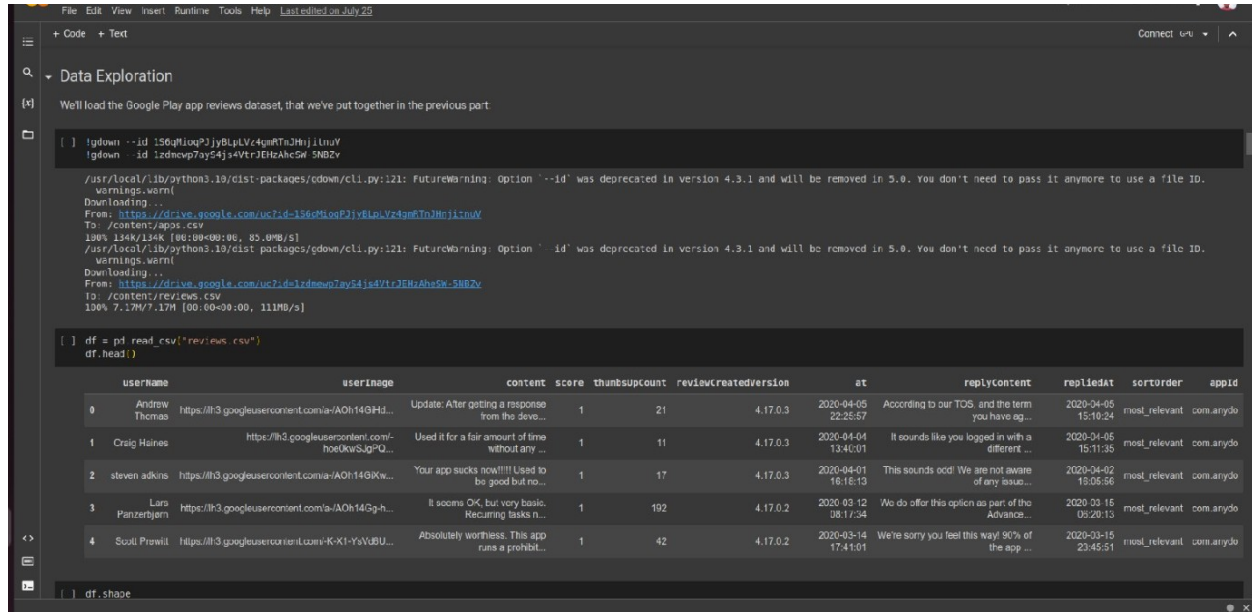


Figure 4. Data exploration.

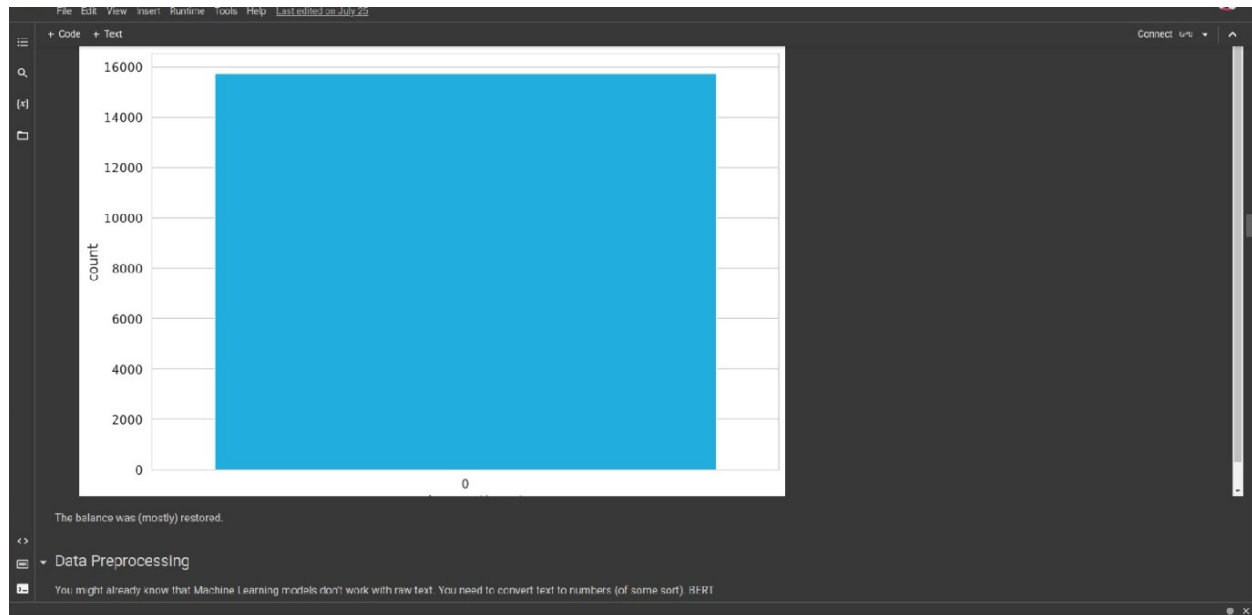


Figure 5. Data pre-processing.

The two images shown below in Figure 6 are the encoders used for modeling and analyzing social media sentiment. The second image shows its setup and configuration. Figure 7 is the screenshot that shows the predicting model on raw text; and how to use the sentiment of raw text.

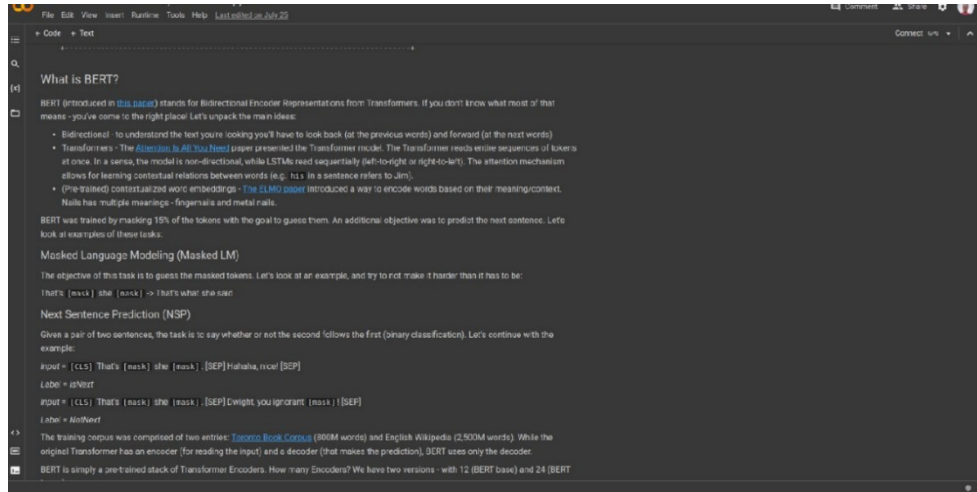


Figure 6. BERT representations

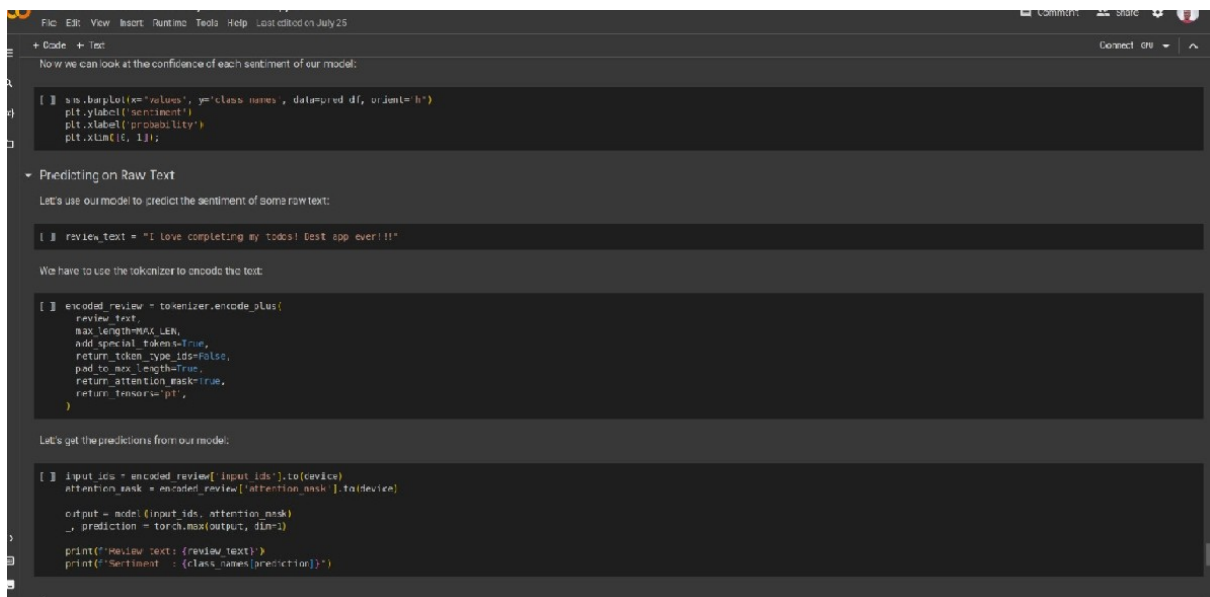


Figure 7. Predicting on raw text

The image in Figure 8 depicts the training and validation accuracy of sentimental prediction. The image in Figure 9 shows the classification report, which explains its overview and relative frequency effects.

```

File Edit View Insert Runline Tools Help Last edited on July 25
+ Code + Text
Connect 100 % ^

Whoa, this took some time! We can look at the training vs validation accuracy:

[ ] plt.plot(history['train_acc'], label='train accuracy')
    plt.plot(history['val_acc'], label='validation accuracy')

    plt.title('Training history')
    plt.ylabel('Accuracy')
    plt.xlabel('Epoch')
    plt.legend()
    plt.ylim([0, 1]);

The training accuracy starts to approach 100% after 10 epochs or so. You might try to fine-tune the parameters a bit more, but this will be good enough for us.

Don't want to wait? Uncomment the next cell to download my pre-trained model:

[ ] # !wget --id 1U81tWt0uCVn02R-6K1K95v0ff9aunagA

    # model = SentimentClassifier(len(class_names))
    # model.load_state_dict(torch.load('test_model_state.bin'))
    # model = model.to(device)

Evaluation

So how good is our model on predicting sentiment? Let's start by calculating the accuracy on the test data:

[ ] test_acc, _ = eval_model(
    model,
    test_data_loader,
    loss_fn,
    device,
    len(df_test)
)

test_acc.item()

```

Figure 8. Training vs validation accuracy

```

File Edit View Insert Runline Tools Help Last edited on July 23
+ Code + Text
Connect 100 % ^

[ ] y_review_texts, y_pred, y_pred_probs, y_test = get_predictions(
    model,
    test_data_loader
)

Let's have a look at the classification report:

[ ] print(classification_report(y_test, y_pred, target_names=class_names))

Looks like it is really hard to classify neutral (3 stars) reviews. And I can tell you from experience, looking at many reviews, those are hard to classify.

We'll continue with the confusion matrix:

[ ] def show_confusion_matrix(confusion_matrix):
    hmap = sns.heatmap(confusion_matrix, annot=True, fmt='d', cmap='Blues')
    hmap.yaxis.set_ticklabels(hmap.yaxis.get_ticklabels(), rotation=90, ha='right')
    hmap.xaxis.set_ticklabels(hmap.xaxis.get_ticklabels(), rotation=30, ha='right')
    plt.ylabel('True sentiment')
    plt.xlabel('Predicted sentiment')

    cm = confusion_matrix(y_test, y_pred)
    df_cm = pd.DataFrame(cm, index=class_names, columns=class_names)
    show_confusion_matrix(df_cm)

This confirms that our model is having difficulty classifying neutral reviews. It mistakes these for negative and positive at a roughly equal frequency.

That's a good overview of the performance of our model. But let's have a look at an example from our test data:

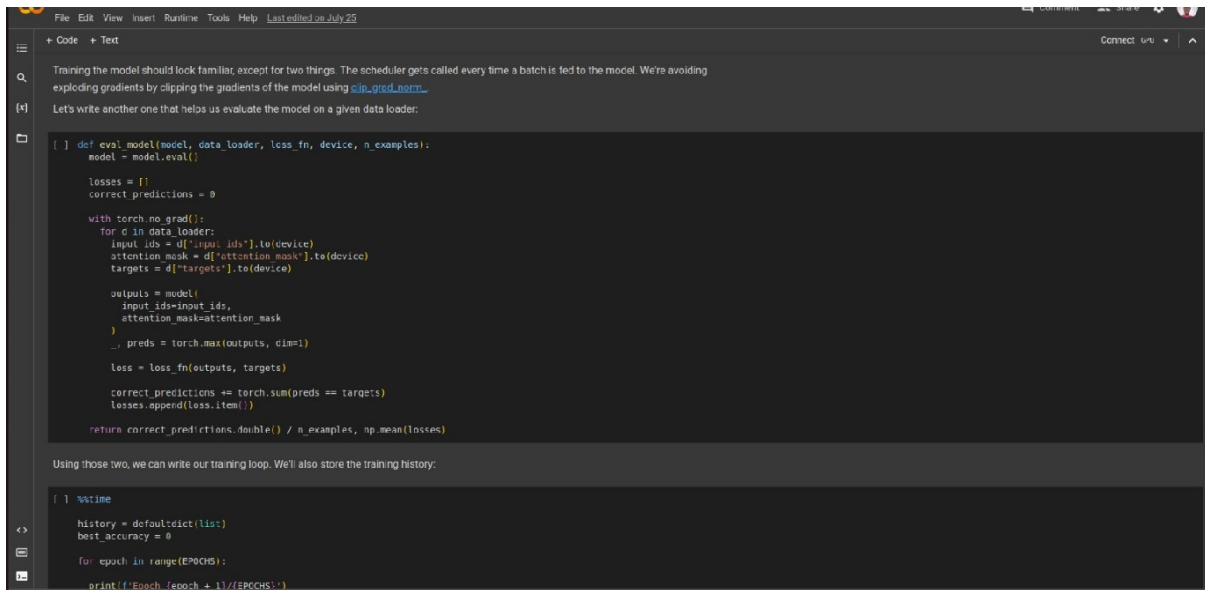
[ ] idx = 2

review_text = y_review_texts[idx]
true_sentiment = y_test[idx]
pred_df = pd.DataFrame({
    'class_names': class_names,
    'values': y_pred_probs[idx]
})

```

Figure 9. Classification report

The evaluation of models is shown in Figure 10.



The screenshot shows a Jupyter Notebook interface with a dark theme. The top toolbar includes 'File', 'Edit', 'View', 'Insert', 'Runtime', 'Tools', and 'Help'. The notebook has two cells. The first cell contains a text block explaining the evaluation process and a code block for the `eval_model` function. The second cell contains a text block explaining the training loop and a code block for the training loop logic.

```

def eval_model(model, data_loader, loss_fn, device, n_examples):
    model = model.eval()

    losses = []
    correct_predictions = 0

    with torch.no_grad():
        for e in data_loader:
            input_ids = d["input_ids"].to(device)
            attention_mask = d["attention_mask"].to(device)
            targets = d["targets"].to(device)

            outputs = model(
                input_ids=input_ids,
                attention_mask=attention_mask
            )
            preds = torch.max(outputs, dim=1)

            loss = loss_fn(outputs, targets)

            correct_predictions += torch.sum(preds == targets)
            losses.append(loss.item())

    return correct_predictions.double() / n_examples, np.mean(losses)

Using those two, we can write our training loop. We'll also store the training history:

! %time
history = defaultdict(list)
best_accuracy = 0

for epoch in range(EPOCHS):
    print(f'Epoch {epoch + 1}/{EPOCHS}')
  
```

Figure 10. Model evaluation

5 Summary, Conclusion, and Future Work

5.1 Summary

The tests performed during the development of the implementation of social media sentiment analysis using machine learning to verify and validate the module functionalities to provide necessary data; for database connection testing, pre-processed text data for data preprocessing testing, polarity for the tweet text for sentiment results testing, data visualization testing, and response time testing. Database connection was successful using the MongoDB connection driver Pymongo, for sentiment analysis, the system retrieved the text data from the tweets. Data pre-processing was successful in that the repeating characters were removed, replaced #hashtags and @mention symbols, and removed URLs. Sentiment results were successful in that using the classifier model was able to assign polarity to each tweet and display the tweet along with its polarity. However, unigrams did not perform well on some words. Finally, data visualization was successful in that the system retrieved numeric data for Twitter user followers, friends, and status counts and created the charts to visualize the data.

5.2 Conclusion

The Social Media applications and algorithms has successfully been developed with the basic functionalities as in System Requirements Specifications. The application was able to connect and download tweets from the Twitter App using Twitter Streaming API and saved the data in the MongoDB database. It also performed data pre-processing to remove, replace and convert some tweet/message characters such as repetitions, replaces all URLs with the word URL, @mention with

the word AT_USER, and #hashtag with hashtag word. In addition, it converted the tweet texts into lowercase letters. Using the framework, Jinja2 template engine, and HTML, the application displayed the sentiment analysis results on the web application. It also displayed exploratory visualization using charts and tweets on a map using coordinates.

5.3 Future Work

Future research can aid in the better enhancement of Social Media Sentiment Analysis using machine learning and should be able to create a new-age project by creating a search engine so that users can search for a particular word or text from the database. Otherwise, creating a bag of words using unigrams that some positive emotional words negated classified as positive such as not good or not happy. With this, future enhancements should consider the bigrams for improved classification accuracy.

References

- [1] Y . Acar, G. Demet, and M. Kaynar, “Data and discourse: an assessment of Taksim urban design competition in terms of populism and participation”, *Journal of Urban Design*, no. 28, vol. 6, pp 682-698, 2023.
- [2] S. Anno, Y. Kimura, and S. Sugita, “Using transformer-based models and social media posts for heat stroke detection”, *Scientific Reports*, vol. 15, no. 1, pp. 742, 2025.
- [3] M. G. Albino, “Opinion-Mining Technique on Generative Artificial Intelligence Topic Using Data Classification Algorithms”.
- [4] J. P. Bharadiya, “A review of Bayesian machine learning principles, methods, and applications”, *International Journal of Innovative Science and Research Technology*, vol. 8, no. 5, pp. 2033-2038, 2023.
- [5] S. H. Chowdhury, M. Pathan, K.E. Arefin, D. Mohd, and Noorul Huq, “Prevalence and Effect of Computer Vision Syndrome during COVID-19: among Bangladeshi People”, *SAS J Med*, vol. 4, pp. 204-211, 2024.
- [6] K. Chhutlani, V. Takrani, A. Motwani, T. Harchandani, and S. Sahu, “Sentiment Analysis of OYO Hotel Reviews Using NLP”, In *2023 14th International Conference on Computing Communication and Networking Technologies (ICCCNT)*, pp. 1-6, IEEE, 2023.
- [7] R. K. Godara, A. Mengi, A. Sharma, and S. Sharma, “Detecting Depressive Symptoms on Social Media: A Comprehensive Review of Methodologies and Strategies for Suicide Prevention”, In *International Conference on Cognitive Computing and Cyber Physical Systems*, pp. 87-100, Singapore: Springer Nature Singapore, 2023.
- [8] A. K. Jha, and N. K. Verma, “Social media sustainability communication: an analysis of firm behaviour and stakeholder responses”, *Information Systems Frontiers*, vol. 25, no. 2, pp. 723-742, 2023.

- [9] A. Likas, N. Vlassis, and J. J. Verbeek, “The global k-means clustering algorithm”, *Pattern recognition*, vol. 36, no. 2, pp. 451-461, 2023.
- [10] T. Mahmud, R. Karim, R. Chakma, T. Chowdhury, M. S. Hossain, and K. Andersson, “A benchmark dataset for cricket sentiment analysis in bangla social media text”, *Procedia Computer Science*, vol. 238, pp. 377-384, 2024.
- [11] M. K. Mali, R. R. Pawar, S. A. Shinde, S. D. Kale, S. V. Mulik A. A. Jagtap, and P. U. Rajput, “Automatic detection of cyberbullying behaviour on social media using Stacked Bi-Gru attention with BERT model”. *Expert Systems with Applications*, vol. 262, pp. 125641, 2025.
- [12] M. Z. Naeem, F. Rustam, A. Mehmood, I. Ashraf, and G. S. Choi, “Classification of movie reviews using term frequency-inverse document frequency and optimized machine learning algorithms”, *PeerJ Computer Science*, vol. 8, e914, 2022.
- [13] K. Nizam and N. Ahsan, “THE IMPACT OF E-DETERMINANTS ON CUSTOMER LOYALTY: A SOCIAL SUSTAINABILITY PARADIGM”, *Journal of Research in Social Development and Sustainability*, vol. 2, no. 2, pp. 87-115, 2023.
- [14] D. Patel, S. Saxena, T. Verma, and P. G. Student, “Sentiment analysis using maximum entropy algorithm in big data”, *International Journal of Innovative Research in Science, Engineering and Technology*, vol. 5, no. 5, 2016.
- [15] K. Qian, A. Belyi, F. Wu, S. Khorshidi, A. Nikfarjam, R. Khot, and Y. Li, “Open Domain Knowledge Extraction for Knowledge Graphs”, *arXiv preprint arXiv:2312.09424*, 2023.
- [16] R. S. Rana, K. Jain, and M. Hema, “Information retrieval on disaster tweets using NLP”, In *AIP Conference Proceedings*, vol. 3075, no. 1, AIP Publishing, 2024.
- [17] B. Rosenthal and Airoidi, “Consumer morality formation on social media platforms: the case of guns in Brazil”, *Journal of micromarketing*, vol. 44, no. 1, pp. 178-198, 2024.
- [18] C. Song, S. Chen, X. Cai, and H. Chen, “Sentiment Analysis of Spanish Political Party Tweets Using Pre-Trained Language Models”, *arXiv e-prints*, arXiv-2411, 2024.
- [19] S. Suryawanshi, B. R. Chakravarthi, P. Verma, M. Arcan, J. P. McCrae, and P. Buitelaar, “A dataset for troll classification of TamilMemes”, In *Proceedings of the WILDRE5–5th workshop on indian language data: resources and evaluation*, pp. 7-13, 2020.
- [20] W. Ullah, P. Oliveira-Silva, M. Nawaz, R. M. Zulqarnain, I. Siddique, and M. Sallah, “Identification of depressing tweets using natural language processing and machine learning: Application of grey relational grades”. *Journal of Radiation Research and Applied Sciences*, vol. 18, no. 1, 2025.
- [21] S. Vyavahare, S. Teraiya, and S. Kumar, “FDM manufactured auxetic structures: an investigation of mechanical properties using machine learning techniques”. *International Journal of Solids and Structures*, vol. 265, pp. 112-126, 2023.
- [22] L. Wang, “Support vector machines: theory and applications”, vol. 177, Springer Science & Business Media, 2005.

APPENDIX A Implementation code

```
!nvidia-smi
```

```
+-----+
| NVIDIA-SMI 525.105.17    Driver Version: 525.105.17    CUDA Version: 12.0    |
+-----+-----+-----+-----+
| GPU Name      Persistence-M| Bus-Id        Disp.A | Volatile Uncorr. ECC |
| Fan  Temp  Perf  Pwr:Usage/Cap|      Memory-Usage | GPU-Util  Compute M. |
|               |            MIG M. |                    |
+=====+=====+=====+=====+
| 0 Tesla T4           Off | 00000000:00:04.0 Off |             0 |
| N/A   55C    P8     10W / 70W | 0MiB / 15360MiB | 0%      Default |
|               |            N/A |                    |
+-----+-----+-----+-----+
```

```
+-----+
| Processes:                                     |
|  GPU   GI    CI      PID   Type   Process name                      GPU Memory |
|  ID   ID                                   Usage   |
+=====+=====+=====+=====+
| No running processes found                      |
```

```
!pip install -q -U watermark
```

```
!pip install -qq transformers
```

```
%reload_ext watermark
```

```
%watermark -v -p numpy,pandas,torch,transformers
```

```
#@title Setup & Config
```

```
import transformers
```

```
from transformers import BertModel, BertTokenizer, AdamW, get_linear_schedule_with_warmup
```

```
import torch
```

```
import numpy as np
```

```
import pandas as pd
```

```
import seaborn as sns
```

```
from pylab import rcParams
```

```
import matplotlib.pyplot as plt
```

```
from matplotlib import rc
```

```
from sklearn.model_selection import train_test_split
```

```
from sklearn.metrics import confusion_matrix, classification_report
```

```
from collections import defaultdict
```

```
from textwrap import wrap
```

```
from torch import nn, optim
```

```
from torch.utils.data import Dataset, DataLoader
```

```
import torch.nn.functional as F
```

```
%matplotlib inline
```

```
%config InlineBackend.figure_format='retina'
```

```
sns.set(style='whitegrid', palette='muted', font_scale=1.2)
```

```
HAPPY_COLORS_PALETTE = ["#01BEFE", "#FFDD00", "#FF7D00", "#FF006D", "#ADFF02",  
"#8F00FF"]
```

```
sns.set_palette(sns.color_palette(HAPPY_COLORS_PALETTE))
```

```
rcParams['figure.figsize'] = 12, 8
```

```
RANDOM_SEED = 42
np.random.seed(RANDOM_SEED)
torch.manual_seed(RANDOM_SEED)
device = torch.device("cuda:0" if torch.cuda.is_available() else "cpu")
device
!gdown --id 1S6qMioqPJyBLpLVz4gmRTnJHnjitnuV
!gdown --id 1zdmewp7ayS4js4VtrJEHzAheSW-5NBZv
df = pd.read_csv("reviews.csv")
df.head()
sns.countplot(df.score)
plt.xlabel('review score');
def to_sentiment(rating):
    rating = int(rating)
    if rating <= 2:
        return 0
    elif rating == 3:
        return 1
    else:
        return 2
df['sentiment'] = df.score.apply(to_sentiment)
```




Diversity of Information Diffusion in Online Social Networks: A Comparative Study

Aaquib Hussain Ganai^{1, *}, Rana Hashmy², Hilal Ahmad Khanday³, Hufsa Manzoor³

¹ Department of computer Applications, Mohan Babu University, Tirupati, Andhra Pradesh, India
hussainaaquib332@gmail.com

² Department of Information Technology, Central University of Kashmir, Ganderbal, J&K, India
ranahashmy@gmail.com

³ Department of computer Science, University of Kashmir, Srinagar, J&K, India
hilalhyder@gmail.com, hufsamanzoorbhat@gmail.com

*Corresponding author: (H. Aaquib), Email Address: hussainaaquib332@gmail.com

Abstract

Online social networks are being created for social interactions and those users that fulfill this paradigm are the real users of online social networks. As these interactions became diverse, the information that these diverse interactions were carrying also flood the online social networks, thereby creates the diffusions of this diverse information and which in turn creates the numerous phenomena among the users of online social networks. These phenomena are so diverse that as you will change the scale of your view, you will notice a different phenomenon that has been adopted by online social network under scanner, from macroscopic view to microscopic view you will notice this flip of phenomena. Keeping an eye on the already sorted out diversity of works, that are hidden or prevalent, we are going to lay a concrete survey to this diversity in this paper by keeping the motive that every existing attempt paves a way for the new one.

Keywords: Social networks, Online social networks, Social Network Analysis (SNA), Information diffusion, Influential user, Spam, Online social graph.

<https://doi.org/10.63070/jesc.2025.015>

Received 14 December 2024; Revised 25 April 2025; Accepted 26 May 2025.

Available online 28 May 2025.

Published by Islamic University of Madinah on behalf of *Islamic University Journal of Applied Sciences*. This is a free open access article.

1. Introduction:

The term “social networks” was coined by Barnes in the human relations Journal in 1954[1]. The social networks are the networks involving people and their interactions [2]. The social networks of the present era have made an elite formalization into the so called online social networks. Online social networks are the usage of the dedicated website to be interactive with other people[3][4]. The first step towards the online social networks was made by the creation of email, then with the evolution of human societies more and more online social network platforms were created. This evolution of online social networks can be traced as facebook and flicker in 2004, twitter in 2006 and sina microblogging in 2009. Every day a lot of information travels through online social networks and this huge amount of data serves as a base for the computational analysis and scientific work. Due to abundance of online social network data, this data fits in the category of big data [5]. The complexities of this data have made evolutions from fine grain to coarse grain [6] as web shifted from web1.0 to web 2.0 [7]. Since the creation of ARPANET [8] to the creation of complex networks, whether technological such as internet, world wide web etc. or online social networks such as Facebook, twitter etc. [9] content dissemination has been the implicit means for their creation. This content dissemination has now been formalized as information diffusion, particularly for the online social networks it is information diffusion in online social networks. This information diffusion in online social networks is a variant of an area of study in social sciences called “diffusion of innovation”, which seeks to explain how, why and at what rate new ideas and technology spread through cultures [47]. As human beings have an innate desire to share information with others [10], so the wide availability of online social network services have encouraged and engaged users to share information and increased the ability of individuals to share information [11]. Social networks are creating a complete virtual environment [12] clearly supports this challenging task of information diffusion [13], because of its diversity and usage; 62% of adults worldwide use online social networks and spend 22% of their online time on online social networks on an average [14] and in India people spend one in four minutes online using online social networking sites; more than any other internet websites [15]. Thus, to mine knowledge and analyze this mined knowledge [16] from the data of information diffusion in online social networks is a need of an hour. The information diffusion over online social networks can be better understood as depicted in the figure Fig.1 below.

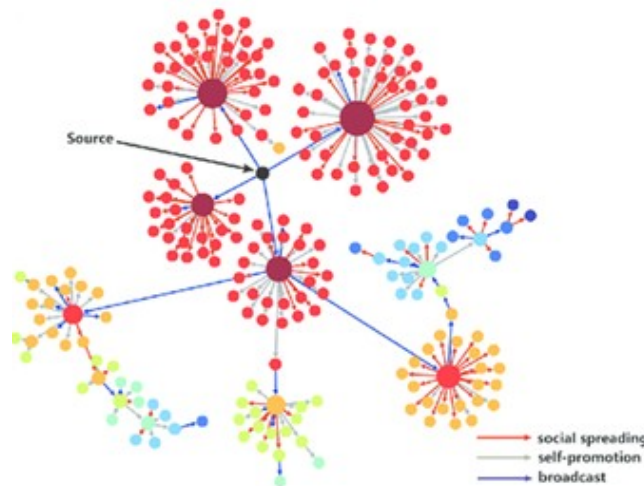


Fig. 1: Information Diffusion in Online Social Networks

OSNs and social media analysis are popular research areas in the contemporary network science [17]; particularly when we talk of information diffusion in OSNs, the diversity and prevalence is apparent almost everywhere; whether it is the case of epidemics in biology, viral marketing in economics, gossip and rumor mongering in sociology and heat diffusion in physics etc. [18]. Researchers have tried to analyze OSNs since the fundamental research discoveries by Girvan and Newman in 2002 [19] and researchers have unveiled this field of information in OSNs through varied dimensions.

2. Related Work

Online social networks and social Media analysis are popular research areas in the contemporary network science [17]; particularly when we talk of information diffusion in online social networks, whose diversity and prevalence is apparent almost everywhere; whether that can be the case of epidemics in biology, viral marketing in economics, gossip and rumor in sociology and heat diffusion in physics etc. [18]. Researchers have tried to analyze the online social networks since the research discoveries by Girvan and Newman in 2002 [19] and particularly to this subfield of information diffusion in online social networks; researchers have unveiled this field of information in online social networks through varied dimensions. Some of attempts related to this paper are:

S. Wu et. al. classified users of online social networks [20], A. Guille et. al. used T-BASIC model to study information diffusion in online social networks [21], w. chengjun et.al. extended ABXC model to ABXCT model for online social networks [22], A. Das et. al. studied the effect of persuasion properties of messages in online social networks [23], A. Silva et. al. proposed profile rank method for finding relevant content and influential users in online social networks [24], Y. Matsubara et.al.





proposes a SPIKEM model for studying the rise and fall patterns of influence propagation in online social networks [25], Y. Yang et. al. uses RAIN model for modeling information diffusion in online social networks [26], L. Liu et. al. proposed a susceptible view forward removed (SVFR) model to describe the information diffusion in online social networks [27], X. Ren et. al. proposed a Role and Topic Aware Independent cascade (RIIC) model to uncover information diffusion in online social networks [28], A. Susarra et. al. analyzed channels that are central to the information diffusion in online social networks [29], L. Taxidou et. al. proposed Prov-SAID model to tackle diffusion and provenance in online social networks [30], M. Farajtabar et. al. Proposed a probabilistic model for finding out dynamics of information diffusion and network evolution in online social networks [31], S. Dhamal et. al. used independent cascade to tackle the problem of finding K users in many phases [32], J. Ping Huang et. al. proposes a game theoretic approach to capture information diffusion in online social networks [33], L. Taxidou et. al. proposes an information cascade model to find the influence paths in online social networks [34], Y. Jianget. et. al. proposed a multi agent perspective for information diffusion in online social networks [35], L. Weng proposed an agent-based model to demonstrate the role of finite individual attention to explain heterogeneity of global patterns [36], Y. Matsubara et. al. proposes SPIKEM model for uncovering information diffusion in online social networks [37], A. Kunle et. al. proposes a Multiplex Influence Maximization (MIM) approach to find influential users [14], F. Wang et. al. proposes a mathematical equation for modeling information diffusion in online social networks [38], V. Arnaboldi et. al. models information diffusion as ego networks [12], M. Farajtabar et. al. uses associative rule learning approach for finding influential users in online social networks [39], A. Guillie et. al. proposes a K core method to find influential spreaders [4], C. Yang et. al. proposes a Neural Diffusion Model (NDM) of deep learning for tackling the micro level independent cascade [40], C. Gatti et. al. proposes a multiagent social network simulation for tackling information diffusion in online social networks [41], H. Kim et. al. proposes a hydrodynamics prediction model for information diffusion in online social networks [42], A. Davoudi et. al. proposes a nonlinear differential equation to study information diffusion in online social networks [43], K. Saito et. al. proposes a model for hot span detection in online social networks [44], Z. Wang et. al. proposes a polling-based method to tackle the activity maximization problem [45], Q. Wang studies the problems associated with online social network data [46], E. Yoneki et. al. studies influence maximization problem [47], P. Sermpezis et. al. studies information diffusion in online social networks as epidemics [48], M. Farajtabar et. al. proposes a probabilistic generative model for information diffusion and network evolution [49], N. Diu et. al. proposes TOPIC CASCADE for topic specific information cascade [50], E. Bakshy studies influence of users with each other [51], S. Jalali et. al. proposes a dynamic model to target petition diffusion in online social networks [52], C. Jiang et. al. a game

theoretic formulization for information diffusion in online social networks [53], M.K. Mahdi et .al. Proposes SFA-ICBM model for modeling independent cascades and finding influentials [54], F. Wang et. al. proposes linear diffusive model for finding influence power of spreading and decaying of news stories [55], P. Tanwar et. al. studies spam detection using Latent Dirichlet Allocation model [56], J.Bright et. al. studies the sentimental analysis [57], J.Obregon et. al. proposes a process model based on extension of Flexible Heuristic Miner [58], L. Jain et. al. uses a Firefly algorithm to find global and local opinion leaders [59], J.Dai et. al. proposes LNC Local Neighbor Communication model to find influential users [60], D. Pothineni et al. attempts to measure different thermodynamic variables when taking online social networks as thermodynamic system [61], J. Alemany et. al. presents a new Risk model based on friend layers [62].

3. Components of Information Diffusion and Models for their handlings

In this research area of information diffusion in online social networks, we are always revolving around the four components: (1) People (2) Content (3) Network and (4) Diffusion [20][36] as depicted in the Table. 1 below:

Table1: Components of Information Diffusion

Component	Representation	Function
People		These are the actors of seen who produce information(content) for diffusion in OSN's
Content		This is the element that people create for diffusions in OSN's
Network		This is the output that people with diffusing contents create in OSN's
Information Diffusion		This is process that can reveal varied pattern formations that have led to network formations in OSN's

Each of these components acts a full-fledged dimension for researchers of information diffusion in online social networks, to tackle the problems intrinsic in these components, so we are going to take each component as dimension of information diffusion in online social networks and the popular problems associated with each component.

3.1 People:

People are the real physical entities that are apparent on online social networks. Their reflections on online social networks are felt as user accounts, pages, handles etc., when online social networks are represented by underlying online social graphs, they are modeled as nodes of the given graph.

The most popular problem that is studied in the study of information diffusion under this domain is influential user detection in online social networks. Much research has been done in this problem area of information diffusion in online social networks, so we are going to explore some of the good attempts that have been made to tackle this problem of finding influential users in online social networks.

3.1.1 Influential User Detection:

There is no concrete definition of influence and so influential user in online social networks [35], each researcher takes it according to implicit character of users in datasets of online social networks under scanner [59]. Influence may be loosely defined as the capacity of effecting the character, development, growth, popularity and behavior of others in online social networks [61] and the people that show this character at the peak scale are referred to as influential users. To detect these influential users is a young problem in the domain of information diffusion in online social networks. Some of the works that have taken the cognizance of finding influential users in online social networks are:

a) Profile Rank

Profile rank is similar to the idea of Page Rank Algorithm. This method finds influential users; Measures Profile Rank using random walks in user content graph. This method can also work for the content relevance [24].

b) Multiplex Influence Maximization (MIM):

Multiples Influence Maximization (MIM) method finds influential users that are acting as seeds. Most users are overlapping [14].

c) Associative Rule:

This method finds influential users and belongs to the machine learning domain of studies. Uses support, confidence, and lift parameters to learn influential Users. This method is faster, but its application for bigger pages/contents is not natural [39].

d) K Core Approach

K core approach finds influential users. Uses graph structure of the given network for finding core K and uses minimum degree concept to tackle problem. This approach uses maximal connected sub graph concept to uncover k-Core of given online social graph [4].

e) SFA-ICDBM:

This method finds most Influential users in the given Network and Uses extended CPM to find initial communities. Makes use of belonging coefficient to find influentials. Takes the cognizance of overlapped nodes while considering the solution [54].

f) Modified firefly Algorithm:

This Approach finds local and global influential users (opinion leaders). Opinion leaders are found in inter-class community and intra-class community that have been found by modified Louvain method earlier. This Algorithm Ranks users based on attractiveness score to find opinion leaders. Results show that the method performs best when operated by different SNA measures [59].

g) Interest Group based influential user detection:

This Approach finds influential users in each Interest Group. Model is based on local graphical traversal in each Group. Model works well for finding observer nodes in each Interest Group [63].

These are some of the problem solutions that are considered by different Researchers and every solution creates new window for making the solutions possible for finding the people (users), whom we call as influentials.

3.2 Content:

It is this content that brings people to online social networks; some to view the content, some to share the content and some to comment on content. Content takes many forms depending on the online social network platform under usage; twittes on twitter and messages on Facebook etc. [36]. Content of online social networks are mostly modeled as weights of links when represented in graphical form and the movements of contents depicted as directed links when represented by online social network graphs. One of most difficulties that have posed the hurdles to research on information diffusion in online social networks is the lack of sufficient and complete communication content (data) of online social networks [47]. The problem that is related to this content in the area of information diffusion in online social networks is Spam detection, so we are going to address the same problem and the associated solutions here:

3.2.1 Spam detection and its solutions:

Cyber criminals are generating the attacks using a growing arsenal of weapons such as spam [64]. Spam was first invented by Monty Python in year 1970[56].It is possible for attackers to use unwanted data to be send as content called spam over Online Social Networks[65],so our problem in hand is to

detect this spam as a content under the of information diffusion in online social networks; some of the attempts are:

a) Latent Dirichlet Allocation (LDA):

This Method Detects spam and no spam data. Uses a corpus and Dictionary built on twitter data sets and Uses LDA as classifier that classifies matrix (corpus) into two matrices Document-topics matrix and Topics-term matrix. LDA detects spam data mostly up to thirty characters [56].

3.3. Network:

The online social networks which involves social interactions can be modeled as graphic networks; graphs with adopted weights as communication contents[66], so online social networks can be represented by a graph $G(V,E)$ with V as a set of nodes as people(users) and E as set of edges representing communication contents[28][2]. these online social graphs can be directed or undirected based on the character of underlying online social network[36]. these online social graphs can be represented by adjacency list, adjacency matrix[3][67], incidence lists, incidence matrix[5]; use list representation when complexity of online social network under scanner is small and uses matrices when network is dense [67]. the best problem that is being studied with related to structure of a social graph of underlying online social network in the field of information diffusion in online social networks is network evolution; which captures how network evolve during diffusions of interactions in online social networks. Many researchers have opted to go for the discourse of this problem and solve it as:

3.3.1 Probabilistic model:

This Model tackles the problem of network evolution in online social networks; Models network link creation as “information driven” survival process and couples the intensity of survival process with retweeting events. This Model Uncovers the joint dynamics of information diffusion and network evolution and develops a convex optimization frame work to learn the parameters of the model from the network evolution traces. This Model performs best on real and synthetic data [31][49].

The network evolution is still emergent problem and needs ocean of ventures to solve the real social evolutions in online social networks.

3.4 Information Diffusion:

when a piece of content (information) flows from one individual to another or from one community to another in an online social network, an act of information diffusion is said to have occurred in that online social network[1][68]. when this act of information diffusion in online social networks is studied under the broad domain of information diffusion of SNA, we often encounter the “3 w issue”, the three W’s are “what”, “why” and “where”. the first w “what” refers to the question “what information is

there to be found in online social networks”, the second w is “why” refers to the question “why has the information propagated this way”, the third w is “where” refers to the question “where will the information be diffused in the future” [1][48].this 3W issue has been best studied under the broad spectrum of two information diffusion process models:-

Explanatory models and prediction models.

3.4.1 Explanatory Models:

Such models explain the process of information diffusion that has been adopted by the given online socialnetwork under scanner. These models reflect the real human behavior. The best example of these models is epidemic models such as SIS, SIRetc. Models [7]. Parameters of these models are easily available and are little complexin case of modeling complexities [12][3].

3.4.2 Prediction Models:

Such models long for tackling the decision problem [66] which can take yes or no states for deciding whether diffusion will usher or not from current known state to unknown state; unknown state belongs to future.

These models do not reflect the true nature of human socialism.

Parameters of models are hard to model, so these models are highly complex in nature.

The best examples of these models are independent cascade model, linear threshold model etc..., [12][3][46][7][69][70].

Keeping these two models of information in eye, we can look at these two models with respect to the “3W issue” and their capabilities of modeling real human behavior; this is shown below in the Table 2:

Table 2. Comparative Analysis of Information Diffusion Models

Model of Information Diffusion	Tackle W1 of 3W Issue	Tackle W2 of 3W Issue	Tackle W3 of 3W Issue	Reflect True Human Behavior
Explanatory model	Yes	Yes	No	Yes
Prediction model	Yes	Yes	Yes	No

This table reflects the real functionalities of the two-process models of information diffusion in online social networks.

Researchers have used both the models to put their efforts on information diffusion in online social networks keeping the two model paradigms as base, so we are going to uncover some of the efforts that have been made for each of the models here.

The components of information diffusion in collective and comparative way can be shown as depicted in the table Table3.

Table 3. Research Components of Information Diffusion in Online Social Networks

Research Component of Information Diffusion	Modes of Handling	Purpose of Component in the Light of Handling Mode
Information Dissemination	Independent Cascade Model	Studies the information cascades by identifying the transmission of activeness from active node at time t to inactive node at time $t+1$ depending on the weight of connecting edge.
	Linear Threshold Model	Studies the information cascades by identifying the transmission of activeness by simply using the threshold function at an inactive node by taking the input from previous active nodes.
	Epidemic model	Studies the information cascades by identifying the transmission of activeness based on epidemiology of medical science.
Community Detection	Disjoint Community Detection	Finds the community structure in OSNs but node belongs to a single community.
	Overlapping Community Detection	Finds the community structure in OSNs but node may belong to multiple communities.
Influence Maximization	Influential Users as Seeds	Finds the limited influential users by selecting them in such a way that they increase the influence dissemination in the given OSN.
Influential User Detection	Global and Local Influential Users	Finds the influential users that are unlimited in nature depending on the given OSN, but those users are global or local to the network of the given OSN.

4. Conclusion

We have taken a focusable view on the exiting windows that have been projected by different researchers in the field of information diffusion in online social networks. We should bring this legacy of work into vigil and should transform our new ideas into the real models of this day in the light of already existing work that has been made.

References:

- [1] Li, M., Wang, X., Gao, K., & Zhang, S. (2017). A Survey on Information Diffusion in Online Social Networks: Models and Methods. *Information*, 8(4), 118. <https://doi.org/10.3390/info8040118>
- [2] Iacopini, I., Karsai, M., & Barrat, A. (2024). The temporal dynamics of group interactions in higher-order social networks. *Nature Communications*, 15, 7391. <https://doi.org/10.1038/s41467-024-50918-5>
- [3] Wong, A., Ho, S., Olusanya, O., Antonini, M. V., & Lyness, D. (2021). The use of social media and online communications in times of pandemic COVID-19. *Journal of the Intensive Care Society*, 22(3), 255–260. <https://doi.org/10.1177/1751143720966280>.
- [4] Guille, A., Hacid, H., Favre, C., & Zighed, D. A. (2013). Information Diffusion in Online Social Networks: A Survey. *SIGMOD Record*, 42(2), 17-28. <https://doi.org/10.1145/2503792.2503797>
- [5] Kurka, D. B. (2015). *Online social networks: Knowledge extraction from information diffusion and analysis of spatio-temporal phenomena* (Dissertation). Retrieved from [Institution repository link]
- [6] Sima, D., Fountain, T., & Karasuk, P. (n.d.). *Advanced Computer Architecture: A Design Space Approach* (1st ed.). Pearson.
- [7] Cole, W. D. (n.d.). *An Information Diffusion Approach for Detecting Emotional Contagion in Online Social Networks* (Master's thesis, Arizona State University). Retrieved from [Institution repository link]
- [8] Tenenbaum, A. S. (n.d.). *Computer Networks* (1st ed.). Pearson.
- [9] Sermpezis, P., & Spyropoulos, T. (2013). Information diffusion in heterogeneous networks: The configuration model approach. In *IEEE INFOCOM 2013* (pp. 3261-3266). IEEE. <https://doi.org/10.1109/INFCOM.2013.6566986>
- [10] Kumar, K. P. K. (2015). *Information Diffusion Modeling to Counter Semantic Attacks in Online Social Networks* (PhD thesis). Retrieved from <http://hdl.handle.net/10603/123660>
- [11] Sun, Q., Li, Y., Hu, H., & Cheng, S. (2019). A model for competing information diffusion in social networks. *IEEE Access*, 7, 67916-67922. <https://doi.org/10.1109/ACCESS.2019.2918812>
- [12] Arnaboldi, V., Conti, M., Passarella, A., & Dunbar, R. (2017). Online social networks and information diffusion: The role of ego networks. *Online Social Networks and Media*, 1, 44-55. <https://doi.org/10.1016/j.osnem.2017.04.001>
- [13] Wang, F., Wang, H., Xu, K., Wu, J., & Jia, X. (2013). Characterizing information diffusion in online social networks with linear diffusive model. In *Proceedings - 2013 IEEE 33rd International Conference on Distributed Computing Systems, ICDCS 2013* (pp. 307-316). IEEE. <https://doi.org/10.1109/ICDCS.2013.14>
- [14] arXiv:1802.01729
- [15] Behera, P. C. (2020). Data mining technique for tracking of information diffusion in online social network. *International Journal of Latest Research in Science and Technology*, 5.
- [16] Han, J., Kamber, M., & Pei, J. (n.d.). *Data Mining* (3rd ed.).
- [17] Erlandsson, F., Bródka, P., Borg, A., & Johnson, H. (2016). Finding influential users in social media using association rule learning. *Entropy*, 18(5), 164. <https://doi.org/10.3390/e18050164>
- [18] Wang, F., Wang, H., & Xu, K. (n.d.). *Dynamic Mathematical Modeling of Information Diffusion in Online Social Networks*. Arizona State University. Retrieved from [Arizona State University link].
- [19] Cazabet, R., Amblard, F., & Hanachi, C. (2010). Detection of overlapping communities in dynamical social networks. In *2010 IEEE International Conference on Social Computing* (pp. 309-314). IEEE. <https://doi.org/10.1109/SocialCom.2010.51>
- [20] Wu, S. (n.d.). *The Dynamics of Information Diffusion on Online Social Networks* (PhD thesis).

- [21] Guille, A., Hacid, H., Favre, C., & Zighed, D. A. (2013). Information diffusion in online social networks: A survey. *SIGMOD Record*, 42(2), 17–28. <https://doi.org/10.1145/2503792.2503797>
- [22] Wang, C. (2014). Jumping over the network threshold: Information diffusion on information sharing websites. *PhD Thesis*, City University of Hong Kong. Retrieved from [https://scholars.cityu.edu.hk/en/theses/theses\(6f918870-1270-4232-bb3c-e66ce4bb4a05\).html](https://scholars.cityu.edu.hk/en/theses/theses(6f918870-1270-4232-bb3c-e66ce4bb4a05).html)
- [23] Das, A., Gollapudi, S., & Kiciman, E. (2014). Effect of persuasion on information diffusion in social networks.
- [24] Silva, A., Guimarães, S., Meira Jr., W., & Zaki, M. (2013). ProfileRank: Finding relevant content and influential users based on information diffusion. <https://doi.org/10.1145/2501025.2501033>
- [25] Matsubara, Y., Sakurai, Y., Prakash, B. A., Li, L., & Faloutsos, C. (2012). Rise and fall patterns of information diffusion: Model and implications. *Proceedings of the 18th ACM SIGKDD International Conference on Knowledge Discovery and Data Mining* (pp. 6–14). <https://doi.org/10.1145/2339530.2339537>
- [26] Yang, Y., Tang, J., Leung, C. W., Sun, Y., Chen, Q., Li, J., & Yang, Q. (2015). RAIN: Social role-aware information diffusion. In *Proceedings of the Twenty-Ninth AAAI Conference on Artificial Intelligence (AAAI'15)* (pp. 367–373).
- [27] Liu, L., Qu, B., Chen, B., Hanjalic, A., & Wang, H. (2017). Modeling of information diffusion on social networks with applications to WeChat. arXiv:1704.03261
- [28] Ren, X., & Zhang, Y. (2016). Predicting information diffusion in social networks with users' social roles and topic interests. In *Ma, S. et al. (Eds.), Information Retrieval Technology. AIRS 2016. Lecture Notes in Computer Science*, vol. 9994 (pp. 343–354). Springer. https://doi.org/10.1007/978-3-319-48051-0_30
- [29] Susarla, A., Oh, J. H., & Tan, Y. (2012). Social networks and the diffusion of user-generated content: Evidence from YouTube. *Information Systems Research*, 23(1), 23–41. <https://doi.org/10.1287/isre.1110.0404>
- [30] Taxida, L., Fischer, P. M., De Nies, T., Mannens, E., Verborgh, R., & Van de Walle, R. (2015). Modeling information diffusion in social media as provenance in W3C Prov. *ACM Transactions on the Web*.
- [31] Farajtabar, M., Gomez-Rodriguez, M., Wang, Y., Li, S., Zha, H., & Song, L. (2015). Co-evolutionary dynamics of information diffusion and network structure. In *Proceedings of the 24th International Conference on World Wide Web* (pp. 619–620). ACM.
- [32] Dhamal, S., Prabuchandran, K. J., & Narahari, Y. (2015). A multi-phase approach for improving information diffusion in social networks. In *The 14th International Conference on Autonomous Agents & Multiagent Systems (AAMAS 2015)*, May 4–8, 2015, Istanbul, Turkey.
- [33] Huang, J.-P., Wang, C.-Y., & Wei, H.-Y. (2011). Strategic information diffusion through online social networks. In *Proceedings of the 4th International Symposium on Applied Sciences in Biomedical and Communication Technologies (ISABEL '11)*. ACM. <https://doi.org/10.1145/2093698.2093786>
- [34] Taxidou, I., & Fischer, P. M. (2014). Online analysis of information diffusion in Twitter. In *Proceedings of the 23rd International Conference on World Wide Web (WWW '14 Companion)* (pp. 1313–1318). ACM. <https://doi.org/10.1145/2567948.2580050>
- [35] Jiang, Y., & Jiang, J. C. (2015). Diffusion in social networks: A multi-agent perspective. *IEEE Transactions on Systems, Man, and Cybernetics: Systems*, 45(2), 198–213. <https://doi.org/10.1109/TSMC.2014.2339198>
- [36] Weng, L. (n.d.). *Information Diffusion on Online Social Networks* (PhD thesis, Indiana University). Retrieved from <http://hdl.handle.net/2027.42/89838>
- [37] Matsubara, Y., Sakurai, Y., Prakash, B. A., Li, L., & Faloutsos, C. (2017). Nonlinear dynamics of information diffusion in social networks. *ACM Transactions on the Web*, 11(2), Article 11, 40 pages. <https://doi.org/10.1145/3057741>

- [38] Wang, F., Wang, H., & Xu, K. (n.d.). Dynamic Mathematical Modeling of Information Diffusion in Online Social Networks. Arizona State University. Retrieved from <https://www2.cs.arizona.edu/~bzhang/CCW2012/slides/xu.pdf>
- [39] Farajtabar, M., Wang, Y., Rodriguez, M., Li, S., Zha, H., & Song, L. (2015). COEVOLVE: A joint point process model for information diffusion and network co-evolution. *Journal of Machine Learning Research*, 18, 1305–1353.
- [40] Yang, C., Sun, M., Liu, H., Han, S., Liu, Z., & Luan, H. (2018). Neural Diffusion Model for Microscopic Cascade Prediction. arXiv:1812.08933
- [41] Gatti, M. A. de C., Appel, A. P., dos Santos, C. N., Pinhanez, C. S., Cavalin, P. R., & Neto, S. B. (2013). A simulation-based approach to analyze information diffusion in microblogging online social network. In *2013 Winter Simulations Conference (WSC)* (pp. 1685-1696). IEEE. <https://doi.org/10.1109/WSC.2013.6721550>
- [42] Kim, H., & Yoneki, E. (2012). Influential neighbours selection for information diffusion in online social networks. In *2012 21st International Conference on Computer Communications and Networks (ICCCN)* (pp. 1-7). IEEE. <https://doi.org/10.1109/ICCCN.2012.6289230>
- [43] Hu, Y., Song, R. J., & Chen, M. (2017). Modeling for information diffusion in online social networks via hydrodynamics. *IEEE Access*, 5, 128-135. <https://doi.org/10.1109/ACCESS.2016.2605009>
- [44] Davoudi, A., & Chatterjee, M. (2016). Prediction of information diffusion in social networks using dynamic carrying capacity. In *2016 IEEE International Conference on Big Data (Big Data)* (pp. 2466–2469). IEEE. <https://doi.org/10.1109/BigData.2016.7840883>
- [45] Saito, K., Kimura, M., Ohara, K., & Motoda, H. (2013). Detecting changes in information diffusion patterns over social networks. *ACM Transactions on Intelligent Systems and Technology*, 4(3), Article 55. <https://doi.org/10.1145/2499862>
- [46] Wang, Z., Yang, Y., Pei, J., & Chen, E. (2016). Activity Maximization by Effective Information Diffusion in Social Networks. *IEEE Transactions on Knowledge and Data Engineering*, PP. <https://doi.org/10.1109/TKDE.2017.2740284>.
- [47] Kim, H., & Yoneki, E. (2012). Influential Neighbours Selection for Information Diffusion in Online Social Networks. *2012 21st International Conference on Computer Communications and Networks, ICCCN 2012 - Proceedings*, 1–7. <https://doi.org/10.1109/ICCCN.2012.6289230>.
- [48] Wang, Q. (2016). Towards Understanding Information Diffusion about Infrastructure, An Empirical Study of Twitter Data. Retrieved from https://www.irbnet.de/daten/iconda/CIB_DC29666.pdf.
- [49] Farajtabar, M., Wang, Y., Gomez-Rodriguez, M., Li, S., Zha, H., & Song, L. (2017). COEVOLVE: A Joint Point Process Model for Information Diffusion and Network Evolution. *Journal of Machine Learning Research*, 18, 1305–1353.
- [50] Du, N., Song, L., Woo, H., & Zha, H. (2013). Uncover Topic-Sensitive Information Diffusion Networks. *AISTATS*.
- [51] Bakshy, E. (2011). Information Diffusion and Social Influence in Online Networks. *PhD Thesis*, University of Michigan. Retrieved from <http://hdl.handle.net/2027.42/89838>.
- [52] Jalali, M. S., Ashouri rad, A., Herrera-Restrepo, O., & Zhang, H. (2016). Information Diffusion through Social Networks: The Case of an Online Petition. *Expert Systems with Applications*, 187–197. <https://doi.org/10.1016/j.eswa.2015.09.014>.
- [53] Jiang, C., Chen, Y., & Liu, K. J. R. (2014). Modeling Information Diffusion Dynamics over Social Networks. *ICASSP, IEEE International Conference on Acoustics, Speech and Signal Processing - Proceedings*, 1095–1099. <https://doi.org/10.1109/ICASSP.2014.6853766>.
- [54] Mahdi, M. K., & Almanory, H. N. (2019). Modeling the Information Diffusion Overlapped Nodes Using SFA-ICBDMA. *IJRTE*. <https://doi.org/10.35940/ijrte.B1710.078219>.
- [55] Wang, F., Wang, H., Xu, K., Wu, J., & Jia, X. (2013). Characterizing Information Diffusion in Online Social Networks with Linear Diffusive Model. In *2013 IEEE 33rd International*

- Conference on Distributed Computing Systems* (pp. 307–316). IEEE. <https://doi.org/10.1109/ICDCS.2013.105>.
- [56] Tanwar, P., & Priyanka. (2019). Spam Diffusion in Social Networking Media Using Dirichlet Allocation. *IJITEE*. Retrieved from <https://www.ijitee.org/wp-content/uploads/papers/v8i12/I7898078919.pdf>.
- [57] Bright, J., Margetts, H., Hale, S., & Yasseri, T. The Use of Social Media for Research and Analysis: A Feasibility Study. *Oxford Institute Press*. Retrieved from <https://www.bl.uk/collection-items/use-of-social-media-for-research-and-analysis-a-feasibility-study#>.
- [58] Obregon, J., Song, M., & Jung, J.-Y. (2019). InfoFlow: Mining Information Flow Based on User Community in Social Networking Services. *IEEE Access*, 7, 48024–48036.
- [59] Jain, L., & Katarya, R. (2019). Discover Opinion Leader in Online Social Network Using Firefly Algorithm. *Expert Systems with Applications*, 122, 1–15.
- [60] Dai, J., Wang, B., Sheng, J., Sun, Z., Khawaja, F. R., Ullah, A., Dejene, D. A., & Duan, G. (2019). Identifying Influential Nodes in Complex Networks Based on Local Neighbor Contribution. *IEEE Access*, 7, 131719–131731.
- [61] Pothineni, D., Mishra, P., & Rasheed, A. (2012). Social Thermodynamics: Modeling Communication Dynamics in Social Networks. In *The First International Conference on Future Generation Communication Technologies* (pp. 76–82). IEEE.
- [62] Alemany, J., Del Val, E., Alberola, J. M., & García-Fornés, A. (2019). Metrics for Privacy Assessment when Sharing Information in Online Social Networks. *IEEE Access*, 7, 143631–143645.
- [63] Al-Azim, N. A. R., Gharib, T. F., Afify, Y., & Hamdy, M. (2020). Influence Propagation: Interest Groups and Node Ranking Models. *Physica A: Statistical Mechanics and its Applications*, 124247.
- [64] Carey, A. (2000). Global Information Workforce Study. Retrieved from www.idc.com.
- [65] Gregg, M., Watkins, S., Mays, G., Ries, C., Bandes, R. M., & Franklin, B. (2006). Hack the Stack: Using Snort and Ethereal to Master the 8 Layers of an Insecure Network. Elsevier.
- [66] Horowitz, E., Sahni, S., & Rajasekaran, S. (2008). *Fundamentals of Computer Algorithms* (2nd ed.).
- [67] Rosen, K. H., & Krithivasan, K. *Discrete Mathematics and Its Applications* (McGraw-Hill).
- [68] Anh, N., Son, D., Thu, H., Kuznetsov, S., & Vinh, N. T. Q. (2018). A Method for Determining Information Diffusion Cascades on Social Networks. *Eastern-European Journal of Enterprise Technologies*, 6, 61–69. <https://doi.org/10.15587/1729-4061.2018.150295>.
- [69] Ganai, A.H., Hashmy, R. & Khanday, H.A. Finding Information Diffusion's Seed Nodes in Online Social Networks Using a Special Degree Centrality. *SN COMPUT. SCI.* **5**, 333 (2024). <https://doi.org/10.1007/s42979-024-02683-x>
- [70] Ganai, A.H., Hashmy, R., Khanday, H.A. *et al.* IDT-Cascade: a novel information dissemination tree model for influential cascade detection in online social networks. *Int. j. inf. tecnol.* (2025). <https://doi.org/10.1007/s41870-025-02573-2>



Recent Advances in Stability and Seepage Analysis of Earth Dams: A Review Leveraging Numerical Methods and Computational Intelligence

Hicham Charrak

RISAM Lab, University of Tlemcen.

Department of Architecture, Faculty of Sciences, University of Algiers 1, Algeria.

h.charrak@univ-alger.dz

<https://orcid.org/0000-0001-8482-7862>

Abstract

Ensuring the safety and long-term performance of earth dams is paramount due to their critical role in water management and the potential consequences of failure. Dams are susceptible to stability issues and internal erosion driven by complex hydraulic conditions, including seepage and fluctuating water levels. Traditional analytical methods often fall short in capturing the full complexity of these interactions and optimizing mitigation measures. This review fills a notable gap in the existing literature by holistically integrating numerical modeling (FEM, Limit Equilibrium) and artificial intelligence (ANN, GA) techniques to provide a comprehensive assessment of earth dam behavior. This review synthesizes recent research applying advanced computational techniques, including numerical methods like the Finite Element Method (FEM) and Limit Equilibrium methods, alongside computational intelligence approaches such as Artificial Neural Networks (ANN) and Genetic Algorithms (GA), to analyze the stability and seepage characteristics of earth dams and evaluate the effectiveness of seepage control measures. Drawing insights from several recent studies, this article examines the influence of rapid drawdown on dam slope stability, the impact of fissured soil orientation, and critically, the effectiveness of various seepage control measures (cutoff walls, horizontal drains, pipe drains, injections) and their optimal configurations, including combined approaches. It highlights the capabilities of numerical modeling for detailed analysis and optimization and the potential of AI and hybrid methods for improved prediction and parameter identification in complex, nonlinear scenarios. The findings underscore the importance of integrating diverse computational tools for robust design, risk assessment, and monitoring of earth dams.

Keywords: Earth dams; Stability assessment; Seepage mitigation; Finite Element Method; Neural networks; Genetic algorithms.

<https://doi.org/10.63070/jesc.2025.016>

Received 02 April 2025; Revised 12 May 2025; Accepted 26 May 2025.

Available online 28 May 2025.

Published by Islamic University of Madinah on behalf of *Islamic University Journal of Applied Sciences*.

This is a free open access article.

1. Introduction

Earth dams are essential components of modern infrastructure, serving vital functions such as water supply, hydropower generation, and irrigation. However, their performance and stability are subject to complex interactions between soil mechanics and hydraulic conditions. Challenges such as internal erosion, piping, rapid water level changes (rapid drawdown), and the presence of heterogeneous or fissured materials pose significant risks to their structural integrity. Water seepage through the dam body and foundation is a primary concern, contributing to over 35% of earth dam accidents [6].

Historically, the analysis of dam stability and seepage relied primarily on simplified analytical or limit equilibrium methods [12]. While foundational, these approaches often fall short in capturing the nuanced, nonlinear behavior of geomaterials and the intricate geometries of dams and their foundations. The advent of high-performance computing has paved the way for sophisticated numerical methods, particularly the Finite Element Method (FEM) and various Limit Equilibrium techniques, which offer powerful tools for detailed simulation of stress-strain behavior, fluid flow, and potential failure mechanisms [1, 3, 4, 5, 7, 8, 12]. Software like GeoSlope (SEEP/W, SLOPE/W) and OptumG2 have become indispensable in this domain, enabling engineers to model complex scenarios and analyze critical parameters like factor of safety, displacement fields, and pore water pressures [1, 3, 7, 8]. More recently, computational intelligence techniques, notably Artificial Neural Networks (ANN) and Genetic Algorithms (GA), are emerging as valuable complements to traditional numerical methods. These data-driven approaches excel at identifying complex, often nonlinear, relationships within large datasets and show promise in areas like parameter estimation, prediction, and optimization, which can enhance the capabilities of physics-based models [5]. Despite the increasing application of numerical and AI methods in geotechnical research, there is a clear lack of comprehensive reviews that synthesize both perspectives in the context of dam seepage and stability assessment. This article aims to bridge this gap by critically examining and comparing recent work that leverages these complementary approaches. This review article consolidates findings from recent studies that leverage these advanced computational tools to address critical problems in the analysis of earth dams. By synthesizing insights from the provided set of research papers, it aims to highlight the current state of practice, identify key findings regarding dam behavior under challenging conditions, and underscore the synergistic potential of combining numerical modeling with computational intelligence for optimizing seepage control and enhancing stability.

2. Dam Stability and Seepage Analysis

Earth dams, as critical water impoundment structures, are particularly susceptible to stability issues driven by internal seepage and fluctuating water levels. Ensuring their stability requires thorough analysis under various operational scenarios.

2.1 Impact of Rapid Drawdown

Rapid drawdown of water from the reservoir is a particularly challenging condition for the upstream slope stability of earth dams. This phenomenon leads to a rapid reduction in the stabilizing external hydrostatic pressure on the upstream face, while the pore water pressure within the saturated embankment fill dissipates much more slowly due to limited permeability. This imbalance significantly reduces the effective stresses and, consequently, the shear strength of the soil, potentially leading to slope failure [1, 10].

Numerical studies, such as the case study of the Sidi Abdelli dam using Geo-SLOPE/W [1], and other FEM analyses [10, 11], confirm that the factor of safety (FS) of the upstream slope decreases significantly with the initiation of rapid drawdown. Berilgen (2007) highlighted that the rate of pore water fall has a significant impact on stability during drawdown, influencing the magnitude of displacement [9]. The analysis shows that pore water pressures near the toe of the dam are high before drawdown, decrease as elevation rises, and become very low at the toe after rapid drawdown initiates, only to increase as dissipation begins before decreasing again with elevation. Velocity vectors of seepage reverse direction during rapid drawdown, exiting from the upstream side, indicating a potential seepage face on the upstream slope. The Factor of Safety drops below 1.0 in the initial days of rapid drawdown, signifying an unsafe condition, but gradually increases above 1.0 after a certain period (e.g., 13 days in the Sidi Abdelli case), as pore water pressure dissipates and effective stresses recover [1]. This highlights the transient nature of the stability issue during rapid drawdown and the importance of considering the rate of pore pressure dissipation [1, 11].

2.2 Stability in Fissured Materials

The presence of fissures in dam foundation or embankment materials introduces planes of weakness that can significantly influence stability and seepage patterns. Unlike intact soil, fissured soil behavior depends not only on the inherent soil properties but also on the orientation, spacing, and properties of the fissures themselves [4]. Research by Davis (1980) and Zheng et al. (2000) has established failure criteria for fissured soil, providing a foundation for understanding their behavior [13, 14].

Numerical investigations using FEM software like OptumG2, which incorporate failure criteria accounting for fissured planes with varying orientations, demonstrate the substantial impact of fissure

angles on dam stability. Studies analyzing different orientations (using angles α_1 and α_2 , and their coupled effects) reveal that the factor of safety and resulting slope displacements vary significantly depending on the fissure angles. While intact soil exhibits a certain baseline FoS, the presence of fissures generally leads to lower FoS values. The critical failure surface location and type (circular, infinite, or plane slides) are also dictated by the fissure orientation. Notably, findings suggest that dams built on or with fissured materials where fissures are oriented closer to the vertical tend to exhibit higher stability compared to those with fissures oriented closer to the horizontal. Displacement patterns and magnitudes are also strongly influenced by fissure orientation, with maximum displacements often observed near the core and varying significantly with coupled fissure angles [4]. This underscores the necessity of detailed site investigation and analysis considering the specific characteristics and orientation of fissured planes in dam design and stability assessment.

2.3 Seepage Control Measures in Dams

Controlling seepage through the dam body and foundation is crucial for preventing internal erosion, reducing uplift pressures, and maintaining overall stability. Common measures include cutoff walls and drainage systems (horizontal drains, pipe drains, injection curtains) [3, 6, 7, 8]. Numerical modeling is extensively used to optimize the design parameters of these measures.

Studies on injection curtains and horizontal drains highlight the influence of various parameters on seepage characteristics like uplift pressure, discharge seepage, and exit gradient [3, 6]. For injection curtains, depth, permeability, position, inclination, number, and spacing are key factors [6]. Analysis shows that cutoff wall depth significantly impacts seepage, with maximum efficiency in reducing exit gradient and discharge seepage achieved when the penetration depth exceeds 75% of the foundation depth, especially with low permeability. Permeability of the cutoff wall is paramount; lower permeability dramatically reduces flow and changes seepage paths. Optimal configurations involving cutoff walls and horizontal drains are sought to minimize uplift pressure and exit gradient, parameters critical for preventing piping and ensuring stability [3].

A comparative analysis of horizontal and pipe drains reveals differences in their effectiveness. Numerical simulations show that pipe drains generally outperform horizontal drains in managing seepage and enhancing stability. Pipe drains, particularly those with larger diameters, lead to a more significant reduction in pore pressure compared to horizontal drains. Optimal placement of these drains is critical; studies indicate that for pipe drains, locations within a specific relative distance ($X/B=0.2$ to 0.4 , where X is distance from toe and B is dam base width) from the dam toe result in maximum safety factors. While horizontal drains also contribute to seepage control, their impact on pore pressure reduction and overall stability appears less pronounced than that of optimally placed pipe drains. Analyzing statistical error

metrics (RMS, MAE, MSE) confirms that pipe drains provide more consistent predictions of discharge seepage and exit gradient compared to horizontal drains, indicating better control over erosion risk [7].

Further investigation into combined countermeasures is crucial for comprehensive seepage control. A case study on the Krerish Dam in Algeria, utilizing SEEP/W, examined the combined effects of cutoff wall depth and position, and horizontal drain length on seepage characteristics including discharge seepage, exit gradient, and uplift pressure [8]. The study provides valuable quantitative insights into the performance of different combined configurations, as summarized in Table 1.

Table 1. Summary of Performance Improvements for Key Combined Seepage Control Configurations Adapted from Krerish Dam Study [8].

Configuration	Reduction in Discharge Seepage (%)	Reduction in Exit Gradient (%)	Reduction in Uplift Pressure (%)
Cutoff Wall Depth 1.0H (vs 0.5H)	35	28	<i>Decreases with depth</i>
Cutoff Wall Central Position (vs Downstream)	<i>Lower Q, i central vs downstream</i>	<i>Lower Q, i central vs downstream</i>	22 (Central lower)
Horizontal Drain Length 0.3X (vs 0.1X)	15	<i>Decreases with length.</i>	40
Optimal Combined: CW 1.0H Central + HD 0.3X	45	38	50

As shown in Table 1, increasing cutoff wall depth from 0.5H to 1.0H significantly decreased discharge seepage (by 35%) and outlet gradient (by 28%). The position of the cutoff wall also mattered; a central placement within the dam base was more effective than a downstream placement, reducing uplift pressure by 22% compared to the downstream position [8]. Horizontal drain length also played a critical role; increasing the length from 0.1X to 0.3X (where X is the dam width) led to a 40% reduction in uplift pressure and a 15% reduction in discharge seepage. The most effective configuration identified was a combination of a centrally located cutoff wall at a depth of 1.0H and a horizontal drain with a length of 0.3X. This optimal setup achieved substantial overall reductions: a 45% decrease in discharge seepage, a 38% decrease in exit gradient, and a 50% decrease in uplift pressure. Error analysis of different configurations using RMS, MAE, and MSE metrics further highlighted the importance of incorporating cutoff wall depth, particularly when combined with horizontal drains, for achieving more accurate predictions and better seepage control [8].

3. Integration of Advanced Computational Techniques

Beyond traditional numerical methods, the integration of computational intelligence techniques offers promising avenues for enhancing geotechnical analysis, particularly in dealing with data-driven prediction and complex nonlinear systems.

Artificial intelligence methods, such as Back Propagation Neural Networks (BPNN) and hybrid approaches combining BPNN with Genetic Algorithms (GA), are being explored for tasks like predicting piezometric levels in earth dams. These models learn complex, nonlinear relationships directly from monitoring data, complementing physics-based FEM models that rely on defined material properties and boundary conditions. A hybrid BPNN-GA model leverages GA for optimizing the initial weights and thresholds of the BPNN, potentially improving its training efficiency and predictive performance. Comparison studies evaluating these AI models against FEM and actual monitoring data show that AI models, especially standard BPNN in one studied case, can achieve a more precise alignment with observed piezometric level variations compared to FEM, which relies on idealized conditions. While FEM provides a useful reference based on theoretical assumptions, AI models demonstrate strong potential for predicting real-world behavior influenced by unmodeled environmental factors. The use of performance metrics like MSE, MAE, and MAPE quantifies the predictive accuracy and allows for comparison between different models, highlighting the benefits of AI in handling nonlinearity and learning from historical data [5].

Table 2. Comparison of Prediction Model Performance based on Error Metrics (Adapted from AI Prediction Study [5] for Piezometer P06)

Prediction Model	MSE	MAE	MAPE (%)
BPNN	0.0214	0.0164	4.03
BPNN-GA	0.0676	0.0590	14.63

As shown in Table 2, comparison studies evaluating these AI models against FEM and actual monitoring data show that AI models, especially standard BPNN in this case, can achieve a more precise alignment with observed piezometric level variations compared to FEM, which relies on idealized conditions. While FEM provides a useful reference based on theoretical assumptions, AI models demonstrate strong potential for predicting real-world behavior influenced by unmodeled environmental factors. The use of performance metrics like MSE, MAE, and MAPE quantifies the predictive accuracy and allows for comparison between different models, highlighting the benefits of AI in handling nonlinearity and learning from historical data. The lower error metrics for BPNN compared to BPNN-GA for this specific piezometer indicate its superior predictive accuracy in this context [5].

4. Discussion

The reviewed studies collectively demonstrate the significant advancements in geotechnical analysis of earth dams driven by the integration of numerical methods and computational intelligence. Numerical tools like FEM and Limit Equilibrium methods [2] provide the fundamental framework for simulating complex geotechnical processes (stress-strain, fluid flow, stability analysis, failure mechanisms) under

various boundary conditions and material properties. This is evident in analyses of rapid drawdown [3,9,10, 11], fissured soil [6,12,13], and various seepage control designs [4,1,7,8]. These methods allow for detailed visualization of critical phenomena such as changing pore pressure fields, evolution of safety factors, formation of slip surfaces, and spatial distribution of displacements and internal forces.

The challenges posed by complex material behavior (fissured soil), transient conditions (rapid drawdown), and the need for optimizing mitigation measures highlight the need for sophisticated modeling capabilities. Parametrized numerical studies, such as the detailed analysis of combined cutoff walls and horizontal drains at the Krerish Dam [8], are invaluable for optimizing design choices, revealing optimal depths, solubilities, types (pipe vs. horizontal), positions, and lengths [4,1, 7, 8]. The Krerish Dam study specifically highlights the significant benefits of combining measures and optimizing their configuration for substantial reductions in discharge seepage, exit gradient, and uplift pressure [8], as quantitatively summarized in Table 1.

Furthermore, the integration of AI and hybrid techniques represents a promising avenue for enhancing geotechnical analysis, particularly in dealing with data-driven prediction and complex nonlinear systems [5]. As shown in the case of piezometric level prediction [5], and summarized by error metrics in Table 2, data-driven models can complement or even outperform traditional physics-based models in capturing real-world variability and nonlinearities, especially when validated against comprehensive monitoring data. AI offers potential for enhanced prediction, parameter identification (inverse problems), and optimization of design parameters.

Future research directions could involve more tightly coupled multi-physics simulations (e.g., integrating seepage, mechanical deformation, and thermal effects), developing more sophisticated constitutive models that explicitly account for complex features like anisotropy and evolving fissure networks, and further leveraging AI for real-time monitoring data interpretation, anomaly detection, and predictive maintenance of earth dams. Validating these advanced models with extensive field data remains crucial for ensuring their reliability and practical applicability.

5. Conclusion

This review, based on a set of recent research articles, illustrates the state-of-the-art in applying computational techniques to analyze the stability and seepage of earth dams. Numerical methods like FEM and Limit Equilibrium are established tools providing fundamental insights into structural behavior under challenging conditions such as rapid drawdown and the presence of fissured materials. Parametric numerical studies are essential for optimizing seepage control measures like cutoff walls and drainage systems, with findings highlighting the critical influence of design parameters like depth, permeability, drain type, location, and diameter on effectiveness and overall stability.

Specifically, detailed studies on the Krerish Dam demonstrate the significant benefits of combined countermeasures. Optimizing the depth and position of cutoff walls and the length of horizontal drains can achieve substantial reductions in discharge seepage, exit gradient, and uplift pressure, crucial for preventing internal erosion and maintaining stability. The analysis of error metrics further underscores the importance of integrating cutoff wall depth into seepage control designs for increased prediction accuracy and effectiveness. The review also highlights the growing capacity of engineers to leverage AI and hybrid techniques for predicting complex geotechnical variables like piezometric levels, offering improved accuracy and robustness compared to traditional methods in specific scenarios. Collectively, these papers underscore the importance of integrating and developing sophisticated computational tools for robust analysis, optimization, and prediction in the design and monitoring of earth dams. Continued validation with field data is key to ensuring the safety, reliability, and resilience of these critical structures.

References

- [1] International Commission on Large Dams ICOLD (2017) Internal Erosion of Existing Dams, Levees and Dikes, and their Foundations. Accessed 15 Sep 2022.
- [2] Duncan, J. M. (1996). State of the art: limit equilibrium and finite-element analysis of slopes. *J Geotech Eng*, 122, 577–596.
- [3] Charrak, H., Smail, N., Rouissat, B., Basri, H., & Alsamawi, A. B. (2024). Analysis of upstream slope stability during rapid drawdown - Sidi Abdelli dam as a case study. *J. Geomec. Geoeng.*, 2, 1-6.
- [4] Charrak, H., Smail, N., & Rouissat, B. (2022). Parameterized analysis relating to the influence parameters of injections and drainages in dams foundations. Case of El izdihar dam, Sidi Abdelli, Algeria. *Modeling Earth Systems and Environment*, 8, 2991–3004. <https://doi.org/10.1007/s40808-021-01277-3>
- [5] Harbi, L., Smail, N., Rouissat, B., & Charrak, H. (2024). Assessing single and hybrid AI approaches in conjunction with FEM to enhance seepage prediction in earth dams. *Modeling Earth Systems and Environment*, 10, 2421–2433. <https://doi.org/10.1007/s40808-023-01903-2>
- [6] Taleb, H. A., Guemidi, I., & Charrak, H. (2024). Numerical investigation of dam stability in the presence of fissured materials with varying angles. *Natural Hazards*, 120, 5743–5761. <https://doi.org/10.1007/s11069>
- [7] Charrak, H., Taleb, H. A., Loualbia, H., & Bouguerba, S. E. (2025). Comparative analysis of horizontal and pipe drains in earth dams: optimizing seepage control and stability (case study). *Environmental Earth Sciences*, 84, 39. <https://doi.org/10.1007/s12665-024-12065-4>
- [8] Charrak, H., Loualbia, H., & Kismoune, Y. (2025). Optimizing Seepage Control in Earth Dams: A Case Study of Krerish Dam with Combined Countermeasures. *Sadhana Journal*, Pages 1-17.
- [9] Berilgen, M. M. (2007). Investigation of stability of slopes under drawdown conditions. *Computers and Geotechnics*, 34(2), 81-91.
- [10] Fattah, M. Y., Omran, H. A., & Hassan, M. A. (2015). Behavior of an earth dam during rapid drawdown of water in reservoir—case study. *International Journal of Advanced Research*, 3(10), 110-122.
- [11] Azadi, A., Esmatkhan Irani, A., Azarafza, M., Hajialilue Bonab, M., Sarand, F. B., & Derakhshani, R. (2022). Coupled numerical and analytical stability analysis charts for an earth-fill dam under rapid drawdown conditions. *Applied Sciences*, 12(9), 4550.
- [12] Davis, E. H. (1980). The behavior of fissured soil with regular sets of joints. *Géotechnique*, 30(1), 47–65.
- [13] Zheng, H. W., Chen, J. J., & Wu, J. Y. (2000). Failure criteria for fissured soil. *Computer Geotech*, 27(6), 495–512.
- [14] Duncan, J. M. (1996). State of the art: limit equilibrium and finite-element analysis of slopes. *J Geotech Eng*, 122, 577–596.



Vitamin C as adjuvant therapy in diabetes management

Wesam M. Hussein

Chemistry Department, Faculty of Science, Islamic University of Madinah, KSA,

wesammeckawy@yahoo.com, 400750@iu.edu.sa

Abstract:

Diabetes mellitus is a long-term metabolic condition marked by high blood sugar levels due to issues with insulin secretion, its action, or a combination of both. Effective management of blood glucose levels is essential to prevent complications associated with diabetes. Recent studies have highlighted the potential role of Vitamin C, a vital water-soluble vitamin, in diabetes management. This review aims to explore the relationship between Vitamin C and diabetes, focusing on its antioxidant properties, effects on glucose metabolism, and implications for diabetes-related complications.

Vitamin C, or ascorbic acid, is renowned for its antioxidant capabilities and essential functions in various biological processes. Emerging research underscores its significance in glucose metabolism, particularly regarding insulin sensitivity and diabetes management. This article examines how Vitamin C influences glucose metabolism through mechanisms such as insulin signaling, modulation of oxidative stress, reduction of inflammation, and facilitation of glucose transport.

Additionally, the review discusses recent findings on Vitamin C's effects on glycemic control and its potential to alleviate diabetes-related complications. By elucidating these relationships, this review provides insights into the therapeutic potential of Vitamin C in enhancing metabolic health and improving outcomes for individuals with diabetes.

Keywords: Vitamin C, Diabetes, Antioxidant, Insulin Resistance.

<https://doi.org/10.63070/jesc.2025.017>

Received 12 April 2025; Revised 15 May 2025; Accepted 24 May 2025.

Available online 28 May 2025.

Published by Islamic University of Madinah on behalf of *Islamic University Journal of Applied Sciences*. This is a free open access article.

1. Introduction

Vitamin C, scientifically referred to as ascorbic acid, is a vitamin that dissolves in water, is essential for various bodily functions and is vital for many physiological processes. It functions as a strong antioxidant and is important for immune support [1]. Additionally, Vitamin C serves as a cofactor in several enzymatic reactions [2]. Its antioxidant characteristics come from its ability to neutralize free radicals and regenerate other antioxidants like Vitamin E [3]. Furthermore, it protects cells from oxidative stress, which is a major factor in the onset of diabetes and its complications [4].

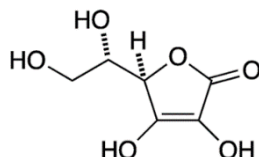


Figure1: Vitamin C Structure

1.1. Vitamin C functions as a potent water-soluble antioxidant in several ways:

Direct Scavenging of Free Radicals: Vitamin C can directly interact with free radicals like superoxide radicals, hydroxyl radicals, and singlet oxygen, effectively neutralizing them. This process helps to prevent oxidative damage to lipids, proteins, and nucleic acids [5], which in turn reduces oxidative stress on pancreatic β -cells and enhances insulin secretion [6].

Regeneration of Other Antioxidants: Vitamin C also plays a role in regenerating other antioxidants, such as Vitamin E, thereby bolstering the body's antioxidant defenses and protecting cells from oxidative harm [7].

Metal Ion Chelation: Vitamin C has the ability to bind with metal ions, such as iron and copper, which can catalyze free radical formation through Fenton reactions. By chelating these metal ions, Vitamin C helps to diminish the risk of oxidative stress [8].

Influence on Gene Expression: Research has demonstrated that Vitamin C can influence the expression of genes related to oxidative stress responses and antioxidant defense mechanisms. For instance, it can promote the expression of heme oxygenase-1, an enzyme known for its antioxidant properties [9].

2. Health Benefits of Vitamin C

1. Immune Support and Infection Resistance

Vitamin C boosts immune defense by strengthening epithelial barrier function and increasing phagocytic activity [1]. A meta-analysis indicated that vitamin C supplementation can lessen both the duration and severity of respiratory infections [10]. It enhances the activity of leukocytes, supports the integrity of epithelial barriers, and modulates cytokine production [11]. Additionally, it has been shown to stimulate the production of white blood cells, which are crucial for combating infections [12].

2. Cardiovascular Health

Vitamin C enhances endothelial function and diminishes oxidative stress, potentially reducing the risk of cardiovascular disease. Its antioxidant properties help prevent the oxidation of LDL cholesterol, a significant factor in the development of atherosclerosis [13].

3. Skin Health and Wound Healing

Vitamin C is crucial for the hydroxylation of proline and lysine residues during collagen synthesis, which is vital for the structure of skin, blood vessels, bones, and connective tissues [14].

4. Cognitive Function and Neuroprotection

Vitamin C may offer protection against neurodegenerative diseases by counteracting oxidative stress in the brain. Studies suggest that individuals with higher dietary intake of Vitamin C may experience a lower risk of cognitive decline [15].

Unlike most animals, humans cannot synthesize Vitamin C due to a mutation in the L-gulonolactone oxidase (GULO) gene, making dietary sources essential [16]. Vitamin C is plentiful in fruits and vegetables, particularly in citrus fruits, strawberries, kiwi, bell peppers, and leafy greens [17].

3. Diabetes mellitus

Diabetes mellitus (DM) is a chronic condition characterized by inadequate insulin secretion or insulin resistance [18]. It affects nearly half a billion people worldwide, with projections indicating that this number could rise to 700 million by 2045 [19]. The prevalence of abnormal glucose tolerance among adults is expected to reach 8.0% by 2030 and increase to 8.6% by 2045 [20]. Poor glycemic control can lead to serious complications, including retinopathy, neuropathy, and nephropathy [21].

Various strategies, including physical activity, diet, and dietary supplements, have been proposed to improve DM complications [22-26]. There is also evidence that oxidative stress and chronic low-grade inflammation contribute to the progression and onset of DM. Therefore, a healthy diet rich in antioxidants may help reduce the risk of developing diabetes [27, 28].

Optimal antioxidant intake may lower the likelihood of developing DM and its associated complications, as antioxidant supplements can normalize lipid peroxidation levels and cellular markers of oxidative stress [28]. Oxidative reactions may exacerbate DM by promoting insulin resistance and hindering insulin secretion [29]. The antioxidant properties of Vitamin C can mitigate oxidative stress, potentially lowering the risk of DM [30].

Some studies have shown that Vitamin C supplementation can significantly reduce hemoglobin A1c (HbA1c) and fasting blood glucose (FBG) levels [31, 32]. However, other research has found no significant effects of Vitamin C supplements on HbA1c, FBG, or insulin levels [33, 34].

Effective diabetes management typically includes lifestyle changes, glucose monitoring, and pharmacological treatments. Recently, there has been increasing interest in the role of dietary antioxidants, particularly Vitamin C, in enhancing glycemic control and reducing diabetes-related complications.

Oxidative stress is crucial in developing insulin resistance and advancing diabetes [35]. By scavenging reactive oxygen species (ROS) and regenerating other antioxidants like Vitamin E, Vitamin C helps alleviate oxidative damage, potentially improving insulin sensitivity and glucose metabolism [36].

4. Vitamin C and glucose metabolism

Several studies have suggested that Vitamin C may influence glucose metabolism through various mechanisms:

- **Enhancing Insulin Sensitivity:** Vitamin C may improve insulin sensitivity by modulating the signaling pathways involved in insulin action [37].
- **Reducing Inflammation:** Chronic inflammation is a characteristic of type 2 diabetes. Vitamin C may exert anti-inflammatory effects, indirectly enhancing insulin sensitivity and glycemic control [38].
- **Regulating Glucose Transporters:** Vitamin C has been shown to upregulate glucose transporter proteins, facilitating glucose uptake in tissues [39].

A randomized controlled trial by Rahman et al. evaluated the impact of Vitamin C supplementation on glycemic control in patients with type 2 diabetes. Participants received 500 mg of Vitamin C daily for 12 weeks, resulting in significant reductions in fasting blood glucose levels and HbA1c, suggesting improved insulin sensitivity. The study indicated that Vitamin C enhances insulin signaling pathways, possibly through AMPK activation [40].

A meta-analysis by Nascimento et al. reviewed multiple studies assessing Vitamin C supplementation's effects on glycemic control and found significant improvements in fasting blood glucose and HbA1c levels across different populations, highlighting its potential as an adjunct therapy for diabetes management [41]. A cross-sectional study indicated that individuals with higher dietary Vitamin C intake had a lower risk of developing type 2 diabetes mellitus (T2DM), particularly among those with elevated BMI. This protective effect may be due to Vitamin C's antioxidant and anti-inflammatory properties, as well as its role in enhancing insulin sensitivity [42].

Vitamin C has been shown to enhance the expression and translocation of GLUT4, thereby increasing glucose uptake in muscle and adipose tissues:

- **Insulin Signaling Pathway:** In addition to its effects on AMPK, Vitamin C may amplify insulin signaling pathways that facilitate GLUT4 translocation. Insulin binding to its receptor triggers a cascade of signaling events that lead to GLUT4 movement to the cell membrane [43]. Vitamin C may enhance this response, promoting increased glucose uptake.
- **Direct Modulation of GLUT4:** Some studies suggest that Vitamin C can directly influence GLUT4 expression and activity, independently of insulin. This mechanism may provide an alternative pathway for enhancing glucose uptake, particularly in insulin-resistant states [39].

5. Vitamin C and Insulin Resistance

Insulin resistance is a key feature of type 2 diabetes, and improving insulin sensitivity is crucial for effective diabetes management. This section explores the impact of Vitamin C on insulin resistance.

Vitamin C may enhance insulin sensitivity through several mechanisms, including:

- **Reduction of Oxidative Stress:** By decreasing oxidative stress, Vitamin C may enhance insulin signaling pathways and improve glucose uptake in tissues [35].
- **Modulation of Inflammatory Cytokines:** Vitamin C has been shown to lower levels of pro-inflammatory cytokines, which contribute to insulin resistance [38].

A study demonstrated that Vitamin C supplementation improved insulin sensitivity in overweight and obese individuals with insulin resistance [44]. Additionally, a meta-analysis indicated significant reductions in insulin resistance parameters, including HOMA-IR, in diabetic patients [45].

Insulin sensitivity refers to how responsive cells are to insulin, the hormone responsible for facilitating glucose uptake. Impaired insulin sensitivity is a primary contributor to the development of T2DM. Vitamin C has been shown to enhance insulin sensitivity through several pathways:

- **AMP-Activated Protein Kinase (AMPK) Activation:** AMPK is crucial for regulating cellular energy homeostasis. Vitamin C activates AMPK, leading to increased glucose uptake in muscle cells and improved insulin sensitivity. This activation promotes the translocation of glucose transporter type 4 (GLUT4) to the cell membrane, facilitating glucose uptake [39, 43].
- **Reduction of Lipid Accumulation:** Excessive lipid accumulation in tissues can lead to insulin resistance. Vitamin C inhibits lipid accumulation and promotes fatty acid oxidation, which contributes to improved insulin sensitivity [37].

Chronic inflammation is closely linked to the development of insulin resistance and T2DM. Vitamin C exerts anti-inflammatory effects that can positively influence glucose metabolism:

- **Reduction of Pro-inflammatory Cytokines:** Vitamin C decreases levels of cytokines such as tumor necrosis factor-alpha (TNF- α) and interleukin-6 (IL-6), which are involved in insulin resistance [38]. By modulating inflammation, Vitamin C may mitigate its adverse effects on insulin signaling.
- **Regulating Nuclear Factor Kappa B (NF- κ B):** NF- κ B is a transcription factor that regulates inflammatory gene expression. Vitamin C can inhibit NF- κ B activation, leading to reduced inflammation and improved insulin sensitivity [46].

6. Vitamin C and Diabetes-Related Complications

Diabetes is associated with several complications, including cardiovascular disease, neuropathy, retinopathy, and nephropathy. Vitamin C may offer protective effects against these complications:

Cardiovascular Disease: Individuals with diabetes are at higher risk for cardiovascular diseases due to oxidative stress and inflammation. Vitamin C's antioxidant properties may help reduce this risk. A systematic review found that Vitamin C supplementation was associated with lower blood pressure and improved endothelial function in diabetic patients [42].

Diabetic Neuropathy: This common complication involves nerve damage due to hyperglycemia and oxidative stress. Research demonstrated that Vitamin C supplementation improved nerve conduction velocity and reduced neuropathic symptoms in patients with diabetic neuropathy [47].

Diabetic Retinopathy: A leading cause of blindness among diabetic patients, diabetic retinopathy may be mitigated by Vitamin C, which protects retinal cells from oxidative damage and inhibits progression in animal models [48].

7. Conclusion

Vitamin C is an essential nutrient that offers a wide range of health benefits, from supporting immune function to aiding in collagen synthesis. Its emerging role in diabetes management, particularly through its antioxidant properties and effects on glycemic control, highlights its potential as a complementary strategy for individuals with diabetes. While the current evidence is promising, further research is crucial to determine optimal dosages and treatment protocols for Vitamin C supplementation.

Incorporating Vitamin C-rich foods into the diet can enhance overall well-being and may help mitigate diabetes-related complications. As diabetes prevalence continues to rise globally, understanding the mechanisms by which Vitamin C influences glucose metabolism will be vital for developing effective therapeutic approaches. Future studies should prioritize these areas to fully unlock the potential of Vitamin C in diabetes management, ultimately leading to improved health outcomes for those affected by this condition.

References

- [1] Carr, A. C., & Maggini, S. (2017). Vitamin C and immune function. *Nutrients*, 9(11), 1211.
- [2] Carr, A. C., & Frei, B. (2020). Vitamin C and cancer: a review. *Journal of Nutritional Biochemistry*, 78, 108319.
- [3] Halliwell, B. (2020). Free radicals and antioxidants: A personal view. *Nutrition Reviews*, 78(8), 680-686.
- [4] Bendich, A., & Langseth, L. (2020). The health effects of vitamin C. *Journal of the American College of Nutrition*, 39(7), 631-636.
- [5] Carr, A. C., & Frei, B. (1999). Toward a new recommended dietary allowance for vitamin C based on antioxidant and health effects in humans. *The American Journal of Clinical Nutrition*, 69(6), 1086-1107.
- [6] Takahashi, M., et al. (2020). Vitamin C improves insulin secretion and protects β -cells from oxidative stress in a type 2 diabetes model. *Diabetes*, 69(7), 1406-1418.
- [7] Packer, L., et al. (2020). Vitamin C and the regulation of cellular oxidative stress. *Free Radical Biology and Medicine*, 158, 1-10.
- [8] Halliwell, B., & Gutteridge, J. M. C. (2007). *Free Radicals in Biology and Medicine*. Oxford University Press.

- [9] Bendich, A., & Langseth, L. (1995). The health effects of vitamin C. *Journal of the American College of Nutrition*, 14(3), 227-230.
- [10] Hemilä, H., & Chalker, E. (2019). Vitamin C for preventing and treating the common cold. *Cochrane Database of Systematic Reviews*, 2019(6) .
- [11] Hemilä, H. (2017). Vitamin C and infections. *Nutrients*, 9(4), 339. <https://doi.org/10.3390/nu9040339>
- [12] Carr, A. C., & Frei, B. (2000). Does vitamin C act as a pro-oxidant under physiological conditions? *The FASEB Journal*, 14(9), 1007-1024.
- [13] Rosenblat, M., et al. (2006). Vitamin C and cardiovascular disease: a review. *Journal of Nutritional Biochemistry*, 17(10), 657-670.
- [14] DePhillipo, J. J., Aman, Z. S., Kennedy, M. I., Begley, J. P., Moatshe, G., & LaPrade, R. F. (2018). Efficacy of vitamin C supplementation on collagen synthesis and oxidative stress after musculoskeletal injuries: A systematic review. *Sports Health*, 10(6), 537–543. <https://doi.org/10.1177/1941738118804544>
- [15] Morris, M. C., et al. (2002). Dietary intake of antioxidant nutrients and the risk of incident Alzheimer disease. *Archives of Neurology*, 59(6), 940-946.
- [16] Drouin, G., Godin, J.-R., & Pagé, B. (2011). The genetics of vitamin C loss in vertebrates. *Genetics*, 188(4), 773–783. <https://doi.org/10.1534/genetics.111.127696>
- [17] National Institutes of Health (NIH), Office of Dietary Supplements. (2021). Vitamin C: Fact sheet for health professionals. <https://ods.od.nih.gov/factsheets/VitaminC-HealthProfessional/>
- [18] Roden M, Shulman GI. The integrative biology of type 2 diabetes. *Nature* 2019;576 (7785):51–60.
- [19] Saeedi P, Petersohn I, Salpea P, et al. Global and regional diabetes prevalence estimates for 2019 and projections for 2030 and 2045: results from the international diabetes federation diabetes atlas. *Diabetes Res Clin Pract* 2019;157: 107843.
- [20] Atlas D. International diabetes federation. IDF diabetes atlas. seventh ed. Brussels, Belgium: International Diabetes Federation; 2015.
- [21] Stratton IM, Adler AI, Neil HAW, et al. Association of glycaemia with macrovascular and microvascular complications of type 2 diabetes (UKPDS 35): prospective observational study. *Bmj* 2000;321(7258):405–12.
- [22] Asbaghi O, Fouladvand F, Gonzalez MJ, Ashtary-Larky D, Choghakhori R, Abbasnezhad A. Effect of green tea on glycemic control in patients with type 2 diabetes mellitus: a systematic review and meta-analysis. *Diabetes Metabol Syndr: Clin Res Rev* 2021;15(1):23–31.
- [23] Asbaghi O, Fouladvand F, Moradi S, Ashtary-Larky D, Choghakhori R, Abbasnezhad A. Effect of green tea extract on lipid profile in patients with type 2 diabetes mellitus: a systematic review and meta-analysis. *Diabetes Metabol Syndr: Clin Res Rev* 2020;14(4):293–301.
- [24] Namkhah Z, Ashtary-Larky D, Naeini F, Clark CC, Asbaghi O. Does vitamin C supplementation exert profitable effects on serum lipid profile in patients with type 2 diabetes? A systematic review and dose-response meta-analysis. *Pharmacol Res* 2021;169:105665.
- [25] Noormohammadi M, Eslamian G, Malek S, Shoaibinobarian N, Mirmohammadali SN. The association between fertility diet score and polycystic ovary syndrome: a Case-Control study. *Health Care Women Int* 2022;43(1–3): 70–84. 13 S. Nosratabadi et al. Diabetes & Metabolic Syndrome: Clinical Research & Reviews 17 (2023) 102824
- [26] Shoaibinobarian N, Eslamian G, Noormohammadi M, Malek S, Rouhani S, Mirmohammadali SN. Dietary total antioxidant capacity and risk of polycystic ovary syndrome: a case-control study. *International Journal of Fertility and Sterility* 2022;16(3):200–5.
- [27] Paolisso G, Balbi V, Volpe C, et al. Metabolic benefits deriving from chronic vitamin C supplementation in aged non-insulin dependent diabetics. *J Am Coll Nutr* 1995;14(4):387–92.

- [28] Jafari N, Shoaibinobarian N, Dehghani A, et al. The effects of purslane consumption on glycemic control and oxidative stress: a systematic review and dose–response meta-analysis. *Food Sci Nutr*. 2023 Mar 15;11(6):2530-2546
- [29] Scott JA, King GLJ. Oxidative stress and antioxidant treatment in diabetes. *Ann N Y Acad Sci* 2004;1031(1):204–13.
- [30] Christie-David DJ, Girgis CM, Gunton JE. Effects of vitamins C and D in type 2 diabetes mellitus. *Nutr Diet Suppl* 2015;7:21–8.
- [31] Eshak ES, Iso H, Muraki I, Tamakoshi A. Among the water-soluble vitamins, dietary intakes of vitamins C, B 2 and folate are associated with the reduced risk of diabetes in Japanese women but not men. *Br J Nutr* 2019;121(12):1357–64.
- [32] Afkhami-Ardekani M, Shojaoddiny-Ardekani A. Effect of vitamin C on blood glucose, serum lipids & serum insulin in type 2 diabetes patients. *Indian J Med Res* 2007;126(5):471.
- [33] Mahmoudabadi MMS, Djalali M, Djazayeri SA, et al. Effects of eicosapentaenoic acid and vitamin C on glycemic indices, blood pressure, and serum lipids in type 2 diabetic Iranian males, vol. 16; 2011. p. S361. Suppl1.
- [34] Mason SA, Rasmussen B, van Loon LJ, Salmon J, Wadley GD. Ascorbic acid supplementation improves postprandial glycaemic control and blood pressure in individuals with type 2 diabetes: findings of a randomized cross-over trial. *Diabetes Obes Metabol* 2019;21(3):674–82.
- [35] Bae, H., Kim, J., & Lee, M. (2020). The role of oxidative stress in diabetes: A review. *Molecules*, 25(24), 6183.
- [36] Packer, L., et al. (2020). Vitamin C and the regulation of cellular oxidative stress. *Free Radical Biology and Medicine*, 158, 1-10.
- [37] Huang, X., et al. (2021). Vitamin C inhibits lipid accumulation and improves insulin sensitivity in 3T3-L1 adipocytes. *Nutrients*, 13(4), 1177.
- [38] Jiang, Y., et al. (2020). Vitamin C reduces inflammation and improves insulin sensitivity in type 2 diabetes. *Journal of Clinical Endocrinology & Metabolism*, 105(7), 1120-1130.
- [39] Cao, Y., Yang, H., & Liu, J. (2021). Vitamin C enhances glucose uptake in L6 myotubes through the AMPK signaling pathway. *Nutrients*, 13(1), 85.
- [40] Rahman, M. M., et al. (2021). The effect of vitamin C supplementation on glycemic control in patients with type 2 diabetes: A randomized controlled trial. *Diabetes & Metabolic Syndrome: Clinical Research & Reviews*, 15(2), 613-620.
- [41] Nascimento, C. M., et al. (2022). The effects of vitamin C supplementation on glycemic control in patients with type 2 diabetes: A meta-analysis. *Clinical Nutrition*, 41(3), 575-583.
- [42] Zhang, X., et al. (2020). Dietary vitamin C intake and risk of type 2 diabetes: A cross-sectional study. *Nutrients*, 12(9), 2662.
- [43] Kahn, B. B., et al. (2005). Insulin action in insulin-resistant states. *Diabetes*, 54(Supplement 2), S5-S10.
- [44] Gao, Y., Zhang, X., & Wang, Y. (2021). Effects of vitamin C supplementation on insulin sensitivity in overweight and obese individuals: A randomized controlled trial. *Nutrients*, 13(2), 561.
- [45] Zhao, L., et al. (2023). Effects of vitamin C supplementation on insulin resistance: A systematic review and meta-analysis. *Nutrients*, 15(1), 123.
- [46] Li, Y., et al. (2021). Vitamin C inhibits NF-κB activation and reduces inflammation in insulin-resistant hepatocytes. *Journal of Nutritional Biochemistry*, 96, 108802.
- [47] Hamza, M., et al. (2021). Vitamin C supplementation improves diabetic neuropathy: A randomized controlled trial. *Journal of Diabetes Research*, 2021, 1-8.
- [48] Kowluru, R. A., et al. (2020). Vitamin C protects retinal cells from oxidative stress and inhibits the progression of diabetic retinopathy in animal models. *Diabetes*, 69(4), 874-885.